Ligand exchange reactions on thiolate-protected gold nanoclusters

Wang, Yanan

UNIVERSITÉ DE GENÈVE
Section de chimie et biochimie
Département de chimie physique

FACULTÉ DES SCIENCES

Professeur Thomas Bürgi

Ligand Exchange Reactions on Thiolate-protected Gold Nanoclusters

THÈSE

présentée à la Faculté des sciences de l'Université de Genève
pour obtenir le grade de Docteur ès sciences, mention chimie

par

Yanan WANG

de
Jinan (Chine)

Thèse N°5628

GENÈVE
Atelier Repromail – Uni Mail
2021

UNIVERSITÉ DE GENÈVE

FACULTÉ DES SCIENCES

DOCTORAT ÈS SCIENCES, MENTION CHIMIE

Thèse de Madame Yanan WANG

intitulée :

«Ligand Exchange Reactions on Thiolate-protected Gold Nanoclusters»

La Faculté des sciences, sur le préavis de Monsieur T. BÜRGI, professeur ordinaire et directeur de thèse (Département de chimie physique), Madame E. BORDIGNON, professeure ordinaire (Département de chimie physique), Madame R. ODA, professeure (Institut Européen de Chimie et Biologie, Pessac, France), autorise l'impression de la présente thèse, sans exprimer d'opinion sur les propositions qui y sont énoncées.

Genève, le 16 décembre 2021

Thèse - 5628 -

Le Doyen

N.B. - La thèse doit porter la déclaration précédente et remplir les conditions énumérées dans les "Informations relatives aux thèses de doctorat à l'Université de Genève".

Acknowledgements

First of all, I would like to thank my supervisor Prof. Thomas Bürgi for the past four years of help and support during my PhD study. To me, Thomas is more than a supervisor, he was always willing to guide me not only for the science but also for my mental and physical health. The evaluations he offered me every half year witness my growing up as an independent researcher and really give me a lot of motivation to become better and better. The flexible atmosphere he built in the group give us enough space to explore the science and encouraged me to develop my own idea even sometimes it did not work. I am so glad I can work in his group and participate to international conferences, external meetings, and seminars with him together. Thomas is the role model for my further career.

Next, I would like to show my appreciation to my jury members Dr. Reiko Oda and Prof. Enrica Bordignon for taking time to review my thesis.

I would like to thank Dr. Belen Nieto-Ortega, who guided me for my first year and a half during my PhD study. As a postdoc, she really took the responsibility to show me the lab and design the experiments at the beginning of my PhD. I really learned a lot from her about how to balance the daily life and work. Even now, we are still close friends and contact with each other frequently. Belen offers me important advice for my research and further plan from her view which is important to me.

I am also grateful to Ewa and Ani for their help concerning the HPLC measurements. Because of their endless patience to answer my questions even after work, I get to know and working with HPLC faster. I also want to pass my thanks to Rania for the MALDI measurements and plate cleaning, also to Sahar for the homemade cake during the time we shared the office. I also pass my thanks to Khadijetou Ahmed Ethmane for helping me translate the Résumé. For the present and former group members, I will remember the time we share the lab life together for the birthday cake, group BBQ and apéro.

The mass spectrometry core facility group, especially Eliane Sandmeier and Harry Theraulaz, are acknowledged for the ESI measurements and MALDI-TOF training.

I also want to say thanks to Catherine Ludy for her help. The connection between me and Catherine started 5 months before I came to Geneva, and without her help with the related paperwork and guidance I would probably not be here today.

A very special acknowledgment to all my friends in Geneva and near around who have encouraged me all the time as my best support, especially Xiaoyue, Deliah, Jiaotao, and Luca…for their emotional support and the many discussions about life. They always give me light when I was suffering during the dark times.

And last but not least, I am grateful to my family in China who always provided me all the motivation and support during my study in Geneva. They are the final reason for all my effort in my life.

Thank you for all your encouragement!

Abstract

Thiolate-protected gold nanoclusters are ultra-small, large specific surface area multifunctional materials, and have gained large interest from chemists, biologist, and medical scientists during the past decades. The progress in this field, for example, on precise synthesis, metal doping, and application of gold nanoclusters have shown huge acceleration. In general, the chemical properties of gold nanoclusters, like solubility and interactions with the environment, mainly depend on the ligand shell. In order to impart complex properties to the nanoclusters, modifying the ligand shell with the desired functions is a promising strategy.

Ligand exchange reaction (LER), in which one or more ligands are replaced by a different one, is an important post-synthesis method for modifying the ligand shell and extending the properties and functions of gold nanoclusters. The flexibility of the gold-sulfur interface of gold nanoclusters is the driving force for the process. During this thesis, we will investigate the ligand exchange reaction on thiolate-protected gold nanoclusters.

Normally, LER will not cause structure and size change of the reacting cluster. However, at specific conditions, this may happen. In our project, the $Au_{25}(SR)_{18}$ clusters transformed into $Au_{28}(SR)_{21}$ clusters induced by LERs. In contrast to other reported cluster transformations, which proceed during LERs with elevated temperature and large excess of incoming ligands, the transformation illustrated here occurs under mild condition (room temperature and very low thiol excess) with a chiral ligand. A difference of one methyl group between incoming and outgoing thiol is sufficient to induce the transformation.

Many factors affect the LER of clusters, like chirality, electronic properties and so on. Some of these factors are not well understood and need further exploration. Here, by using a chiral fluoro-substituted ligand, the stereoelectronic and stereospecific effects of ligand during LER on achiral Au_{25} cluster has been investigated. It is demonstrated

that the fluoro-substituted BINAS significantly slows down the LER reaction both at the molecular and the related cluster level. The stereoelectronic effect is global and can be transmitted at the cluster surface, but the stereospecific effect is marginal.

Besides the monothiol ligand, the LERs of gold nanoclusters also takes place with dithiols, for instance, 1,1'-binaphthyl-2,2'-dithiol (BINAS). More interesting, by adsorbing a small amount of a chiral molecule R-BINAS in $Au_{38}(2\text{-PET})_{24}$ cluster (2-PET = 2-phenylethylthiolate) ligand shell, the system will create an amplification of enantiomeric excess at 70 °C. Thus, the anti-clockwise clusters will increase at the expense of the clockwise antipode of the $Au_{38}(2\text{-PET})_{24}$ cluster. Here we show the first successful deracemization of a thiolate-protected nanocluster.

Apart from the LERs taking place between cluster and free ligands, the ligands and metal atoms also easily exchange between clusters. The study of the mechanism of such processes turns out to be challenging. Here, we use a configurationally labile, axially chiral ligand, biphenyl-2,2'-dithiol (R/S-BiDi), as a probe to study dynamic cluster processes. It is shown that the ligand exchange of free R/S-BiDi on a chiral $Au_{38}(2\text{-PET})_{24}$ cluster is diastereospecific. Upon heating, the cluster framework racemizes, whereas the R/S-BiDi ligand does not. This finding demonstrates that during cluster racemization and/or ligand exchange between clusters, the R/S-BiDi ligand is sufficiently confined thus preventing its racemization and excludes the possibility that the ligand desorbs from the cluster surface.

Résumé

Les nanoclusters d'or protégés par des thiolates sont des matériaux multifonctionnels ultra-petits et à grande surface spécifique, et ont suscité un grand intérêt de la part des chimistes, des biologistes et des scientifiques médicaux au cours des dernières décennies. Les progrès dans ce domaine, par exemple, sur la synthèse précise, le dopage des métaux et les applications de nanoclusters d'or ont montré une énorme accélération. En général, les propriétés chimiques des nanoclusters d'or, comme la solubilité et les interactions avec l'environnement, dépendent principalement des ligands. Afin de conférer des propriétés complexes aux nanoclusters, la modification de la coquille de ligands avec les fonctions souhaitées est une stratégie prometteuse.

La réaction d'échange de ligand (LER), dans laquelle un ou plusieurs ligands sont remplacés par un autre, est une méthode post-synthèse importante pour modifier la coquille de ligands et étendre les propriétés et les fonctions des nanoclusters d'or. La flexibilité de l'interface or-soufre des nanoclusters d'or est la force motrice du processus. Au cours de cette thèse, nous étudierons la réaction d'échange de ligand sur des nanoclusters d'or protégés par des thiolates.

Normalement, le LER ne provoquera pas de changement de structure et de taille du réactif. Cependant, dans des conditions spécifiques, cela peut arriver. Dans notre projet, les clusters $Au_{25}(SR)_{18}$ se sont transformés en clusters $Au_{28}(SR)_{21}$ induits par les LER. Contrairement à d'autres transformations de cluster reportées, qui se déroulent au cours de LER avec une température élevée et un grand excès de ligands entrants, la transformation illustrée ici se produit dans des conditions douces (température ambiante et très faible excès de thiol) avec un ligand chiral. Une différence d'un groupe méthyle entre le thiol entrant et sortant est suffisante pour induire la transformation.

De nombreux facteurs affectent le LER des clusters, comme la chiralité, les propriétés électroniques, etc. Certains de ces facteurs ne sont pas bien compris et nécessitent une

exploration plus approfondie. Ici, en utilisant un ligand chiral fluoro-substitué, les effets stéréoélectroniques et stéréospécifiques du ligand pendant le LER sur le cluster Au25 achiral ont été étudiés. Il est démontré que le BINAS fluoro-substitué ralentit considérablement la réactivité du LER à la fois au niveau moléculaire et au niveau du cluster associé. L'effet stéréoélectronique est global et peut être transmis à la surface du cluster, mais l'effet stéréospécifique est marginal.

Mise à part les ligands monothiol, les LER des nanoclusters d'or existent également avec les dithiols, par exemple le 1,1'-binaphtyl-2,2'-dithiol (BINAS). Plus intéressant, en adsorbant une petite quantité d'une molécule chirale R-BINAS dans la coquille de ligand du cluster $Au_{38}(2\text{-PET})_{24}$ (2-PET = 2-phényléthylthiolate), le système créera une amplification de l'excès énantiomérique sous 70 °C. Ainsi, les clusters anti-horaires augmenteront au détriment de l'antipode horaire du cluster $Au_{38}(2\text{-PET})_{24}$. Nous montrons ici la première déracémisation réussie d'un nanocluster protégés par des thiolates.

Outre les LER qui se sont produits entre les clusters et les ligands libres, les ligands et les atomes de métal s'échangent également facilement entre les clusters. L'étude des mécanismes de tels processus s'avère difficile. Ici, nous utilisons un ligand de configuration labile, axialement chiral, le biphényl-2,2'-dithiol (R/S-BiDi), comme sonde pour étudier les processus de cluster dynamique. Il est montré que l'échange de ligand de R/S-BiDi libre sur un cluster $Au_{38}(2\text{-PET})_{24}$ chiral est diastéréospécifique. Lors du chauffage, la structure du cluster racémise, contrairement au ligand R/S-BiDi. Cette découverte démontre que pendant la racémisation et/ou l'échange de ligands entre les clusters, le ligand R/S-BiDi est suffisamment confiné empêchant ainsi sa racémisation et exclut la possibilité que le ligand se désorbe de la surface des clusters.

Contents

Chapter 1

Introduction

1.1 Flexibility of the gold-sulfur interface of gold nanoclusters

During the past decade, the interest in monolayer-protected metal clusters has drastically increased. The progress in the field, for example, on precise synthesis[1-5], metal doping[6,7], and applications of gold nanoclusters[8,9] has huge acceleration. In general, the chemical properties of nanomaterials largely depend on their surface properties and the flexible gold-sulfur interface of nanoclusters. The formation of gold-sulfur bond is the driving force for the anchoring of thiol ligands on either gold surfaces, nanoclusters or nanoparticles[10], leading to the formation of self-assembled monolayers (SAM)[11]. From the available structural and surface property investigations, it revealed that the staple-type binding motif is the preferred structure elements of the gold-sulfur interface, as first been demonstrated by the crystal structure of $Au_{102}SR_{44}$[12]. After the structural clarification of various nanoclusters such as $Au_{25}SR_{18}$, $Au_{38}SR_{24}$ and $Au_{28}SR_{20}$, the bridging motif (Fig. 1.1 A), monomeric staple (Fig. 1.1 B) and dimeric staple motif (Fig 1.1 C) are the common surface structure elements. Actually, the tetrameric staple motif also has been demonstrated in the structure of $Au_{24}(SCH_2Ph\text{-}^tBut)_{20}$[13], and other staple motifs are expected in order to fulfil the different curvature of nanocluster surface.

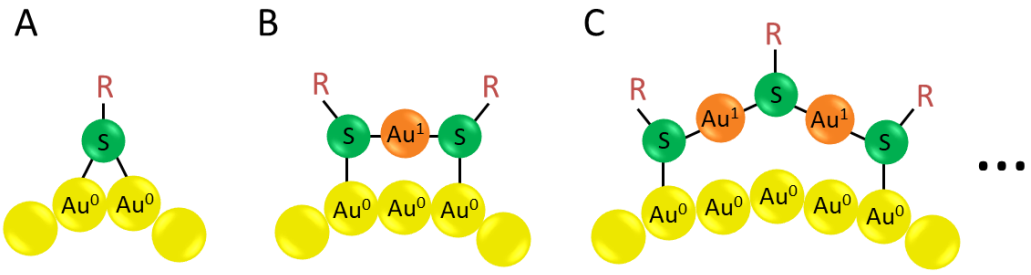

Figure 1.1 Schematic drawing of the bridging thiolate (A), monomeric Au-SR-Au staple motif (B) and dimeric Au-SR-Au-SR-Au staple motif (C). Yellow: Au(0) atom; orange: Au(I) atom; green: sulphur atom.

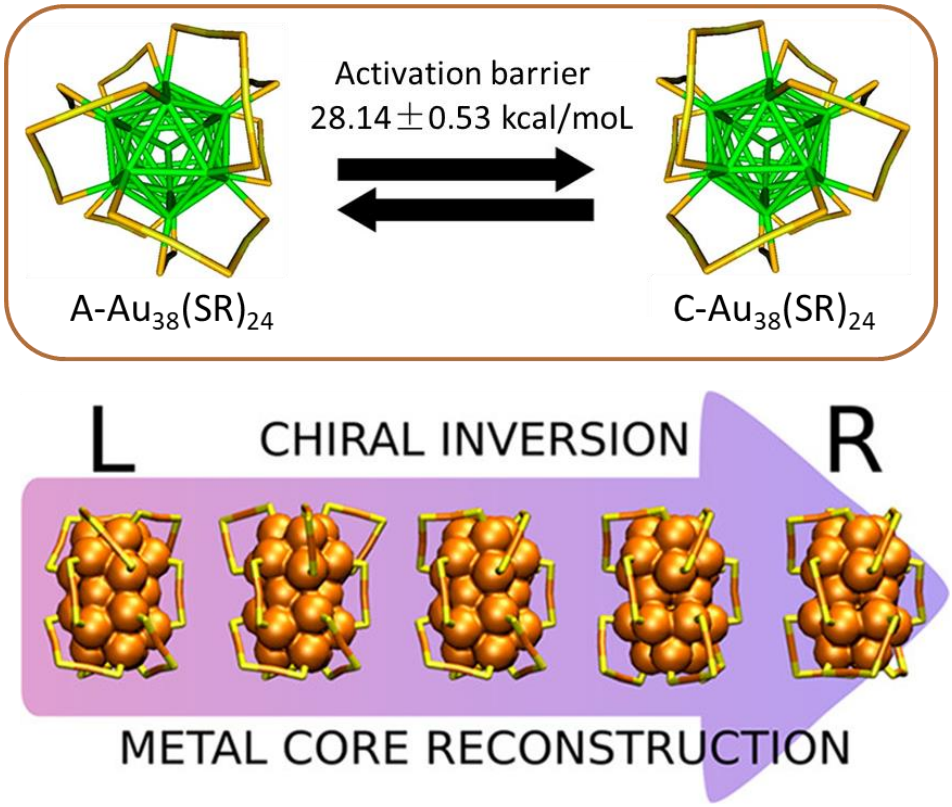

Figure 1.2 Schematic drawing of the racemization reaction of $Au_{38}(SR)_{24}$ clusters along the principal axis of the cluster. (Top) In this scheme, the left-handed cluster (left, A-$Au_{38}(SR)_{24}$) is converted into the right-handed enantiomer (right, C-$Au_{38}(SR)_{24}$) with activation barrier ca. 28 kcal/mol which depending on the experimental results. (Bottom) Density functional theory computational simulation of the chiral inversion on $Au_{38}(SR)_{24}$ clusters through rotation of the gold core. Copyright from references[16,17].

The properties of gold-sulfur interface and its dynamics determine the further functionalization of the thiolate-protected gold nanoclusters and their applications. However, due to the lack of experimental method focusing on the interface, this field was barren for a long time. Since the structure of $Au_{38}(SR)_{24}$ cluster has been solved and shown to be intrinsically chiral due to the chiral arrangement of the dimeric staples at the polar position of the cluster, $Au_{38}(SR)_{24}$ became a good candidate for studying the gold-sulfur interface[14]. Dolamic and co-workers reported the first separation of the enantiomers of Au_{38}(2-PET)$_{24}$ (2-PET = 2-phenylethylthiolate) [15] by chiral high-performance liquid chromatography (HPLC). Using enantiopure $Au_{38}(SR)_{24}$ clusters, Knoppe and co-workers showed that the cluster can racemize (Fig. 1.2 top)[16]. The reaction was started with A-Au_{38}(2-PET)$_{24}$ and C-Au_{38}(2-PET)$_{24}$ (A: anticlockwise, C: clockwise), respectively, and the evolution of the clusters was

followed by circular dichroism spectroscopy. From their investigation, the racemization of the enantiopure $Au_{38}(SR)_{24}$ clusters takes place at modest temperatures without significant decomposition. Furthermore, from the temperature-dependent kinetic data, the activation barrier for the rearrangement within the thiolate-gold interface of the $Au_{38}(SR)_{24}$ clusters is about 28 kcal/mol, which is lower than the gold-sulfur bond energy (50 kcal/mol). The relatively low activation barrier indicated that the racemization process of $Au_{38}(SR)_{24}$ proceeds without complete Au-S bond breaking and evidenced the flexibility of the gold-thiolate interface. In addition, using density functional theory (DFT) computations, Häkkinen and co-workers proposed a mechanism for this inversion of the Au-S framework of $Au_{38}(SR)_{24}$ as shown in Fig. 1.2 (bottom)[17]. In their model, the racemization proceeds via a rotational reconstruction of the metal core without any Au-S bonds being broken.

The flexibility of the gold-sulfur interface was affected by many factors, such as Pd doping, which is normally used for increasing the stability and enhance reactivity in catalytic and ligand exchange reactions. Barrabés and co-workers reported that the racemization process takes place at significantly lower temperature after the $Au_{38}(SR)_{24}$ cluster was doped with two Pd atoms compared with the parent clusters[18]. This case indicated that the Pd doping of the cluster renders the Au-S interface more flexible. In contrast, after introducing of a rigid dithiolate, 1,1'-binaphthyl-2,2'-dithiol (BINAS), into the ligand shell of the $Au_{38}(SR)_{24}$ cluster, the racemization drastically slows down[19]. For example, the racemization at 70^{o}C of $Au_{38}(2\text{-PET})_{22}(BINAS)_1$ is about 27 times slower compared to the parent cluster, meaning that the introduction of the dithiol reduces the flexibility of the Au-S interface. Interestingly, the vibrational spectrum of the Au-S interface is also dramatically influenced by introducing one BINAS dithiol into the ligand shell of the cluster, possibly related to the fact that the dithiol bridges two staples[20]. Similarly, the racemization of the $Au_{40}(SR)_{24}$ clusters was reported to take place at high temperature compared with $Au_{38}(SR)_{24}$ but with a similar activation barrier, further confirming the flexibility of gold-sulfur interface[21].

The racemization described above is not the only dynamic process observed for the $Au_{38}(SR)_{24}$ cluster. Such flexibility of the gold-sulfur interface was also demonstrated by the observation of the migration of ligand on the shell. As reported, HPLC can be used to separate and isolate one specific regioisomer after ligand exchange between $Au_{38}(2\text{-PET})_{24}$ clusters and enantiopure planar chiral [2.2] paracyclophane-4-thiol (PCP-4-SH)[22]. The isolated species is stable at room temperature however, the absorbed thiolate migrates between the different symmetry-unique sites at 80^{o}C as followed by HPLC[22]. The mechanism underlying this observation is not yet clear: it might involve the exchange of two ligands between different sites on one cluster or the exchange of ligands between clusters (see below).

The chemical properties and flexibility of the gold-sulfur interface form the basis for the post-synthesis modification and further functionalization of the gold nanoclusters. Among them, ligand exchange reaction is extraordinarily sparkly, and we will focus on the mechanism of this reaction following.

1.2 Mechanism of ligand exchange reactions

Depending on the flexibility and the reactivity of the gold-sulfur interface, the thiolates within the ligand shell can be displaced by other thiols in the solution, which is named place-exchange reactions, or more commonly ligand exchange reactions (LERs). For thiolate-protected clusters this reaction was first reported by Murry and coworkers[26-30]. Until now, the LERs already became an important post-synthesis method for the modification and further functionalization of gold nanoclusters. For example, Zhu and co-worker summarized the transformations of precise nanoclusters induced by ligand exchange[25]. In general, LERs were investigated by ^{1}H NMR, thermal analysis and IR spectroscopy[26,27,29,30]. The results of these experiments revealed some factors which may affect the process. The chemical reactivity is mostly independent of the nanoparticles or nanoclusters size[29], but the stability of the sample is a factor determining the fate of the cluster after the ligand exchange reactions[31]. The rate and extent of ligand exchange reactions will increase with increasing positive

electronic charge on the Au cluster core[27], but decrease with an increasing size of the entering ligand and the chain length of the protecting monolayer[30]. In this introduction, many ligand exchange reactions will be discussed, and an overview is provided in Table 1.1. In order to provide more convenient information, a summary of the ligands, used in the thesis also listed at Table 1.2.

Table 1.1 Summary of the examples of LERs mentioned in each subsection.

Subchapter	*topic*	*reaction*	*reference*
1.2	Ligand exchange with free ligand	Au_{102}(*p*-MBA)$_{44}$ + parabromobenzene thiol (*p*-BBT) → Au_{102}(*p*-MBA)$_{40}$(*p*-BBT)$_4$	33
		Anti-influenza N9 neuraminidase NC10 antibody + $Au_{25}(SG)_{18}$ → ScFv--$Au_{25}(SG)_{18}$ -complex	32
		$[Au_{25}(SC_2H_4Ph)_{18}]^-$+ $HSCH_2Ph$-^{t}But → $Au_{24}(SCH_2Ph$-^{t}But$)_{20}$ $Au_{24}Cd(SC_2H_4Ph)_{18}$ + $HSCH_2Ph$-^{t}But → $Au_{24}Cd(SCH_2Ph$-^{t}But$)_{18}$ + $Au_{24}Cd(SCH_2Ph$-^{t}But$)_{17}(SC_2H_4Ph)_1$	31
	Intercluster ligand exchange	$[Au_{25}(SC_{10}H_{21})_{18}]^-$ + $[Au_{25}(SC_{12}H_{25})_{18}]^-$ → $Au_{25}(SC_{12}H_{25})_{18-x}(SC_{10}H_{21})_x$	35
		Au_{25}(SBut)$_{18}$ + Au_{25}(2-PET)$_{18}$ → Au_{25}(SBut)$_{18-x}$(2-PET)$_x$	34
1.3	Site-selective ligand exchange	$Au_{24}Pd(SC_2H_4Ph)_{18}$ + $C_{12}H_{25}SH$ → $Au_{24}Pd(SC_2H_4Ph)_{18-x}(SC_{12}H_{25})_x$	39
		$[Au_{25}(SC_2H_4Ph)_{18}]^-$ + HSePh / HTePh → $[Au_{25}(SC_2H_4Ph)_{18-x}$(SePh/TePh)$_x$	48
		$Au_{24}Cd(SCH_2Ph)_{18}$ + SCH_2Ph-^{t}But → $Au_{24}Cd(SCH_2Ph$-^{t}But$)_{17}(SCH_2Ph)_1$	31
		$PdAu_{24}$(2-PET)$_{18}$ + S-BINAS → $PdAu_{24}$(2-PET)$_{16}$(S-BINAS)$_1$	55
1.4	Ligand exchange induced size transformation	Au_{28}(SPh-^{t}But)$_{20}$ + HS-c-C_6H_{11} ←→ Au_{28}(S-c-C_6H_{11})$_{20}$ + HSPh-^{t}But	62
		Au_{25}(2-PET)$_{18}$ + 4-tert-butylbenzenelthiol (TBBTH) → Au_{28}(TBBT)$_{20}$	63
		$Au_{11}(PPh_3)_7Cl_3$ + L-glutathione (GSH) → $Au_{25}(GS)_{18}$	66，67
		$Au_{144}(SC_2H_4Ph)_{60}$ + HSPh → Au_{99}(SPh)$_{42}$	68
		$Au_{38}(SC_2H_4Ph)_{24}$ + HSPh-^{t}But → Au_{36}(SPh-^{t}But)$_{24}$	56
		Au_{23}(S-c-C_6H_{11})$_{16}$ + HTBBT → Au_{36}(TBBT)$_{24}$	65
		Au_{329}(2-PET)$_{84}$ + HSPh-^{t}But→ Au_{279}(SPh-^{t}But)$_{84}$	70
		Au_{36}(SPhX)$_{24}$ (where X = -H or -^{t}But) + HS-^{t}But → Au_{30}(S-^{t}But)$_{18}$ Au_{30}(S-^{t}But)$_{18}$ +HSPhX (where X = -H or -^{t}But) → Au_{36}(SPhX)$_{24}$	61
		Au_{44}(TBBT)$_{28}$ + 2,4-dimethylbenzenethiol (2,4-DMBTH) ←→ Au_{44}(2,4-DMBT)$_{26}$ + TBBTH Au_{43}(S-c-C_6H_{11})$_{25}$ + 2,4-DMBTH ←→ Au_{44}(2,4-DMBT)$_{26}$ + HS-c-C_6H_{11} Au_{43}(S-c-C_6H_{11})$_{25}$ + TBBTH → Au_{44}(TBBT)$_{28}$ + HS-c-C_6H_{11}	71, 72
1.5	Ligand exchange induced chirality	$[Au_{25}(2\text{-}PET)_{18}^-][TOA^+]$ + R/S-BINAS →$[Au_{25}(2\text{-}PET)_{18\text{-}2X}(R/S\text{-}BINAS)_X^-][TOA^+]$	54
		$[Au_{38}(SR)_{24}]$ / $[Au_{40}(SR)_{24}]$ + R/S-BINAS →$[Au_{38}(SR)_{24\text{-}2X}(R/S\text{-}BINAS)_X]$ / $[Au_{40}(SR)_{24\text{-}2X}(R/S\text{-}BINAS)_X]$	53
1.6	Addition of fluorescence properties	AuNC@DDAB + Dihydrolipoic acid (DHLA) → AuNC@DHLA	89
		AuNAC@Ag (NAC= N-acetylcysteine) + L-glutathione (GSH) → AuNAC@AgSG	90
1.7	Ligand exchange induced phase transfer	$Au_{24}Ag_{20}$(2-Spy)$_4$(PA)$_{20}Cl_2$ + Mercaptosuccinic acid (MSA) → $Au_{24}Ag_{20}$-MSA	97
		$[Ag_{141}Br_{12}(S\text{-}Adm)_{40}]^{3+}$ + Phenylacetylene(PAH) → $[Ag_{141}Br_{12\text{-}n}Cl_n(S\text{-}Adm)_{38}PA_2]^{3+}$	98
		$Au_xAg_{44\text{-}x}(PhC\Xi C)_m(Ph_3P)_nCl_P$ + Tiopronin → $Au_xAg_{44\text{-}x}(SR)_wCl_z$	99

Table 1.2 Summary of the ligands, used in the thesis

Name of ligand	Abbreviation	Chiral
1,1'-binaphthyl-2,2'-dithiol	BINAS	Yes
2-phenylethylthiolate	2-PET	No
Biphenyl-2,2'-dithiol	BiDi	Yes
[2.2] paracyclophane-4-thiol	PCP-4-SH	Yes
Parabromobenzene thiol	*p*-BBT	Yes
p-mercaptobenzoic acid	p-MBA	No
Glutathione	GSH/SG	Yes
1-Butanethiol	SBut	No
4-tert-butylbenzene thiolate	TBBT	No
2,4-dimethylbenzenethiol	2,4-DMBT	No
2-phenylpropane-1-thiol	PET*/PPT	Yes
Captopril	Capt	Yes
Dihydrolipoic acid	DHLA	Yes
Didodecyldimethylammonium bromide	DDAB	No
N-acetylcysteine	NAC	Yes
Mercaptosuccinic acid	MSA	Yes
Phenylacetylene	PAH	No
(R)-5,5',6,6',7,7',8,8'-octafluoro- [1,1'-binaphthalene]-2,2'-dithiol	8F-R-BINAS	Yes

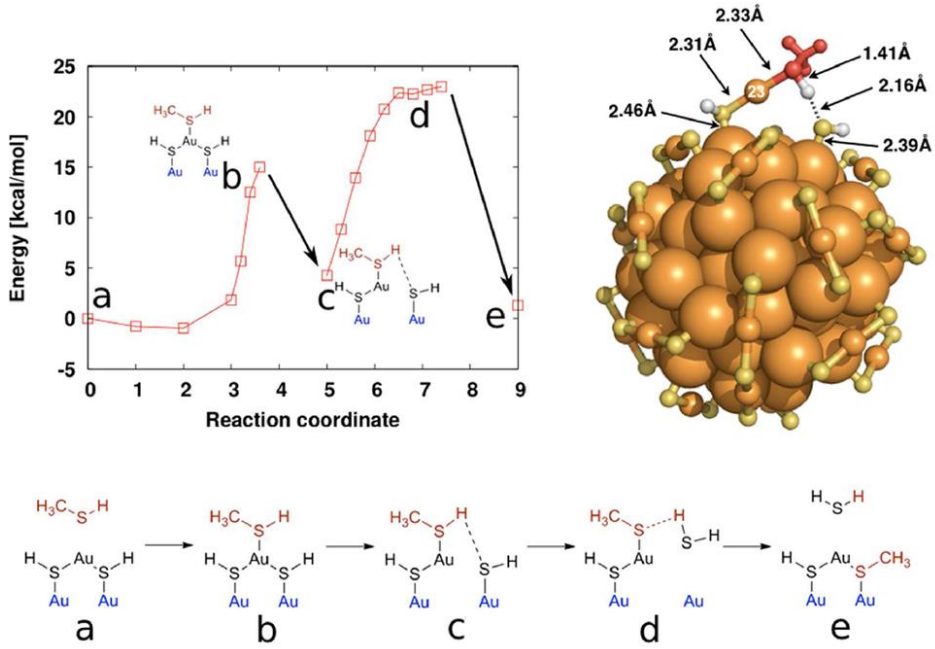

Figure 1.3 Scheme of ligand exchange process with methane thiol and $Au_{102}(SR)_{44}$ clusters. Top-left panel: energy behavior during exchange process (corresponding configuration were depicted as a sketch in the bottom panel); Top-right panel: full rendering of the hemiring-like transition state c. Configurations close to b and d have been confirmed to be at the local energy maximum by structural relaxations to the intermediate and final states. Copyright from reference[33].

Evidences from related investigations proposed an associative pathway for the mechanism of ligand exchange reactions, which has been proved by various experimental and computational studies[32-34]. For example, Heinecke and coworkers reported the first crystal structure of Au_{102}(*p*-MBA)$_{40}$(*p*-BBT)$_4$ (*p*-MBA = p-mercaptobenzoic acid, *p*-BBT = parabromobenzene thiol), which from the ligand exchange reaction of Au_{102}(*p*-MBA)$_{44}$ with *p*-BBT as the incoming ligand[33]. Available crystal structures of Au_{102}(*p*-MBA)$_{44}$ and Au_{102}(*p*-MBA)$_{40}$(*p*-BBT)$_4$ were underpinned by a computational DFT study on energetics, reaction intermediates and pertinent transition states during the ligand exchange reactions, revealing microscopic details of this process. The associative ligand exchange mechanism, as emerging from a computational study, is illustrated in Fig. 1.3, where methane thiol was used as incoming ligand. For associative ligand exchange, the more solvent exposed sulfur site on Au_{102}(*p*-MBA)$_{44}$ are more reactive and "nucleophilic attacked" by the incoming thiol(ate), creating an intermediate that has both incoming and outgoing ligands simultaneously bound to the accessible gold atom (Fig. 1.3 b). Then the intermediate configuration changed to well-known "hemiring" unit with one Au replaced by an H atom (Fig. 1.3 c). Depending on the orientation of the residue, the observed bond length between the hydrogen of the incoming ligand and the sulfur of ligand shell become shorter and the sulfur of the outgoing ligand released from the gold core (Fig. 1.3 d). To complete exchange, the hydrogen atom of the adsorbed methane thiol is transferred to the outgoing ligand, which is then released to the solution (Fig. 1.3 e). The configuration of intermediates at state b (gold bound to three sulfur atoms) and state d (breaking of S-H bond) have maximum energy during the exchange process.

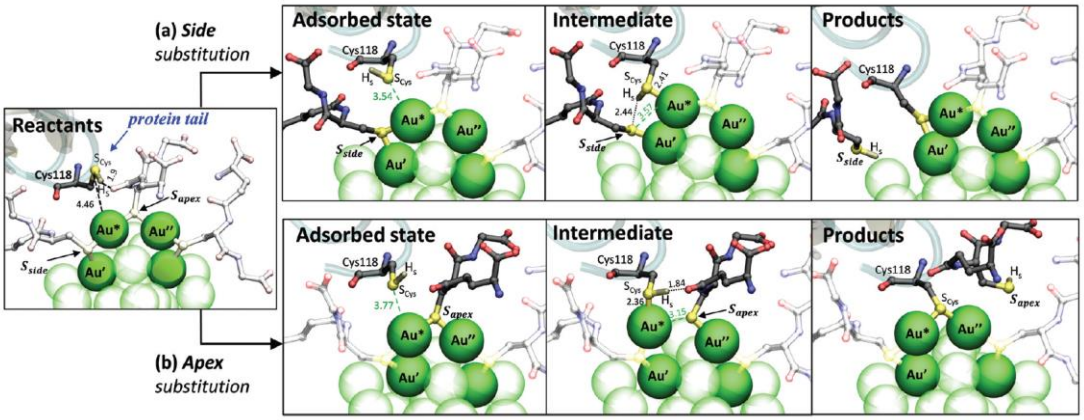

Figure 1.4 Mechanism of the ligand exchange reaction in the scFv···$Au_{25}(SG)_{18}$− complex computed by QM/MM calculations. (a) Substitution at the side SG. (b) Substitution at the apex SG. For simplicity, only three SG ligands of the dimeric staples are shown. Other SG groups and gold atoms which far from the reaction centre are shown as colorless or as semi-transparent. Part of the secondary structure of the protein is displayed, together with the nucleophilic cysteine. Water molecules are not shown for clarity. Copyright from reference[32].

A similar process may take place when labelling proteins with nanoclusters (as shown in Fig. 1.4). The initial reaction of this modification is a ligand exchange reactions of the anti-influenza N9 neuraminidase NC10 antibody against a glutathione-coated gold cluster by means of *ab initio QM/MM* calculations[32]. Compared to the reaction with free thiol, the example displayed here concerns a large protein and may have two substitution modes as illustrated in Fig. 1.4. In the calculations ligand exchange of the side and apex glutathione ligands were considerd, and showed that the intermediate from the side ligand is more stable. This investigation indicates that the essential features of the ligand exchange reaction are independent of the nature of the thiolate ligands and the presence of the protein. But the presence of positive residues at the protein C-terminal tail is critical for forming attractive intermolecular interactions with the carboxylate groups of the SG ligands, facilitating the adsorption of the protein cysteine on the gold cluster surface.

Because of the fast dynamics and complexity of the ligand exchange, it is difficulty to disclose the microscopic details of the S_N2-like process by experiments alone. However, with the assistance of computational methods

such as DFT calculations, some light could be shed on the S_N2-like mechanism of initial ligand exchange. Interestingly, recently Wu and co-workers proposed an unimolecular nucleophilic substitution (S_N1)-like mechanism (in addition to a S_N2-like process)[31], based on single crystal structure analysis of ligand exchanged clusters. The crystal structures showed that part of the sulfur atoms retained their configuration upon ligand exchange, which seems not possible for a S_N2-like process. However, this argument only holds if the configuration at the sulfur atom is retained in solution, which was not addressed.

Apart from the possibility for exchange of thiols via free ligand, there is a second mechanism for thiol exchange, which takes place through intercluster collisions. In 2013, Yoshiki Niihori and co-workers observed the intercluster LERs between $Au_{25}(SC_{10}H_{21})_{18}$ and $Au_{25}(SC_{12}H_{25})_{18}$ when they studied the influence of Pd atom doping of thiolate-protected Au_{25} nanoclusters on ligand exchange reactivity[35]. In that case the authors assumed that this exchange resulted from the detachment of ligand or gold-ligand species from the cluster[35]. Later, Salassa and co-workers carried out the intercluster LERs between $Au_{25}(SBut)_{18}$ (SBut = 1-Butanethiol) and $Au_{25}(2\text{-PET})_{18}$, and experimentally proved that the process has fast dynamics as shown in Fig. 1.5 A, 15 min after mixing two clusters at room temperature, peaks from clusters with mixed

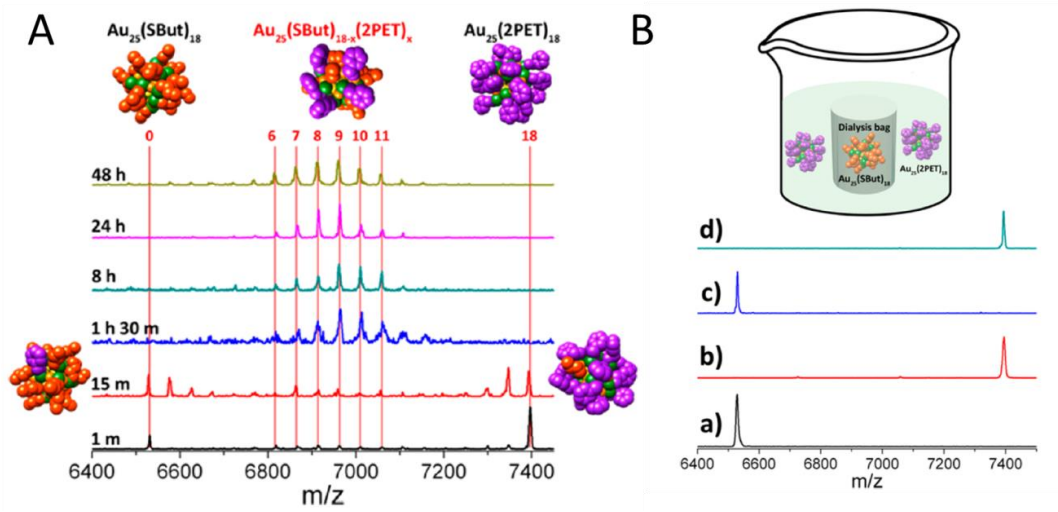

Figure 1.5 Positive-ion MALDI mass spectra of $Au_{25}(SBut)_{18}$ and $Au_{25}(2\text{-PET})_{18}$ (A) collected at different time after mixing two clusters; (B) with $Au_{25}(SBut)_{18}$ put inside the dialysis membrane and put $Au_{25}(2\text{-PET})_{18}$ outside solution for 5 days. Copyright from reference[34].

ligand layer already appears in the mass spectrum[34]. In addition, the interclusters ligand exchange seems without release of low molecular free thiol or thiol-gold complex which was proved by the reaction as illustrated in Fig. 1.5 B. In this experiment $Au_{25}(SBut)_{18}$ was put inside a dialysis membrane and thus the two clusters were physically separated, whereas the low molecular species could still penetrate and pass the membrane. The MALDI results show that the original clusters did not undergo any exchange of the thiol[34].

Over the past decades, since the first report of ligand exchange reactions for gold nanoclusters, this reaction, which used to introduce new ligands to the parent nanoclusters[33,36-39], has been widely applied for adding functionalities or chemical properties to clusters as a post-modification method[40,32]. This methodology strongly extends the possibilities to modify surface properties of gold nanoclusters, normally without any change of the metal core[40]. Understanding of the mechanism of the ligand exchange reaction may help us engineer the surface chemistry of nanometerials and to build multifunctional nano-platform.

1.3 Site-selective ligand exchange reactions

Several reports show that during the ligand exchange reactions, many sites on ligand shell exchange slowly or not at all, whereas others are comparatively reactive[30,41,42]. These observations revealed that the ligand shell is heterogeneous and offers a diversity of ligand binding sites and the exchange reaction occurs preferentially at selected ones[28]. Before exploring the priority reactive site during ligand exchange reactions, we would like first to discuss the diverse sulfur groups in the ligand shell which represent the reactive site.

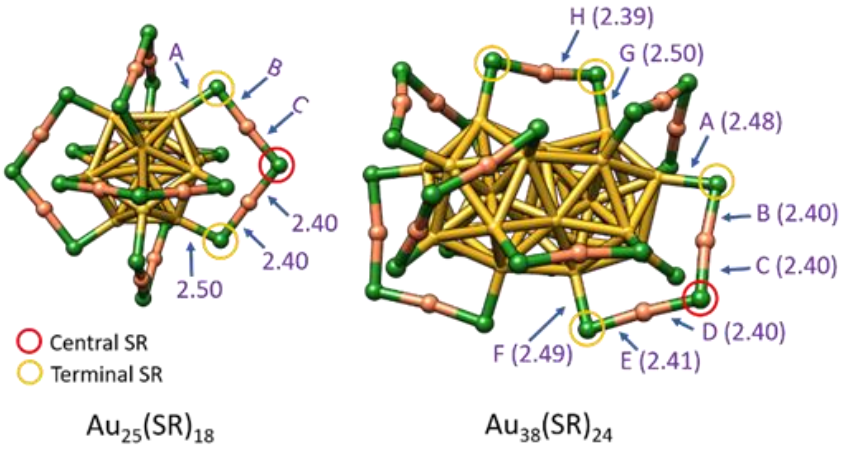

Figure 1.6 Crystal structures of $Au_{25}(SR)_{18}$ and $Au_{38}(SR)_{24}$ clusters. Some terminal -SR (orange circle) and central –SR (red circle) are marked in the scheme. $Au_{25}(SR)_{18}$ nanocluster has three possible ligand substitution sites marked as A, B, C, and $Au_{38}(SR)_{24}$ has eight possible ligand substitution sites marked as A-H. Bond distances also are given in Å. Color code: Au core = gold, Au staple = orange, S = green. Adapted with permission from Reference[43] and Reference[44].

Since the dynamic exchange process were mostly investigated through $Au_{25}(SR)_{18}$ and $Au_{38}(SR)_{24}$[22,45], which are easily prepared and relatively stable, we focus more on their crystal structures as illustrated in Fig. 1.6. The $Au_{25}(SR)_{18}$ cluster (Fig. 1.6 left structure) has an icosahedral Au_{13} core surrounded by six SR-Au-SR-Au-SR staple units as we mentioned before[35,37,39,46-48]. Because of the symmetry of $Au_{25}(SR)_{18}$, six dimeric staples share same chemical enviroment, but the SR groups in one staple were divided into central -SR group, which is attached to the two gold atoms in the staple, and terminal -SR groups, which are linked to the gold core[43]. In contrast, $Au_{38}(SR)_{24}$ consists of a biicosahedral Au_{23} core (Fig. 1.6 right structure) covered not only by six dimeric units but also by three monomeric units. The structure of $Au_{38}(SR)_{24}$ is elongated, with the three monomeric staples at the equator and the six dimeric staples at the two poles[49]. The dimeric staples also can be divided into central -SR group and terminal -SR groups. However, the two terminal -SR groups in one dimeric staple of $Au_{38}(SR)_{24}$ have different chemical enviroment[22,44]. Overall the 24 thiolate ligands are divided into four groups of symmetry unique sites with different chemical enviroment, which can give rise to preferential exchange site during LERs[33,39].

Recently, depending on the experimental and computational studies, it is clear that when LERs happened between clusters and free monothiolate in solution, the exchange reaction start preferebly at the terminal SR groups of $Au_{25}(SR)_{18}$ and $Au_{38}(SR)_{24}$ clusters[39,43,44], via an associative S_N2-like mechanism[33]. This trendency was experimentally proved by Yoshiki Niihori and co-workers[39]. In this case the isomer distributions of the product after ligand exchange between $Au_{24}Pd(SC_2H_4Ph)_{18}$ and $C_{12}H_{25}SH$ were determined by high resolution high-performance liquid chromotography. The quantitative evaluation of the expected coordination isomers and the products obtained by the reactions, revealed that the exchange reaction starts at the thiolate which is bound to the core site. This also holds for exchange with other chalcogenate ligands such as HSePh or PhTeH[48]. Niihori and co-workers also inverstigated that $Au_{25}(SR)_{18}$ clusters with Pd doping will drastically increase the rate of ligand exchange reaction. Pd doping reduce the number of valance electrons of the metal core, which facilitates the attrack by the incoming ligand. Furthermore, Pd doping induce the distortion of the cluster geometry[35].

Table 1.3 Summary of Energies (in eV) for Ligand Exchange (modified from reference[44])

	TS1	Int	TS2	Products
Au_{25} A	0.56	0.19	0.76	-0.01
Au_{25} B	0.62	0.29	0.65	0.05
Au_{25} C	0.78	0.35	1.15	-0.04
Au_{38} A	0.68	0.22	0.80	-0.06
Au_{38} B	0.61	0.29	0.76	-0.07
Au_{38} C	0.85	0.21	0.85	-0.05
Au_{38} D	0.59	0.34	0.89	-0.11
Au_{38} E	0.59	0.21	0.80	-0.04
Au_{38} F	0.75	0.06	0.56	-0.04
Au_{38} G	0.54	0.21	0.65	-0.05
Au_{38} H	0.91	0.15	0.77	-0.05

In addition, the site preference of LERs can be investigated by computational methods. Aikens and co-workers employed density functional theory (DFT) to

examine the ligand exchange on model $Au_{25}(SH)_{18}^-$ and $Au_{38}(SH)_{24}$ clusters with an incoming methanethiol seperately[43,44]. They calculated the intermediates and transition states, and predicted the barrier heights and reaction energies for this ligand exchange process. As illustrated in Fig. 1.6, the different possible ligand substitution sites aremarked on the crystal structure of $Au_{25}(SH)_{18}^-$ (Fig. 1.6 left) and $Au_{38}(SR)_{24}$ (Fig. 1.6 right) nanoclusters. The former cluster offers three different sites and the later one offers eight different sites. The energies of the intermediates, transition state and products corresponding to ligand exchange at different sites were summarized at Table 1.3. The results from Au_{25} indicated that the most favourable ligand exchange process is at site B, and the site C has highest energy barrier, which resulted in ligand exchange at the central SR group. This tendency was consistent with $Au_{38}(SR)_{24}$ cluster as shown from the predicted energies listed at Table 1.3, LERs at site C had higher energy barriers compared with other sites, which means the reaction between the staple gold atom and the sulfur atom of the central -SH units will proceed at a slower rate. Here, we should mention that each sulfur atom is participating in two bonds, for example Au_{25} A&B, Au_{38} C&D, and Au_{38} E&F, which represent different reactive sites, however, those two sites will be consonant with the same product. Above prediction from calculations on $Au_{25}(SH)_{18}^-$ and $Au_{38}(SR)_{24}$ indicated that the exchange is preferent at the terminal SR groups in all reactions, which is in agreement with the experimental results. However, this might not always be the case as shown by Zhu and co-workers. After the ligand exchange reaction between $Au_{24}Cd(SCH_2Ph)_{18}$ and SCH_2Ph-^{t}But, the specise $Au_{24}Cd(SCH_2Ph\text{-}^t But)_{17}(SCH_2Ph)_1$ has been obtained[31]. The integrated areas extracted from ^{1}H NMR spectra of this specise illustrated the single SCH_2Ph ligand is equaily distruibuted to the terminal and central sulfur atoms, which is in contrast with the results discussed above. This result may be caused by several reasons, such as steric hindrance within the ligand shell or the inevitable migration of the ligand on the cluster surface at 80^{o}C. In addition, Pengo and co-workers also showed by NMR spectroscopy that the distribution of incoming ligand on the central and terminal sites depends on the properties of the ligand[47].

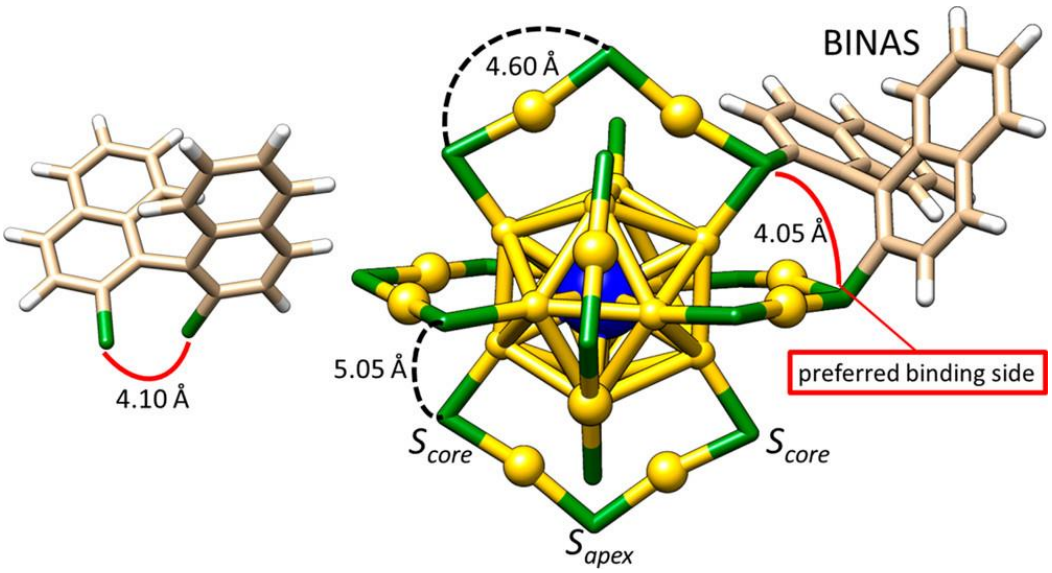

Figure 1.7 3D sketch of S-BINAS (left) and $MAu_{24}(SR)_{16}$(S-BINAS)$_1$ (right), where M = Pt, Pd. Other ligands apart from BINAS are omitted for clarity. The two types of sulfur environments are indicated with S_{core} (also called terminal) and S_{apex} (also called central). Color code: Au = yellow, S = green, C = beige, H= white, Pt and Pd = blue. Copyright from reference[52].

Apart from the monothiolate ligand, nanoclusters are also reactive towards dithiol ligands. Dass and co-workers systematic study LERs with aliphatic dithiolate ligand of various chain length, HS-$(CH_2)_n$-SH[50]. They documented that C_3 and C_4 are prefer interstaple coupling, and C_5 and C_6 are good candidates for intrastaple binding, and the length of C_2 ligand is not enough for the bidentate binding. Aromatic dithiolates also have been used for the LERs. However, they are sterically more demanding and more rigid compared to aliphatic thiols. For instance, 1,1'-binaphthalene-2,2'-dithiol (BINAS), which is a chiral rigid dithiol ligand (Fig. 1.7 left)[37,51], exist in R/S configurations and easily introduce chirality to the achiral clusters. Several studies provide insight into the LERs of BINAS with Au_{25} and Au_{38} clusters[19,37,51-55], and from the experimental and computational results it emerges that the bidentate ligand connects two neighboring staples by interstaple coupling, which is most stable regioisomer[51,52,55]. Sels and co-workers reported the isolation of different exchange products and isomers of clusters containing one or two BINAS adsorbed on $PdAu_{24}(2\text{-PET})_{18}$ clusters[55]. The investigated structure of the $PdAu_{24}(SR)_{16}$(S-BINAS)$_1$ cluster is shown in Fig. 1.7. The two types of sulfur

environment are indicated and bond distance were marked in the scheme[52]. As displayed in Fig. 1.7, there are several possible binding sites for BINAS at the ligand shell, which are indicated with a curved line. However, considering the distances between the two S-atoms in undistorted BINAS, 4.1 Å, the interstaple binding between a apex and a core sulfur atom has the appropriate distance, 4.05 Å, for BINAS. Based on the X-ray absorption spectroscopy (XAS), the authors also proved that the BINAS interstaple binding mode does not perturb the cluster structure[52].

Compared with the monothiolate ligand exchange, it may be easier to isolate isomers of clusters with mixed ligand shell when using dithiolate ligands. A better understanding of the preferred reactive sites of the LERs will enable the rational design of mixed ligand shell clusters.

1.4 LERs induced size transformation of clusters

LERs is a process that takes advantage of the dynamic nature of the thiol-gold interface[11], and in most cases it does not cause any change in size or structure of the cluster, only replacing one capping ligand (or two capping ligands) by another one (the latter in excess in solution)[41]. During the past decade, due to the development of precise synthesis methods and structure determination by X-ray single-crystal diffraction, numerous new nanoclusters were reported. LERs became an important new methodology for controlling the size and structure of nanoclusters, and the process was named ligand-exchange-induced size/structure transformation (LEIST for short), which was first proposed by the Jin`s group[56].

Up to now, most of the presented LEIST works, which related to Au nanoclusters, focus on PPh_3-stabilized[57,58] and thiolate-protected Au nanoclusters[59-61]. However, the driving forces for LEIST are quite different for these two kinds of Au nanoclusters[25]. First, for LEIST of PPh_3-stabilized Au nanoclusters, exchanging the phosphine ligands with thiolate ligands changes

the surface bonding completely (from Au−P to Au−S). The different coordination modes, Au−P vs. Au−S, lead to different surface motifs and drives the structural transformation of the clusters[25,57]. Second, for LEIST of thiolate-protected Au nanoclusters, the new thiolates would not significantly alter the gold−ligand coordination; however, due to the distinctly different physical−chemical properties (e.g., size, rigidity, bulkiness, etc.) of different thiolate ligands, the original structures may not be the most stable for the ligand-exchanged nanoclusters, and thus the structural transformation takes place[25]. Here, we will briefly focus on the LEIST on thiolate-protected Au nanoclusters. Depending on the size or structural change of the thiolate-protected Au nanoclusters resulting from the LEIST, this process can be classified into three groups.

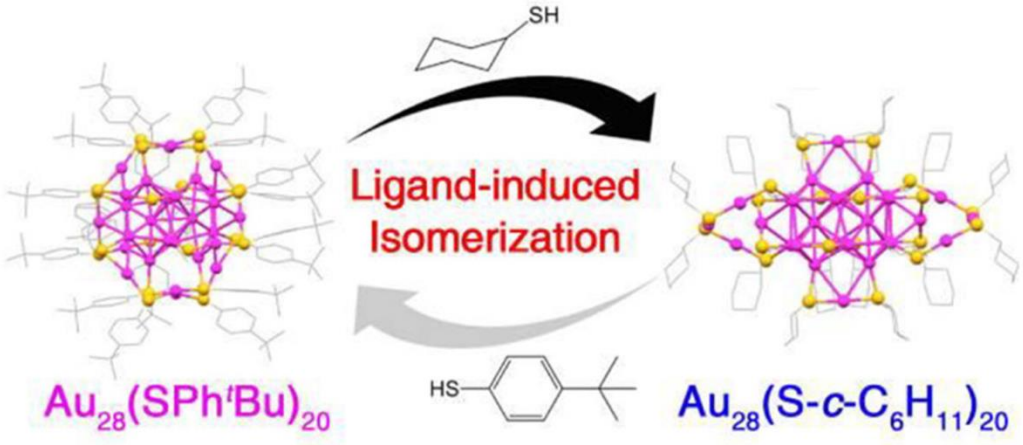

Figure 1.8 Ligand-exchange induced transformation between $Au_{28}(SPh\text{-}^{t}But)_{20}$ and $Au_{28}(S\text{-}c\text{-}C_6H_{11})_{20}$ nanoclusters. Color codes: purple/blue sphere, Au; yellow/red sphere, S; gray sphere, C. For clarity, all H atoms are omitted. Copyright from references[25,62].

(I) Transformation between structural isomers without size change. For example, $Au_{28}(SR)_{20}$ nanocluster reversibly changes its structure upon ligand exchange between R= $c\text{-}C_6H_{11}$ and R= $Ph\text{-}^{t}But$ at elevated temperatures (e.g., 80 °C) as shown in Fig. 1.8[62]. The geometric structures of these two nanoclusters are remarkable different from the investigation. $Au_{28}(SPh\text{-}^{t}But)_{20}$ contained an FCC Au_{20} kernel capped by four $Au_2(SR)_3$ staple motifs and eight bridging thiolates, whereas $Au_{28}(S\text{-}c\text{-}C_6H_{11})_{20}$ adopted a looser configuration

with an FCC Au_{20} kernel plus two $Au_1(SR)_2$, two $Au_3(SR)_4$, and eight bridging SR staple-like structures. DFT calculations revealed that the origin of reversible isomerization lay in the thiolate ligand's carbon tail structure, which was found to dictate the specific isomer's stability[62]. In LEIST system, the isomerization of clusters is rare.

(II) Transformations from a smaller to a larger nanocluster[13,61,63-65]. An interesting example is the transformation of Au_{25}(2-PET)$_{18}$ into Au_{28}(TBBT)$_{20}$ (TBBT = 4-tert-butylbenzene thiolate)[63]. Au_{25}(2-PET)$_{18}$ is probably the most studied thiolate-protected nanocluster, due to its prototypical character. At 80°C and in large excess of TBBT the cluster is transformed into Au_{28}(TBBT)$_{20}$. It is worth to mention that the resulting Au_{28}(TBBT)$_{20}$ cluster is chiral, and the origin of chirality is primarily rooted in the rotating arrangement of the four dimeric staples and the arrangement of the bridging thiolates. Moreover, the pair of enantiomers of Au_{28}(TBBT)$_{20}$ can be separated by chiral-HPLC[63]. Another example is the transformation of Au_{11} grow up to Au_{25} upon ligand exchange with GSH in solution[66,67].

(III) Transformations from a larger to a smaller nanocluster[25,56,59-61,68-70]. For instance, highly stable $Au_{144}(SC_2H_4Ph)_{60}$ reacted with thiophenol, HSPh, to form a different 99 atom cluster species $Au_{99}(SPh)_{42}$[68]. In addition, Zeng and co-worker reported that, by LEIST the very stable and widely investigated $Au_{38}(SC_2H_4Ph)_{24}$ was transformed to $Au_{36}(SPh\text{-}^tBut)_{24}$ as shown in Fig. 1.9 A[56]. To unravel the intriguing one-size-to-another size transformation, Zeng carried out time-dependent mass spectrometry and optical spectroscopy analyses (Fig. 1.9 B), and

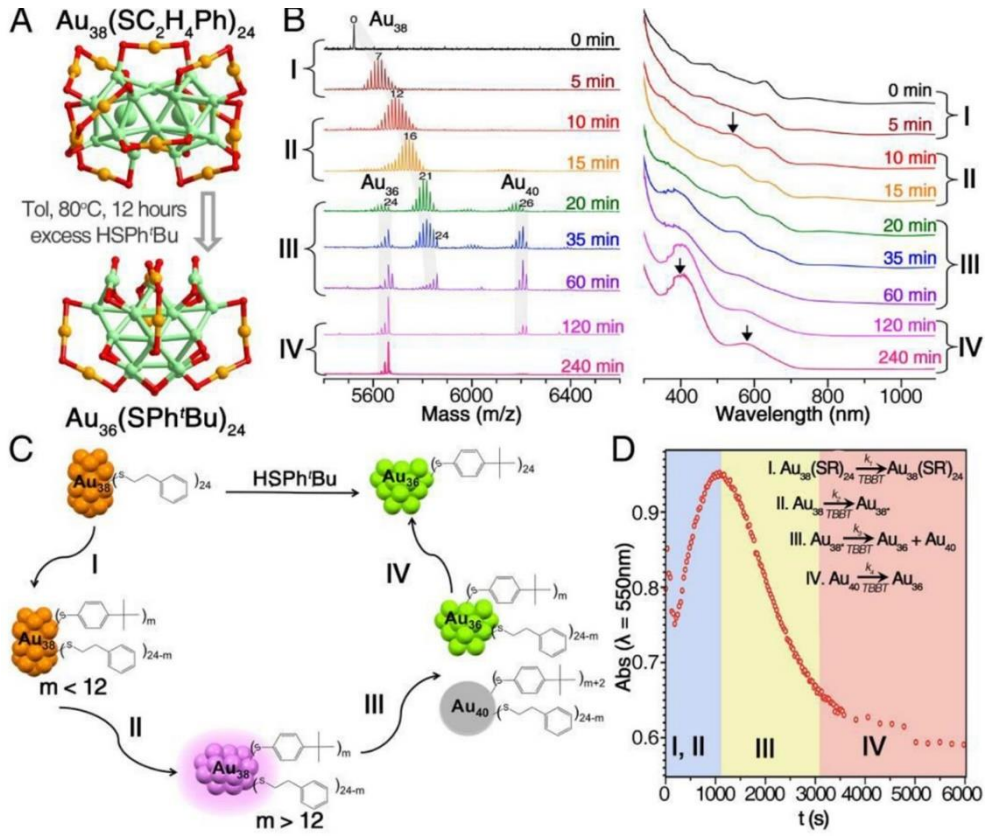

Figure 1.9 (A) Ligand-exchange induced transformation from $Au_{38}(SC_2H_4Ph)_{24}$ to $Au_{36}(SPh\text{-}^tBut)_{24}$. (B) Time-dependent ESI-MS and UV−vis spectra of the transformation. (C) Reaction pathway for the transformation. (D) Kinetic curve (monitored by absorbance at 550 nm) for the transformation. Copyright from references[25,56].

found a remarkable disproportionation in the transformation of rod-like biicosahedral $Au_{38}(SC_2H_4Ph)_{24}$ to tetrahedral $Au_{36}(SPh\text{-}^tBut)_{24}$. From the evolution of the mass spectra and corresponding UV curves, the reaction pathway can be roughly divided into four stages (Fig. 1.9 C): (i) (0-5 min) ligand exchange reaction occurs between 2-PET and TBBT; (ii) (10-15min) ligand exchange reaction continues leading to TBBT-triggered structural distortion of Au_{38} with an optical feature at 550 nm (Fig 3.2 D); (iii) (20-60min) critical stage for the disproportionation of Au_{38} to Au_{36} and Au_{40}, and (iv) size conversion of Au_{40} to Au_{36} evidenced by the decrease and complete disappearance of the Au_{40} peak in time-dependent mass spectra. Recently, other LEIST, such as transformations from $Au_{23}(S\text{-}c\text{-}C_6H_{11})_{16}$ to $Au_{36}(TBBT)_{24}$ and from $Au_{329}(2\text{-}PET)_{84}$ to $Au_{279}(SPh\text{-}^tBut)_{84}$ also revealed the similar pathway but without disproportionation. In these cases the conversion through ligand exchange followed by the size focusing ultimately led to size growth[65,70].

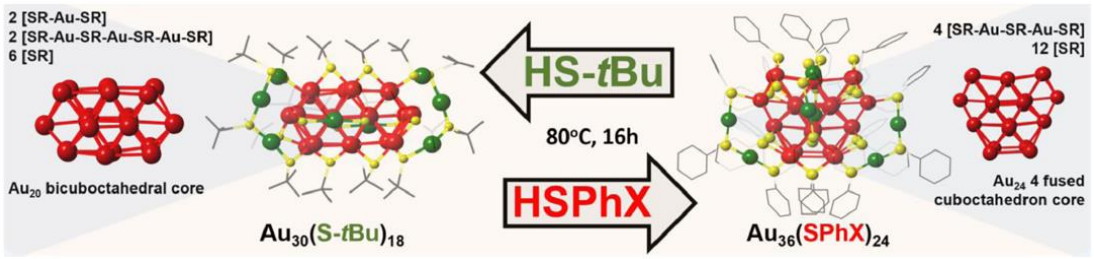

Figure 1.10 Schematic of the conditions for the interconversion between $Au_{30}(S\text{-}^{t}But)_{18}$ and $Au_{36}(SPhX)_{24}$. Reaction take place under the same thermochemical conditions with different thiol ligands (thiophenol and tert-Butyl). Copyright from reference[61].

Apart from the ireversible transformation mentioned above, Dass and co-workers presented the first interconversion between two nanomolecules $Au_{36}(SPhX)_{24}$, (where X = -H or -^{t}But) and $Au_{30}(S\text{-}^{t}But)_{18}$ as illustrated in Fig. 1.10[61]. In this case, the gold core converted between bicuboctahedral Au_{20} and 4 fused cuboctahedron Au_{24}, and the staple arrangement of these two clusters surfaces was also different. More interesting, the reversible conversion easily takes place under the same thermochemical conditions with different thiol ligands. Later, Wu and co-workers achieved the interconversion among $Au_{44}(TBBT)_{28}$, $Au_{44}(2,4\text{-}DMBT)_{26}$ (2,4-DMBT = = 2,4-dimethylbenzenethiol), and $Au_{43}(S\text{-}c\text{-}C_6H_{11})_{25}$ nanoclusters by the ligand exchange[71,72], and they also investigated the thermostability of these nanoclusters. As monitored by the time-dependent optical absorption, the $Au_{44}(2,4\text{-}DMBT)_{26}$ was less thermostable than $Au_{44}(TBBT)_{28}$, and much more stable than the $Au_{43}(S\text{-}c\text{-}C_6H_{11})_{25}$ at 80 °C[71]. The interconversion not only offer many possibilities to obtain new nanoclusters but also leads to valuable insight into the inherent influence of the ligand on the composition and atomic structure of thiolate-protected gold clusters.

The experimental conditions of the LEIST we mentioned above are summarized in Table 1.4. From the detailed information, it can be concluded that the necessary conditions for LEIST are large excess of incoming ligand, normally more than 100 times compared to the endogenous ligand, and elevated temperatures to proceed[60]. In addition, Jin and co-workers argued that the incoming thiol must be significantly different from the endogenous thiol for the transformation to happen[13]. Briefly, LEIST provides new and exciting views to explore novel atom-precise nanoclusters

and open a new strategy to investigate the size growth of nanoclusters.

Table 1.4 Summary of the conditions for ligand exchange induced cluster transformation.

Transformation	Ratio between $L_{incoming}$ /$L_{outgoing}$	T(^{0}C)	Reaction time
Structural Isomerism			
Au_{28}(S-c- $C_6H_{11})_{20}$ → Au_{28}(SPh-^{t}But)$_{20}$	200 :1	80^{0}C	2h[62]
Larger → Smaller			
Au_{25}(2-PET)$_{18}$ → Au_{20}(TBBT)$_{16}$	150:1	40^{0}C	8h[69]
Au_{36}(SPhX)$_{24}$ → Au_{30}(S-^{t}But)$_{18}$	800:1	80^{0}C	2h[61]
Au_{38}(2-PET)$_{24}$ → Au_{36}(TBBT)$_{24}$	160:1	80^{0}C	12h[56]
Au_{144}(2-PET)$_{60}$ → Au_{99}(SPh)$_{42}$	530:1	80^{0}C	3h[68]
Au_{144}(2-PET)$_{60}$ → Au_{133}(TBBT)$_{52}$	370:1	80^{0}C	4 h[59]
Au_{329}(2-PET)$_{84}$ → Au_{279}(SPh-^{t}But)$_{84}$	---	80^{0}C	6 days[70]
Smaller → Larger			
Au_{25}(2-PET)$_{18}$ → Au_{28}(TBBT)$_{20}$	120:1	80^{0}C	2h[63]
$Au_{11}(PPh_3)_7Cl_3$ + GSH → Au_{25}(GS)$_{18}$	400:1	55^{0}C	17h[66,67]
Au_{30}(S-^{t}But)$_{18}$ → Au_{36}(SPhX)$_{24}$	220:1	80^{0}C	16h[61]
$Au_{38}(SC_2H_4Ph)_{24}$→ $Au_{60}S_6(SCH_2Ph)_{36}$	180:1	100^{o}C	overnight[64]
Au_{23}(S-c-$C_6H_{11})_{16}$→ $Au_{24}(SCH_2Ph$-^{t}But)$_{20}$	380:1	40^{o}C	36h[13]
Au_{23}(S-c-$C_6H_{11})_{16}$→ Au_{36}(TBBT)$_{24}$	226:1	80^{o}C	48h[65]

1.5 Chirality introduced by LERs

Chirality is a geometric property of objects, which widely exists in nature from molecules over proteins to even larger structures[73,74]. During the past decade, depending on x-ray single-crystal diffraction, it has emerged that chirality is a novel feature for gold nanoclusters. Because of the potential applications in sensing, catalysis, molecular recognition and so on, chiral gold nanoclusters have attracted a

lot of interest[75-77].

The reported chiral gold nanoclusters can be categorized into three types: (i) chiral Au-S framework with achiral ligands, (ii) achiral Au-S framework with chiral ligands[76,77], and (iii) a combination of the two (chiral Au-S framework and chiral ligand). The type I chiral nanoclusters are also mentioned as intrinsic chiral nanoclusters, such as $Au_{20}(SR)_{16}$, $Au_{28}(SR)_{20}$, $Au_{38}(SR)_{24}$, $Au_{102}(SR)_{44}$ and $Au_{133}(SR)_{52}$, in which all the different R groups are achiral. The chirality of type II nanoclusters is due to the ligands SR. Fundamentally, such chiral clusters can be prepared by direct synthesis using a chiral thiol[78]. However, resulting from the solubility and steric effect of different ligands, direct synthesis of nanoclusters with some ligands was unsuccessful[40]. Alternatively, ligand exchange is a good method to incorporate chirality or other selective functionality onto the gold nanoclusters.

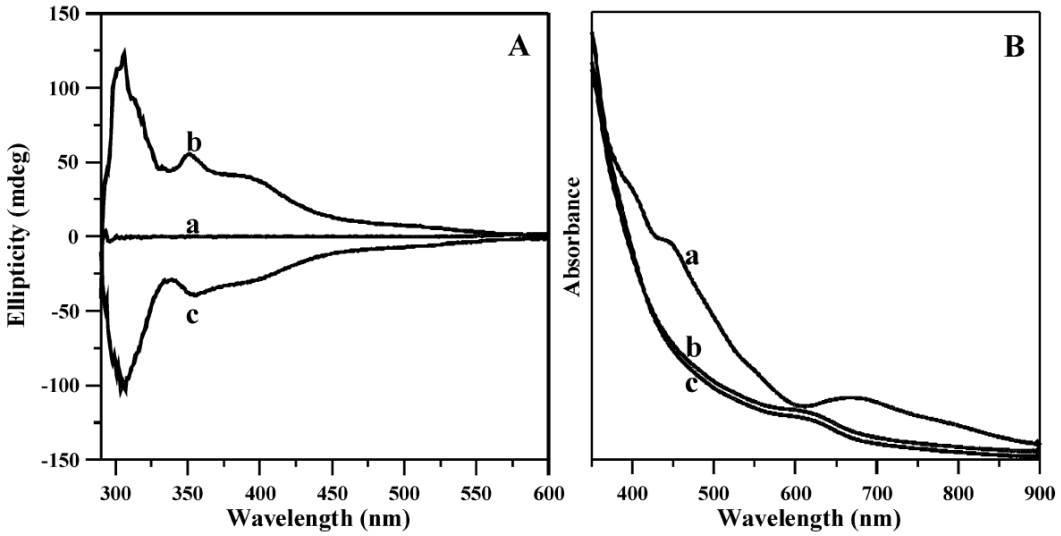

Figure 1.11 (A) CD spectra of Au_{25} clusters before exchange with R/S-BINAS (a), after exchange with R-BINAS (b), and after exchange with S-BINAS(c); (B) UV-vis absorption spectra of the corresponding samples. Copyright from reference[54].

By using ligand exchange on achiral $Au_m(SR)_n$ with chiral thiols (SR*), a series of chiral $Au_m(SR)_{n-x}(SR^*)_x$ clusters with chiroptical activity have become available[54,79-81]. For example, Si and co-workers reported the ligand exchange on $[Au_{25}(2\text{-PET})_{18}^-][TOA^+]$ (follow written as Au_{25}) with R/S-BINAS[54]. As illustrated in Fig. 1.11, the CD (left panel) and UV-Vis (right panel) spectra of Au_{25} clusters before

(a) and after exchange with R/S-BINAS (b/c) were recorded. As expected, the Au_{25} cluster is optically inactive before ligand exchange. Once the cluster exchange with BINAS, intense bands at 305, 352, and 390 nm are observed in the CD spectra with opposite sign for clusters covered by the two enantiomers of BINAS. The CD signal refer to the chiral ligand, but the spectra are different compared with the one of free BINAS. Furthermore, the Fig. 1.11 B reveals that the absorption spectrum of the cluster became less defined after exchange with BINAS. Apart from Au_{25} clusters, similar exchange also takes place on Au_{38} and Au_{40} clusters with R/S-BINAS[53]. In addition, as we mentioned before, the introduction of the BINAS ligand on Au_{38} clusters stabilized the structure against inversion (enantiomerization) and reduces the flexibility of the gold-sulfur interface[19]. Also, different from the fast reaction rate of LERs with monothiol, exchange with dithiol ligand dramatically reduce the number of diastereomers. Due to the reduction of the reaction rate after the first exchange, it is relatively easy to obtain just one ligand exchange species[37,51].

Compared with the direct synthesis, the ligand exchange of nanoclusters may lead to a heterogeneous system with a distribution of different number of incoming ligand when the exchange is incomplete. In order to obtain completely exchanged nanoclusters, large excess of free ligand concerning to the clusters and duplication of the exchange reaction are necessary, with purification of the intermediate cluster after each step.

The optical activity is usually considerably stronger for the type I chiral clusters, i.e. clusters with intrinsic chirality in their Au-S framework, compared to type II chiral clusters, i.e. achiral Au-S framework with chiral ligands. The absorption spectrum of a given cluster is roughly ligand independent. In contrast, when the chirality of the nanoclusters is due to the ligand, the optical properties will be ligand-dependent[54], which offer various possibility of the optical response. As revealed in Fig. 1.12, the Au_{25} and Au_{38} clusters are stabilized with three different chiral R* groups (PET*=2-phenylpropane-1-thiol, SG=glutathione and Capt=captopril) separately. All such chiral $Au_{25}(SR^*)_{18}$ nanoclusters show a typical absorption spectrum to that of

achiral $Au_{25}(2\text{-PET})_{18}$, but their CD signals are quite different depending on the different R* groups (Fig. 1.12 left panel)[80]. A similar phenomenon was also observed in the $Au_{38}(SR^*)_{24}$ nanoclusters with different chiral thiolate ligands (Fig. 1.12 right panel)[82]. This ligand-dependence provides a possibility to engineer the optical characteristics on a given gold nanocluster. Overall, the ligand exchange reaction with chiral ligands will continue to add new impetus to applications in chiral technology.

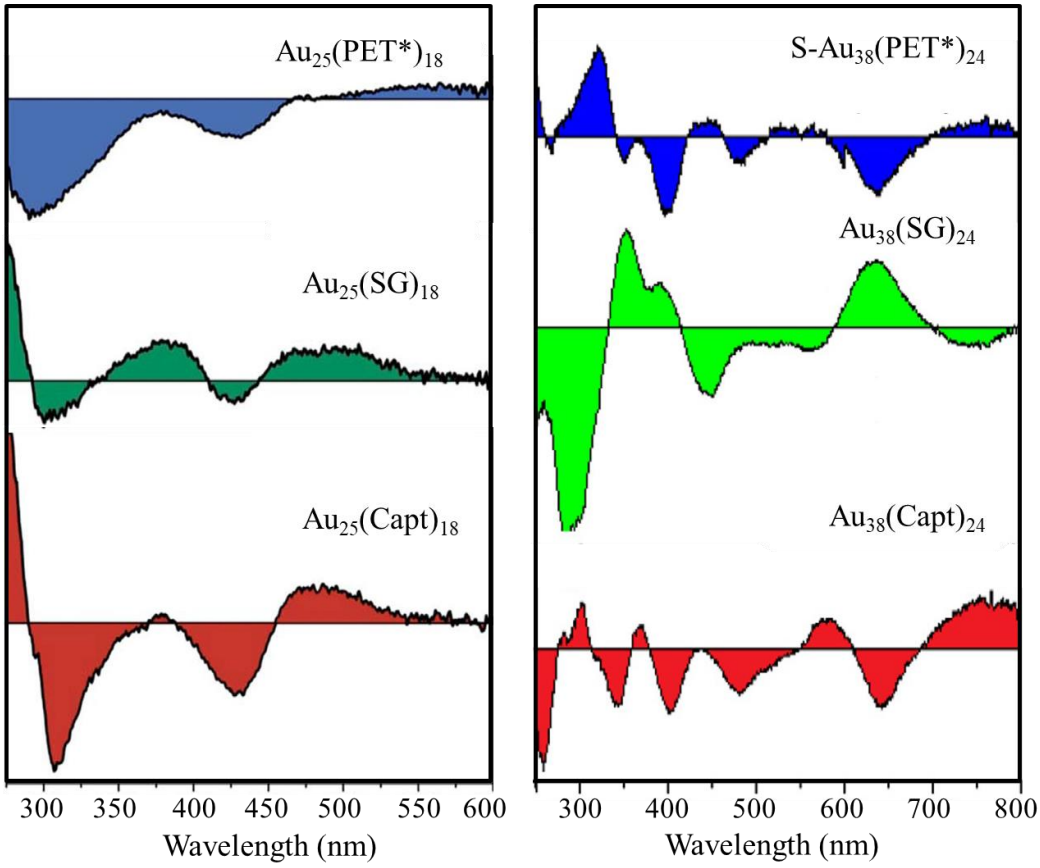

Figure 1.12 Effect of the chiral ligand type on the CD spectra of $Au_{25}(SR^*)_{18}$ and $Au_{38}(SR^*)_{24}$. SG=glutathione, Capt=captopril, copyright from references[80,82].

1.6 Fluorescence introduced by LERs

Fluorescent gold nanoclusters have been widely used for biological applications such as cell identification, interaction, differentiation, and tracking[83-87]. Compared with the traditional QDs, fluorescent gold nanoclusters have decent QY, excellent biocompatibility, good photostability, and lower cytotoxicity. The clusters had negligible influence on the cell viability at the considered dose[88]. However, because of

the synthesis method and the solubility of ligands, the diversity of the fluorescent gold nanoclusters has been limited.

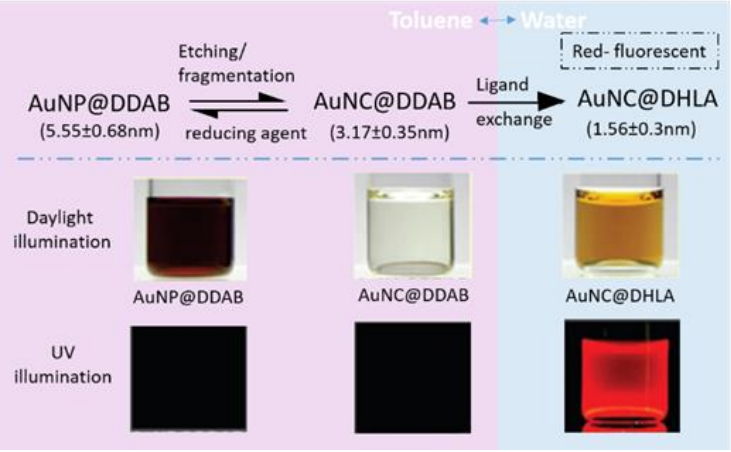

Figure 1.13 Strategy to fabricate hydrophilic fluorescent Au nanoclusters. Size distribution of three different Au nanoclusters extracted from 100 particles. Pictures of particle solutions under daylight and UV excitation, respectively. Adapted with permission from reference[89].

LER is a very efficient strategy for preparing fluorescent gold nanoclusters. As one of the most intuitive cases, the non-fluorescent AuNCs (AuNC@DDAB) (DDAB = Didodecyldimethylammonium bromide) can be converted to brightly red emitting nanoclusters (AuNC@DHLA) through an elegant ligand exchange reaction with dihydrolipoic acid (DHLA) as shown in Fig. 1.13[89]. In this system, the DDAB-stabilized gold nanoparticles (AuNP@DDAB) are etched by the addition of Au precursors ($HAuCl_4$ or $AuCl_3$) to smaller nanoclusters (AuNC@DDAB), and the organic soluble and hydrophobic AuNC@DDAB become water soluble upon ligand exchange with dihydrolipoic acid (AuNC@DHLA). The AuNP@DDAB solution shows red color due to surface plasmon absorption, which is absent to AuNC@DDAB and AuNC@DHLA. More interesting, after ligand exchange with DHLA, the AuNC@DHLA solution shows strong red photoluminescence as shown in the Fig. 1.13. Here, the phase transfer and addition of fluorophore been achieved together by the LERs.

In addition, Xu and co-workers reported the ligand exchange by GSH and N-acetylcysteine (NAC) on AuNAC@Ag, and the products showed maximum 20-fold fluorescent enhancement[90]. During this ligand exchange process, silver ions and GSH

have synergistic effects and the PL enhancement was proportional to the concentration of GSH. This fluorescence enhancement was also used for selective imaging of intracellular glutathione[90]. Besides the solution system, the fluorescence can also be introduced to supported nanoclusters by using ligand exchange on immobilized sample, which also proved that LERs takes place at supported gold nanoclusters[86].

1.7 LERs induced organic/aqueous phase transfer of clusters

There are many types of ligands that can be used to stabilize the nanoparticles or nanoclusters as shown in Fig. 1.14[91]. Depending on the solubility of the surface ligand, one can distinguish hydrophobic and hydrophilic clusters. However, for some biological applications, the hydrophobic clusters need to be dissolved in aqueous solutions. Also, hydrophilic clusters sometimes need to be made accessible to reactions in organic solvent. In this situation, phase transfer will be the first option to relocate the clusters to the desired phase.

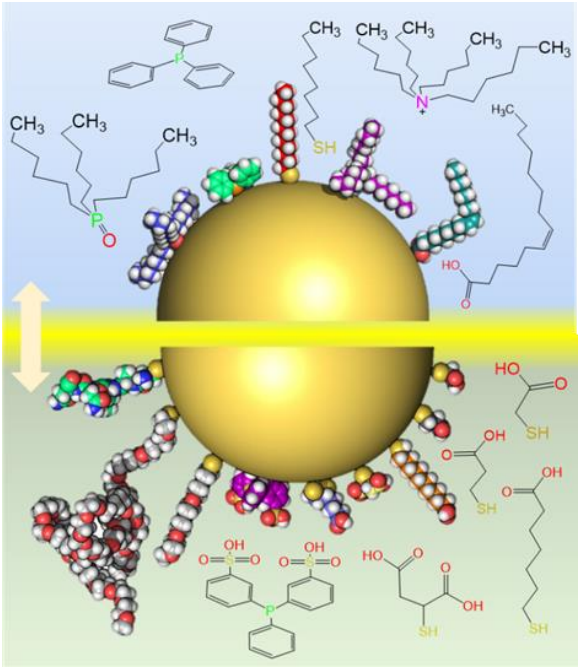

Figure 1.14 A nanoparticle (nanoclusters) stabilized with different hydrophobic (top panel) and hydrophilic (bottom panel) ligand molecules. The central nano-object has been idealized as a smooth sphere. The structure of molecules is illustrated with chemical structure or space filling models. Adapted with permission from reference[91].

In general, for phase transfer process, reagents such as tetraoctylammonium bromide[92,93], (-)-1R,2S-N-dodecyl-N-methylephedrinium bromide[94] and others have provided many successful cases. Here the chemical reagents offer an additional molecular layer on the clusters and change the surface properties. This strategy is mainly used for the phase transfer from aqueous to organic phase[92-96]. In addition to this strategy, ligand exchange has also been utilized as an important strategy for the phase transfer. For instance, when hydrophobic $Au_{11}(PPh_3)_7Cl_3$ reacted with GSH ligand in solution, the Au_{11} clusters grew up to form water-soluble Au_{25} nanoclusters[66,67], which is a good evidence for ligand exchange. In addition, Zheng and co-workers reported the crystal structure of intermetallic nanoclusters $Au_{24}Ag_{20}(2\text{-}SPy)_4(PA)_{20}Cl_2$ and also investigated the phase transfer process after performing ligand exchange with mercaptosuccinic acid (MSA)[97], leading to transfer of the $Au_{24}Ag_{20}$ cluster from DCM to water phase. Other reported cases of phase transfer induced by ligand exchange reactions include ligands such as (phenylacetylene) PAH[98] and tiopronin[99]. The latter ligand also introduced cancer therapy functions to the cluster.

It emerges from the cases mentioned above, that the phase transfer from aqueous to organic phase relies on phase transfer reagents or ligand modification, and in many cases the core size of the cluster is maintained. However, the inverse process, transfer from organic to aqueous phase, mostly relies on the ligand exchange reactions. Furthermore, the phosphine-stabilized clusters are more prone to be transferred to another phase after reaction with thiol ligands. For the choice of the ligand used for the phase transfer, three considerations have to be made. (i) The affinity to the metal core of new ligand compared with the original one; (ii) the solubility of the new ligand in the target solvent, and (iii) the capability of the ligand to maintain the core size of the cluster after phase transfer.

1.8 Summary and motivation

In conclusion, ligand exchange reaction plays an important role in the field of

nanoclusters. As one of the post-synthesis methods for the modification and functionalization of the nanoclusters, the process is enabled by the flexibility of the gold-sulfur interface. Experimental and computational investigations show that LERs between clusters and free monothiols in solution starts preferably at the terminal SR groups of the staple motifs, which are linked to the gold core, via an associative S_N2-like mechanism. The process not only takes place in solution phase but also on immobilized Au nanoclusters. Understanding of the preferred reactive sites of the process will help us engineer precise clusters with mixed ligand shell. Compared with the monothiolate ligand exchange, dithiolate ligands may offer an easier way to obtain precise clusters with mixed ligand shell. Intercluster ligand exchange is also an important property of thiolate-protected metal clusters and must be considered whenever clusters with different ligands are in the same solution. Ligand exchange reactions are in general easy to perform and offer a great potential to introduce or amplify properties of the clusters, such as introduction of chirality to achiral clusters, size transformation of the cluster, phase transfer, and the addition of fluorescent groups.

Despite all those considerable efforts made already, still many aspects remain obscure, thus more explorations are needed. The related questions that will be examined in this thesis are the following:

(I) LERs inducing size transformation of gold nanoclusters typically require large excess of incoming ligand, normally more than 100 times compared to the endogenous ligand, and elevated temperatures to proceed. In addition, the incoming thiol must be significantly different from the endogenous thiol for the transformation to happen. Herein we would like to further explore the limitation of reaction condition for size transformation, which will offer more insight for the latter evolution of nanoclusters.

(II) There are many factors involved in the dynamic process of LERs, such as the stability of the samples, length of surface ligand, metal doping, stereoselective properties of intrinsically chiral nanoclusters, chemical properties of the

involved ligands, and the flexibility of the gold-sulfur interface. Furthermore, the electronic properties of the ligand and nanoclusters also play a role, as indicated by the early work of Murry and co-workers. However, after two decades only little advancements have been added to this electronic effect. So, here we will also investigate the electronic effect of ligand during LERs.

(III) The Au_{38} cluster, as one of the intrinsic chiral nanoclusters, is prepared as racemic mixture, and the two enantiomers of Au_{38} can be easily separated using chromatography. Previous studies show the cluster racemizes at reasonably low temperature, which decreases the enantiomeric excess of the system. We are wondering if, by inducing some chiral factors, the enantiomeric excess of the cluster can be amplified. As an ideal candidate, Au_{38} cluster will be applied in this exploration.

(IV) Besides the LERs between clusters and free ligands, there is second pathway for LERs, namely the reaction between clusters (in absence of free ligand). This process remains obscure, especially also for the exchange of dithiolates. In this thesis, by using a configurationally labile axially chiral dithiolate ligand, we shed some more light on intercluster LERs.

1.9 References

(1) Jin, R. *Nanoscale* **2010**, *2*, 343.

(2) Jin, R.; Qian, H.; Wu, Z.; Zhu, Y.; Zhu, M.; Mohanty, A.; Garg, N. *The Journal of Physical Chemistry Letters* **2010**, *1*, 2903.

(3) Qian, H.; Zhu, M.; Wu, Z.; Jin, R. *Accounts of Chemical Research* **2012**, *45*, 1470.

(4) Jin, R.; Zeng, C.; Zhou, M.; Chen, Y. *Chemical Reviews* **2016**, *116*, 10346.

(5) Chakraborty, I.; Pradeep, T. *Chemical Reviews* **2017**, *117*, 8208.

(6) Ghosh, A.; Mohammed, O. F.; Bakr, O. M. *Accounts of Chemical Research* **2018**, *51*, 3094.

(7) Kang, X.; Li, Y.; Zhu, M.; Jin, R. *Chemical Society Reviews* **2020**, *49*, 6443.

(8) Song, X.-R.; Goswami, N.; Yang, H.-H.; Xie, J. *Analyst* **2016**, *141*, 3126.

(9) Maity, S.; Bain, D.; Patra, A. *Nanoscale* **2019**, *11*, 22685.

(10) Pensa, E.; Cortés, E.; Corthey, G.; Carro, P.; Vericat, C.; Fonticelli, M. H.; Benítez, G.; Rubert, A. A.; Salvarezza, R. C. *Accounts of Chemical Research* **2012**, *45*, 1183.

(11) Bürgi, T. *Nanoscale* **2015**, *7*, 15553.

(12) Jadzinsky, P. D.; Calero, G.; Ackerson, C. J.; Bushnell, D. A.; Kornberg, R. D. *Science* **2007**, *318*, 430.

(13) Das, A.; Li, T.; Li, G.; Nobusada, K.; Zeng, C.; Rosi, N. L.; Jin, R. *Nanoscale* **2014**, *6*, 6458.

(14) Qian, H.; Eckenhoff, W. T.; Zhu, Y.; Pintauer, T.; Jin, R. *J. Am. Chem. Soc.* **2010**, *132*, 8280.

(15) Dolamic, I.; Knoppe, S.; Dass, A.; Bürgi, T. *Nature Communications* **2012**, *3*, 798.

(16) Knoppe, S.; Dolamic, I.; Bürgi, T. *Journal of the American Chemical Society* **2012**, *134*, 13114.

(17) Malola, S.; Häkkinen, H. *Journal of the American Chemical Society* **2019**, *141*, 6006.

(18) Barrabés, N.; Zhang, B.; Bürgi, T. *Journal of the American Chemical Society* **2014**, *136*, 14361.

(19) Knoppe, S.; Michalet, S.; Bürgi, T. *The Journal of Physical Chemistry C* **2013**, *117*, 15354.

(20) Varnholt, B.; Oulevey, P.; Luber, S.; Kumara, C.; Dass, A.; Bürgi, T. *The Journal of Physical Chemistry C* **2014**, *118*, 9604.

(21) Varnholt, B.; Dolamic, I.; Knoppe, S.; Bürgi, T. *Nanoscale* **2013**, *5*, 9568.

(22) Beqa, L.; Deschamps, D.; Perrio, S.; Gaumont, A.-C.; Knoppe, S.; Bürgi, T. *The Journal of Physical Chemistry C* **2013**, *117*, 21619.

(23) Dinkel, R.; Peukert, W.; Braunschweig, B. *Journal of Physics: Condensed Matter* **2017**, *29*, 133002.

(24) Xu, M.-M.; Chen, Q.; Xie, L.-H.; Li, J.-R. *Coordination Chemistry Reviews* **2020**, *421*, 213421.

(25) Kang, X.; Zhu, M. *Chemistry of Materials* **2019**, *31*, 9939.

(26) Templeton, A. C.; Hostetler, M. J.; Kraft, C. T.; Murray, R. W. *Journal of the American Chemical Society* **1998**, *120*, 1906.

(27) Song, Y.; Murray, R. W. *Journal of the American Chemical Society* **2002**, *124*, 7096.

(28) Donkers, R. L.; Song, Y.; Murray, R. W. *Langmuir* **2004**, *20*, 4703.

(29) Guo, R.; Song, Y.; Wang, G.; Murray, R. W. *Journal of the American Chemical Society* **2005**, *127*, 2752.

(30) Hostetler, M. J.; Templeton, A. C.; Murray, R. W. *Langmuir* **1999**, *15*, 3782.

(31) Yan, N.; Xia, N.; Wu, Z. *Small* **2020**, 2000609.

(32) Rojas-Cervellera, V.; Raich, L.; Akola, J.; Rovira, C. *Nanoscale* **2017**, *9*, 3121.

(33) Heinecke, C. L.; Ni, T. W.; Malola, S.; Mäkinen, V.; Wong, O. A.; Häkkinen, H.; Ackerson, C. J. *Journal of the American Chemical Society* **2012**, *134*, 13316.

(34) Salassa, G.; Sels, A.; Mancin, F.; Bürgi, T. *ACS Nano* **2017**, *11*, 12609.

(35) Niihori, Y.; Kurashige, W.; Matsuzaki, M.; Negishi, Y. *Nanoscale* **2013**, *5*, 508.

(36) Kluenker, M.; Mondeshki, M.; Tahir, M. N.; Tremel, W. *Langmuir* **2018**, *34*, 1700.

(37) Knoppe, S.; Bürgi, T. *Physical Chemistry Chemical Physics* **2013**, *15*, 15816.

(38) Ni, T. W.; Tofanelli, M. A.; Phillips, B. D.; Ackerson, C. J. *Inorganic Chemistry* **2014**, *53*, 6500.

(39) Niihori, Y.; Kikuchi, Y.; Kato, A.; Matsuzaki, M.; Negishi, Y. *ACS Nano* **2015**, *9*, 9347.

(40) Shibu, E. S.; Muhammed, M. A. H.; Tsukuda, T.; Pradeep, T. *The Journal of Physical Chemistry C* **2008**, *112*, 12168.

(41) Woehrle, G. H.; Brown, L. O.; Hutchison, J. E. *Journal of the American Chemical Society* **2005**, *127*, 2172.

(42) Brown, L. O.; Hutchison, J. E. *Journal of the American Chemical Society* **1997**, *119*, 12384.

(43) Fernando, A.; Aikens, C. M. *The Journal of Physical Chemistry C* **2015**, *119*, 20179.

(44) Fernando, A.; Aikens, C. M. *The Journal of Physical Chemistry C* **2016**, *120*, 14948.

(45) Kang, X.; Chong, H.; Zhu, M. *Nanoscale* **2018**, *10*, 10758.

(46) Fields-Zinna, C. A.; Parker, J. F.; Murray, R. W. *Journal of the American Chemical Society* **2010**, *132*, 17193.

(47) Pengo, P.; Bazzo, C.; Boccalon, M.; Pasquato, L. *Chemical Communications* **2015**, *51*, 3204.

(48) Hossain, S.; Kurashige, W.; Wakayama, S.; Kumar, B.; Nair, L. V.; Niihori, Y.; Negishi, Y. *The Journal of Physical Chemistry C* **2016**, *120*, 25861.

(49) Knoppe, S.; Azoulay, R.; Dass, A.; Bürgi, T. *Journal of the American Chemical Society* **2012**, *134*, 20302.

(50) Jupally, V. R.; Kota, R.; Dornshuld, E. V.; Mattern, D. L.; Tschumper, G. S.; Jiang, D.-e.; Dass, A. *Journal of the American Chemical Society* **2011**, *133*, 20258.

(51) Molina, B.; Sánchez-Castillo, A.; Knoppe, S.; Garzón, I. L.; Bürgi, T.; Tlahuice-Flores, A. *Nanoscale* **2013**, *5*, 10956.

(52) Sels, A.; Salassa, G.; Pollitt, S.; Guglieri, C.; Rupprechter, G.; Barrabés, N.; Bürgi, T. *The Journal of Physical Chemistry C* **2017**, *121*, 10919.

(53) Knoppe, S.; Dharmaratne, A. C.; Schreiner, E.; Dass, A.; Bürgi, T. *Journal of the American Chemical Society* **2010**, *132*, 16783.

(54) Si, S.; Gautier, C.; Boudon, J.; Taras, R.; Gladiali, S.; Bürgi, T. *The Journal of Physical Chemistry C* **2009**, *113*, 12966.

(55) Sels, A.; Barrabés, N.; Knoppe, S.; Bürgi, T. *Nanoscale* **2016**, *8*, 11130.

(56) Zeng, C.; Liu, C.; Pei, Y.; Jin, R. *ACS Nano* **2013**, *7*, 6138.

(57) Li, M.-B.; Tian, S.-K.; Wu, Z.; Jin, R. *Chemistry of Materials* **2016**, *28*, 1022.

(58) Wang, S.; Abroshan, H.; Liu, C.; Luo, T.-Y.; Zhu, M.; Kim, H. J.; Rosi, N. L.; Jin, R. *Nature Communications* **2017**, *8*, 848.

(59) Nimmala, P. R.; Theivendran, S.; Barcaro, G.; Sementa, L.; Kumara, C.; Jupally, V. R.; Apra, E.; Stener, M.; Fortunelli, A.; Dass, A. *The Journal of Physical Chemistry Letters* **2015**, *6*, 2134.

(60) Zeng, C.; Chen, Y.; Das, A.; Jin, R. *The Journal of Physical Chemistry Letters* **2015**, *6*, 2976.

(61) Dass, A.; Jones, T. C.; Theivendran, S.; Sementa, L.; Fortunelli, A. *The Journal of Physical Chemistry C* **2017**, *121*, 14914.

(62) Chen, Y.; Liu, C.; Tang, Q.; Zeng, C.; Higaki, T.; Das, A.; Jiang, D.-e.; Rosi, N. L.; Jin, R. *Journal of the American Chemical Society* **2016**, *138*, 1482.

(63) Zeng, C.; Li, T.; Das, A.; Rosi, N. L.; Jin, R. *Journal of the American Chemical Society* **2013**, *135*, 10011.

(64) Gan, Z.; Chen, J.; Wang, J.; Wang, C.; Li, M.-B.; Yao, C.; Zhuang, S.; Xu, A.; Li, L.; Wu, Z. *Nature Communications* **2017**, *8*, 14739.

(65) Maman, M. P.; Nair, A. S.; Cheraparambil, H.; Pathak, B.; Mandal, S. *The Journal of Physical Chemistry Letters* **2020**, *11*, 1781.

(66) McKenzie, L. C.; Zaikova, T. O.; Hutchison, J. E. *J. Am. Chem. Soc.* **2014**, *136*, 13426.

(67) Shichibu, Y.; Negishi, Y.; Tsukuda, T.; Teranishi, T. *J. Am. Chem. Soc* **2005**, *127*, 13464.

(68) Nimmala, P. R.; Dass, A. *Journal of the American Chemical Society* **2014**, *136*, 17016.

(69) Zeng, C.; Liu, C.; Chen, Y.; Rosi, N. L.; Jin, R. *Journal of the American Chemical Society* **2014**, *136*, 11922.

(70) Eswaramoorthy, S. K.; Sakthivel, N. A.; Dass, A. *The Journal of Physical Chemistry C* **2019**, *123*, 9634.

(71) Dong, H.; Liao, L.; Wu, Z. *The Journal of Physical Chemistry Letters* **2017**, *8*, 5338.

(72) Liao, L.; Zhuang, S.; Yao, C.; Yan, N.; Chen, J.; Wang, C.; Xia, N.; Liu, X.; Li, M.-B.; Li, L.; Bao, X.; Wu, Z. *Journal of the American Chemical Society* **2016**, *138*, 10425.

(73) Mason, S. *Trends in Pharmacological Sciences* **1986**, *7*, 20.

(74) Bada, J. L. *Nature* **1995**, *374*, 594.

(75) Gautier, C.; Bürgi, T. *Chemphyschem* **2009**, *10*, 483.

(76) Yao, H. *Progress in Natural Science: Materials International* **2016**, *26*, 428.

(77) Zeng, C.; Jin, R. *Chemistry – An Asian Journal* **2017**, *12*, 1839.

(78) Zhu, M.; Qian, H.; Meng, X.; Jin, S.; Wu, Z.; Jin, R. *Nano Letters* **2011**, *11*, 3963.

(79) Knoppe, S.; Kothalawala, N.; Jupally, V. R.; Dass, A.; Bürgi, T. *Chem. Commun.* **2012**, *48*, 4630.

(80) Kumar, S.; Jin, R. *Nanoscale* **2012**, *4*, 4222.

(81) Wang, Y.; Nieto-Ortega, B.; Bürgi, T. *Chem. Commun.* **2019**, *55*, 14914.

(82) Xu, Q.; Kumar, S.; Jin, S.; Qian, H.; Zhu, M.; Jin, R. *Small* **2014**, *10*, 1008.

(83) Bai, Y.; Shu, T.; Su, L.; Zhang, X. *Crystals* **2020**, *10*, 357.

(84) Guo, Y.; Amunyela, H. T. N. N.; Cheng, Y.; Xie, Y.; Yu, H.; Yao, W.; Li, H.-W.; Qian, H. *Food Chemistry* **2021**, *335*, 127657.

(85) Zheng, Y.; Lai, L.; Liu, W.; Jiang, H.; Wang, X. *Advances in Colloid and Interface Science* **2017**, *242*, 1.

(86) Truttmann, V.; Herzig, C.; Illes, I.; Limbeck, A.; Pittenauer, E.; Stöger-Pollach, M.; Allmaier, G.; Bürgi, T.; Barrabés, N.; Rupprechter, G. *Nanoscale* **2020**, *12*, 12809.

(87) Shang, L.; Stockmar, F.; Azadfar, N.; Nienhaus, G. U. *Angewandte Chemie International Edition* **2013**, *52*, 11154.

(88) Wang, Y.; Hu, L.; Li, L.; Zhu, J.-J. *Journal of Analysis and Testing* **2017**, *1*, 13.

(89) Lin, C.-A. J.; Yang, T.-Y.; Lee, C.-H.; Huang, S. H.; Sperling, R. A.; Zanella, M.; Li, J. K.; Shen, J.-L.; Wang, H.-H.; Yeh, H.-I.; Parak, W. J.; Chang, W. H. *ACS Nano* **2009**, *3*, 395.

(90) Hu, X.; Zheng, Y.; Zhou, J.; Fang, D.; Jiang, H.; Wang, X. *Chem. Mater.* **2018**, *30*, 1947.

(91) Sperling, R. A.; Parak, W. J. *Philos. Trans. Royal Soc. A* **2010**, *368*, 1333.

(92) Habeeb Muhammed, M. A.; Pradeep, T. *J. Cluster Sci.* **2009**, *20*, 365.

(93) Padelford, J. W.; Wang, T.; Wang, G. *ChemElectroChem* **2016**, *3*, 1201.

(94) Knoppe, S.; Wong, O. A.; Malola, S.; Häkkinen, H.; Bürgi, T.; Verbiest, T.; Ackerson, C. J. *J. Am. Chem. Soc* **2014**, *136*, 4129.

(95) Yao, H.; Iwatsu, M. *Langmuir* **2016**, *32*, 3284.

(96) Yao, H.; Tsubota, S. *Chem. Phys.* **2017**, *493*, 149.

(97) Wang, Y.; Su, H.; Xu, C.; Li, G.; Gell, L.; Lin, S.; Tang, Z.; Häkkinen, H.; Zheng, N. *J. Am. Chem. Soc* **2015**, *137*, 4324.

(98) Ren, L.; Yuan, P.; Su, H.; Malola, S.; Lin, S.; Tang, Z.; Teo, B. K.; Häkkinen, H.; Zheng, L.; Zheng, N. *J. Am. Chem. Soc* **2017**, *139*, 13288.

(99) Zan, X.; Li, Q.; Pan, Y.; Morris, D. J.; Zhang, P.; Li, P.; Yu, H.; Zhu, M. *ACS Appl. Nano Mater.* **2018**, *1*, 6773.

Chapter 2

Methods

This chapter will focus on the general synthesis of common materials, which used in the thesis. In addition, the methods widely used for the purification and characterization will also be listed one by one.

Because the gold nanoclusters are the main objects of this thesis, the first subchapter will illustrate the synthesis protocol for different precise gold nanoclusters, such as $Au_{25}(SBut)_{18}$[1], $Au_{25}(2\text{-}PET)_{18}$[2] and $Au_{38}(SR)_{24}$[3]. During the thesis, various thiol ligands have been applied for the ligand exchange reaction[4,5], and the corresponding synthesis protocol of identified ligands will not be included here, but will be explained in the corresponding chapter.

Afterwards, the methods used for purification and separation of the gold nanoclusters, for instance, size exclusion chromatography (SEC)[6] and high-performance liquid chromatography (HPLC)[7] will be discussed, and details on the setup and experimental considerations will also be presented.

In order to characterize the gold nanoclusters or the reactions, the most common methods, such as UV-vis, circular dichroism (CD), mass spectroscopy and nuclear magnetic resonance (NMR) will also be included in the next subchapter. These characterization methods are also used to follow the ligand exchange reactions, which is the main typical reaction among the thesis.

2.1 Protocol for synthesis of monodisperse gold nanoclusters

Synthesis and purification of $[Au_{25}(SBut)_{18}]^0$. A solution (100 ml) of $HAuCl_4 \cdot 3H_2O$ (1 g, 2.54 mmol) and tetra-n-octylammonium bromide (TOAB) (1575 mg, 2.85 mmol) in tetrahydrofuran (THF) was prepared. 12 equiv. of 1-butanethiol (1632 µl, 15.24 mmol) were added dropwise to the solution under stirring and at room temperature. After 1 h, a freshly prepared ice-cold solution of $NaBH_4$ (970 mg, 25.4 mmol) in

milli-Q water (20 ml) was rapidly added under vigorous stirring. The resulting black mixture was stirred for ca. 3 days. Afterwards, the THF was removed by rotary evaporation to leave a red-brownish oil covered by an aqueous phase. The latter was removed by adding 200 mL of cold methanol and then filtered on paper. To remove excess thiol and other byproducts, the product was washed with methanol, filtered and dissolved in dichloromethane (DCM) at least three times. Finally, the product was dried in a vacuum rotary evaporator at room temperature. By this procedure, the cluster is obtained as $[n\text{-}Oct_4N^+][Au_{25}(SBu)_{18}^-]$. By dissolution in dichloromethane (DCM, 5 ml) followed by passing through a silica gel column under aerobic conditions, the product was then further oxidized to obtaine $[Au_{25}(SBut)_{18}]^0$. The sample was stored at -18 °C. Further purification and characterization of the samples was carried out by size exclusion chromatography (SEC), UV-Vis spectroscopy and matrix-assisted laser desorption ionization time-of-flight (MALDI-TOF) mass spectrometry.

Synthesis and purification of Au_{25}(2-PET)$_{18}$. Similarly, to the synthesis of $[Au_{25}(SBut)_{18}]^0$ described above, $[Au_{25}(2\text{-}PET)_{18}]^0$ was prepared by first synthesizing $Au_{25}(2\text{-}PET)_{18}^-$ (anion cluster) followed by oxidation by a silica gel column under aerobic conditions. Typically, $HAuCl_4 \cdot 3H_2O$ (1 g, 2.54 mmol) and TOAB (1.641 mg, 0.30 mmol) were combined in a 1 L round bottom flask, to which 250 mL THF solvent was added. After vigorous stirring for 15 min, the solution color changed from yellow to red. Then, C_8H_9SH (1.62 mL, 7.25 mmol) was slowly added to the flask at room temperature without changing the stirring speed. The solution color gradually changed from red to yellow and then to colorless within ~30 min. After that, an aqueous solution of $NaBH_4$ (0.918 g, 0.5 mmol, freshly dissolved in 50.0 mL of ice-cold milli-Q water) was added to the flask all at once. The reaction generated some bubbles and the solution turned black immediately, indicating the formation of Au nanoclusters. The reaction was allowed to proceed under constant stirring for ca. 2 days and eventually we obtained pure $Au_{25}(2\text{-}PET)_{18}^-$. After this point the purification and characterization followed the same procedure as described for $[Au_{25}(SBut)_{18}]^0$.

Purification and characterization of the samples were carried out by size exclusion chromatography (SEC), UV-Vis and MALDI-TOF mass spectrometry.

Synthesis and size-selection of *rac*-$Au_{38}(2\text{-PET})_{24}$. 1 gram of $HAuCl_4 \cdot 3H_2O$ and 3.12 gram of L-glutathione were dissolved in 100 mL of acetone in a 500mL round bottom flask and stirred vigorously at room temperature for 5-10min. Then the flask was put into an ice bath and kept at 0˚C for 20-25min, obtaining a yellow suspension. Freshly prepared $NaBH_4$ (960mg) in 30 mL H_2O (0˚C) was added to the solution, which turned from yellow-white to black-brown immediately. This solution was kept stirring for 20min at 0˚C at lower stirring speed. After that, the black precipitate was stuck on the wall of the flask, removed from the wall in acetone followed by drying the precipitate with air. The clusters were redissolved in a mixture of H_2O (30mL), EtOH (1.6mL) and toluene (10mL), followed by addition of 10mL of 2-phenylethanethiol to the clusters. The system was heated to 80 ˚C and reacted for 24h. After cooling to room temperature, large amounts of methanol were added to the flask and left overnight. Methanol was removed by decanting and filtration. The collected clusters were rinsed with methanol, dissolved in DCM and dried by rotatory evaporation. This washing step was repeated several times to remove free thiol and small clusters. Size exclusion chromatography (SEC column) was used to purify the raw clusters. Purity of the $Au_{38}(2\text{-PET})_{24}$ sample was verified by UV–vis spectroscopy, MALDI-TOF mass spectrometry and HPLC. Separation of the enantiomers can be done by chiral HPLC[7].

2.2 Purification and separation of gold nanoclusters

After the synthesis of the gold nanoclusters, free thiols, reactants and by-products remain in the system. In order to obtain pure monodisperse nanoclusters for the further characterization and reaction, it is necessary to remove any impurity from the sample. Normally, size exclusion chromatography (SEC) is the first option for this purpose, which allowed treating large amount of sample and easy operating. In addition, depending on the properties of the cluster, high-performance liquid

chromatography (HPLC) can also be applied to isolate the aimed nanoclusters from the sample[8]. Various columns are available such that HPLC can be used for a wide range of applications (including cases where high resolutions is needed), however, usually only small quantities of sample are involved.

Size exclusion chromatography (SEC). Size exclusion chromatography is an important separation technique that depends on the relative size or hydrodynamic volume of a macromolecule[9]. SEC with porous stationary phase SX1 bio-beads (Biorad, particle sizes 40-80 μm) has become an essential method for the separation of ligand protected nanoparticles[10]. As shown at Figure 2.1, when the sample solution flows through a porous packed bed, the macromolecules with different size will pass through different path and give identified elution time. When a sample of clusters with different size is added to the SEC column the small clusters are able to enter more pores compared to bigger ones which leads to longer elution times. As a consequence the clusters with largest hydrodynamic volumes elute first, followed by the intermediated size and finally the smallest size clusters. SEC column has wide tolerance for the solvent, so DCM, THF and toluene are used for the separation. Typically for the separation of Au_{25} and Au_{38} clusters, toluene is most commonly used solvent.

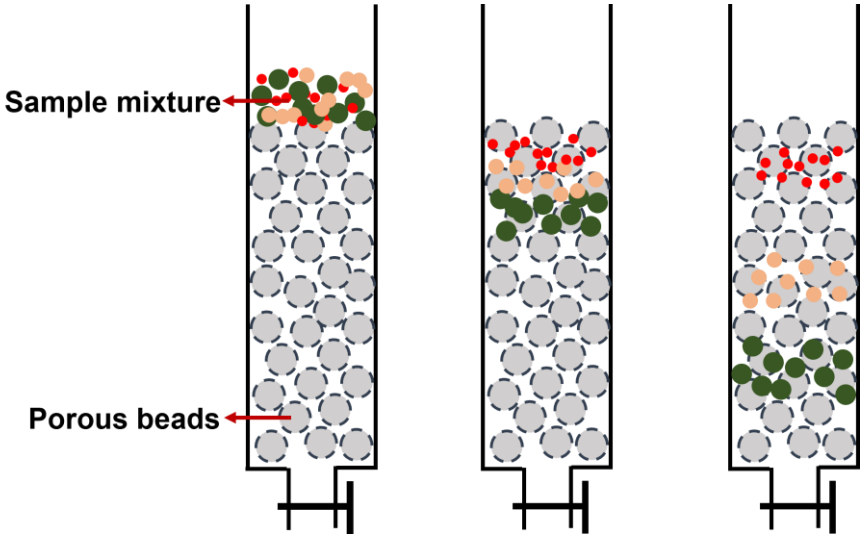

Figure 2.1 Schematic representation of SEC for a mixed clusters sample.

HPL Chromatography (HPLC). High performance liquid chromatography (HPLC), which can be used for separating, identifying, and quantifying components in a mixture, has become an important technique in analytical chemistry. This method depends on pumps to pass a pressurized liquid solvent containing the sample mixture through a column filled with a solid adsorbent material. Because of the different affinity and reactivity between the component and adsorbent phase, each component in the sample interacts slightly differently with the adsorbent material, causing different flow rates for the different components and leading to the separation of the components as they flow out of the column at different retention time. The efficient separation of samples in HPLC mainly relies on the different specialized column materials used in the system.

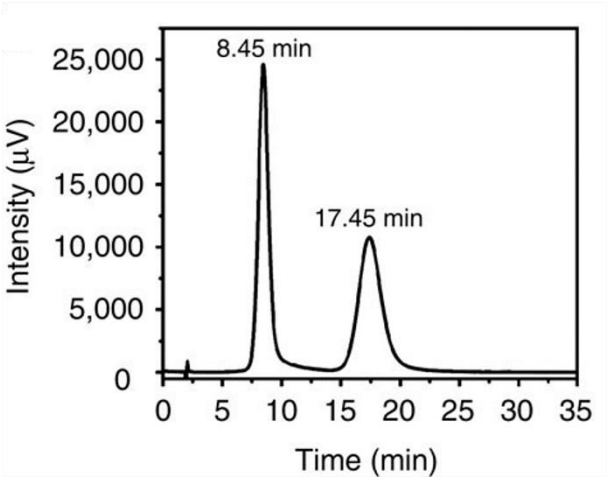

Figure 2.2 HPL chromatogram of the enantioseparation of rac-$Au_{38}(SCH_2CH_2Ph)_{24}$ with the ultraviolet-visible detector at 380 nm. The peak at 8.45 min (17.45min) corresponds to enantiomer 1 (2)[7].

In the field of nanomaterials, since some particles or clusters are chiral, and the related enantiomers cannot be separated by conventional SEC columns, special columns are needed containing chiral stationary phases. For instance, our group separated the two enantiomers of Au_{38}(2-PET)$_{24}$ for the first time as shown in Fig. 2.2[7]. The enantiomers of the cluster were characterized by circular dichroism spectra separately. Furthermore, by in-situ chiral HPLC the LERs between Au_{38}(2-PET)$_{24}$ and chiral ligand R-BINAS was monitored, as illustrated in Fig. 2.3[11], which indicated the diastereoselective ligand exchange reaction. This significant phenomenon may not be

investigated without chiral HPL chromatography. In addition, Sels and co-workers also performed ligand exchange reactions on $PdAu_{24}(SR)_{18}$ clusters with R-BINAS monitored in situ by chiral HPLC[12]. The different exchange products and isomers after LERs with a precise composition and location of the mixed ligand shell were successfully separated.

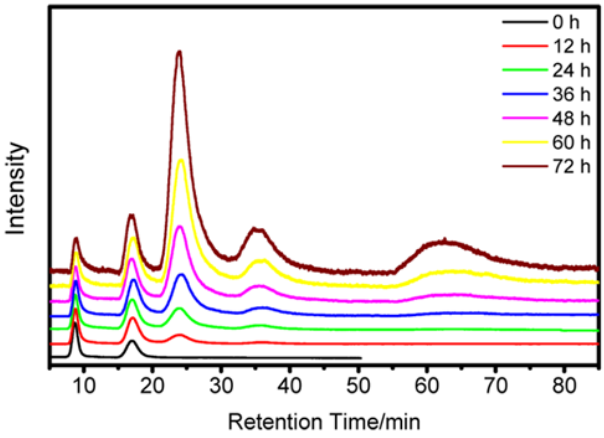

Figure 2.3 Evolution HPLC (0−72 h) of the ligand exchange reaction between rac-Au_{38}(2-PET)$_{24}$ and R-BINAS. The detector wavelength was set to 630 nm to avoid contribution from BINAS to the overall absorbance[11].

The HPLC experiments in chapter 5 and 6 were performed on a JASCO 20XX HPLC system equipped with a semi-preparative Phenomenex Lux-5u-cellulose-1 column (5µm, 250 x 10 mm). The sample was injected in toluene and eluted with n-hexane/iso-propanol 75:25 at a flow rate of 2.5mL/min. A JASCO 2070 plus UV-vis detector was used for the detection. For thermal treatment, the concentrated sample was heated in an oil bath to 70°C and injected to HPLC after various times. Peak areas were determined using PeakFit (seasolve, version 4.12) in Chapter 5. Fitting was performed after subtracting a background and by using chromatography peak type (exponentially modified Gaussian) with varying peak width and shape.

2.3 Characterization of gold nanoclusters

Ultraviolet-visible spectroscopy (UV-vis). UV-vis spectroscopy as one of the initial and easiest way to identify the nanoclusters, usually directly used after SEC column separation. The UV-vis spectrum is characteristic for a specific cluster and can be

used for its identification. However, for LER reactions, the distribution and composition of the ligands on the clusters surface does not lead to large spectral changes. Therefore, this method is not suitable for identifying the LERs. The UV-vis spectra shown in this thesis were measured on a Varian Cary 50 spectrometer. A quartz cuvette of 2 mm path length was used.

In Fig. 2.4 the typical UV-vis spectra of $[Au_{25}(SBut)_{18}]^0$, $[Au_{25}(2\text{-}PET)_{18}]^0$ and $Au_{38}(2\text{-}PET)_{24}$ are shown.

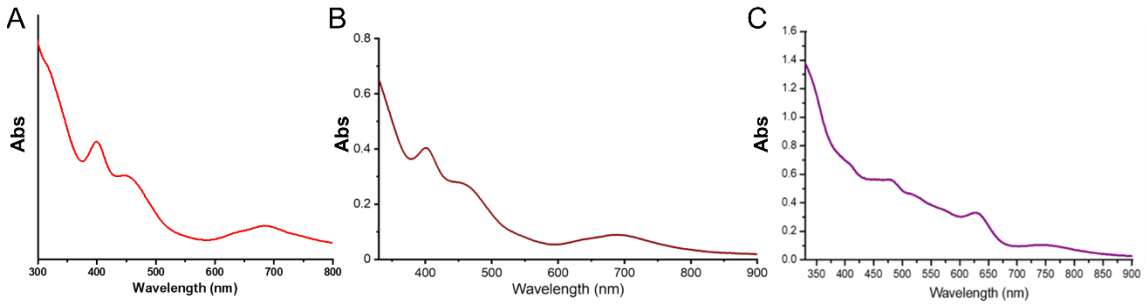

Figure 2.4 UV-vis absorption spectra of $[Au_{25}(SBut)_{18}]^0$ (A), $[Au_{25}(2\text{-}PET)_{18}]^0$ (B) and $Au_{38}(2\text{-}PET)_{24}$ (C) in DCM. The spectra were obtained using a quartz cuvette with a 2 mm optical-path length, at room temperature.

Circular dichroism (CD). Circular Dichroism (CD) is an absorption spectroscopy method based on the differential absorption of left and right circularly polarized light (CPL). In the system, optically active chiral molecules will preferentially absorb one direction of the circularly polarized light, and the difference in absorption of the left and right circularly polarized light can be measured and quantified. Some thiolate-protected gold nanoclusters are chiral because of the chiral arrangement of the staple motifs (e.g. $Au_{38}(2\text{-}PET)_{24}$) or the chiral ligand on the surface. In addition, when chiral ligand was involved in the LERs for achiral clusters, the CD spectrum can be used for the products identification, and provides information about the chiroptical properties of the clusters. As shown in Fig. 2.5, the various chiroptical properties of clusters were revealed by the CD spectra. Compared with the signal from achiral $Au_{25}(2\text{-}PET)_{18}$ clusters without optical activity, as expected (Fig. 2.5 A black), the signal of cluster progressively shows increasing intensity after ligand exchange with S-BINAS (Fig. 2.5 A), which was also consistent with the increasing

anisotropy factors (Fig. 2.5 B). More important, compared with other measurements, CD spectra can discriminate between the handedness of the ligand, as illustrated in Fig. 2.5 C. After $Au_{38/40}(2\text{-PET})_{24}$ reacted with R-BINAS and S-BINAS for 44h separately, these two CD spectra show mirror image behaviour.

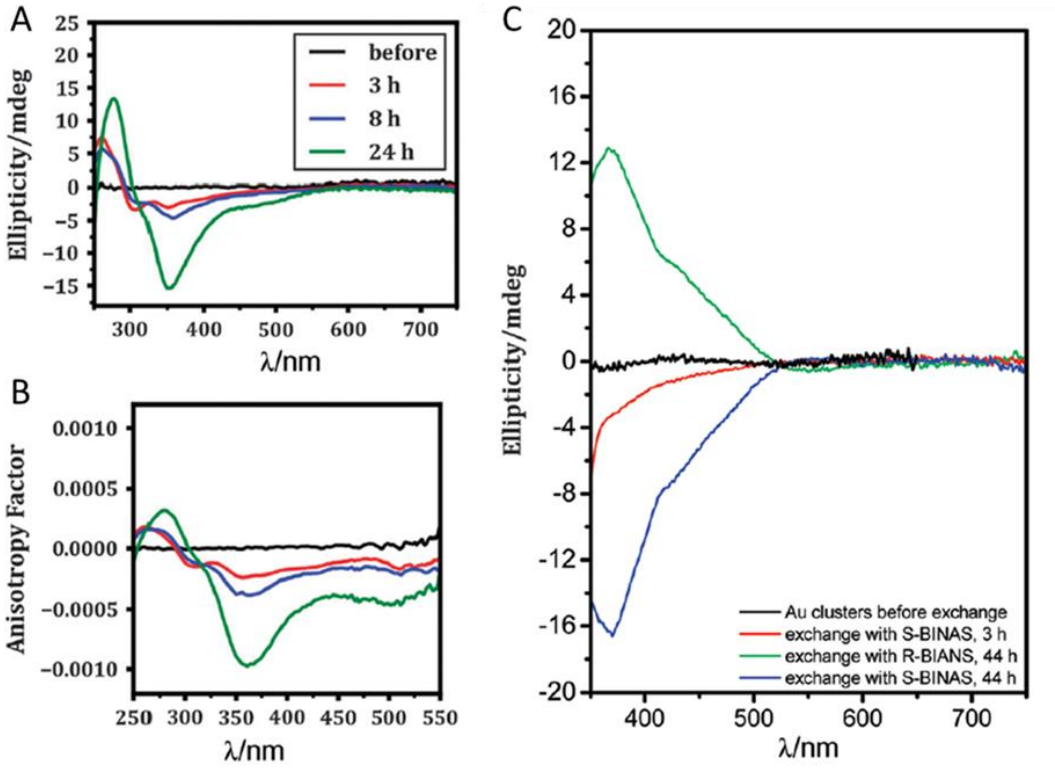

Figure 2.5 CD spectra (A) and anisotropy factors (B) of $Au_{25}(2\text{-PET})_{18}$ clusters prior (black) and after ligand exchange with S-BINAS, (C) CD spectra of $Au_{38/40}(2\text{-PET})_{24}$ prior (black) and after 3h (red) and 44 h (green and blue) ligand exchange with BINAS. Copyright from references[13,14].

However, the CD spectrum just reveals the change of the optical activity of samples and do not quantify the number of exchanged ligands. The main reason for this is the strong non-linear effects in the chiroptical properties with respect to the number of chiral ligands present. This phenomenon was investigated by Knoppe and co-workers as shown in Fig. 2.6[15]. $Au_{38}(2\text{-PET})_{24}$ and $Au_{40}(2\text{-PET})_{24}$ were used for the LERs with S-BINAS, and the anisotropy factor at 370 nm of samples with different number of BINAS ligand were recorded separately. It is obvious that in both cases the evolution of the optical activity is strongly non-linear with the number of the exchanged ligands. The behavior of these two clusters is also different. The maximum number of

exchanged ligands for these two clusters are different. The non-linear effect may be due to the intrinsic chirality of the clusters and the possible diastereomers formed with the chiral ligand. Overall, CD spectroscopy provides important chiroptical properties for LERs, and normally it needs to be combined with other measurements, such as MALDI and HPLC.

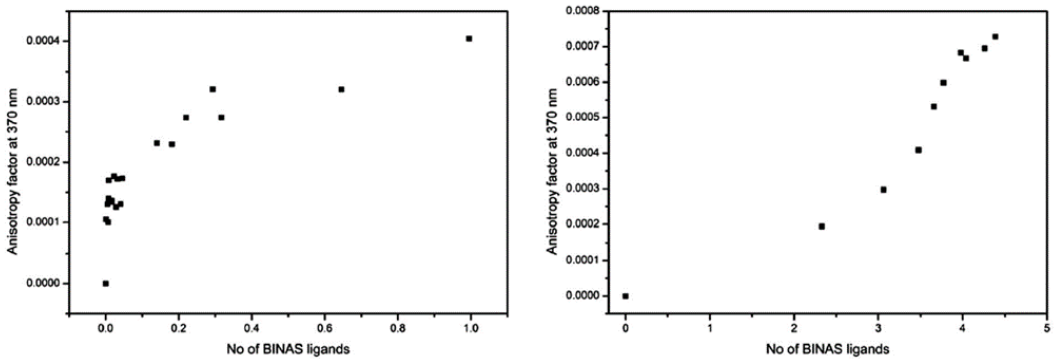

Figure 2.6 Left: anisotropy factor (at 370 nm) of $Au_{38}(2\text{-PET})_{24\text{-}2x}(\text{S-BINAS})_x$ compared to the average number of S-BINAS ligands determined by mass spectrometry (x-axis); right: the same comparison with $Au_{40}(2\text{-PET})_{24\text{-}2x}(\text{S-BINAS})_x$. Copyright from references[15].

The CD spectra shown in this thesis were recorded on a JASCO J-815 CD-spectrometer. A quartz cuvette of 2mm path length was used. For each CD spectrum ten scans were averaged at a scanning speed of 200nm min^{-1} with a data pitch of 1 nm. The anisotropy factors $g=\theta[\text{mdeg}]\ (32980\text{xA})^{-1}$ were calculated from the UV-vis and CD spectra. In Fig. 2.7, the CD spectra of two enantiomers of $Au_{38}(2\text{-PET})_{24}$ after separation by chiral HPL chromatography are shown.

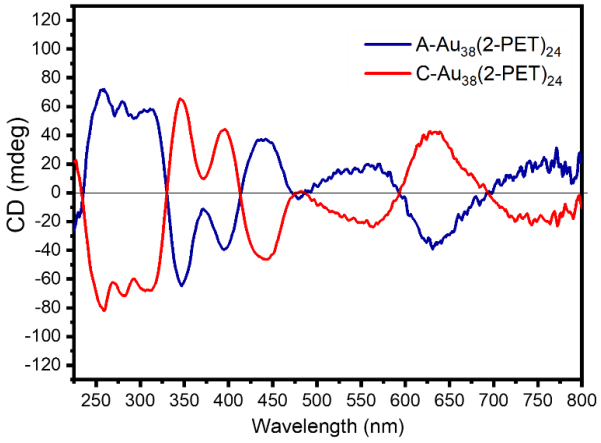

Figure 2.7 Experimental CD spectra of enantiopure A/C-$Au_{38}(2\text{-PET})_{24}$, the clusters were dissolved in dichloromethane and the spectra were recorded at the same concentration for the two enantiomers.

Mass spectrometry. Mass spectrometry is a powerful characterization, providing rich information on the composition and its distribution of the sample. Among the mass spectrometry techniques, matrix-assisted laser desorption/ionization (MALDI) is an ionization technique using laser energy to create ions from large molecules. Due to the soft ionization and applied matrix, MALDI gives minimal fragmentation and has been widely applied to the analysis of biomolecules. During the past decades, MALDI mass spectrometry has been widely applied for the investigation of nanoclusters and LERs reactions.

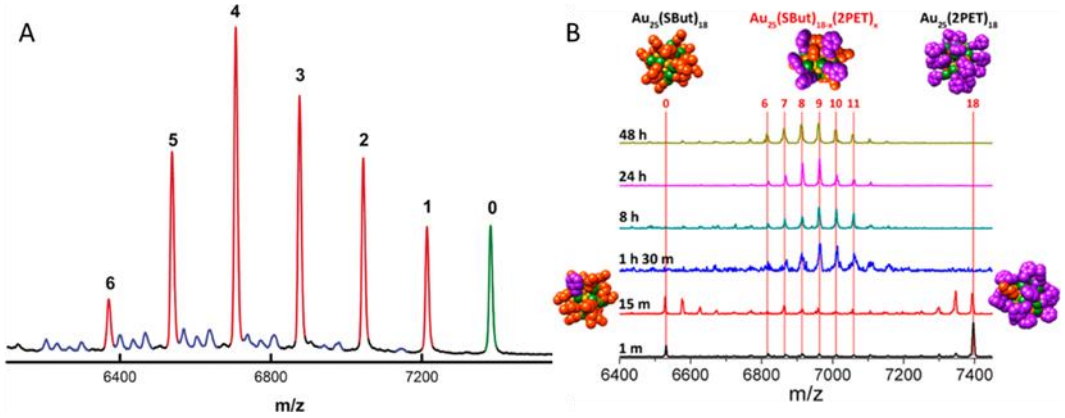

Figure 2.8 (A) MALDI MS of $Au_{25}(2\text{-PET})_{18}$ ligand exchanged with 1,3-propanedithiol[16]. The green peak: $Au_{25}(2\text{-PET})_{18}$, the red peaks: exchanged species of $Au_{25}(2\text{-PET})_{18}$, the numbers denote the number of such exchanges of dithiol. (B) MALDI mass spectra collected at different times after the mixing of $Au_{25}(SBut)_{18}$ (orange) and $Au_{25}(2\text{-PET})_{18}$ (purple) with a ratio of 1:1 in DCM[5].

The basis of this methodology for identified the LERs is the mass difference between the incoming and outgoing ligands in the reaction. For instance, Fig. 2.8 A shows the MALDI results from the $Au_{25}(2\text{-PET})_{18}$ clusters after ligand exchange with 1,3-propanedithiol[16]. The green peak corresponds to original $Au_{25}(2\text{-PET})_{18}$ without exchanges and the red peaks correspond to exchanged species. From the spectrum it is revealed that the sample has a distribution of different compositions and the mass of exchanged species is consistent with one dithiol exchanging with two monothiols. In addition, the intercluster LERs also can be inspected by MALDI mass spectrometry as shown in Fig. 2.8 B, which illustrates the collected MALDI mass spectra of sample at different times after mixing $Au_{25}(SBut)_{18}$ (orange) and $Au_{25}(2\text{-PET})_{18}$ (purple) together[5]. Here, the reaction was monitored by MALDI, which gives insight into the

composition of clusters and offers a quantitative analysis of the reaction products. From the information provided by real-time MALDI mass spectra, it is also possible to explore the kinetics and reaction pathway of LERs[17].

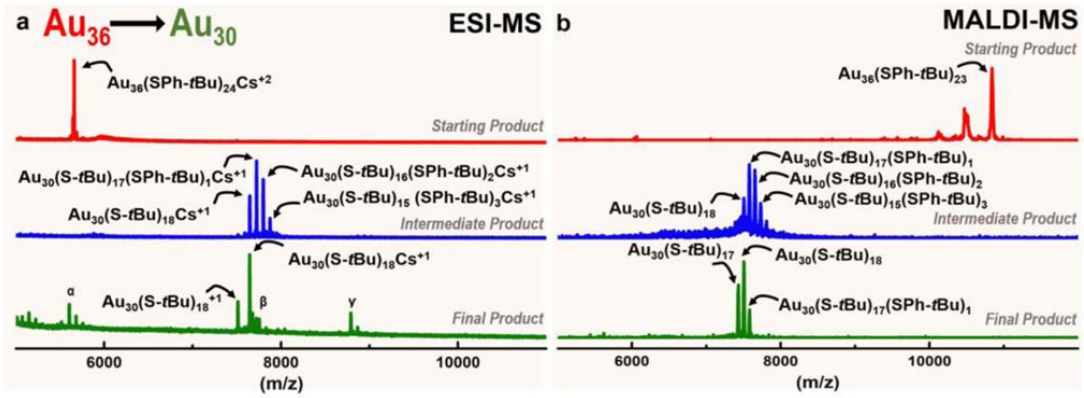

Figure 2.9 (A) Core size conversion of $Au_{36}(SPh\text{-}^{t}But)_{24}$ to $Au_{30}(S\text{-}^{t}But)_{18}$: (a) ESI-MS showing the starting product $Au_{36}(SPh\text{-}^{t}But)_{24}$ (red, top spectrum), the intermediate product in blue, and the final product, in green, $Au_{30}(S\text{-}^{t}But)_{18}$. (b) MALDI-MS of the monodisperse $Au_{36}(SPh\text{-}^{t}But)_{24}$ starting material (top red spectrum) transforming to $Au_{30}(S\text{-}^{t}But)_{18}$ (bottom spectrum) upon thermochemical treatment with t-butyl thiol at 75−80 °C. Copyright from reference[18].

Apart from MALDI spectrometry, electrospray ionization mass spectrometry (ESI-MS) is also used to investigate the LERs process. Different from MALDI, ESI-MS produces ions using an electrospray, and applying a high voltage to sample liquid to create an aerosol. Due to the fundamental difference between MALDI and ESI in the generation of ions, the signals from both methodologies for investigating LERs show some differences. ESI may produce multiple-charged ions and extending the mass range to be analyzed. As illustrated in Fig 2.9, the start, intermediate and final products during core size conversion of $Au_{36}(SPh\text{-}^{t}But)_{24}$ to $Au_{30}(S\text{-}^{t}But)_{18}$ were measured with MALDI and ESI separately[18]. The difference between ESI and MALDI is evident from the red curves in Fig. 2.9 which correspond to the starting clusters shown as $Au_{36}(SPh\text{-}^{t}But)_{24}Cs^{+2}$ from ESI and detected as $Au_{36}(SPh\text{-}^{t}But)_{23}$ in MALDI. The molecular ions from MALDI and the +1 charged ions from ESI should give similar signal, however, multiple-charged ions of ESI extended the signal range whereas the MALDI spectrum may be more clear.

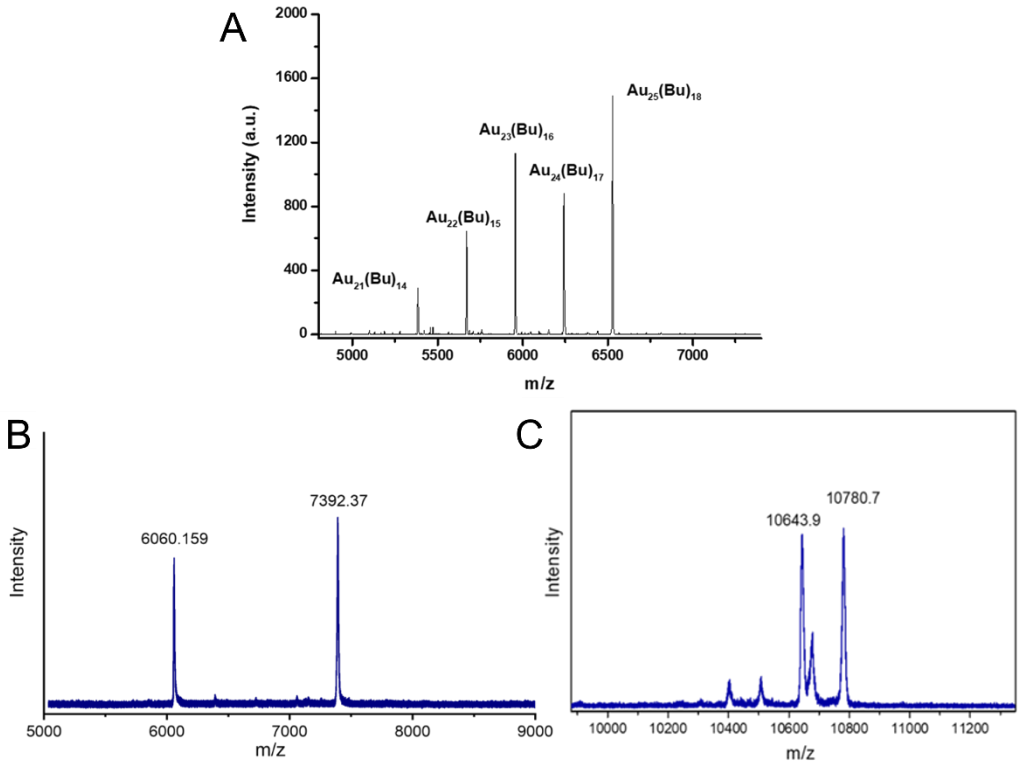

Figure 2.10 Positive-ion MALDI mass spectra of $[Au_{25}(SBut)_{18}]^0$ (A), $[Au_{25}(2\text{-PET})_{18}]^0$ (B) and $Au_{38}(2\text{-PET})_{24}$ (C).

The MALDI-TOF mass spectra in this thesis were recorded on a Bruker Autoflex mass spectrometer in positive linear mode with a nitrogen laser at near-threshold laser intensity. As matrix *trans-2-[3-(4-tert-Butylphenyl)-2-methyl-2-propenylidene] -malononitrile* was used. 3.5mg matrix was dissolved in 100µL toluene. Matrix and sample were mixed at volume ratio 1:1, and 2µL of the mixture was applied to the MALDI plate and air-dried. The MALDI mass spectra of $[Au_{25}(SBut)_{18}]^0$, $[Au_{25}(2\text{-PET})_{18}]^0$ and $Au_{38}(2\text{-PET})_{24}$ are shown at Fig. 2.10.

Nuclear magnetic resonance (NMR). Nuclear magnetic resonance (NMR) is a physical observation method where nuclei are put in a strong constant magnetic field and perturbed by a weak oscillating magnetic field. Since the discovery of this phenomenon, NMR spectroscopy has become an important methodology and has been used widely for identification and analysis of the structure of organic molecules and other materials in solution and in solid state.

NMR results from specific magnetic properties of certain atomic nuclei, and ^1H and

^{13}C are the most commonly used nuclei. Compared with ^{13}C NMR, which has low sensitive and need long acquisition time, ^{1}H NMR has higher sensitivity. In addition, ^{1}H NMR was also the foremost methodology to investigate ligand exchange reactions, since Murray and co-workers started to explore the field two decade years ago[19-21]. During the LERs, the H protons of the incoming and outgoing ligands possess different chemical environment, and the evolution of specific ^{1}H NMR signal can be used to monitor the extent of the ligand exchange reactions.

2.4 References

(1) Parker, J. F.; Weaver, J. E. F.; McCallum, F.; Fields-Zinna, C. A.; Murray, R. W. *Langmuir* **2010**, *26*, 13650.

(2) Heaven, M. W.; Dass, A.; White, P. S.; Holt, K. M.; Murray, R. W. *Journal of the American Chemical Society* **2008**, *130*, 3754.

(3) Qian, H.; Zhu, Y.; Jin, R. *ACS Nano* **2009**, *3*, 3795.

(4) Beqa, L.; Deschamps, D.; Perrio, S.; Gaumont, A.-C.; Knoppe, S.; Bürgi, T. *The Journal of Physical Chemistry C* **2013**, *117*, 21619.

(5) Salassa, G.; Sels, A.; Mancin, F.; Bürgi, T. *ACS Nano* **2017**, *11*, 12609.

(6) Pitkänen, L.; Striegel, A. M. *TrAC Trends in Analytical Chemistry* **2016**, *80*, 311.

(7) Dolamic, I.; Knoppe, S.; Dass, A.; Bürgi, T. *Nature Communications* **2012**, *3*, 798.

(8) Zhang, Y.; Hu, Q.; Paau, M. C.; Xie, S.; Gao, P.; Chan, W.; Choi, M. M. F. *The Journal of Physical Chemistry C* **2013**, *117*, 18697.

(9) Kostanski, L. K.; Keller, D. M.; Hamielec, A. E. *Journal of Biochemical and Biophysical Methods* **2004**, *58*, 159.

(10) Gautier, C.; Taras, R.; Gladiali, S.; Bürgi, T. *Chirality* **2008**, *20*, 486.

(11) Knoppe, S.; Azoulay, R.; Dass, A.; Bürgi, T. *Journal of the American Chemical Society* **2012**, *134*, 20302.

(12) Sels, A.; Barrabés, N.; Knoppe, S.; Bürgi, T. *Nanoscale* **2016**, *8*, 11130.

(13) Knoppe, S.; Bürgi, T. *Physical Chemistry Chemical Physics* **2013**, *15*, 15816.

(14) Knoppe, S.; Dharmaratne, A. C.; Schreiner, E.; Dass, A.; Bürgi, T. *Journal of the American Chemical Society* **2010**, *132*, 16783.

(15) Knoppe, S.; Dass, A.; Bürgi, T. *Nanoscale* **2012**, *4*, 4211.

(16) Jupally, V. R.; Kota, R.; Dornshuld, E. V.; Mattern, D. L.; Tschumper, G. S.; Jiang, D.-e.; Dass, A. *Journal of the American Chemical Society* **2011**, *133*, 20258.

(17) Maman, M. P.; Nair, A. S.; Cheraparambil, H.; Pathak, B.; Mandal, S. *The Journal of Physical Chemistry Letters* **2020**, *11*, 1781.

(18) Dass, A.; Jones, T. C.; Theivendran, S.; Sementa, L.; Fortunelli, A. *The Journal of Physical Chemistry C* **2017**, *121*, 14914.

(19) Templeton, A. C.; Hostetler, M. J.; Kraft, C. T.; Murray, R. W. *Journal of the American Chemical Society* **1998**, *120*, 1906.

(20) Hostetler, M. J.; Templeton, A. C.; Murray, R. W. *Langmuir* **1999**, *15*, 3782.

(21) Song, Y.; Murray, R. W. *Journal of the American Chemical Society* **2002**, *124*, 7096.

(22) Shibu, E. S.; Muhammed, M. A. H.; Tsukuda, T.; Pradeep, T. *The Journal of Physical Chemistry C* **2008**, *112*, 12168.

(23) Donkers, R. L.; Song, Y.; Murray, R. W. *Langmuir* **2004**, *20*, 4703.

Chapter 3

Transformation from $[Au_{25}(SCH_2CH_2CH_2CH_3)_{18}]^0$ to $Au_{28}(SCH_2CH(CH_3)Ph)_{21}$ Gold Nanoclusters: Gentle Conditions is Enough

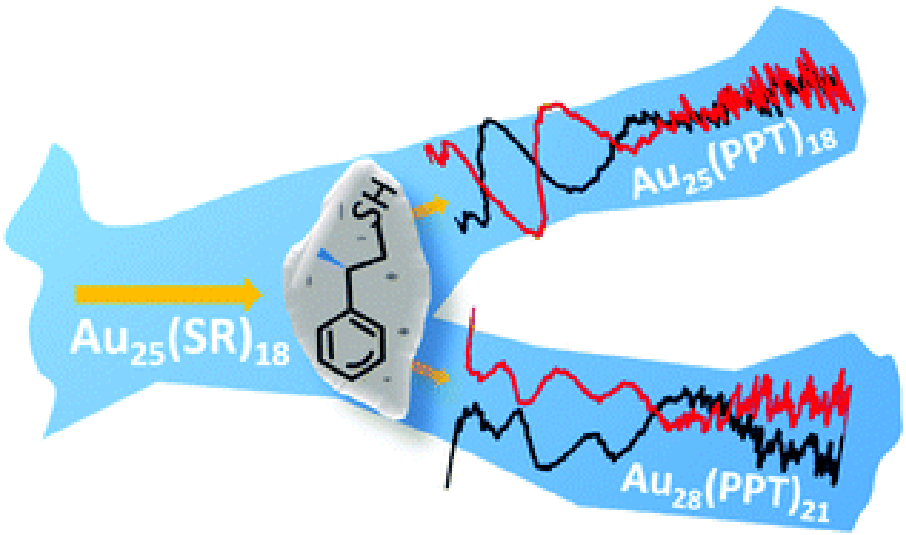

*The results described in this chapter were extracted from my own paper published in "Transformation from $[Au_{25}(SCH_2CH_2CH_2CH_3)_{18}]^0$ to $Au_{28}(SCH_2CH(CH_3)Ph)_{21}$ Gold Nanoclusters: Gentle Conditions is Enough" -Y. Wang, B. Nieto-Ortega and T. Bürgi, Chem. Commun., 2019, 55, 14914 —14917.

3.1 Introduction

In the last decade, thiolate-protected gold nanoclusters have gained significant attention due to possible applications in sensing, catalysis and molecular electronics to name a few[1,2]. Also, the interest has grown because nowadays it is possible to obtain these materials by well-established synthetic methods[3], molecularly pure[4-6], with a precise chemical formula (denoted as $Au_n(SR)_m$, in general), which allows one to address fundamental questions concerning matter at the nanoscale. Interestingly, it has been discovered that these materials could also be obtained by the transformation of one structure into another[7,8].

In a recent work, Maran et al. reported that Au_{25}(2-PET)$_{18}$ (where 2-PET=2-phenylethylthiolate) is able to slowly react with itself, without any co-reagent, generating Au_{38}(2-PET)$_{24}$. The authors propose that the size transformation reaction involves the formation of a precursor complex in which van der Waals interactions between the ligands of the two interacting clusters act as initial driving force[8]. However, according to the current literature, the main way to trigger such cluster transformation is by ligand exchange reactions (LERs, here after), which is a process that takes advantage of the dynamic nature of the thiol-gold surface[9] and in most cases not cause any change in size or structure of the cluster[10].

LERs induced transformations can be classified into three groups as we mentioned before. (I) Transformation between structural isomers without size change. For example, $Au_{28}(SR)_{20}$ nanocluster reversibly changes its structure upon ligand exchange between R= c-C_6H_{11} and R= Ph-^{t}But at elevated temperatures (e.g., 80 °C)[11]. (II) Transformation from a larger to a smaller nanocluster[12-16]. For instance, highly stable $Au_{144}(SC_2H_4Ph)_{60}$ reacted with thiophenol, HSPh, to form a different 99 atom cluster species $Au_{99}(SPh)_{42}$. (III) Transformation from a smaller to a larger nanocluster[16-19]. An interesting example is the transformation of Au_{25}(2-PET)$_{18}$ into Au_{28}(TBBT)$_{20}$ (where

TBBT=4-tert-butylbenzenethiolate)[17]. $Au_{25}(2\text{-PET})_{18}$ is probably the most studied thiolate-protected nanocluster, due to its prototypical character. At 80°C and in large excess of TBBT the cluster is transformed into $Au_{28}(TBBT)_{20}$. It is worth to mention that the resulting $Au_{28}(TBBT)_{20}$ cluster is chiral, presenting a pair of enantiomers which can be separated by chiral HPLC.

Cluster transformations induced by LER typically require large excess of incoming ligand, normally more than 100 times compared to the endogenous ligand, and elevated temperatures to proceed[7]. This becomes evident from the Table 1.3 illustrated at Chapter 1, which compiles the conditions of the reported cluster transformations. In addition, Jin and co-workers argued that the incoming thiol must be significantly different from the endogenous thiol for the transformation to happen[20]. Herein we report a cluster transformation that takes place at room temperature in less than a day and mild condition with ratio of incoming to endogenous ligand of 2:1. Under these conditions $[Au_{25}(SR)_{18}]^0$ transforms into a larger cluster, $Au_{28}(SR)_{21}$, by LERs. To our best knowledge, the $Au_{28}(SR)_{21}$ cluster has not yet been isolated but has been detected previously as $[Au_{28}(TBBT)_{21}]^{3-}$ by mass spectrometry within a mixture of different clusters in a study of seed-mediated growth from Au_{25} to Au_{44}[21].

3.2 Experimental

Synthesis and purification of nanoclusters. Synthesis and purification of $[Au_{25}(SBut)_{18}]^0$ and $Au_{25}(2\text{-PET})_{18}$ clusters have been explained in subchapter 2.1 Protocol for synthesis of monodisperse gold nanoclusters. The measurements for UV-vis, CD, MALDI-TOF, NMR, ESI characterization also been clarified in subchapter 2.3 Characterization of gold nanoclusters.

Ligand exchange reactions. LERs were performed according to previous work[24]. 10 mg of $[Au_{25}(SBut)_{18}]^0$ or $[Au_{25}(2\text{-PET})_{18}]^0$ cluster were dissolved in 10-15 mL of dichloromethane or toluene solvent together with free chiral ligand

R/S-2-phenylpropane-1-thiol (R- or S-PPT). A molar ratio of 1:2 regarding the ligand was used. The reaction mixture was slowly stirred for 18 hours at room temperature. After the LERs, the product was purified by size exclusion chromatography (SEC), and the different fractions analyzed by UV-Vis measurements.

Synthesis of R- and S-2-phenylpropane-1-thiol. Synthesis of (*R*)-2-phenylpropane-1-thiol was performed according to the Scheme 3.1 as below. The synthesis was adapted from previous protocol[22]. With respect to this report the amount of thiourea was changed to 1.8 equivalents. (*S*)-2-phenylpropane-1-thiol was synthesized following the same protocol. Racemic 2-phenylpropane-1-thiol used in the experiments was purchased from Enamine Ltd.

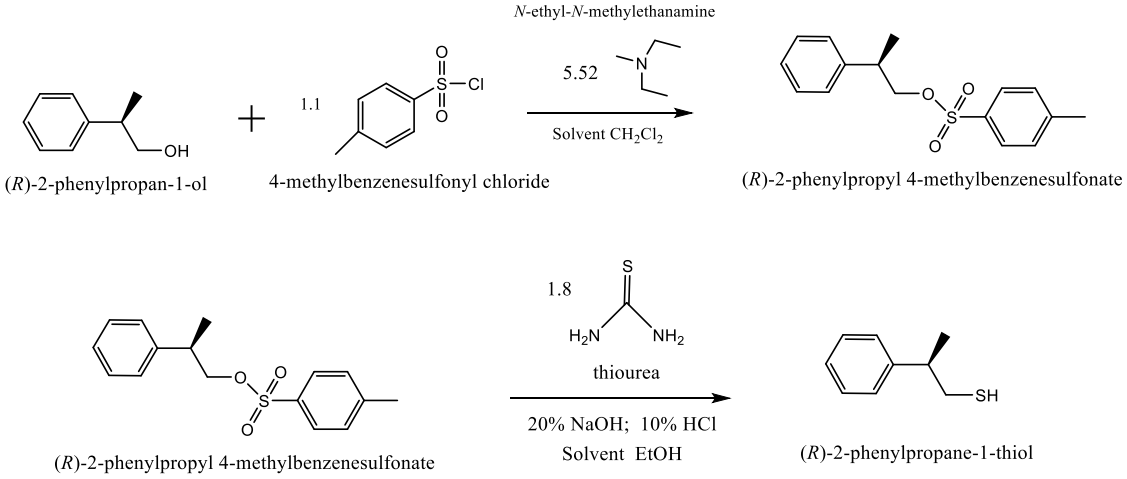

Scheme 3.1 Synthesis of (*R*)-2-phenylpropane-1-thiol.

3.3 Results and discussion

In our work, 2-PET or 1-Butanethiol (abbreviated as SBut) were used as initial ligand for $[Au_{25}(SR)_{18}]^0$, which was synthesized and purified according to reported protocols[23]. LERs were performed with a chiral free ligand: R- or S-2-phenylpropane-1-thiol (Scheme 3.2, abbreviated as R- or S-PPT hereafter, which were synthesized following a published protocol[22] with minor modifications). Neither thermal activation nor large excess of the incoming ligand was required to promote the transformation. Interestingly, this transformation was observed when the only difference between the endogenous

and the incoming thiol is one additional methyl group, which leads to a chiral centre and which changes the bulkiness and steric of the thiolate ligand[19]. It has been suggested that aliphatic, aromatic and bulky ligands produce different series of nanoclusters. R- or S-PPT induced nanoclusters may belong to bulky series[19]. The resulting $Au_{28}(SR)_{21}$ and $[Au_{25}(SR)_{18}]^0$ clusters were characterized by UV-Vis absorption, circular dichroism (CD), NMR, matrix-assisted laser desorption ionization time-of-flight (MALDI-TOF) mass spectrometry and electrospray ionization (ESI) mass spectroscopy.

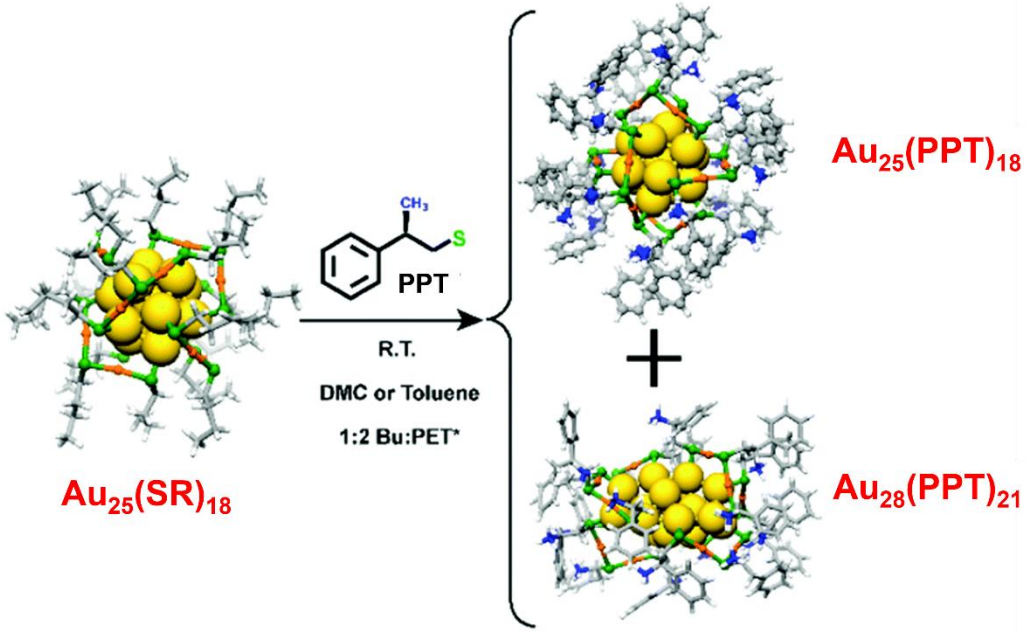

Scheme 3.2 Transformation of $[Au_{25}(SR)_{18}]^0$ cluster to $[Au_{25}(PPT)_{18}]^0$ and $Au_{28}(PPT)_{21}$. The depicted structure of $Au_{28}(PPT)_{21}$ is an illustration. The real structure is unknown.

LERs were similarly performed to that described in previous work[24]. In the following, this transformation will be illustrated by the reaction carried out with $[Au_{25}(SBut)_{18}]^0$ and S-PPT, although consistent results were obtained with $[Au_{25}(SBut)_{18}]^0$ or $[Au_{25}(2\text{-}PET)_{18}]^0$ and R-PPT. After the LERs, the product was purified by size exclusion chromatography (SEC), and the different fractions were analysed by UV-Vis measurements. According to the obtained UV-Vis curves (Fig. 3.1 left), clearly gradual change of the spectra was observed. Apart from the spectrum of $[Au_{25}(SBut)_{18}]^0$, which eluted later, a

different spectrum was observed for the first fraction, indicating a new species. Note that the new

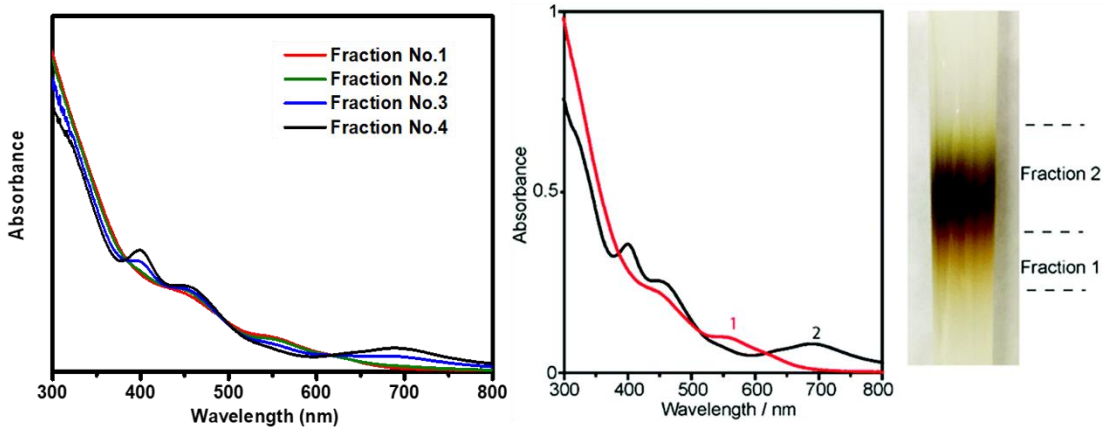

Figure 3.1 Left: UV-Vis spectra of 5 fractions obtained after LER of 0.1 mM of $[Au_{25}(SBut)_{18}]^0$ with S-PPT at room temperature in dichloromethane. Middle: normalized UV-Vis spectra of Fraction No.1(spectrum 1, red) and Fraction No.4 (spectrum 2, black). Right: SEC column after LER of $[Au_{25}(SBut)_{18}]^0$ with S-PPT. The SBut:S-PPT ratio is 1:2.

species and the Au_{25} cluster are not clearly separated in the column (Fig. 3.1 right). Two representative curves after normalization are depicted in Fig. 3.1 which illustrate the distinctly different spectra. The absorption spectra in Fig. 3.1 middle were obtained from an experiment where only the beginning of fraction 1 and the end of fraction 2 from the column were collected, which similar to Fraction No.1 and Fraction No.4 from Fig. 3.1 left, in order to avoid the eluted volume containing mainly a mixture of the two species. The spectrum 2 (Fig. 3.1 middle, black) is characteristic of $[Au_{25}(SBut)_{18}]^0$, and spectrum 1, which corresponding to fraction 1, related to a larger cluster and shows a different spectrum. Compared to $[Au_{25}(SBut)_{18}]^0$ the peaks at 400 and 690 nm are missing, and a new peak appears at 557nm. The purity of both clusters was also investigated by NMR and no remaining free ligand was observed in either of the two samples (Figure 3.2).

Both fractions were analysed by ESI mass spectroscopy in positive mode. As expected, fraction 2 shows a distribution between 6500-7100 Da and the most abundance cluster with mass of 6776.58 Da assigned to [Au_{25}

$(SBut)_{14}(S\text{-}PPT)_4]^0$ (theoretical value is 6777.69 Da). However, the mass spectrum of fraction 1, which has a distribution of clusters reminiscent of the

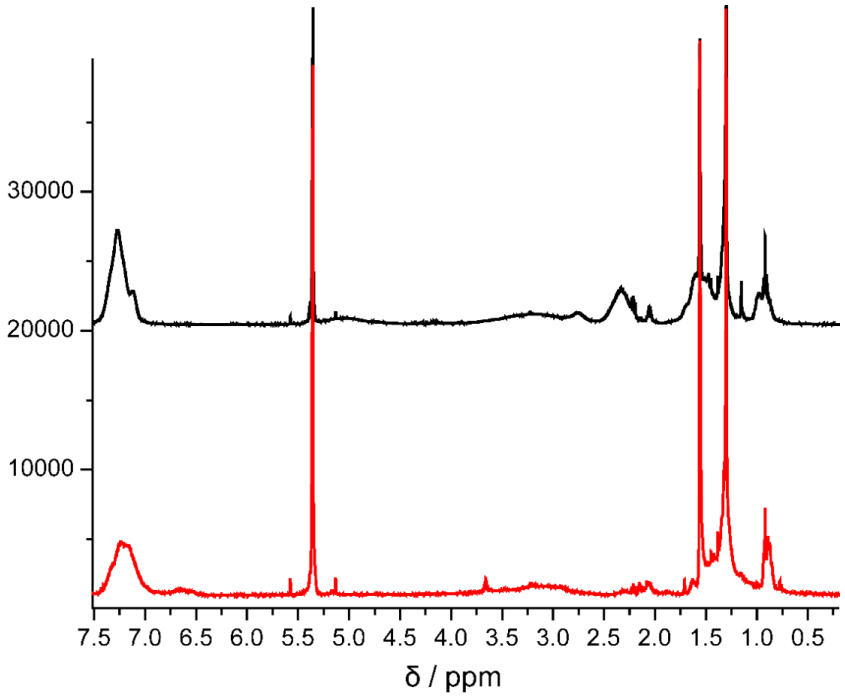

Figure 3.2 H^1-NMR spectra of clusters from fraction 1 (Fig. 3.1 Middle, red) and fraction 2 (Fig. 3.1 Middle, black). Both spectra were recorded in deuterated Dichloromethane.

ligand exchange. The most abundant cluster with a mass of m/z=8255.19 Da is assigned to $Au_{28}(SBut)_7(S\text{-}PPT)_{14}$ (theoretical mass 8257.34 Da). By running the ligand exchange a second time, after removal of free ligands, (under the same conditions) the yield of the new species could be increased. The ESI spectrum of fraction 1 of such an experiment is shown in Fig. 3.3. Again a distribution of $Au_{28}(SBut)_x(S\text{-}PPT)_{21-x}$ species is observed with a peak at m/z=8691.0 Da (theoretical value 8692.04 Da) assigned to the completely exchanged species $Au_{28}(S\text{-}PPT)_{21}$. It is worth to mention that a prominent fragment of $Au_{24}(S\text{-}PPT)_{17}$ is also detected at m/z=7297.4, i.e., after the loss of $Au_4(S\text{-}PPT)_4$ unit, which is very common in mass spectrometry of thiolate-protected clusters. Due to the overlap of the two cluster fractions on the SEC column, clear peaks of $[Au_{25}(SBut)_x(S\text{-}PPT)_{18-x}]^0$ are also observed during the ESI measurements.

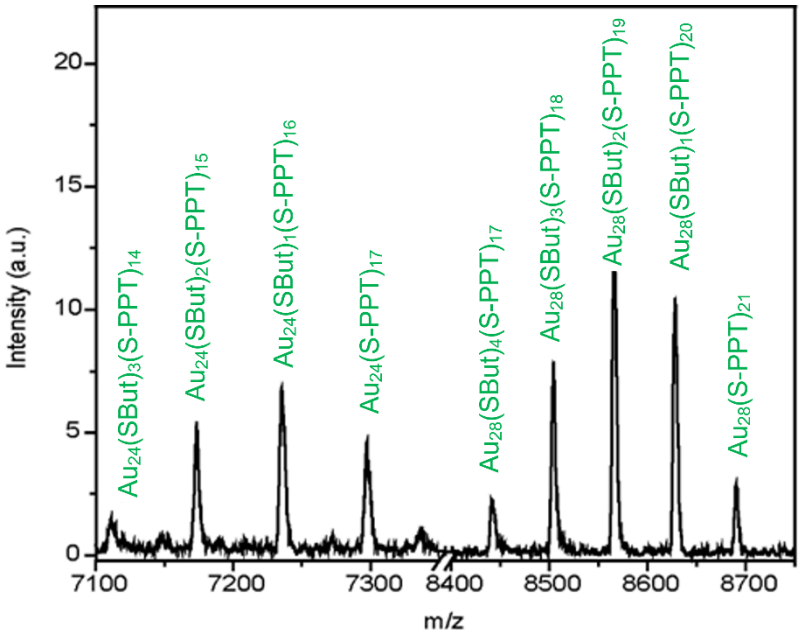

Figure 3.3 Electrospray ionization (ESI) mass spectroscopy of the fraction 1 from Figure 3.1.

The $Au_{28}(S\text{-}PPT)_{21}$ cluster has similar composition as $Au_{28}(TBBT)_{20}$[17] (they differ in one ligand), which has been obtained by LERs induced transformation from $[Au_{25}(2\text{-}PET)_{18}]^0$. Comparing the UV-Vis spectra of both clusters, it is evident that the UV-Vis of $Au_{28}(TBBT)_{20}$ presents three bands at 365, 480 and 580 nm[17], while the spectrum of $Au_{28}(S\text{-}PPT)_{21}$ shows only two bands at 448 and 557 nm (Fig. 3.1 middle). Interestingly, the $Au_{28}(TBBT)_{20}$ cluster undergoes structural change (isomerism) upon LERs with cyclohexanethiol ($S\text{-}c\text{-}C_6H_{11}$). Note that in the former thiol an aromatic ring is directly connected to the sulphur, which is not the case in the latter[11]. The spectrum of $Au_{28}(S\text{-}c\text{-}C_6H_{11})_{20}$ presents bands at 460 and 550 nm similar to the spectrum in Fig. 3.1 Middle, however the band at 355 nm of $Au_{28}(S\text{-}c\text{-}C_6H_{11})_{20}$ spectrum is missing in $Au_{28}(R\text{-}PPT)_{21}$ as well.

The experiments described above indicate the coexistence of $Au_{28}(S\text{-}PPT)_{21}$ and $[Au_{25}(S\text{-}PPT)_{18}]^0$ clusters after the LER in mild conditions. In addition, the LERs at different ratio of incoming/endogenous thiol and via different ligands also implied that an increase in the chiral ligand gives rise to an increase in the proportion of $Au_{28}(R\text{-}PPT)_{21}$ cluster. Moreover, large amount of the incoming

ligand (above 1:5 molar ratio) make both clusters unstable and no clear UV-Vis features were observed for the resulting solution.

CD spectroscopy is a powerful tool, very sensitive to the structure of clusters. Fig. 3.4 shows the CD spectra of R/S-PPT-substituted $Au_{28}(SBut)_{21}$ and $[Au_{25}(SBut)_{18}]^0$ clusters. From the distribution of ligands as determined by ESI analysis, an average formula of these two clusters of $Au_{28}(SBut)_2(PPT)_{19}$ and $[Au_{25}(SBut)_2(PPT)_{16}]^0$ can be obtained. Intense bands at 305nm (positive), 352nm (negative), 415nm (positive) and 480nm (negative) observed in the CD spectra of $[Au_{25}(SBut)_2(R\text{-}PPT)_{16}]^0$, as expected $[Au_{25}(SBut)_2(S\text{-}PPT)_{16}]^0$ showed the opposite signs. This result of $[Au_{25}(SBut)_2(R\text{-}PPT)_{16}]^0$ is in good agreement with the previous published results by Zhu et. al, where the $[Au_{25}(R\text{-}PPT)_{18}]^0$ cluster was prepared by direct synthesis[22]. Compared with CD spectrum of $[Au_{25}(SBut)_2(PPT)_{16}]^0$, the results of $Au_{28}(SBut)_2(PPT)_{19}$ show four more intense bands at 325nm, 380nm, 430 nm and 460 nm and a weak one at 530 nm, except bands at 305nm and 352nm, which were present in both spectra. As expected, the two spectra of $Au_{28}(SBut)_2(PPT)_{19}$ with two enantiomers of the ligand display good mirror image relationship.

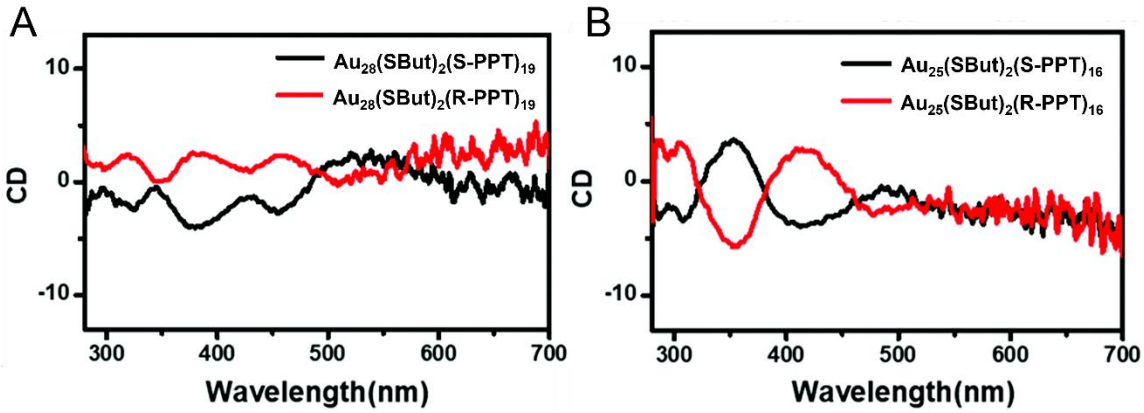

Figure 3.4 CD spectra of R/S-PPT-substituted $Au_{28}(SR)_{21}$ (A) and $[Au_{25}(SR)_{18}]^0$ (B) nanoclusters. The average formulations of clusters are calculated by intensity of related ESI spectra.

In order to find out if the core of $Au_{28}(PPT)_{21}$ is chiral, we performed a LERs in the opposite direction, i.e. the $Au_{28}(S\text{-}PPT)_{21}$ cluster was reacted with an achiral thiol (specifically SBut thiol, 1:2 S-PPT: SBut). A CD spectrum was recorded immediately after purification, but no clear CD bands were observed (Fig. 3.5). That means, either the $Au_{28}(SR)_{21}$ cluster is achiral, or we have a racemic mixture even after LERs. It is worth to mention that after LERs with SBut, the $Au_{28}(SR)_{21}$ remains stable and no formation of Au_{25} was observed. Therefore, the new $Au_{28}(SR)_{21}$ cluster is stable to LERs.

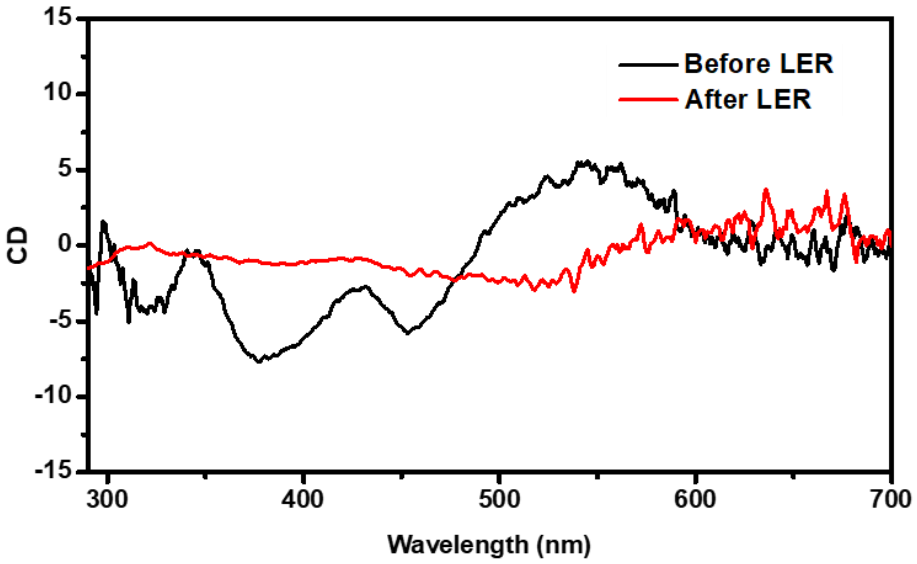

Figure 3.5 CD spectra of sample before (black) and after (Red) $Au_{28}(S\text{-}PPT)_{21}$ ligand exchange reacted with SBut.

This new product of LERs, $Au_{28}(SR)_{21}$, is indeed very unexpected, because Au_{25} has been extensively used for LER with different kind of ligands in mild conditions. However, this transformation has not been reported until now. In our opinion, the main reason is that this new cluster is easily fragmenting in MALDI, much more than $[Au_{25}(SR)_{18}]^0$, making the cluster difficult to be detected. In addition, the cluster is a side-product in LERs with SBut or 2-PET ligands. Further when we performed ligand exchange of $[Au_{25}(2\text{-}PET)_{18}]^0$ with SBut or of $[Au_{25}(SBut)_{18}]^0$ with 2-PET, the amount of Au_{28} that has been obtained was a few % only. This makes the detection of the cluster difficult.

Clearly, the type of thiol ligand plays a critical role in the transformation of clusters by LERs. Jin et al. proposed that the difference between incoming/endogenous ligand, mainly the difference in bulkiness, and the thermal conditions are the driving forces for cluster transformations by LERs[25]. In our case the transformation of $[Au_{25}(2\text{-}PET)_{18}]^0$ into $Au_{28}(R\text{-}PPT)_{21}$ has been observed when the only difference between the two ligands is a methyl group. Moreover, the electronic conjugation and even the thiol structure (primary thiol) is the same and the transformation is still happening in mild conditions. Our work indicates that very small changes (methyl group) of the ligand can be sufficient to drive a cluster transformation at mild conditions. A possible explanation is that the van der Waals interactions between the ligands are significantly altered by the methyl group and that the changed interactions within the ligand shell drive the transformation.

Finally, it is well-known that racemic mixtures often present a larger degree of packing and less steric hindrance than the corresponding pure enantiomers[26]. In order to explore if the transformation depends on the enantiopurity of the ligand, we repeated the LERs in the same experimental conditions but with a racemic mixture of PPT, which is commercially available. The UV-vis spectrum indicated the existence of $Au_{28}(PPT)_{21}$ after LERs without any purification. So we can draw the conclusion that for the formation of $Au_{28}(PPT)_{21}$ an enantiopure ligand is not necessary.

3.4 Conclusion

In summary, we report a new transformation of $[Au_{25}(SR)_{18}]^0$ into $Au_{28}(SR)_{21}$ by LER with a chiral ligand (R- or S-2-phenylpropane-1-thiol) under mild conditions (room temperature, low thiol excess). We believe that the van der Waals interactions within the ligand shell and the "bulkiness" of the methyl are the main factors driving this process. The Au_{28} cluster is only a minor side-product in LER with SBut or 2-PET ligands. The yield of $Au_{28}(SR)_{21}$ was affected by ligand ratio, reaction time and ligand structure. Because of the low yield with LERs using ligands like 2-PET and SBut and due to large fragmentation in MALDI this cluster is generally difficult to detect. An additional methyl group (leading to a chiral centre) of the incoming ligand promotes the formation of $Au_{28}(SR)_{21}$, and the transformation of the clusters also occurs for the racemic mixture of the ligand, which is commercially available. We believe that the transformation to $Au_{28}(SR)_{21}$ should be kept in mind when performing ligand exchange reactions on $[Au_{25}(SR)_{18}]^0$.

3.5 Additional information of ligand exchange reactions

The following part illustrates the LERs at different ratio of incoming/endogenous thiol and via different ligands. Here ligand PPT is marked as the PET* at the figures.

3.5.1 $[Au_{25}(SBut)_{18}]^0$ + 2 equivalents of S-PPT

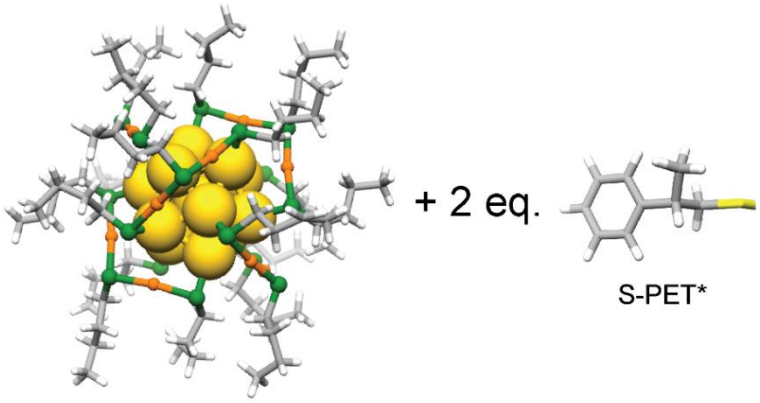

Table 3.1 Experimental conditions

	$[Au_{25}(SBut)_{18}]^0$	S-PPT
MW (g/mol)	6529.40	151.25
mg	10	8.339
mmol	1.532×10^{-3}	5.514×10^{-2}
mmol in thiol	2.757×10^{-2}	5.514×10^{-2}
Equivalents in thiol	1	2

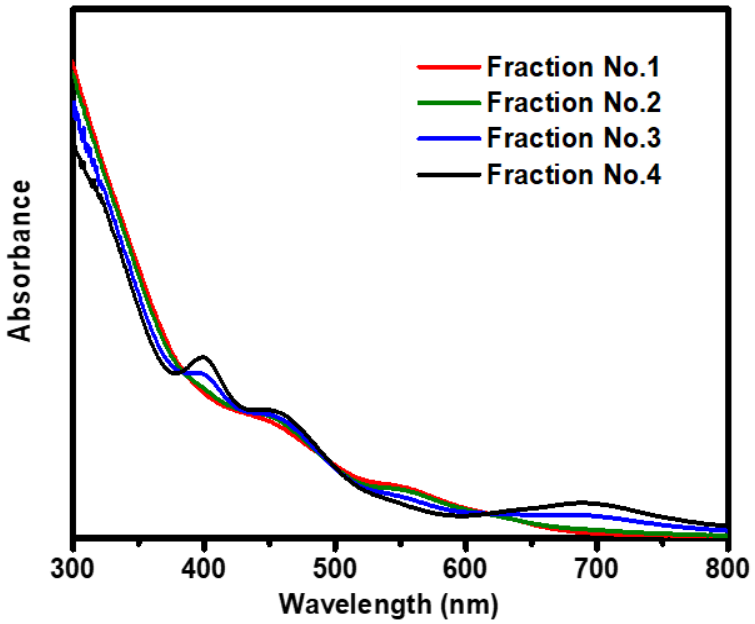

Figure 3.6 UV-Vis spectra of fractions obtained after LER of 0.1 mM of $[Au_{25}(SBut)_{18}]^0$ with S-PPT at room temperature in dichloromethane. The SBut:S-PPT ratio is 1:2.

3.5.2 $[Au_{25}(SBut)_{18}]^0$ + 2 equivalents of R-PPT

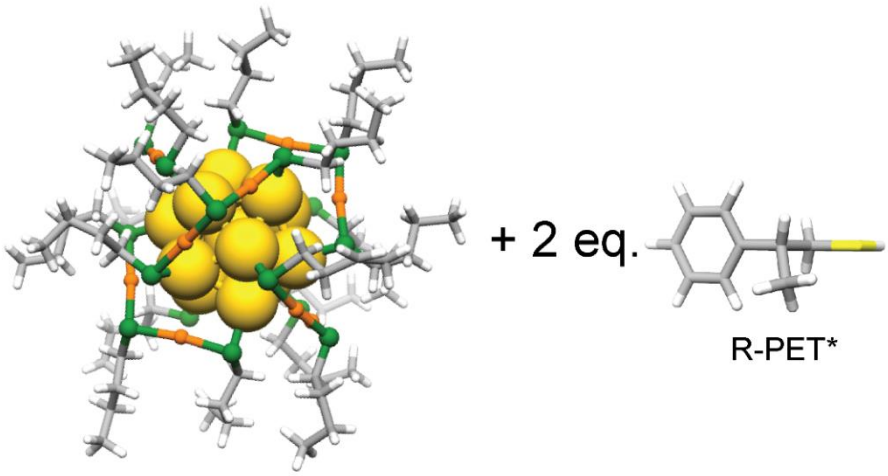

Table 3.2 Experimental conditions

	$[Au_{25}(SBut)_{18}]^0$	R-PPT
MW (g/mol)	6529.40	151.25
mg	10	8.339
mmol	1.532×10^{-3}	5.514×10^{-2}
mmol in thiol	2.757×10^{-2}	5.514×10^{-2}
Equivalents in thiol	1	2

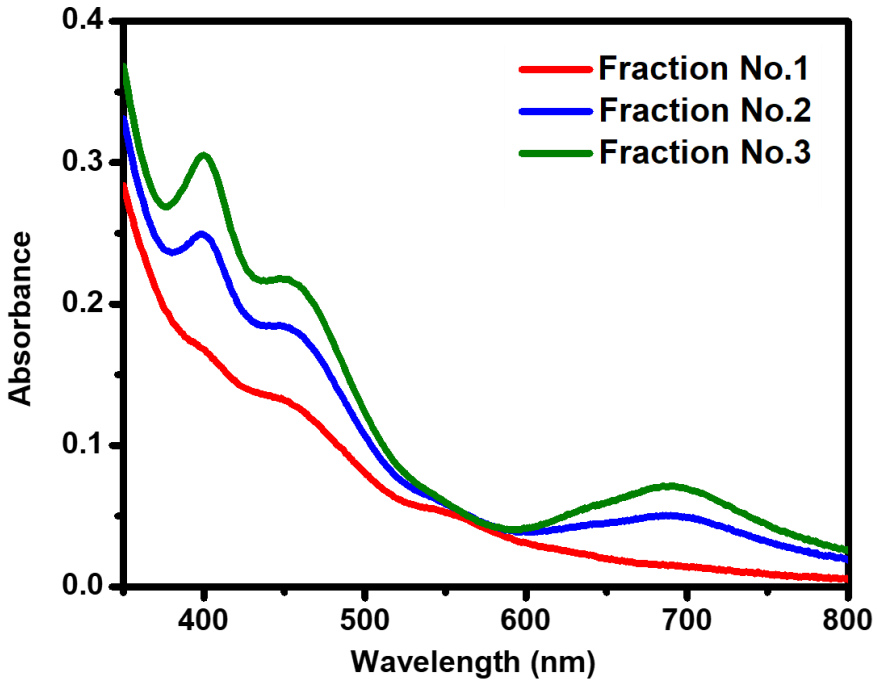

Figure 3.7 UV-Vis spectra of fractions obtained after LER of 0.1 mM of $[Au_{25}(SBut)_{18}]^0$ with R-PPT at room temperature in dichloromethane. The SBut:R-PPT ratio is 1:2.

3.5.3 $[Au_{25}(SBut)_{18}]^0$ + 1 equivalents of R-PPT

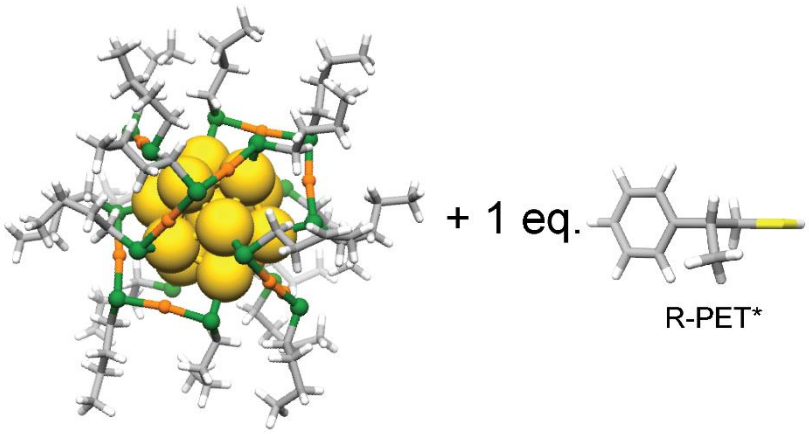

Table 3.3 Experimental conditions

	$[Au_{25}(SBut)_{18}]^0$	R-PPT
MW (g/mol)	6529.40	151.25
mg	10	4.1696
mmol	$1.532x10^{-3}$	$2.757x10^{-2}$
mmol in thiol	$2.757x10^{-2}$	$2.757x10^{-2}$
Equivalents in thiol	1	1

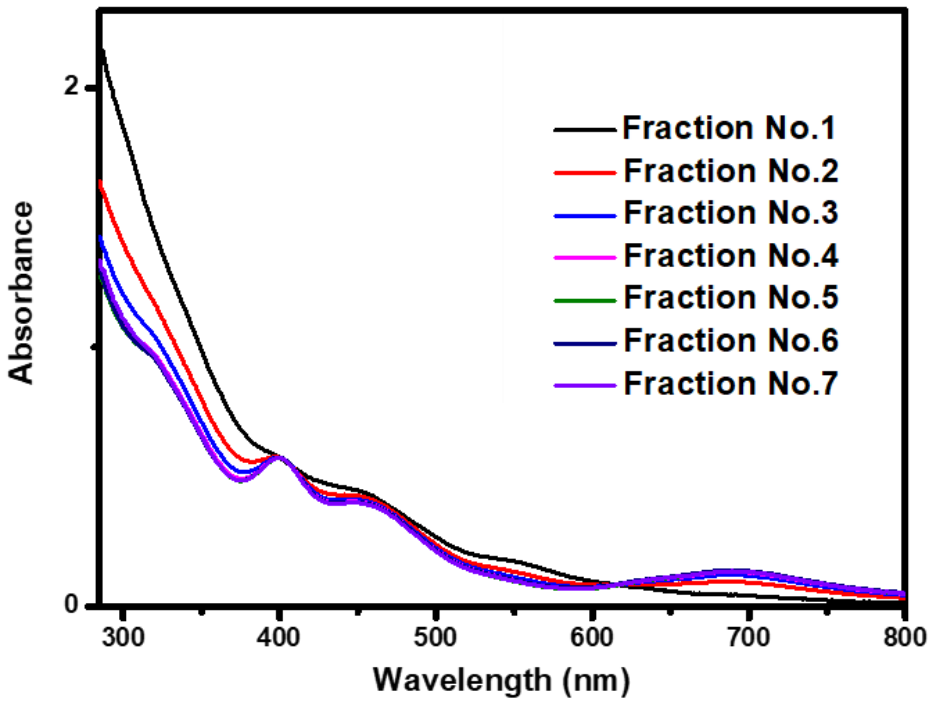

Figure 3.8 UV-Vis spectra of fractions obtained after LER of 0.1 mM of $[Au_{25}(SBut)_{18}]^0$ with R-PPT at room temperature in dichloromethane. The SBut:R-PPT ratio is 1:1.

3.5.4 $[Au_{25}(SBut)_{18}]^0$ + 5 equivalents of R-PPT

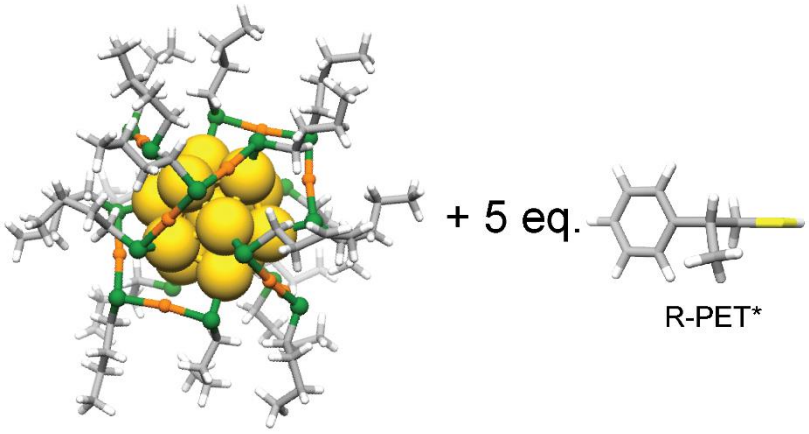

Table 3.4 Experimental conditions

	$[Au_{25}(SBut)_{18}]^0$	R-PPT
MW (g/mol)	6529.40	151.25
mg	10	20.848
mmol	$1.532x10^{-3}$	0.1378
mmol in thiol	$2.757x10^{-2}$	0.1378
Equivalents in thiol	1	5

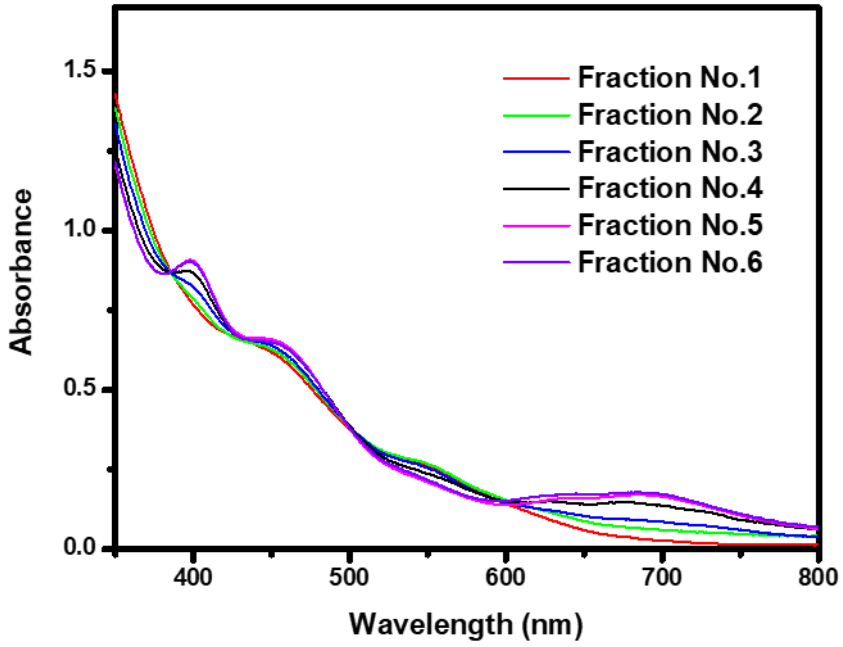

Figure 3.9 UV-Vis spectra of fractions obtained after LER of 0.1 mM of $[Au_{25}(SBut)_{18}]^0$ with R-PPT at room temperature in dichloromethane. The SBut:R-PPT ratio is 1:5.

3.5.5 $[Au_{25}(2\text{-PET})_{18}]^0$ + 2 equivalents of R-PPT

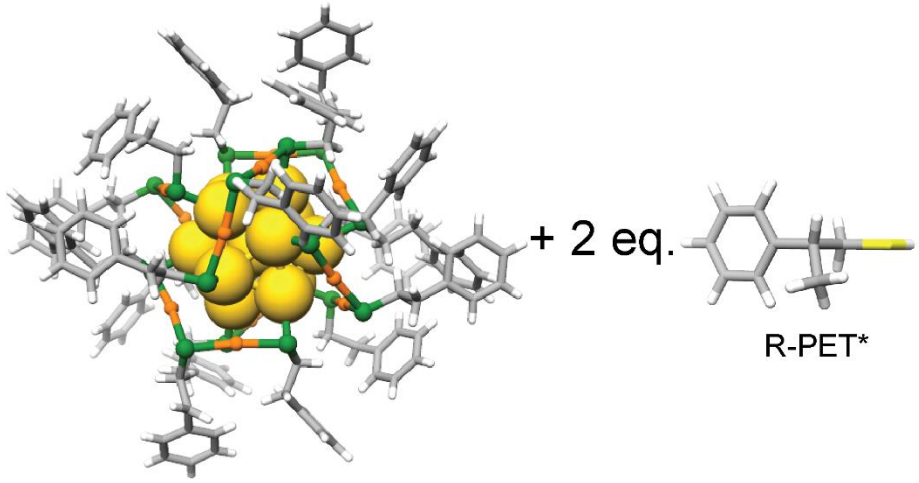

Table 3.5 Experimental conditions

	$[Au_{25}(2\text{-PET})_{18}]^0$	R-PPT
MW (g/mol)	7394.30	151.25
mg	10	7.364
mmol	1.352×10^{-3}	4.869×10^{-2}
mmol in thiol	2.434×10^{-2}	4.869×10^{-2}
Equivalents in thiol	1	2

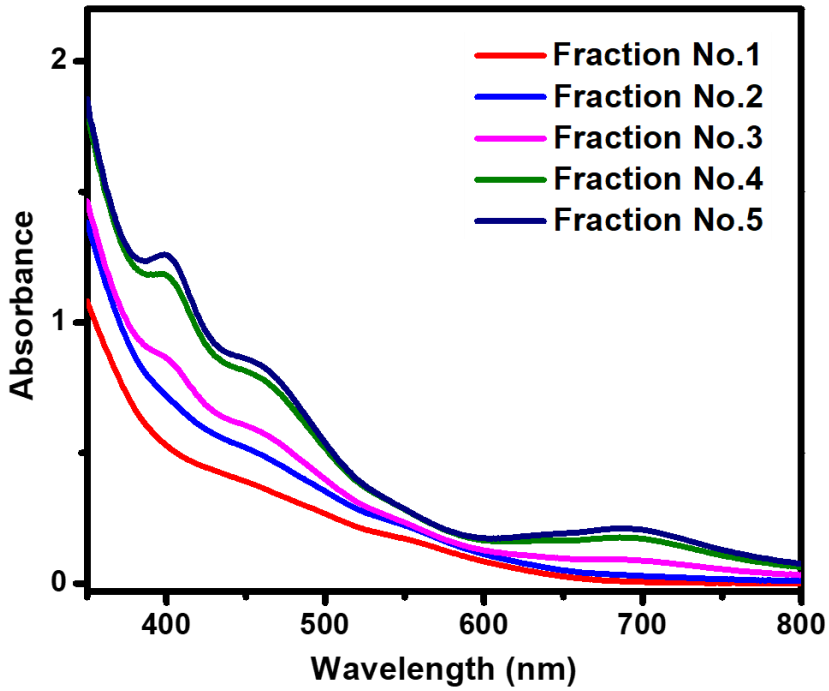

Figure 3.10 UV-Vis spectra of fractions obtained after LER of 0.1 mM of $[Au_{25}(2\text{-PET})_{18}]^0$ with R-PPT. The 2-PET:R-PPT ratio is 1:2.

3.5.6 $Au_{28}(S\text{-}PPT)_{21}$ + 2 equivalents of SBut

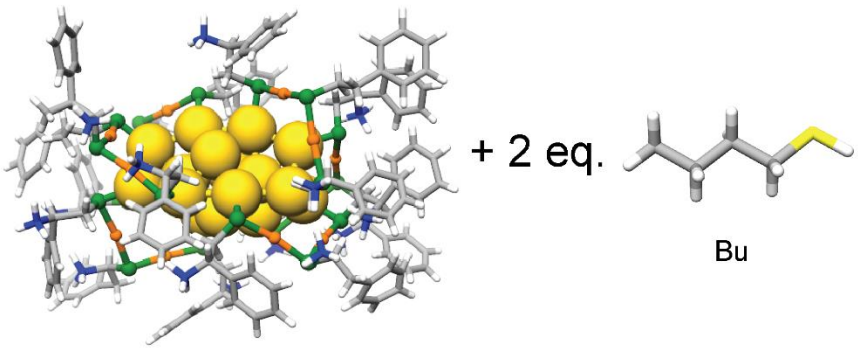

Table 3.6 Experimental conditions

	$Au_{28}(S\text{-}PPT)_{21}$	*SBut*
MW (g/mol)	8691.0	90.19
mg	10	4.358
mmol	$1.151x10^{-3}$	$4.832x10^{-2}$
mmol in thiol	$2.416x10^{-2}$	$4.832x10^{-2}$
Equivalents in thiol	1	2

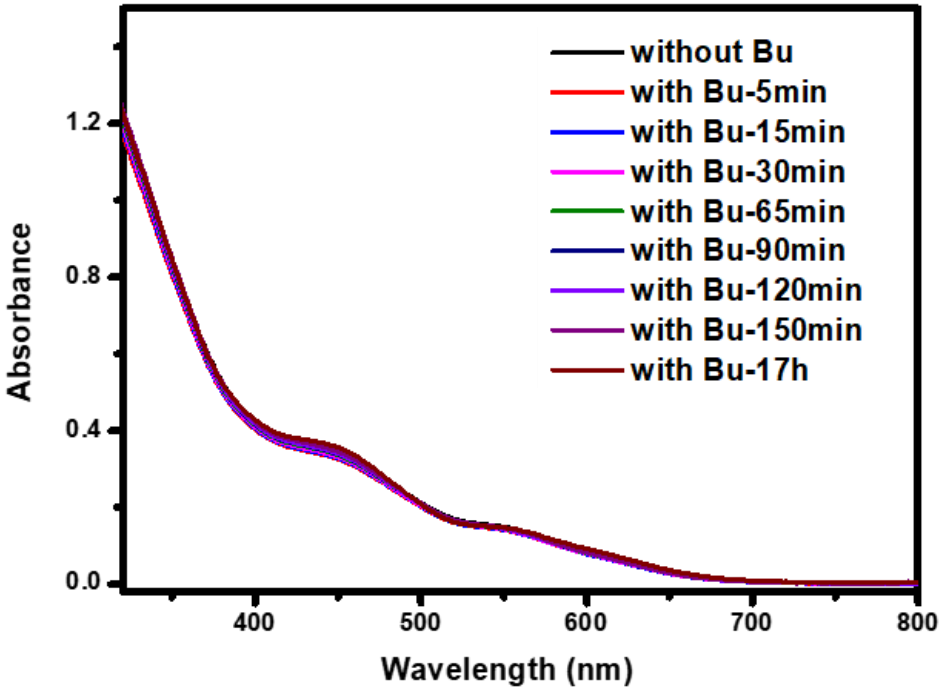

Figure 3.11 UV-Vis spectra of LER between $Au_{28}(S\text{-}PPT)_{21}$ and SBut.

3.5.7 $[Au_{25}(2\text{-PET})_{18}]^0$ + 2 equivalents of SBut

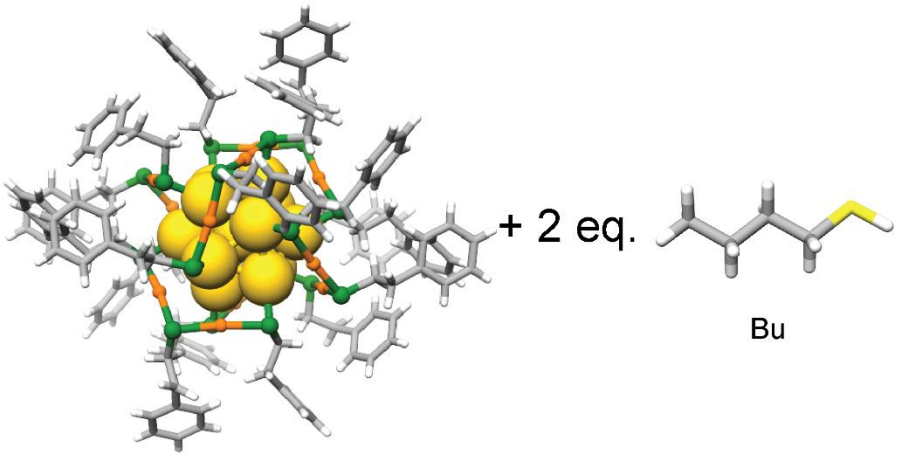

Table 3.7 Experimental conditions

	$[Au_{25}(2\text{-PET})_{18}]^0$	*SBut*
MW (g/mol)	7394.30	90.19
mg	10	4.391
mmol	1.352×10^{-3}	4.869×10^{-2}
mmol in thiol	2.434×10^{-2}	4.869×10^{-2}
Equivalents in thiol	1	2

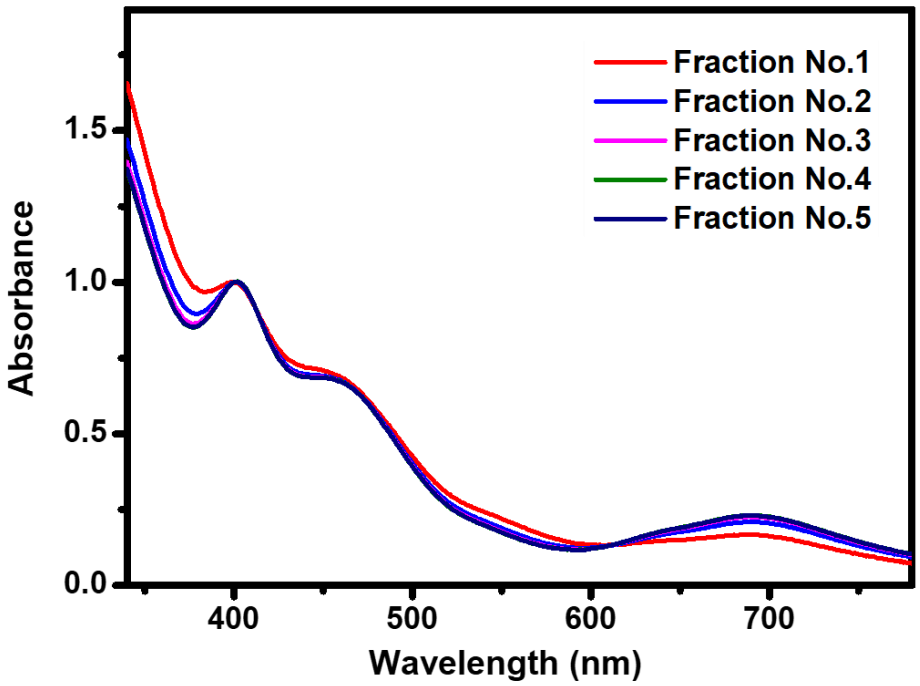

Figure 3.12 UV-Vis spectra of fractions obtained after LER of 0.1 mM of $[Au_{25}(2\text{-PET})_{18}]^0$ with SBut. The 2-PET:SBut is 1:2.

3.5.8 $[Au_{25}(SBut)_{18}]^0$ + 2 equivalents of 2-PET

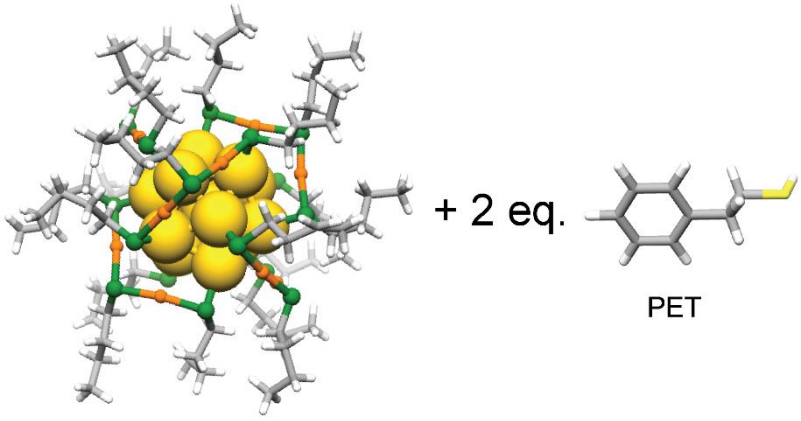

Table 3.8 Experimental conditions

	$[Au_{25}(SBut)_{18}]^0$	*2-PET*
MW (g/mol)	6529.40	138.23
mg	10	7.621
mmol	$1.532x10^{-3}$	$5.514x10^{-2}$
mmol in thiol	$2.757x10^{-2}$	$5.514x10^{-2}$
Equivalents in thiol	1	2

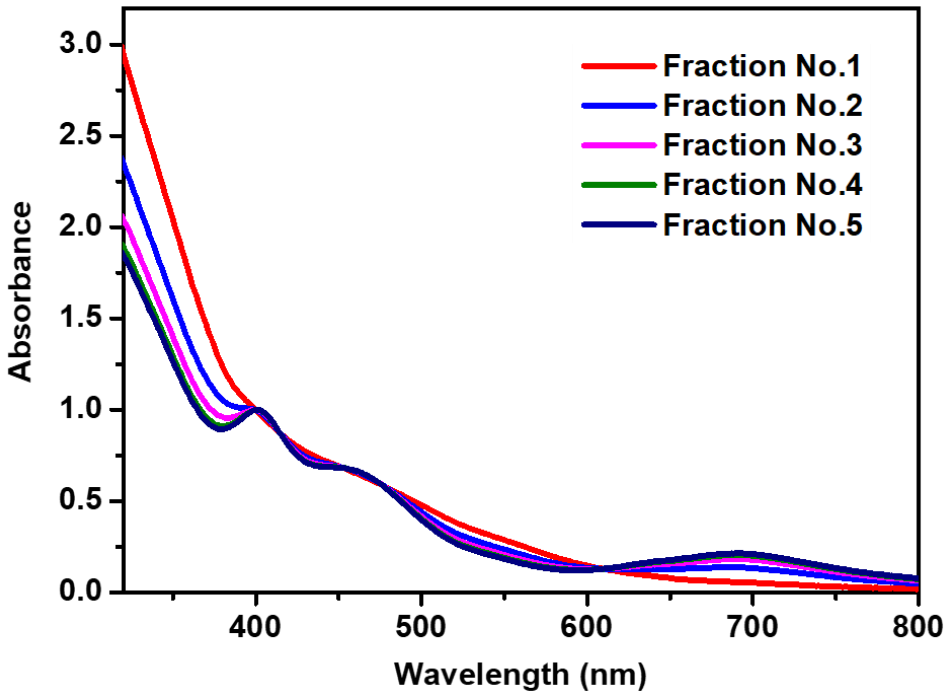

Figure 3.13 UV-Vis spectra of fractions obtained after LER of 0.1 mM of $[Au_{25}(SBut)_{18}]^0$ with 2-PET.

3.5.9 $[Au_{25}(SBut)_{18}]^0$ + 2 equivalents of *rac*-PPT

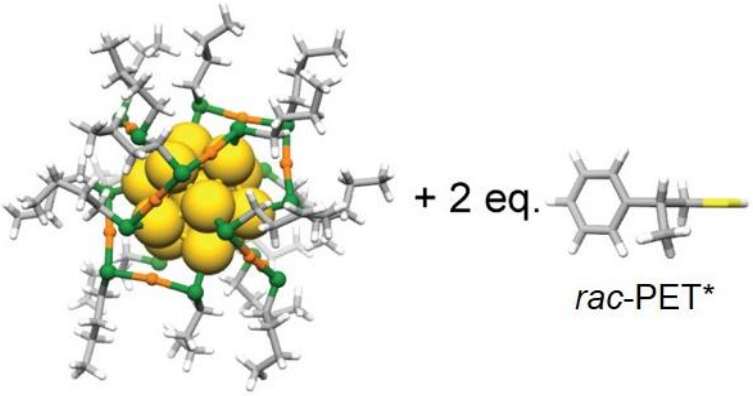

Table 3.9 Experimental conditions

	$[Au_{25}(SBut)_{18}]^0$	*Rac-PPT*
MW (g/mol)	6529.40	151.25
mg	10	8.339
mmol	$1.532x10^{-3}$	$5.514x10^{-2}$
mmol in thiol	$2.757x10^{-2}$	$5.514x10^{-2}$
Equivalents in thiol	1	2

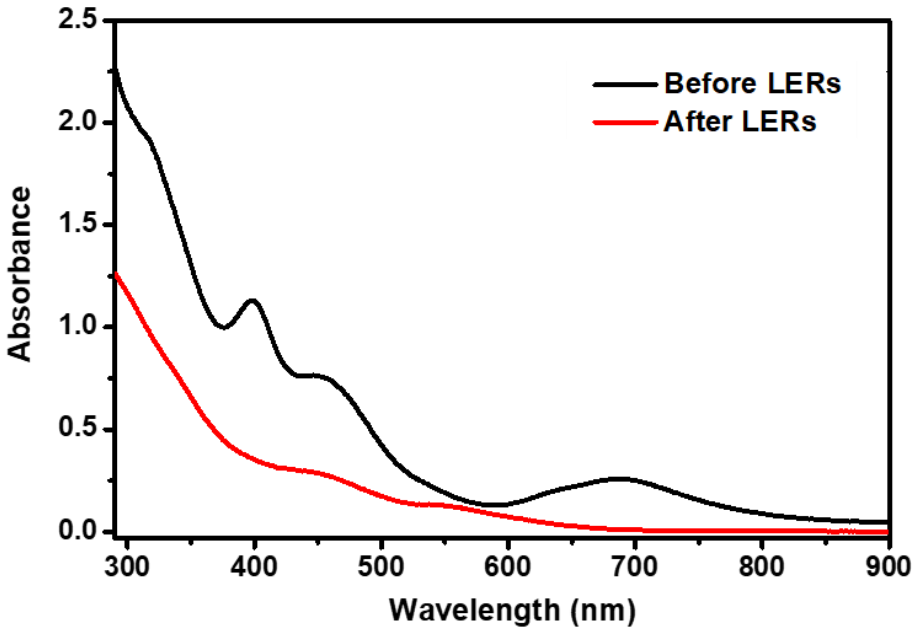

Figure 3.14 UV-Vis spectra of fractions obtained after LER of 0.1 mM of $[Au_{25}(SBut)_{18}]^0$ with *Rac*-PPT at room temperature in dichloromethane. The SBut:*Rac*-PPT ratio is 1:2.

3.6 References

(1) Li, G.; Jin, R. *Acc. Chem. Res.* **2013**, *46*, 1749.

(2) Wang, Y.; Wan, X.-K.; Ren, L.; Su, H.; Li, G.; Malola, S.; Lin, S.; Tang, Z.; Häkkinen, H.; Teo, B. K.; Wang, Q.-M.; Zheng, N. *J. Am. Chem. Soc.* **2016**, *138*, 3278.

(3) Jin, R. *Nanoscale* **2015**, *7*, 1549.

(4) Qian, H.; Jin, R. *Nano Lett.* **2009**, *9*, 4083.

(5) Qian, H.; Zhu, Y.; Jin, R. *ACS Nano* **2009**, *3*, 3795.

(6) Jin, R.; Qian, H.; Wu, Z.; Zhu, Y.; Zhu, M.; Mohanty, A.; Garg, N. *J. Phys. Chem. Lett.* **2010**, *1*, 2903.

(7) Zeng, C.; Chen, Y.; Das, A.; Jin, R. *J. Phys. Chem. Lett.* **2015**, *6*, 2976.

(8) Dainese, T.; Antonello, S.; Bogialli, S.; Fei, W.; Venzo, A.; Maran, F. *ACS Nano* **2018**, *12*, 7057.

(9) Bürgi, T. *Nanoscale* **2015**, *7*, 15553.

(10) Woehrle, G. H.; Brown, L. O.; Hutchison, J. E. *J. Am. Chem. Soc.* **2005**, *127*, 2172.

(11) Chen, Y.; Liu, C.; Tang, Q.; Zeng, C.; Higaki, T.; Das, A.; Jiang, D.-e.; Rosi, N. L.; Jin, R. *J. Am. Chem. Soc.* **2016**, *138*, 1482.

(12) Nimmala, P. R.; Dass, A. *J. Am. Chem. Soc.* **2014**, *136*, 17016.

(13) Nimmala, P. R.; Theivendran, S.; Barcaro, G.; Sementa, L.; Kumara, C.; Jupally, V. R.; Apra, E.; Stener, M.; Fortunelli, A.; Dass, A. *J. Phys. Chem. Lett.* **2015**, *6*, 2134.

(14) Zeng, C.; Liu, C.; Pei, Y.; Jin, R. *ACS Nano* **2013**, *7*, 6138.

(15) Zeng, C.; Liu, C.; Chen, Y.; Rosi, N. L.; Jin, R. *J. Am. Chem. Soc.* **2014**, *136*, 11922.

(16) Dass, A.; Jones, T. C.; Theivendran, S.; Sementa, L.; Fortunelli, A. *J. Phys. Chem. C* **2017**, *121*, 14914.

(17) Zeng, C.; Li, T.; Das, A.; Rosi, N. L.; Jin, R. *J. Am. Chem. Soc.* **2013**, *135*, 10011.

(18) Gan, Z.; Chen, J.; Wang, J.; Wang, C.; Li, M.-B.; Yao, C.; Zhuang, S.; Xu, A.; Li, L.; Wu, Z. *Nat. Commun.* **2017**, *8*, 14739.

(19) Rambukwella, M.; Sakthivel, N. A.; Delcamp, J. H.; Sementa, L.; Fortunelli, A.; Dass, A. *Frontiers in Chemistry* **2018**, *6*.

(20) Das, A.; Liu, C.; Zeng, C.; Li, G.; Li, T.; Rosi, N. L.; Jin, R. *J. Phys. Chem. A* **2014**, *118*, 8264.

(21) Yao, Q.; Yuan, X.; Fung, V.; Yu, Y.; Leong, D. T.; Jiang, D.-e.; Xie, J. *Nat. Commun.* **2017**, *8*, 927.

(22) Zhu, M.; Qian, H.; Meng, X.; Jin, S.; Wu, Z.; Jin, R. *Nano Lett.* **2011**, *11*, 3963.

(23) Lu, Y.; Jiang, Y.; Gao, X.; Chen, W. *Chem. Commun.* **2014**, *50*, 8464.

(24) Salassa, G.; Sels, A.; Mancin, F.; Bürgi, T. *ACS Nano* **2017**, *11*, 12609.

(25) Zeng, C.; Qian, H.; Li, T.; Li, G.; Rosi, N. L.; Yoon, B.; Barnett, R. N.; Whetten, R. L.; Landman, U.; Jin, R. *Angew. Chem. Int. Ed.* **2012**, *51*, 13114.

(26) Hong, R.; Fernández, J. M.; Nakade, H.; Arvizo, R.; Emrick, T.; Rotello, V. M. *Chem. Commun.* **2006**, *22*, 2347.

Chapter 4

Evidence for stereoelectronic effects in ligand exchange reactions on Au_{25} nanoclusters

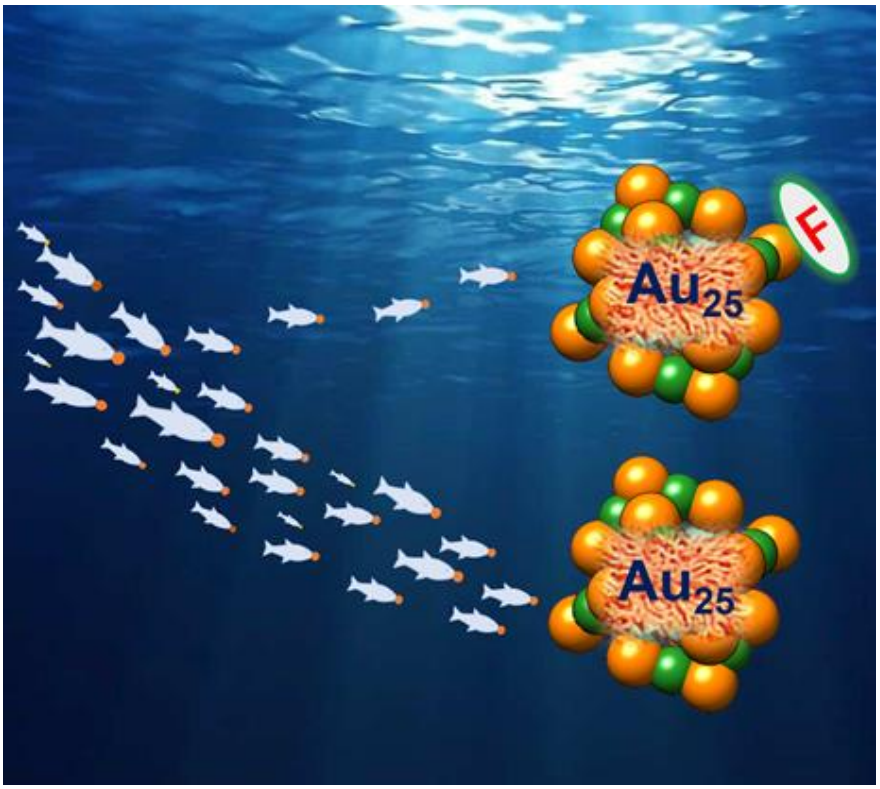

4.1 Introduction

Ligand substitution reactions, in which one or more ligands in a complex are replaced by a different ligand, is a conventional process in inorganic and organic chemistry[1-3]. This reaction is also called ligand exchange reaction (LERs) in some fields. During the past decades, the mechanism of this dynamic process has been explored widely, and two possible pathways, dissociative (S_N1) and associative (S_N2), have been demonstrated[4-6]. This process has been revealed for traditional transition metal-complexes or organic frameworks, but after that it also has been shown for thiolate-protected gold nanoclusters, as first studied by Murry and coworkers[7-11]. Until now LERs developed into an important post-synthesis method, which has been used for extending the properties and functions of nanoclusters[12]. In addition, the mechanism of LERs on nanoclusters is thought to follow an associative (S_N2) pathway, according related experimental and computational studies[13-15]. Understanding the mechanism and the factors that affect this reaction will help the design of atomically precise metal clusters with mixed ligand shells.

LERs on gold nanoclusters are strongly influenced by the chemical properties of the involved ligands and the flexibility of the gold-sulfur interface[16,17]. Other factors involved in this dynamic process which affect the reaction rate are the stability of the samples[18], length of surface ligand[11], metal doping[19], diastereoselective interactions[20], and electronic properties of the ligand[9,21] and nanoclusters[8]. In 2002, Murry and co-workers demonstrated that the rate of LERs increased with increasing positive electronic charge on the Au core[8]. Later they also revealed that the ligands with electron-withdrawing substituents reacted faster at shorter reaction time, and the ligands with electron-donating substituents were more efficient at longer reaction times[9]. However, after two decades only little advancements have been added to this topic[21]. Furthermore, in contrast to the diastereoselective LERs with intrinsically chiral nanoclusters[20], the stereospecific effects in LERs of chiral ligands on achiral nanoclusters have not been quantified yet.

Here, using a chiral fluoro-substituted ligand (R)-5,5',6,6',7,7',8,8'-octafluoro-[1,1'-binaphthalene]-2,2'-dithiol (named 8F-R-BINAS in the following), the electronic and stereospecific effects of the ligand during the exchange reaction on achiral Au_{25} will be systematically investigated. Compared with parent ligand 1,1'-binaphthalene-2,2'-dithiol (BINAS), the fluoro-substituted molecule exhibits higher electron-withdrawing ability without large size change. In addition, the rigid structures of the two chiral ligands also represent good models for the investigation of stereospecific effects. We show that the electronic property of ligand induces significant discrimination to the LERs, however, the absolute configuration of the ligand did not significantly affect the rate of exchange, at least at the early stage of exchange where only few chiral ligands are adsorbed on the achiral cluster.

4.2 Experimental

Chemicals and methods. All chemicals were purchased from commercial suppliers and used as received without any further treatment. The synthesis and purification of $[Au_{25}(2\text{-PET})_{18}]^0$ has been explained in subchapter 2.1 Protocol for synthesis of monodisperse gold nanoclusters. The measurement for UV-vis, CD, and MALDI-TOF characterization also been clarified in subchapter 2.3 Characterization of gold nanoclusters. The synthesis of R-BINAS was according to the reported method[20,22]. 8F-R-BINAS was synthesized starting from 1-chloro-2,3,4,5,6-pentafluorobenzene, and the whole synthesis is described in Scheme 4.1[23].

Ligand exchange reactions. Purified $Au_{25}(2\text{-PET})_{18}$ clusters were reacted with enantiopure ligands and mixture ligands separately. For the reaction between $Au_{25}(2\text{-PET})_{18}$ clusters and R-BINAS or 8F-R-BINAS, the molar ratio between clusters and ligand was 1:20. For the reaction between $Au_{25}(2\text{-PET})_{18}$ clusters and mixture of R-BINAS/8F-R-BINAS or S-BINAS/8F-R-BINAS, the molar ratio between clusters and ligand was 1:15. The reaction was carried out in toluene, and the final concentration of $Au_{25}(2\text{-PET})_{18}$ keep at 1mg/mL and room temperature. During

reaction, drops of sample were taken for the MALDI-TOF measurement at various times. The reactions were followed for at least 90h.

Simulation of kinetics and multinomial distribution. The kinetics of the LERs were simulated using MATLAB. The corresponding codes are shown in the Supporting Note 2 (monomer free ligand) and Note 4 (mixed ligands). The multinomial distribution simulation of LERs was set up at Note 3. The pseudo first order rate constants for reactions with different ligand ratios were determined by MATLAB simulation.

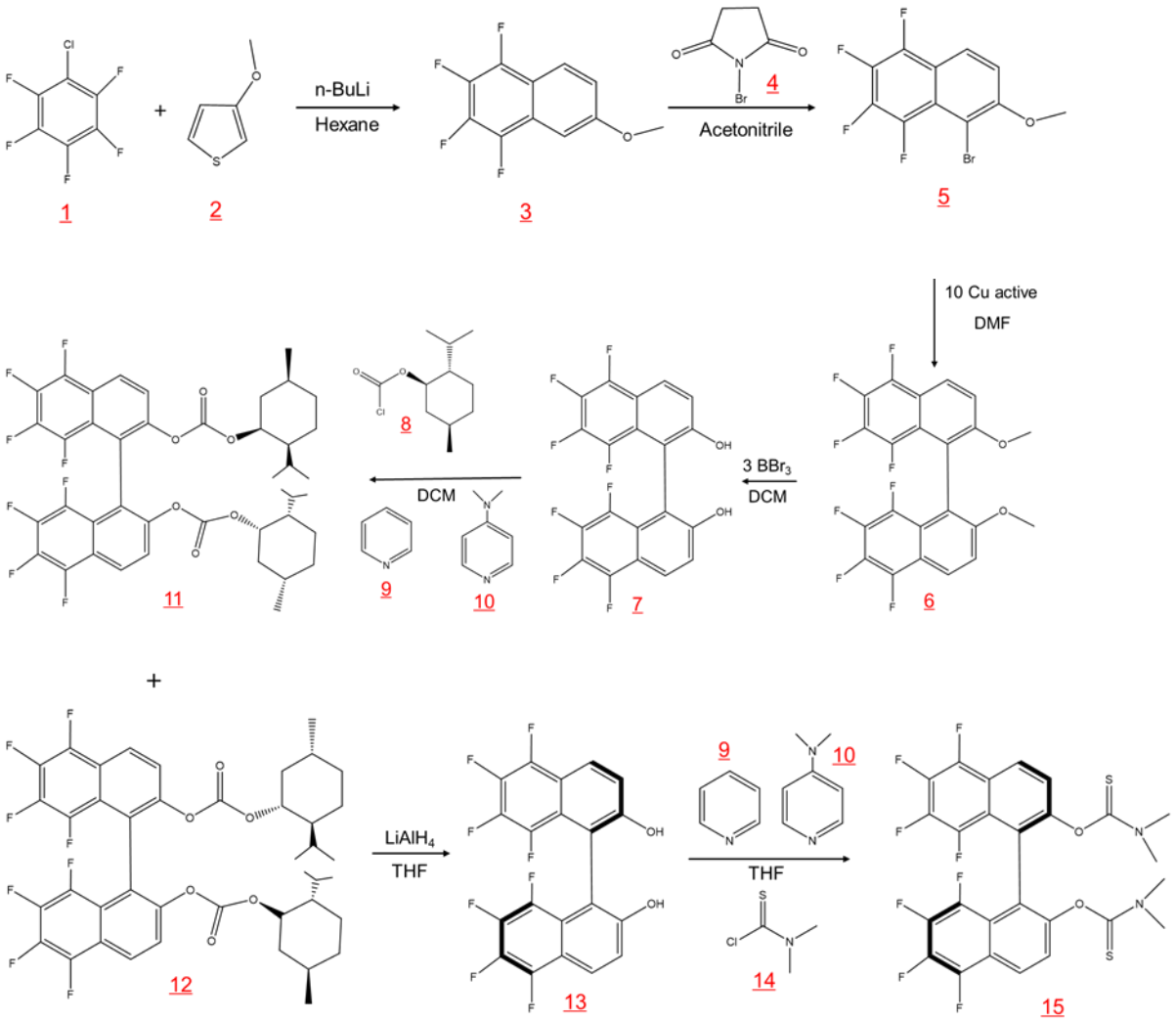

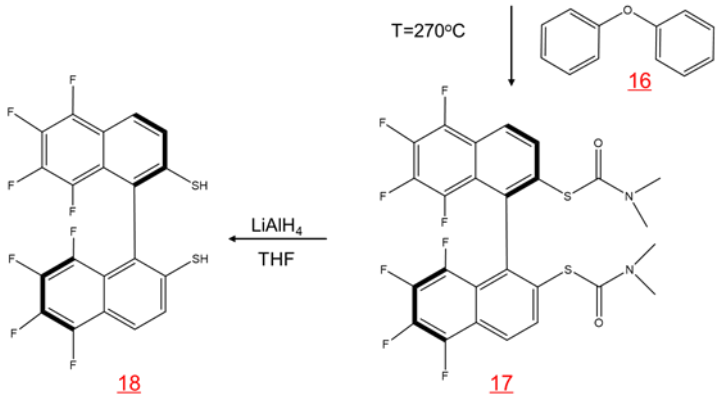

Scheme 4.1 Synthesis of the 8F-R-BINAS: (R)-5,5',6,6',7,7',8,8'-octafluoro-[1,1'-binaphthalene]-2,2'-dithiol. Here the product 7 after reacted under 8,9,10, obtained products 11 and 12 together, for the next reaction just product 12 involved in the reaction. Following are the nomenclatures of corresponding molecules. (1). 1-chloro-2,3,4,5,6-pentafluorobenzene, (2). 3-mthoxythieophene, (3). 1,2,3,4-tetrafluoro-6-methoxynaphthalene, (4). 1-bromopyrrolidine-2,5 -dione, (5). 5-bromo-1,2,3,4-tetrafluoro-6-methoxynaphthalene, (6). 5,5',6,6',7,7',8,8' -octafluoro-2,2'-dimethoxy-1,1'-binaphthalene, (7). 5,5',6,6',7,7',8,8'-octafluoro-[1,1'-binaphthalene] -2,2'-diol, (8). (1R,2S,5R)-2-isopropyl-5-methylcyclohexylcarbonochloridate, (9). Pyridine, (10). N,N-dimethylpyridin-4-amine, (11). bis((1S,2S,5S)-2-isopropyl-5-methylcyclohexyl) (5,5',6,6',7,7',8,8' -octafluoro-[1,1'-binaphthalene]-2,2'-diyl)bis(carbonate), (12). bis((1R,2S,5R)-2- isopropyl-5-methylcyclohexyl)5,5',6,6',7,7',8,8'-octafluoro-[1,1'-binaphthalene]-2,2'-diyl)bis(carbonate), (13). (R)5,5',6,6',7,7',8,8'-octafluoro-[1,1'-binaphthalene]-2,2'-diol, (14). Dimethylcarbamothioic chloride, (15). (R)-5,5',6,6',7,7',8,8'- octafluoro-[1,1'-binaphthalene] -2,2'-diyl)bis(dimethylcarbamothioate), (16). Phenyl ether, (17). R'-(5,5',6,6',7,7',8,8'-octafluoro-[1,1'-binaphthalene]-2,2'-diyl) bis(dimethylcarbamothioate), (18). (R)-5,5',6,6',7,7',8,8'-octafluoro-[1,1'-binaphthalene] -2,2'-dithiol.

4.3 Results and discussion

The $Au_{25}(2\text{-PET})_{18}$ (2-PET: 2-phenylethylthiolate) nanocluster was synthesized according a previous protocol[24]. The purity of the clusters was proved by the UV-vis spectroscopy and MALDI-mass spectrometry. The chemical structures and corresponding CD spectra (except 2-PET) of ligands 2-PET, R/S-BINAS and 8F-R-BINAS are shown in Fig. S1 (Supporting information). The synthesis protocol of 8F-R-BINAS is displayed in scheme 4.1 and followed a previous report[23].

To investigate the electronic effect of ligand during the exchange process, $Au_{25}(2\text{-PET})_{18}$ was first mixed with R-BINAS and 8F-R-BINAS separately. Toluene was used as solvent for the reaction, and the molar ratio of cluster to ligand was equal

to 1:20. A small amount of sample was taken from the reaction mixture at different reaction time and the corresponding MALDI-TOF mass spectra were recorded (Figure 4.1). The calculated mass of different species after $Au_{25}(2\text{-PET})_{18}$ exchange with BINAS (Figure 4.1 A) and 8F-R-BINAS (Figure 4.1 B) are listed in Table S1. As confirmed before, BINAS acts as a bidentate ligand thus substituting two 2-PET ligands on the cluster[25,26]. Ligand exchange numbers (x = number of BINAS/8F-R-BINAS in the ligand shell) are marked in Figure 4.1. The clusters show fragmentation, notably by losing $Au_4(2\text{-PET})_4$. The corresponding fragments are also visible in Figure 4.1 and the related exchange numbers (x`) were also labelled. Since the fragments are formed during the MALDI measurement, the signals of the fragments were also considered by adding them to the ones of the corresponding intact cluster.

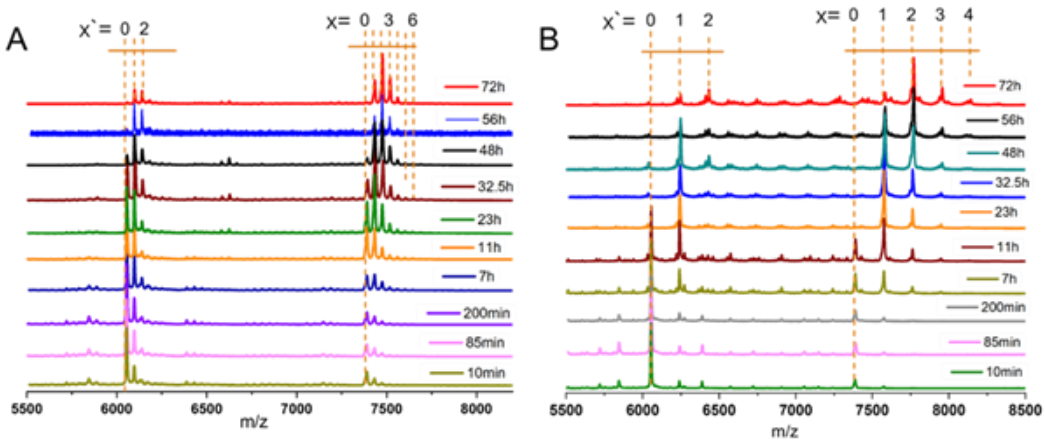

Figure 4.1 Evolution of MALDI-TOF mass spectra during ligand exchange. $Au_{25}(2\text{-PET})_{18}$ were mixed with R-BINAS (A) and 8F-R-BINAS (B), respectively at molar ratio 1:20. Samples were taken at different time and the corresponding mass spectrum recorded. In the labels above the MALDI spectra, x corresponding to the exchanged number of $Au_{25}(2\text{-PET})_{18}$ and x` corresponding to the exchange number of the fragment $Au_{21}(2\text{-PET})_{14}$.

In order to study the kinetics of ligand exchange reactions, the intensity of mass peaks in Fig. 4.1 were quantified (taking into consideration also fragment peaks as mentioned above) and the results are given in Table S2 ($Au_{25}(2\text{-PET})_{18}$ + R-BINAS) and Table S3 ($Au_{25}(2\text{-PET})_{18}$ + 8F-R-BINAS). When reacted with R-BINAS, clusters with up to six R-BINAS ligands were observed after 72h reaction time, whereas for the ligand exchange reaction with 8F-R-BINAS up to four 8F-R-BINAS ligands could

be detected on the cluster. The percentages of the different cluster species were calculated, and their evolution as function of time are shown in Figure 4.2. LER can be considered as a consecutive reaction, where a first ligand is exchanged followed by a second one etc. The equations for the related LERs are shown in the supporting Note 1. The time-dependent concentration of the species with x=1 (one BINAS/8F-R-BINAS in the ligand shell of the cluster), red data points in Figure 4.2, depends on the two rate constants k_1, which describes the first ligand exchange, and k_2, which describes the second ligand exchange. The time dependence of the one ligand-substituted species (x=1) was quantitatively different in the two cases. The maximum fractions of this species were 0.44 for the experiment with R-BINAS and 0.74 in the case of 8F-R-BINAS, which shows that the ratio of the rate constants k_1/k_2 is different for the two ligands. In order to extract these ratios, the abundance of the parent cluster and the cluster with one exchanged ligand in its shell were fit to a kinetics of a consecutive reaction (pseudo first order) using MATLAB (the code is shown in the supporting Note 2). The raw data extracted from the MALDI experiments are given in Table S2 and Table S3, and the fitting curves of these two LERs process are shown in Figure S2. From the fit it emerges that the related ratio of rate constants k_1/k_2 is 2.4 for LERs between $Au_{25}(2\text{-PET})_{18}$ and R-BINAS, and changes to 4.7 when 8F-R-BINAS is used as the incoming ligand. This means that the second ligand exchange performed slower with 8F-R-BINAS compared to R-BINAS. The significant difference for these two ligands can also be discovered at the initial stage (before 5h) of the exchange, where the species with two exchanged BINAS ligands (x=2, green curve) can already be observed before 5h (Fig. 4.2 A), whereas for the experiment with 8F-R-BINAS the corresponding species arises after 5h (Fig. 4.2 B). In addition, also the species with three exchanged ligands were delayed for 8F-R-BINAS compared to BINAS. All these observations are consistent with an increased slowing down of the further ligand exchange reaction once 8F-R-BINAS is incorporated in the ligand shell of the cluster.

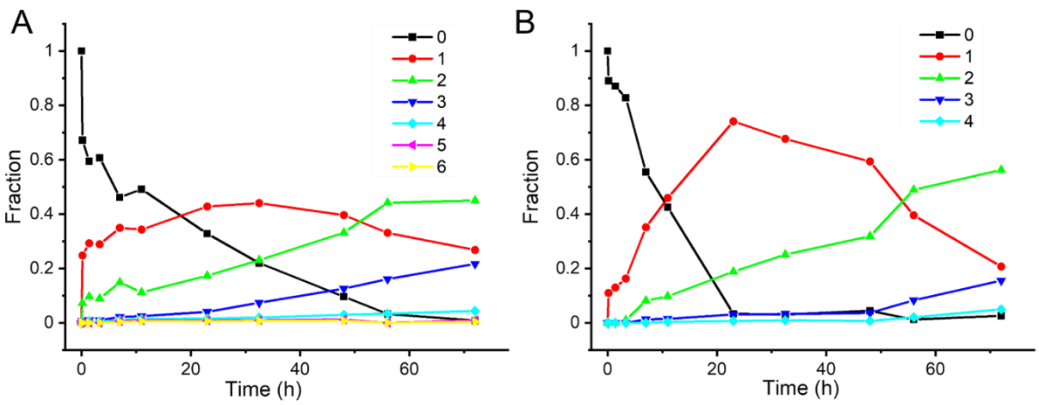

Figure 4.2 Evolution of different cluster species as function of time. (A) Au_{25}(2-PET)$_{18-2x}$(R-BINAS)$_x$ (X_{max}=6), (B) Au_{25}(2-PET)$_{18-2x}$(8F-R-BINAS)$_x$ (X_{max}=4). Numbers in the legend correspond to the number of exchanged ligands X.

The distinct difference in the LER with the two ligands, described above, is ascribed to the electronic effect of fluorine. The 8 fluorine atoms in 8F-R-BINAS have strong electron-withdrawing ability and change the electron density of the aromatic ring. After incorporation of 8F-R-BINAS into the ligand shell, the electronic effect may also extend to the whole cluster (surface). As mentioned before, the mechanism for ligand exchange reaction follows an associative (S_N2) pathway[14]. The first step for the ligand exchange is nucleophilic attack by the incoming thiol, creating a bimolecular intermediate. Consequently, the 8F-substituted BINAS molecular has lower electron density at the sulfur atom compared with BINAS, which decreases its ability to act as nucleophile. The data shown above indicates that the fluorinated ligand may also affect the reactivity of the cluster, decreasing its ability for subsequent ligand exchange. However, the electronic effect of fluorinated ligand on the clusters may be more complex.

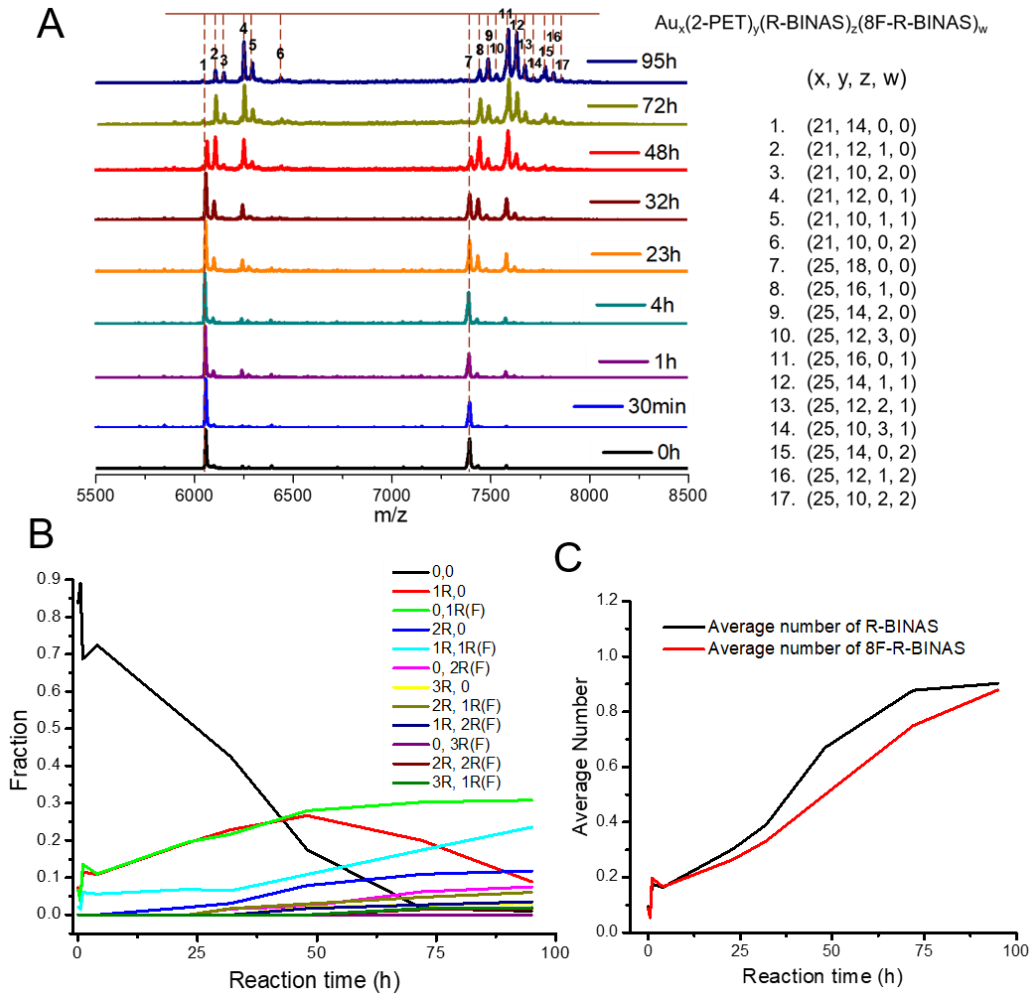

Figure 4.3 Characterizations of $Au_{25}(2\text{-PET})_{18}$ ligand exchange with R-BINAS and 8F-R-BINAS mixture. The ratio between clusters and free ligand is 1:15, and the ratio between R-BINAS and 8F-R-BINAS is 1:4. (A) Evolution of MALDI-TOF mass spectra. (B) Evolution of different $Au_{25}(2\text{-PET})_{18\text{-}2x\text{-}2y}(\text{R-BINAS})_x(\text{8F-R-BINAS})_y$ fractions as function of time. (C) Average number of exchanged R-BINAS and 8F-R-BINAS in the cluster as function of time.

To further study the different properties of BINAS and 8F-R-BINAS in LER and to better distinguish the electronic effects of the fluorinated ligand and the cluster containing the fluorinated ligand, mixtures of R-BINAS and 8F-R-BINAS were used. Here, the molar ratio of $Au_{25}(2\text{-PET})_{18}$ clusters and free ligand is 1:15, and the ratio between R-BINAS and 8F-R-BINAS was chosen as 1:2 and 1:4, respectively in two separate experiments. The calculated mass values of the different cluster species after ligand exchange of $Au_{25}(2\text{-PET})_{18}$ with R-BINAS and 8F-R-BINAS are listed at Table S4. The MALDI-TOF spectra as a function of time for the experiment with 1:4

R-BINAS : 8F-R-BINAS ratio are shown in Figure 4.3 A. The peaks have been labelled using numbers, and the corresponding compositions are given at the right side of the spectra. The mass peak intensities were determined and the percentage of different species were quantified and listed in Table S5. For the calculation of the percentage, the fragmentation peaks (Au_{21} species) were also taken into account. The relative abundance of the different species as a function of time are illustrated in Figure 4.3 B. As expected the fraction of the parent cluster (marked as 0,0) decreased with time and the fractions related to ligand-exchanged species raised. More interesting is the comparison between the cluster species containing one R-BINAS (marked as 1R,0, red trace) and one 8F-R-BINAS molecule (marked as 0,1R(F), green trace) in their ligand shell. Whereas both species increase at about the same rate initially, the abundance of the species containing one R-BINAS ligand decreased again after about 50h while the abundance of the cluster containing one 8F-R-BINAS ligand continued to increase. At the same time the cluster with both one R-BINAS and one 8F-R-BINAS (light blue line in Fig. 4.3 B) increased strongly. The different behavior shows that the cluster containing one 8F-R-BINAS is less reactive compared to the cluster containing one R-BINAS ligand, which is ascribed to the effect of 8F-R-BINAS on the electronic properties of the cluster.

Importantly, the average numbers of exchanged R-BINAS (black curve) and 8F-R-BINAS (red curve) in the cluster (Fig. 4.3 C) are comparable in the course of the time, showing that the behavior described above is not due to the deactivation of the free 8F-R-BINAS ligand.

At R-BINAS : 8F-R-BINAS ratio of 1:2 the behavior was found to be qualitatively similar (Figure S3). The MALDI-TOF spectra at different times are shown in Figure S3 A and the derived values of different mass peaks and calculated fractions of the different species are listed in Table S6. From the evolution plots of the different species in these two experiments (Fig. 4.3 B and Fig. S3 B), some conclusions can be drawn. By increasing the R-BINAS fraction from 20% (ratio 1:4) to 33.3% (ratio 1:2), the species with one R-BINAS ligand (1R,0) becomes predominant. Furthermore, the

species with two R-BINAS ligands (2R, 0) exceeds the abundance of the hybrid species (1R, 1R(F)), which is opposite at 1:4 ratio. At lower ratio considerably more R-BINAS was incorporated in the ligand shell compared to 8F-R-BINAS, which is reflected in the average number of exchanged R-BINAS and 8F-R-BINAS, which is lower for the fluorinated ligand (Figure S3 C). The observations described above are also is in agreement with the associative pathway for the ligand exchange process, the rate constant being dependent on the concentration of incoming ligands.

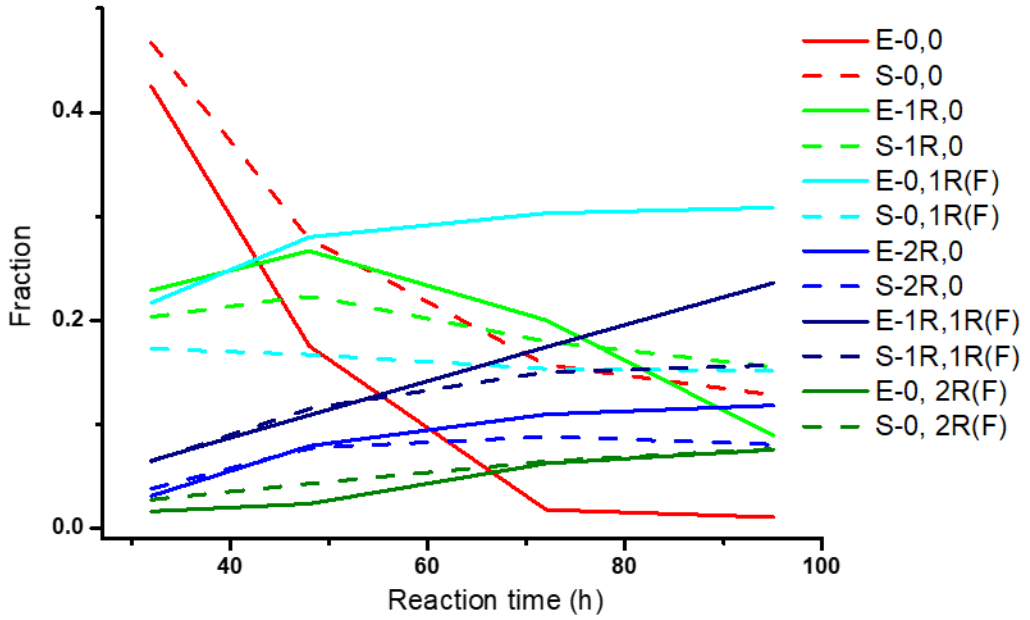

Figure 4.4 Evolution of different species during $Au_{25}(2\text{-PET})_{18}$ ligand exchange with R-BINAS and 8F-R-BINAS mixture as function of time. The solid curves are extracted from Figure 3B (experimental (E)) values, 1:4 R-BINAS and 8F-R-BINAS ratio) and the dash curves are calculated (S) by multinomial distribution program (SI Note 2). For clarity only the species with at least two ligands exchanged are shown (other species are much less abundant) in the time range 32h-95h.

Since the two ligands show distinct behaviour in separate LERs, we may anticipate that using a mixture of the two ligands will not simply lead to a statistical distribution of the two ligands on the cluster. In other words, some combinations of ligands may be more (less) abundant than expected based on the average composition. In order to verify this hypothesis we calculated the statistical distribution (multinomial distribution). For this we first determined the average composition (average x and

average y) for a specific sample by considering all the detected species. Having these numbers from the experiment, one can determine the probabilities required for the calculation of the multinomial distribution. (The program code and related values of probabilities are shown in SI Note 3.) This can be done for every sample collected as a function of time during the experiment. We took the data extracted from the experiment shown in Figure 4.3 (average number of exchanged R-BINAS and 8F-R-BINAS, Figure 4.3 C) to calculate the statistical distribution of the cluster species. It should be noted that this calculation requires knowledge of the total number of available sites. It has been shown that only up to seven BINAS ligands can adsorb on Au_{25} (Ag_{25}) nanoclusters[27], due to steric hindrance, and therefore we chose seven as the number of available sites for the dithiols. The calculated statistical distributions of the different species are illustrated in Fig. S5. The comparison between the experimental evolution of species and the evolution based on the statistical distribution are shown in Figure 4.4.

As demonstrated by Figure 4.4, there are clear differences between experiment (solid curves, E) and simulation (dash curves, S), demonstrating that the distribution is not statistical. For example, the species containing one 8F-R-BINAS ligand (0, 1R(F)) shows significantly higher abundance than expected based on the statistical distribution. The ligand with one R-BINAS in its ligand shell is initially more abundant than expected based on statistical distribution and then becomes less abundant than expected. The above shows that the LERs between $Au_{25}(2\text{-PET})_{18}$ (0,0) and a mixture of R-BINAS and 8F-R-BINAS ligands do not lead to statistical distributions of cluster species. There seems to be some specificity, either due to steric or electronic effects. To shed some more light on this issue we analyzed the kinetics of the reaction in more detail.

The reaction network of ligand exchange reactions between $Au_{25}(2\text{-PET})_{18}$ (0,0) and mixed R-BINAS and 8F-R-BINAS ligands is illustrated in Scheme 4.2. The different involved species of general formula $Au_{25}(2\text{-PET})_{18\text{-}2x\text{-}2y}(\text{R-BINAS})_x(\text{8F-R-BINAS})_y$

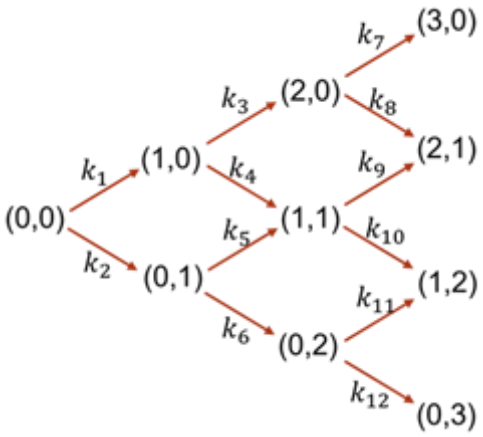

Scheme 4.2 Reactional network for the ligand exchange between $Au_{25}(2\text{-PET})_{18}$ (0,0) and mixed R-BINAS and 8F-R-BINAS ligand. The products $Au_{25}(2\text{-PET})_{18\text{-}2x\text{-}2y}(\text{R-BINAS})_x(\text{8F-R-BINAS})_y$ were labelled as (x,y). Here the maximum x+y=3.

were labelled as (x, y) in the scheme, and only the initial part of the process with maximum total ligand exchange number equal to 3 (maximum x+y=3) is considered. The reaction network in Scheme 4.2 is a simplification, as it does not consider isomers of clusters, which differ in the relative position of the adsorbed R-BINAS and 8F-R-BINAS ligands on the cluster. The reaction network was modelled assuming each ligand exchange reaction as a pseudo first order reaction, which seems reasonable taking into account the excess of the ligands. The experimental data of the LERs were fit to the model outlined in Scheme 4.2 using MATLAB (the code is shown in the supporting Note 4). For example, Figure 4.5 shows the fit of the experiments depicted in Figure 4.3 B (raw data extracted from Table S5; ratio between R-BINAS and 8F-R-BINAS as 1:4). The model fits well the experimental data. Similar fitting was done for the experiment with 1:2 ratio of R-BINAS and 8F-R-BINAS (raw data taken from Table S6, Figure S6 A). The obtained rate constants are given in Figure S6 D. The ratio of the rate constants describing the consecutive exchange of R-BINAS (k1/k3) and 8F-R-BINAS (k2/k6) also are in good agreement with the corresponding ratio extracted in the experiments with the individual ligands (Fig. 4.2), which underlines the reliability of the approach. The electronic effect of the 8F-R-BINAS modified cluster on the exchange rate can be appreciated by comparing k4 and k6, as k4 describes the reaction of

$Au_{25}(2\text{-PET})_{16}(\text{R-BINAS})_1$ with 8F-R-BINAS and k6 the reaction of $Au_{25}(2\text{-PET})_{16}(\text{8F-R-BINAS})_1$ with 8F-R-BINAS. The ratio k4/k6 is about 2.0 for both experiments (1:4 and 1:2 ligand ratios). The effect is also illustrated by the ratio of k3/k5. In this case, however, the fit gave very low values for k5. The kinetic constants indicate the ligand as well as the (ligand- exchanged) Au_{25} cluster exert an electronic effect on the rate of LERs: The 8F-R-BINAS ligand and the related substituted cluster, $Au_{25}(2\text{-PET})_{16}(\text{8F-R-BINAS})_1$, show lower reactivity compared to non-fluorinated counterparts (R-BINAS and $Au_{25}(2\text{-PET})_{16}(\text{R-BINAS})_1$).

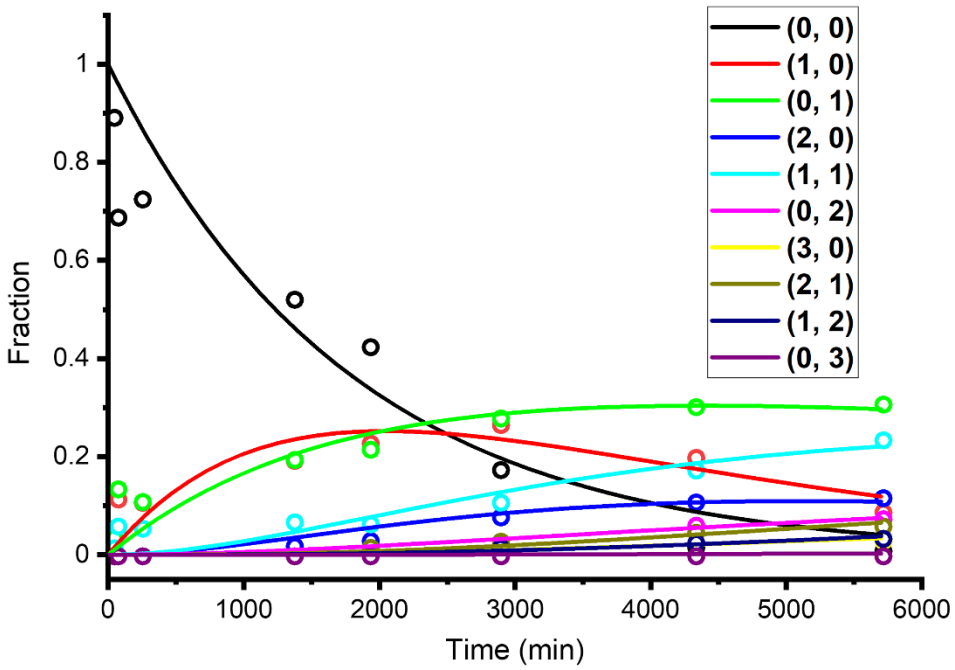

Figure 4.5 MATLAB fitting curves of $Au_{25}(2\text{-PET})_{18}$ ligand exchange with R-BINAS and 8F-R-BINAS mixture with ratio as 1:4. The dots curves illustrated the experimental results (taken from Table S5) and solid curves related to the fitting curves.

R-BINAS and 8F-R-BINAS have same configuration, and the discrimination during LERs is mainly due to electronic effects. By replacing R-BINAS with S-BINAS in the ligand mixture, the stereospecific effect can be investigated as well. Here the conditions for LERs follow the previous experiments, with molar ratio between cluster and ligand set as 1:15, and molar ratio between S-BINAS to 8F-R-BINAS set as 1:2 (Figure S5) and 1:4 (Figure 4.6), respectively. The MALDI-TOF results for 1:4 ratio are shown in Figure 4.6A and the evolution of different species are represented

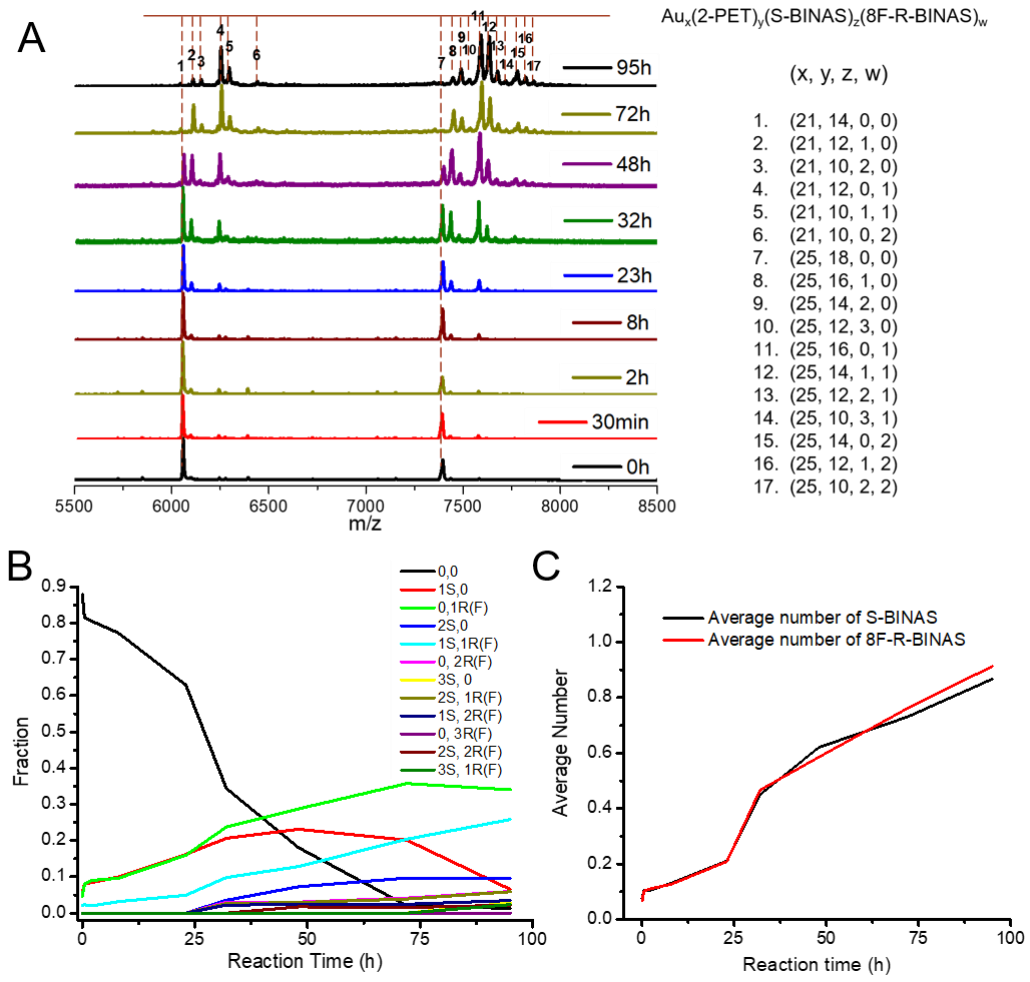

Figure 4.6 Characterization of $Au_{25}(2\text{-PET})_{18}$ ligand exchange with S-BINAS and 8F-R-BINAS mixture. The ratio between clusters and free ligand is 1:15, and the ratio between S-BINAS and 8F-R-BINAS is 1:4. (A) Evolution of MALDI-TOF mass spectra. (B) Evolution of different $Au_{25}(2\text{-PET})_{18\text{-}2x\text{-}2y}(\text{S-BINAS})_x(\text{8F-R-BINAS})_y$ species as function of time. (C) Average number of exchanged S-BINAS and 8F-R-BINAS in the cluster as function of time.

in Figure 4.6 B (data given in Table S7). Comparison with the experiment shown in Figure 4.3 B with the other enantiomer of BINAS (mixture of R-BINAS and 8F-R-BINAS) did not reveal significant differences. Furthermore, the average number of S-BINAS and 8F-R-BINAS on the cluster evolved similarly with time (Figure 4.6 C). Also for the experiment with 1:2 ratio of S-BINAS : 8F-R-BINAS, the related evolution of the different species (Figure S5, Table S8) was very similar to the one with the other BINAS enantiomer (Figure S3). Both experiments were fit using the MATLAB program (Figure S6 B&C). The related rate constants as shown in Figure S6 D also revealed the stereoelectronic effect of 8F-R-BINAS ligand as described

above. From these experiments we can conclude that diastereospecific interactions are negligible under these conditions, which is not surprising, considering the fact that in our experiments only very few chiral ligands are adsorbed on the achiral cluster, leaving many “achiral sites” free for further incoming ligands. The stereospecific effect originating from the adsorbed chiral ligand is a local effect, unlike the stereoelectronic effect which seems to extend over the whole cluster.

4.4 Conclusion

In summary, depending on the enantiopure BINAS ligand and the corresponding fluorine-substituted molecule, the electronic and stereospecific effect of ligand during LERs with achiral $Au_{25}(2\text{-PET})_{18}$ nanoclusters have been investigated. The results show that the electronic properties of ligand induce large discrimination to the LERs. Adsorbed fluorine-substituted BINAS significantly slows down the further ligand exchange on Au_{25} clusters compared to adsorbed parent BINAS. Both electronic effects of the substituted cluster and the ligand were important. However, compared with the electronic effect, stereoselectivity was negligible as the two enantiomers did not display visible difference during LERs with the achiral clusters, at least for the initial stage of the ligand exchange investigated here. This finding shows that the stereospecific effect as a local property at the surface of the cluster whereas the electronic effect due to the adsorbed ligand extends over the whole cluster and significantly influences the kinetics of further LERs. Our discovery offers new insight for the design of new ligands and a strategy to control LERs.

4.5 Supporting information

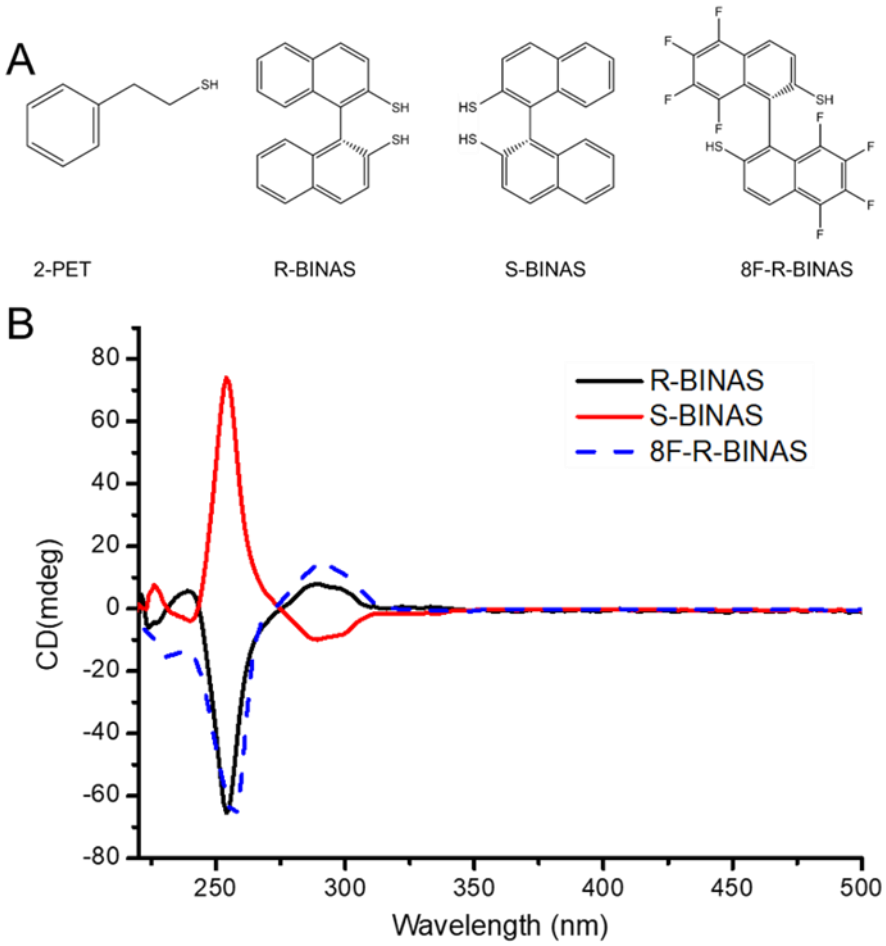

Figure S1. Characterizations of free ligands. (A) Structures of involved ligands in the experiment. 2-PET: 2-phenylethylthiolate, R/S-BINAS: R/S-1,1'-binaphthalene-2,2'-dithiol, 8F-R-BINAS: (R)-5,5',6,6',7,7',8,8'-octafluoro- [1,1'-binaphthalene]-2,2'-dithiol. (B) CD spectra of R/S-BINAS and 8F-R-BINAS, the samples are dissolved in dichloromethane.

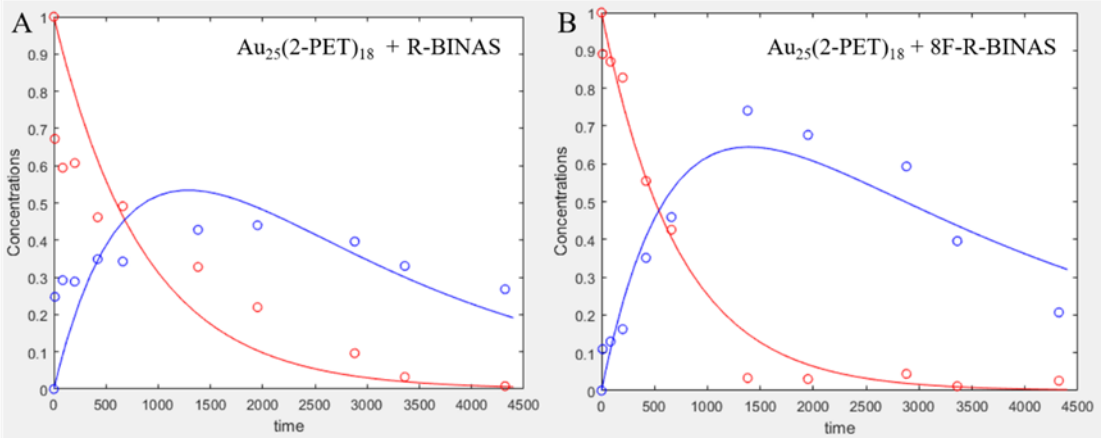

Figure S2. MATLAB simulated concentration plot of the $Au_{25}(2\text{-PET})_{18}$ reacted with R-BINAS (A) and 8F-R-BINAS (B) separately. Red dots ($Au_{25}(2\text{-PET})_{18}$) and blue dots (one-exchange species) related to the raw data extracted from Table S2 (A) and Table S3 (B), solid curves corresponding to the fitting results.

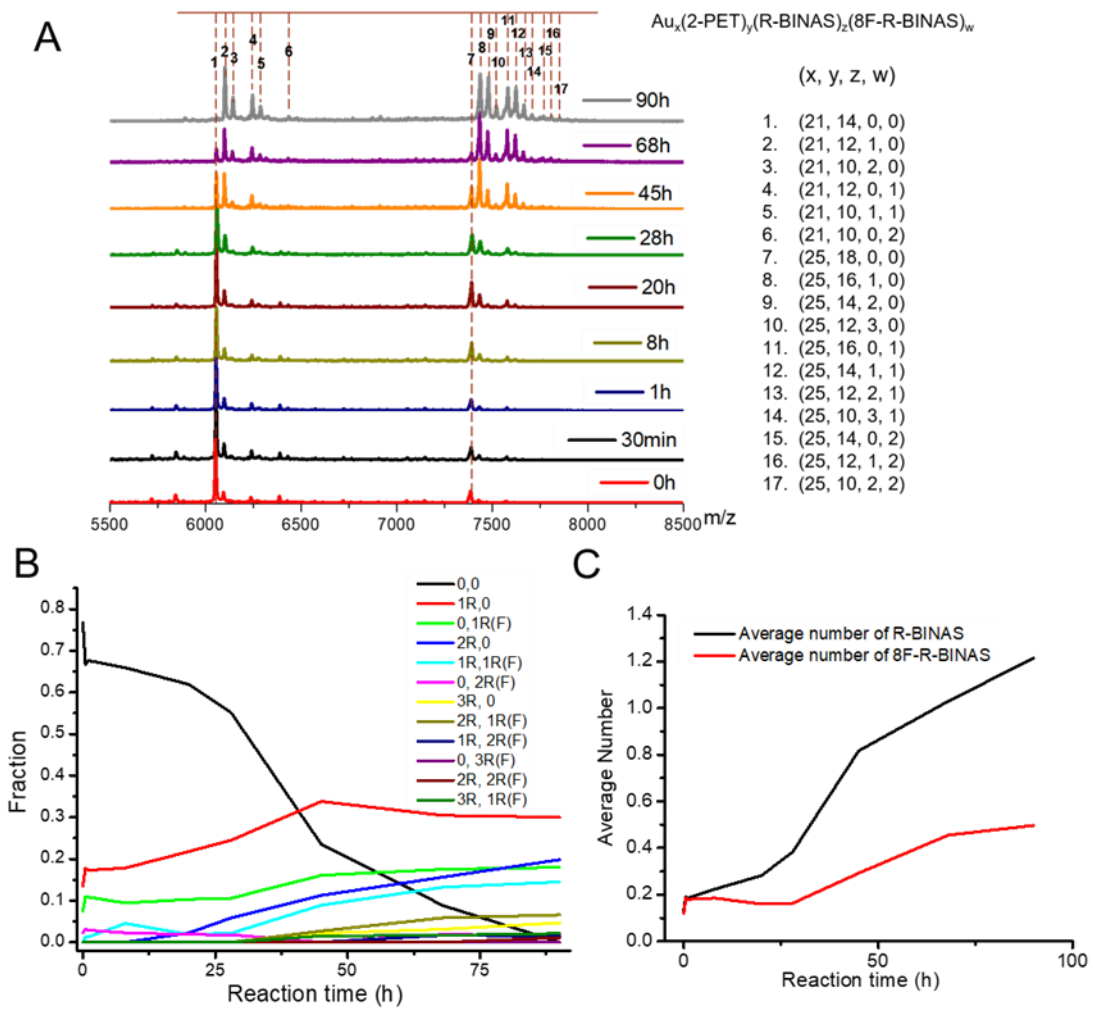

Figure S3. Characterizations of $Au_{25}(2\text{-PET})_{18}$ ligand exchange with R-BINAS and 8F-R-BINAS mixture. The ratio between clusters and free ligand is 1:15, and the ratio between R-BINAS and 8F-R-BINAS is 1:2. (A) Evolution of MALDI-TOF mass spectra. The compositions of different peaks are exhibited at right side. (B) Evolution of different fractions of $Au_{25}(2\text{-PET})_{18\text{-}2x\text{-}2y}(\text{R-BINAS})_x(\text{8F-R-BINAS})_y$ as function of time. (C) Average number of exchanged R-BINAS (black curve) and 8F-R-BINAS (red curve) in the cluster as function of time.

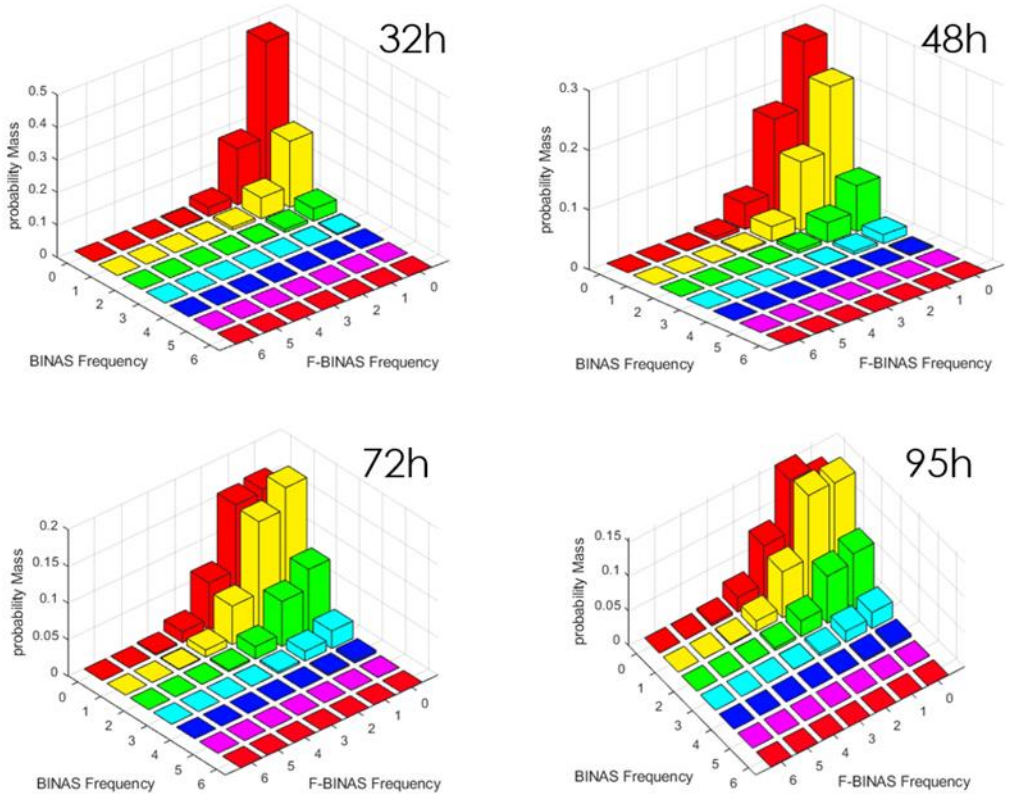

Figure S4. Multinomial distributional diagram of $Au_{25}(2\text{-PET})_{18}$ ligand exchange with R-BINAS and 8F-R-BINAS mixture at various times. The ratio between clusters and free ligand is 1:15, and the ratio between R-BINAS and 8F-R-BINAS is 1:4.

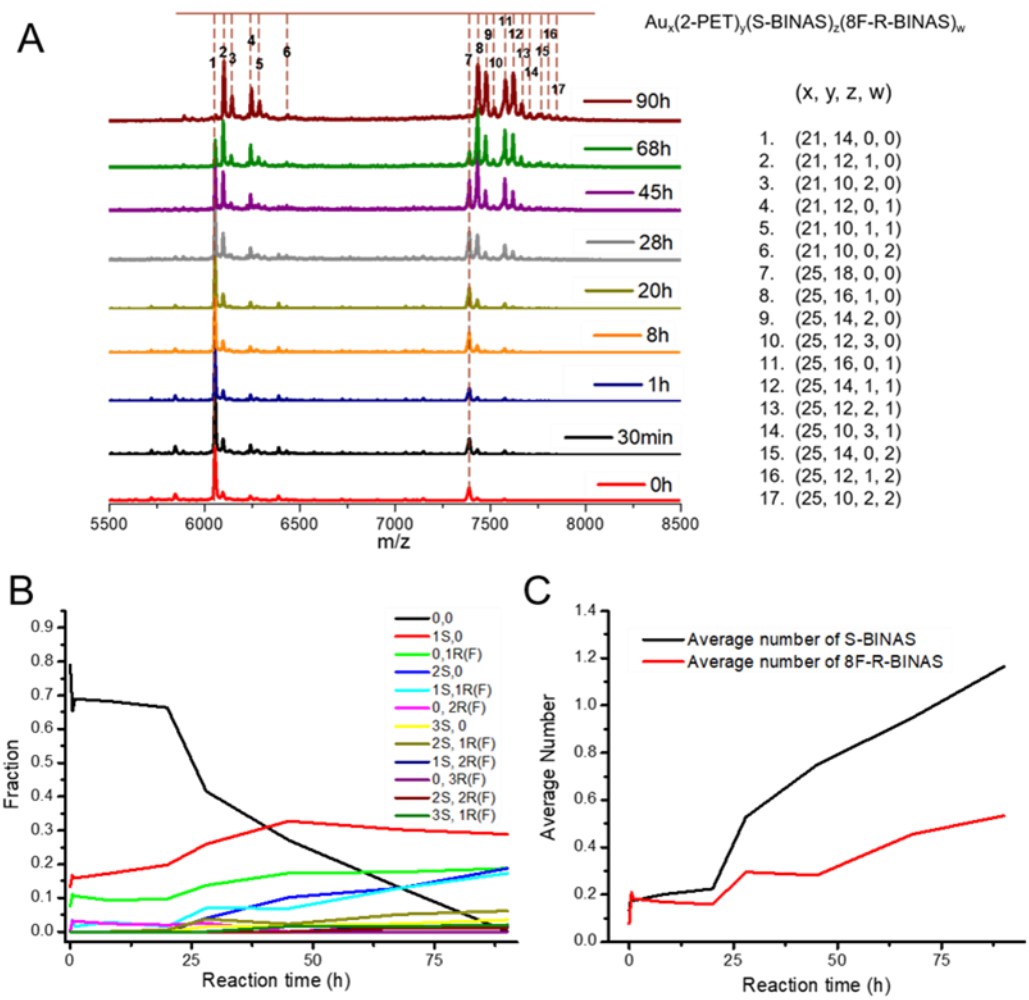

Figure S5. Characterizations of $Au_{25}(2\text{-PET})_{18}$ ligand exchange with S-BINAS and 8F-R-BINAS mixture. The ratio between clusters and free ligand is 1:15, and the ratio between S-BINAS and 8F-R-BINAS is 1:2. (A) Evolution of MALDI-TOF mass spectra. The compositions of different peaks are exhibited at right side. (B) Evolution of different fractions of $Au_{25}(2\text{-PET})_{18\text{-}2x\text{-}2y}(S\text{-BINAS})_x(8F\text{-R-BINAS})_y$ as function of time. (C) Average number of exchanged S-BINAS (black curve) and 8F-R-BINAS (red curve) in the cluster as function of time.

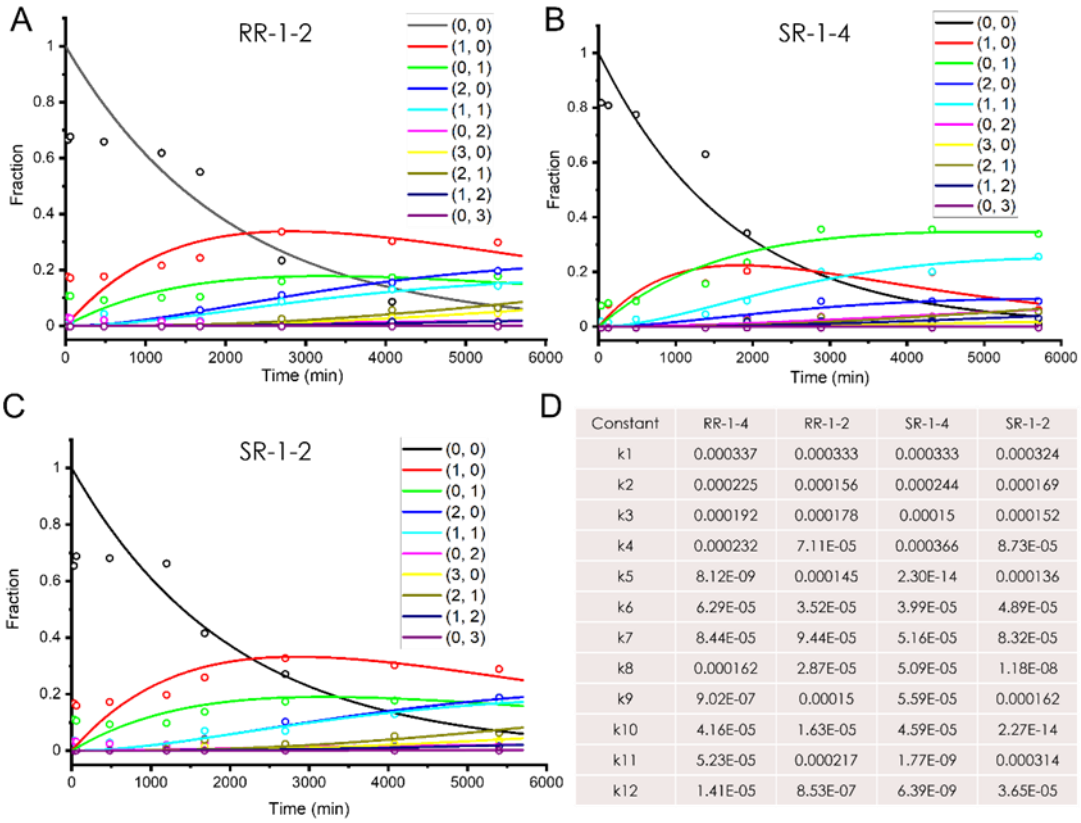

Constant	RR-1-4	RR-1-2	SR-1-4	SR-1-2
k1	0.000337	0.000333	0.000333	0.000324
k2	0.000225	0.000156	0.000244	0.000169
k3	0.000192	0.000178	0.00015	0.000152
k4	0.000232	7.11E-05	0.000366	8.73E-05
k5	8.12E-09	0.000145	2.30E-14	0.000136
k6	6.29E-05	3.52E-05	3.99E-05	4.89E-05
k7	8.44E-05	9.44E-05	5.16E-05	8.32E-05
k8	0.000162	2.87E-05	5.09E-05	1.18E-08
k9	9.02E-07	0.00015	5.59E-05	0.000162
k10	4.16E-05	1.63E-05	4.59E-05	2.27E-14
k11	5.23E-05	0.000217	1.77E-09	0.000314
k12	1.41E-05	8.53E-07	6.39E-09	3.65E-05

Figure S6. MATLAB fitting curves of LERs with mixed ligands. (A) $Au_{25}(2\text{-PET})_{18}$ ligand exchange with R-BINAS and 8F-R-BINAS mixture, ratio of two ligands set as 1:2. (B/C) $Au_{25}(2\text{-PET})_{18}$ ligand exchange with S-BINAS and 8F-R-BINAS mixture, ratio of two ligands set as 1:4 and 1:2 separately. (D) The related rate constants of different experiments from MATLAB fitting are listed.

Table S1. Calculated Mass value of different species after $Au_{25}(2\text{-PET})_{18}$ ligand exchange reaction with BINAS and 8F-R-BINAS, separately. The fragment signals according to the related species losing $Au_4(2\text{-PET})_4$.

	$Au_{25}(2\text{-PET})_{18}$ + BINAS				$Au_{25}(2\text{-PET})_{18}$ + 8F-R-BINAS			
	Au	2-PET	BINAS	Mass	Au	2-PET	8F-R-BINAS	Mass
Complete signal	25	18	0	7394.39	25	18	0	7394.39
	25	16	1	7436.98	25	16	1	7580.83
	25	14	2	7479.57	25	14	2	7767.22
	25	12	3	7522.16	25	12	3	7953.71
	25	10	4	7564.75	25	10	4	8140.15
	25	8	5	7607.34	25	8	5	8326.59
	25	6	6	7649.93	25	6	6	8513.03
Fragment signal	21	14	0	6057.59	21	14	0	6057.59
	21	12	1	6100.18	21	12	1	6244.03
	21	10	2	6142.77	21	10	2	6430.47
	21	8	3	6185.36	21	8	3	6616.91
	21	6	4	6227.95	21	6	4	6803.35
	21	4	5	6270.54	21	4	5	6989.79
	21	2	6	6313.13	21	2	6	7176.23

Table S2. Mass peak intensity and corresponding percentage of different species after $Au_{25}(2\text{-PET})_{18}$ ligand exchange with R-BINAS. Data extracted from Fig. 4.1 A.

$Au_{25}(2\text{-PET})_{18}$ + R-BINAS → $Au_{25}(2\text{-PET})_{18-2x}(R\text{-BINAS})_x$								
x	0	1	2	3	4	5	6	Total
Intensity								
10min	582307	214689	62910	6412	0	0	0	866318
85min	766010	376975	124376	13555	7858	0	0	1288774
200min	888029	422482	131333	13742	7574	0	0	1463160
7h	178515	135049	57496	8405	3782	2304	1312	386863
11h	110824	77350	25290	5583	3215	1962	1358	225582
23h	36019	46973	19078	4454	1731	924	640	109819
32.5h	39583	79238	41486	13310	3473	1719	1266	180075
48h	17255	70939	59411	22526	5308	2144	1407	178990
56h	26	263	351	128	27	0	0	795
72h	89	2975	4990	2404	485	105	45	11093
Percentage	0	1	2	3	4	5	6	
10min	0.672163	0.247818	0.072618	0.007401	0	0	0	
85min	0.594371	0.292507	0.096507	0.010518	0.006097	0	0	
200min	0.606925	0.288746	0.08976	0.009392	0.005176	0	0	
7h	0.461442	0.349087	0.148621	0.021726	0.009776	0.005956	0.003391	
11h	0.49128	0.342891	0.11211	0.024749	0.014252	0.008698	0.00602	
23h	0.327985	0.427731	0.173722	0.040558	0.015762	0.008414	0.005828	
32.5h	0.219814	0.440028	0.230382	0.073914	0.019286	0.009546	0.00703	
48h	0.096402	0.396329	0.331924	0.125851	0.029655	0.011978	0.007861	
56h	0.032704	0.330818	0.441509	0.161006	0.033962	0	0	
72h	0.008023	0.268187	0.449833	0.216713	0.043721	0.009465	0.004057	

Table S3. Mass peak intensity and corresponding percentage of different species after $Au_{25}(2\text{-PET})_{18}$ ligand exchange with 8F-R-BINAS. Data extracted from Fig. 4.1 B.

	$Au_{25}(2\text{-PET})_{18}$ + 8F-R-BINAS → $Au_{25}(2\text{-PET})_{18-2x}(8\text{F-R-BINAS})_x$					
x	0	1	2	3	4	Total
Intensity						
10min	201663	24873	0	0	0	226536
85min	637283	94989	0	0	0	732272
200min	453020	88964	5199	0	0	547183
7h	94320	59750	13894	2145	0	170109
11h	27106	29247	6217	919	229	63718
23h	1631	36307	9230	1512	337	49017
32.5h	778	17156	6374	824	235	25367
48h	2217	29639	15928	1833	356	49973
56h	121	4028	4984	844	208	10185
72h	1319	10458	28428	7852	2505	50562

Percentage	0	1	2	3	4
10min	0.890203	0.109797	0	0	0
85min	0.870282	0.129718	0	0	0
200min	0.827913	0.162585	0.009501	0	0
7h	0.554468	0.351245	0.081677	0.01261	0
11h	0.425406	0.459007	0.097571	0.014423	0.003594
23h	0.033274	0.740702	0.188302	0.030846	0.006875
32.5h	0.03067	0.676312	0.251271	0.032483	0.009264
48h	0.044364	0.5931	0.318732	0.03668	0.007124
56h	0.01188	0.395484	0.489347	0.082867	0.020422
72h	0.026087	0.206835	0.56224	0.155294	0.049543

Table S4. Calculated Mass value of different species after $Au_{25}(2\text{-PET})_{18}$ ligand exchange reaction with mixture of BINAS and 8F-R-BINAS. Maximum 4 ligand exchange species have been calculated here. Fragment signals of $Au_{25}(2\text{-PET})_{18}$ also listed.

	$Au_{25}(2\text{-PET})_{18}$ + BINAS+ 8F-R-BINAS → $Au_{25}(2\text{-PET})_{18-2x-2y}(BINAS)_x(8F\text{-R-BINAS})_y$				
			x	y	
x+y	Au	2-PET	BINAS (x)	8F-R-BINAS (y)	Mass
0	25	18	0	0	7394.39
1	25	16	1	0	7436.98
	25	16	0	1	7580.83
2	25	14	1	1	7623.42
	25	14	2	0	7479.57
	25	14	0	2	7767.27
3	25	12	3	0	7522.16
	25	12	2	1	7666.01
	25	12	1	2	7809.86
	25	12	0	3	7953.71
4	25	10	4	0	7564.75
	25	10	3	1	7708.6
	25	10	2	2	7852.45
	25	10	1	3	7996.3
	25	10	0	4	8140.15
Fragments of $Au_{25}(2\text{-PET})_{18}$	24	17	0	0	7060.19
	23	16	0	0	6725.99
	22	15	0	0	6391.79
	21	14	0	0	6057.59

Table S5. Mass peak intensity and corresponding percentage of different species after $Au_{25}(2\text{-PET})_{18}$ ligand exchange with mixture ligand of R-BINAS and 8F-R-BINAS (molar ratio1:4). Data extracted from Fig. 4.3 A.

R-BINAS: 8F-R-BINAS =1:4	$Au_{25}(2\text{-PET})_{18}$ + R-BINAS+ 8F-R-BINAS → $Au_{25}(2\text{-PET})_{18-2x-2y}(\text{R-BINAS})_x(\text{8F-R-BINAS})_y$											
	0-Exchange	1-Exchange		2-Exchange				3-Exchange			4-Exchange	
Intensity	0, 0	1R, 0	0, 1R(F)	2R, 0	1R, 1R(F)	0, 2R(F)	3R, 0	2R, 1R(F)	1R, 2R(F)	0, 3R(F)	2R, 2R(F)	3R, 1R(F)
0h	56201	4918	4495	0	1413	0	0	0	0	0	0	0
30min	84750	5311	3539	0	1535	0	0	0	0	0	0	0
1h	11065	1856	2187	0	976	0	0	0	0	0	0	0
4h	9985	1498	1519	0	773	0	0	0	0	0	0	0
23h	24695	9189	9279	958	3259	0	0	0	0	0	0	0
32h	17727	9545	9046	1294	2717	671	0	721	0	0	0	0
48h	3786	5762	6049	1707	2348	507	430	641	372	0	0	0
72h	1108	12566	19033	6872	10944	3911	1697	2985	1693	0	907	1092
95h	758	6490	22476	8608	17180	5497	2262	4418	2584	0	1192	1426
Percentage	0, 0	1R, 0	0, 1R(F)	2R, 0	1R, 1R(F)	0, 2R(F)	3R, 0	2R, 1R(F)	1R, 2R(F)	0, 3R(F)	2R, 2R(F)	3R, 1R(F)
0h	0.838483	0.073373	0.067063	0	0.021081	0	0	0	0	0	0	0
30min	0.890839	0.055826	0.0372	0	0.016135	0	0	0	0	0	0	0
1h	0.687951	0.115394	0.135974	0	0.060681	0	0	0	0	0	0	0
4h	0.724864	0.108748	0.110272	0	0.056116	0	0	0	0	0	0	0
23h	0.521211	0.193943	0.195842	0.02022	0.068784	0	0	0	0	0	0	0
32h	0.424894	0.228782	0.216821	0.031016	0.065123	0.016083	0	0.017281	0	0	0	0
48h	0.175262	0.266735	0.28002	0.07902	0.108694	0.02347	0.019906	0.029673	0.017221	0	0	0
72h	0.017641	0.20007	0.303035	0.109413	0.174245	0.062269	0.027019	0.047526	0.026955	0	0.014441	0.017386
95h	0.010399	0.089037	0.308351	0.118094	0.235694	0.075414	0.031033	0.060611	0.03545	0	0.016353	0.019563

Table S6. Mass peak intensity and corresponding percentage of different species after $Au_{25}(2\text{-PET})_{18}$ ligand exchange with mixture ligand of R-BINAS and 8F-R-BINAS (molar ratio1:2). Data extracted from Figure S3 A.

R-BINAS: 8F-R-BINAS =1:2	$Au_{25}(2\text{-PET})_{18}$ + R-BINAS+ 8F-R-BINAS → $Au_{25}(2\text{-PET})_{18-2x-2y}(\text{R-BINAS})_x(\text{8F-R-BINAS})_y$											
	0-Exchange	1-Exchange		2-Exchange			3-Exchange				4-Exchange	
Intensity	0, 0	1R, 0	0, 1R(F)	2R, 0	1R, 1R(F)	0, 2R(F)	3R, 0	2R, 1R(F)	1R, 2R(F)	0, 3R(F)	2R, 2R(F)	3R, 1R(F)
0h	314626	55210	30493	0	0	9346	0	0	0	0	0	0
30min	286679	76738	47145	0	5865	13797	0	0	0	0	0	0
1h	192340	49159	30843	0	3639	8249	0	0	0	0	0	0
8h	348334	94209	49785	0	23929	12059	0	0	0	0	0	0
20h	183989	64680	30578	6659	5703	5519	0	0	0	0	0	0
28h	66034	29345	12683	6991	2592	2134	0	0	0	0	0	0
45h	8005	11496	5463	3827	3025	0	733	917	0	0	0	518
68h	2249	7755	4461	3986	3369	480	801	1492	434	0	0	435
90h	0	21345	12783	14105	10305	1188	3319	4682	1037	0	791	1509
Percentage	0, 0	1R, 0	0, 1R(F)	2R, 0	1R, 1R(F)	0, 2R(F)	3R, 0	2R, 1R(F)	1R, 2R(F)	0, 3R(F)	2R, 2R(F)	3R, 1R(F)
0h	0.767989	0.134765	0.074432	0	0	0.022813	0	0	0	0	0	0
30min	0.666348	0.178368	0.109582	0	0.013632	0.032069	0	0	0	0	0	0
1h	0.676705	0.172955	0.108514	0	0.012803	0.029022	0	0	0	0	0	0
8h	0.659329	0.178319	0.094233	0	0.045293	0.022825	0	0	0	0	0	0
20h	0.619225	0.217684	0.102912	0.022411	0.019194	0.018574	0	0	0	0	0	0
28h	0.551299	0.244993	0.105887	0.058366	0.02164	0.017816	0	0	0	0	0	0
45h	0.235552	0.338277	0.160752	0.112612	0.089012	0	0.021569	0.026983	0	0	0	0.015242
68h	0.088328	0.304572	0.175202	0.156547	0.132315	0.018852	0.031459	0.058597	0.017045	0	0	0.017084
90h	0	0.300363	0.17988	0.198483	0.14501	0.016717	0.046704	0.065884	0.014592	0	0.011131	0.021234

Table S7. Mass peak intensity and corresponding percentage of different species after $Au_{25}(2\text{-PET})_{18}$ ligand exchange with mixture ligand of S-BINAS and 8F-R-BINAS (molar ratio1:4). Data extracted from Figure 4.6 A.

S-BINAS: 8F-R-BINAS =1:4	$Au_{25}(2\text{-PET})_{18}$ + S-BINAS+ 8F-R-BINAS → $Au_{25}(2\text{-PET})_{18-2x-2y}(S\text{-BINAS})_x(8F\text{-R-BINAS})_y$											
	0-Exchange	1-Exchange		2-Exchange				3-Exchange			4-Exchange	
Intensity	0, 0	1S, 0	0, 1R(F)	2S, 0	1S, 1R(F)	0, 2R(F)	3S, 0	2S, 1R(F)	1S, 2R(F)	0, 3R(F)	2S, 2R(F)	3S, 1R(F)
0h	112619	11174	11074	0	3206	0	0	0	0	0	0	0
30min	112619	11174	11074	0	3206	0	0	0	0	0	0	0
2h	356247	37224	39786	0	8742	0	0	0	0	0	0	0
8h	18731	2411	2326	0	762	0	0	0	0	0	0	0
23h	36647	9441	9299	0	2863	0	0	0	0	0	0	0
32h	4821	2896	3334	496	1378	421	0	371	313	0	0	0
48h	4213	5397	6707	1696	2998	711	0	686	534	0	399	0
72h	3092	30300	53732	14533	30638	6229	0	5829	3663	0	2292	0
95h	744	3774	19613	5557	14883	3443	1622	3391	2000	0	1267	1348
Percentage	0, 0	1S, 0	0, 1R(F)	2S, 0	1S, 1R(F)	0, 2R(F)	3S, 0	2S, 1R(F)	1S, 2R(F)	0, 3R(F)	2S, 2R(F)	3S, 1R(F)
0h	0.878667	0.055212	0.046068	0	0.020053	0	0	0	0	0	0	0
30min	0.815648	0.080928	0.080204	0	0.02322	0	0	0	0	0	0	0
2h	0.805991	0.084217	0.090014	0	0.019778	0	0	0	0	0	0	0
8h	0.77305	0.099505	0.095997	0	0.031449	0	0	0	0	0	0	0
23h	0.629133	0.162077	0.159639	0	0.04915	0	0	0	0	0	0	0
32h	0.343621	0.206415	0.237634	0.035353	0.098218	0.030007	0	0.026443	0.022309	0	0	0
48h	0.020571	0.201586	0.357479	0.096688	0.203835	0.041442	0	0.03878	0.02437	0	0.015249	0
72h	0.020571	0.201586	0.357479	0.096688	0.203835	0.041442	0	0.03878	0.02437	0	0.015249	0
95h	0.012907	0.065473	0.340255	0.096405	0.258197	0.059731	0.028139	0.058829	0.034697	0	0.021981	0.023386

Table S8. Mass peak intensity and corresponding percentage of different species after $Au_{25}(2\text{-PET})_{18}$ ligand exchange with mixture ligand of S-BINAS and 8F-R-BINAS (molar ratio1:2). Data extracted from Figure S5 A.

S-BINAS: 8F-R-BINAS =1:2	$Au_{25}(2\text{-PET})_{18}$ + S-BINAS+ 8F-R-BINAS → $Au_{25}(2\text{-PET})_{18-2x-2y}(S\text{-BINAS})_x(8F\text{-R-BINAS})_y$											
	0-Exchange	1-Exchange		2-Exchange				3-Exchange			4-Exchange	
Intensity	0, 0	1S, 0	0, 1R(F)	2S, 0	1S, 1R(F)	0, 2R(F)	3S, 0	2S, 1R(F)	1S, 2R(F)	0, 3R(F)	2S, 2R(F)	3S, 1R(F)
0h	231153	38823	22375	0	0	0	0	0	0	0	0	0
30min	319483	81371	53896	0	16993	15795	0	0	0	0	0	0
1h	261586	60294	39931	0	5868	11768	0	0	0	0	0	0
8h	183693	46384	25018	0	7563	6462	0	0	0	0	0	0
20h	128239	38183	18797	0	3083	3856	0	1077	0	0	0	0
28h	45562	28418	15044	4382	7649	2792	1600	4090	0	0	0	0
45h	10141	12258	6502	3820	2582	0	678	857	0	0	0	589
68h	7379	17204	10066	7363	7374	922	1364	2923	794	0	618	900
90h	0	18923	12309	12286	11327	1229	2290	4049	971	0	776	1333
Percentage	0, 0	1S, 0	0, 1R(F)	2S, 0	1S, 1R(F)	0, 2R(F)	3S, 0	2S, 1R(F)	1S, 2R(F)	0, 3R(F)	2S, 2R(F)	3S, 1R(F)
0h	0.790669	0.132796	0.076535	0	0	0	0	0	0	0	0	0
30min	0.655299	0.166902	0.110547	0	0.034855	0.032397	0	0	0	0	0	0
1h	0.689387	0.1589	0.105235	0	0.015465	0.031014	0	0	0	0	0	0
8h	0.682569	0.172354	0.092962	0	0.028103	0.024012	0	0	0	0	0	0
20h	0.663643	0.197599	0.097275	0	0.015955	0.019955	0	0.005574	0	0	0	0
28h	0.415951	0.259437	0.137342	0.040005	0.06983	0.025489	0.014607	0.037339	0	0	0	0
45h	0.270954	0.327518	0.173725	0.102065	0.068988	0	0.018115	0.022898	0	0	0	0.015737
68h	0.129668	0.302318	0.176885	0.129387	0.12958	0.016202	0.023969	0.051365	0.013953	0	0.01086	0.015815
90h	0	0.288932	0.187944	0.187593	0.17295	0.018765	0.034966	0.061823	0.014826	0	0.011849	0.020353

Note 1. Explicit chemical equations of ligand exchange reaction between Au_{25}(2-PET)$_{18}$ and R-BINAS or 8F-R-BINAS separately.

Reactional equations for Au_{25}(2-PET)$_{18}$ + R-BINAS (until 3 exchange):

$$Au_{25}(2-PET)_{18} + R-BINAS \underset{k1}{\rightarrow} Au_{25}(2-PET)_{16}(R-BINAS)_1 + 2-PET$$
$$Au_{25}(2-PET)_{16}(R-BINAS)_1 + R-BINAS \underset{k2}{\rightarrow} Au_{25}(2-PET)_{14}(R-BINAS)_2 + 2-PET$$
$$Au_{25}(2-PET)_{14}(R-BINAS)_2 + R-BINAS \underset{k3}{\rightarrow} Au_{25}(2-PET)_{12}(R-BINAS)_3 + 2-PET$$

Reactional equations for Au_{25}(2-PET)$_{18}$ + 8F-R-BINAS (until 3 exchange):

$$Au_{25}(2-PET)_{18} + 8F-R-BINAS \underset{k1`}{\rightarrow} Au_{25}(2-PET)_{16}(8F-R-BINAS)_1 + 2-PET$$
$$Au_{25}(2-PET)_{16}(8F-R-BINAS)_1 + 8F-R-BINAS \underset{k2`}{\rightarrow} Au_{25}(2-PET)_{14}(8F-R-BINAS)_2 + 2-PET$$
$$Au_{25}(2-PET)_{14}(8F-R-BINAS)_2 + 8F-R-BINAS \underset{k3`}{\rightarrow} Au_{25}(2-PET)_{12}(8F-R-BINAS)_3 + 2-PET$$

Note 2. Program code of the MATLAB routine for the ligand exchange reaction between Au_{25}(2-PET)$_{18}$ (0,0) and R-BINAS and 8F-R-BINAS up to 2 ligand exchange species.

```
function dydt = kinet(t,y,k)
dydt(1,1) = [-k(1,1)*y(1,1)];
dydt(2,1) = [k(1,1)*y(1,1)] - [k(2,1)*y(2,1)]
```

```
function F = myfun(k,xdata)
global ydata
global y0
tspan = [xdata];
ode = @(t,y) kinet(t,y,k);
[t,y] = ode45(ode, tspan, y0);
F=y
```

Kinetic fitting of LERs between Au_{25}(2-PET)$_{18}$ (0,0) and BINAS up to one exchange species, the data were extracted from Table S2.

```
% Fits data to kinetics defined in kinet using least squares in myfun
% dydt = [-x*y(1)]
clear all
type kinet
type myfun
global xdata
global ydata
global y0
% initial concentrations
y0 = zeros(2,1)
y0(1,1) = 1.0
y0(2,1) = 0.0
% Enter data here time, c1, c2
mydata=[0          1.0     0.0
```

```
          10    0.672163    0.247818
          85    0.594371    0.292507
         200    0.606925    0.288746
         420    0.461442    0.349087
         660    0.49128     0.342891
        1380    0.327985    0.427731
        1950    0.219814    0.440028
        2880    0.096402    0.396329
        3360    0.032704    0.330818
        4320    0.008023    0.268187
];
    xdata=mydata(:,1);
    ydata(:,1)=mydata(:,2);
    ydata(:,2)=mydata(:,3);

% Time span of the simulation
tspan = [0 4400]

%estimation of kinetic constants
k0 = zeros(2,1)
k0(1,1) = 0.001
k0(2,1) = 0.001

%x are the fitted parametrs
[k,resnorm] = lsqcurvefit(@myfun,k0,xdata,ydata)

%Solve problem
ode = @(t,y) kinet(t,y,k);
[t,y] = ode45(ode, tspan, y0);

plot(xdata,ydata(:,1),'ro',xdata,ydata(:,2),'bo',t,y(:,1),'r',t,y(:,2),'b')
xlabel('time')
ylabel('Concentrations')

konstants = k
```

Kinetic fitting of LERs between Au_{25}(2-PET)$_{18}$ (0,0) and 8F-R-BINAS up to one exchange species, the data were extracted from Table S3.

```
% Fits data to kinetics defined in kinet using least squares in myfun
% dydt = [-x*y(1)]

clear all
type kinet
type myfun
```

```
global xdata
global ydata
global y0
% initial concentrations
y0 = zeros(2,1)
y0(1,1) = 1.0
y0(2,1) = 0.0
% Enter data here time, c1, c2
mydata=[0          1.0     0.0
          10     0.890203      0.109797
          85     0.870282      0.129718
         200     0.827913      0.162585
         420     0.554468      0.351245
         660     0.425406      0.459007
        1380     0.033274      0.740702
        1950     0.03067       0.676312
        2880     0.044364      0.5931
        3360     0.01188       0.395484
        4320     0.026087      0.206835
];
    xdata=mydata(:,1);
    ydata(:,1)=mydata(:,2);
    ydata(:,2)=mydata(:,3);

% Time span of the simulation
tspan = [0 4400]

%estimation of kinetic constants
k0 = zeros(2,1)
k0(1,1) = 0.001
k0(2,1) = 0.001

%x are the fitted parametrs
[k,resnorm] = lsqcurvefit(@myfun,k0,xdata,ydata)

%Solve problem
ode = @(t,y) kinet(t,y,k);
[t,y] = ode45(ode, tspan, y0);

plot(xdata,ydata(:,1),'ro',xdata,ydata(:,2),'bo',t,y(:,1),'r',t,y(:,2),'b')
xlabel('time')
ylabel('Concentrations')

konstants = k
```

Note 3. Program Code of the MATLAB routine for the multinomial distribution during ligand exchange reaction between $Au_{25}(2\text{-PET})_{18}$ (0,0) and BINAS and F-BINAS.

```
p = [0.06436 0.0667 0.86894];
n = 7;
reps = 10;
rng('default') % for reproducibility

    count1 = 1:n;
    count2 = 1:n;
    [x1, x2]= meshgrid(count1-1, count2-1);
    x3 = n-(x1 + x2);
    y = mnpdf ([x1(:), x2(:), x3(:)], repmat (p, (n)^2, 1));
    y = reshape (y,n,n);
    bar3 (y)
    set (gca, 'XTicklabel', 0:n);
    set (gca, 'YTicklabel', 0:n);
    xlabel ('BINAS Frequency')
    ylabel ('F-BINAS Frequency')
    zlabel ('probability Mass')
```

R-BINAS : 8F-R-BINAS= 1:4					
Probability (7 sites)	Ligand	32h	48h	72h	95h
P1	Normal BINAS	0.05578	0.095679	0.12532	0.12887
P2	Fluor BINAS	0.04734	0.0714	0.10707	0.12552
P3	2-PET	0.89688	0.832921	0.76761	0.74561

Note 4. Program Code of the MATLAB routine for the ligand exchange reaction between $Au_{25}(2\text{-PET})_{18}$ (0,0) and mixed R-BINAS and 8F-R-BINAS ligand. The abbreviations of species were consistent with Scheme 4.2.

Defined Kinetic file

```
function dydt = kinet(t,y,k)
dydt(1,1) = -[k(1,1)*y(1,1)]-[k(2,1)*y(1,1)];
dydt(2,1) = [k(1,1)*y(1,1)] - [k(3,1)*y(2,1)]-[k(4,1)*y(2,1)];
dydt(3,1) = [k(2,1)*y(1,1)] - [k(5,1)*y(3,1)]-[k(6,1)*y(3,1)];
dydt(4,1) = [k(3,1)*y(2,1)] - [k(7,1)*y(4,1)]-[k(8,1)*y(4,1)];
dydt(5,1) = [k(4,1)*y(2,1)] + [k(5,1)*y(3,1)]- [k(9,1)*y(5,1)]-[k(10,1)*y(5,1)];
dydt(6,1) = [k(6,1)*y(3,1)] - [k(11,1)*y(6,1)]-[k(12,1)*y(6,1)];
dydt(7,1) = [k(7,1)*y(4,1)];
dydt(8,1) = [k(8,1)*y(4,1)] + [k(9,1)*y(5,1)];
dydt(9,1) = [k(10,1)*y(5,1)] + [k(11,1)*y(6,1)];
dydt(10,1) = [k(12,1)*y(6,1)];
```

Defined function file

```
function F = myfun(k,xdata)
global ydata
global y0
tspan = [xdata];
ode = @(t,y) kinet(t,y,k);
[t,y] = ode45(ode, tspan, y0);
F=y;
```

Defined kinetic fitting file

```
clear all
type kinet
type myfun
global xdata
global ydata
global y0

% initial concentrations
y0 = zeros(10,1);
y0(1,1) = 1.0;
y0(2,1) = 0.0;
y0(3,1) = 0.0;
y0(4,1) = 0.0;
y0(5,1) = 0.0;
y0(6,1) = 0.0;
y0(7,1) = 0.0;
y0(8,1) = 0.0;
```

```
y0(9,1) = 0.0;
y0(10,1) = 0.0;

% import data from file "data2.txt"

mydata = importdata ('data3.txt')
    xdata=mydata(:,1);
    ydata(:,1)=mydata(:,2);
    ydata(:,2)=mydata(:,3);
    ydata(:,3)=mydata(:,4);
    ydata(:,4)=mydata(:,5);
    ydata(:,5)=mydata(:,6);
    ydata(:,6)=mydata(:,7);
    ydata(:,7)=mydata(:,8);
    ydata(:,8)=mydata(:,9);
    ydata(:,9)=mydata(:,10);
    ydata(:,10)=mydata(:,11);

% Time span of the simulation
tspan = [0 5700];

% estimation of kinetic constants
k0 = zeros(12,1);
k0(1,1) = 0.009;
k0(2,1) = 0.02;
k0(3,1) = 0.005;
k0(4,1) = 0.001;
k0(5,1) = 0.001;
k0(6,1) = 0.001;
k0(7,1) = 0.001;
k0(8,1) = 0.001;
k0(9,1) = 0.001;
k0(10,1) = 0.001;
k0(11,1) = 0.001;
k0(12,1) = 0.001;

% define lower and upper bounds
lb = [0,0,0,0,0,0,0,0,0,0,0,0]
ub = [1,1,1,1,1,1,1,1,1,1,1,1]

% solve problem
[k,resnorm,residual,exitflag,output,lambda,jacobian]                    =
lsqcurvefit(@myfun,k0,xdata,ydata,lb,ub);
ci = nlparci(k,residual,'jacobian',jacobian);
```

```
% generate kinetic curves with fitted parametrs
ode = @(t,y) kinet(t,y,k);
[t,y] = ode45(ode, tspan, y0);

% plot data
plot(xdata,ydata(:,1),'ro',xdata,ydata(:,2),'bo',xdata,ydata(:,3),'go',xdata,ydata(:,4),'ko',
xdata,ydata(:,5),'ro',xdata,ydata(:,6),'bo',xdata,ydata(:,7),'go',xdata,ydata(:,8),'ko',t,y(:,
1),'r',t,y(:,2),'b',t,y(:,3),'g',t,y(:,4),'k',t,y(:,5),'r',t,y(:,6),'b',t,y(:,7),'g',t,y(:,8),'k')
xlabel('time')
ylabel('Concentrations')

% prepare for output writing
kerr = [k,ci]
reswrite = [t,y]
inpwrite = [xdata,ydata]

% write to excel file
% sheet one: fited kinetics
% sheet two: input data
% sheet three: kinetic constants and 95% confidence intervals
xlswrite('results.xls', reswrite, 1, 'A1')
xlswrite('results.xls', inpwrite, 2, 'A1')
xlswrite('results.xls', kerr, 3, 'A1').
```

4.6 References

(1) Kim, M.; Cahill, J. F.; Su, Y.; Prather, K. A.; Cohen, S. M. *Chemical Science* **2012**, *3*, 126.

(2) Taddei, M.; Wakeham, R. J.; Koutsianos, A.; Andreoli, E.; Barron, A. R. *Angewandte Chemie International Edition* **2018**, *57*, 11706.

(3) Zheng, W.; Wang, W.; Jiang, S.-T.; Yang, G.; Li, Z.; Wang, X.-Q.; Yin, G.-Q.; Zhang, Y.; Tan, H.; Li, X.; Ding, H.; Chen, G.; Yang, H.-B. *Journal of the American Chemical Society* **2019**, *141*, 583.

(4) Amatore, C.; Lexa, D.; Savéant, J. M. *Journal of Electroanalytical Chemistry and Interfacial Electrochemistry* **1980**, *111*, 81.

(5) Hamlin, T. A.; Swart, M.; Bickelhaupt, F. M. *Chemphyschem* **2018**, *19*, 1315.

(6) Lund, T.; Lund, H. *Tetrahedron Letters* **1986**, *27*, 95.

(7) Templeton, A. C.; Hostetler, M. J.; Kraft, C. T.; Murray, R. W. *Journal of the American Chemical Society* **1998**, *120*, 1906.

(8) Song, Y.; Murray, R. W. *Journal of the American Chemical Society* **2002**, *124*, 7096.

(9) Donkers, R. L.; Song, Y.; Murray, R. W. *Langmuir* **2004**, *20*, 4703.

(10) Guo, R.; Song, Y.; Wang, G.; Murray, R. W. *Journal of the American Chemical Society* **2005**, *127*, 2752.

(11) Hostetler, M. J.; Templeton, A. C.; Murray, R. W. *Langmuir* **1999**, *15*, 3782.

(12) Wang, Y.; Bürgi, T. *Nanoscale Advances* **2021**, *3*, 2710.

(13) Rojas-Cervellera, V.; Raich, L.; Akola, J.; Rovira, C. *Nanoscale* **2017**, *9*, 3121.

(14) Heinecke, C. L.; Ni, T. W.; Malola, S.; Mäkinen, V.; Wong, O. A.; Häkkinen, H.; Ackerson, C. J. *Journal of the American Chemical Society* **2012**, *134*, 13316.

(15) Salassa, G.; Sels, A.; Mancin, F.; Bürgi, T. *ACS Nano* **2017**, *11*, 12609.

(16) Knoppe, S.; Dolamic, I.; Bürgi, T. *Journal of the American Chemical Society* **2012**, *134*, 13114.

(17) Varnholt, B.; Dolamic, I.; Knoppe, S.; Bürgi, T. *Nanoscale* **2013**, *5*, 9568.

(18) Yan, N.; Xia, N.; Wu, Z. *Small* **2020**, 2000609.

(19) Barrabés, N.; Zhang, B.; Bürgi, T. *Journal of the American Chemical Society* **2014**, *136*, 14361.

(20) Knoppe, S.; Azoulay, R.; Dass, A.; Bürgi, T. *Journal of the American Chemical Society* **2012**, *134*, 20302.

(21) Hossain, S.; Kurashige, W.; Wakayama, S.; Kumar, B.; Nair, L. V.; Niihori, Y.; Negishi, Y. *The Journal of Physical Chemistry C* **2016**, *120*, 25861.

(22) Fabbri, D.; Delogu, G.; De Lucchi, O. *The Journal of Organic Chemistry* **1993**, *58*, 1748.

(23) Sels, A.; Azoulay, R.; Buma, W. J.; Koenis, M. A. J.; Nicu, V. P.; Bürgi, T. *The Journal of Physical Chemistry C* **2019**, *123*, 22586.

(24) Wang, Y.; Nieto-Ortega, B.; Bürgi, T. *Chemical Communications* **2019**, *55*, 14914.

(25) Knoppe, S.; Dass, A.; Bürgi, T. *Nanoscale* **2012**, *4*, 4211.

(26) Molina, B.; Sánchez-Castillo, A.; Knoppe, S.; Garzón, I. L.; Bürgi, T.; Tlahuice-Flores, A. *Nanoscale* **2013**, *5*, 10956.

(27) Krishnadas, K. R.; Sementa, L.; Medves, M.; Fortunelli, A.; Stener, M.; Fürstenberg, A.; Longhi, G.; Bürgi, T. *ACS Nano* **2020**, *14*, 9687.

Chapter 5

Amplification of enantiomeric excess by dynamic inversion of enantiomers in deracemization of Au_{38} clusters

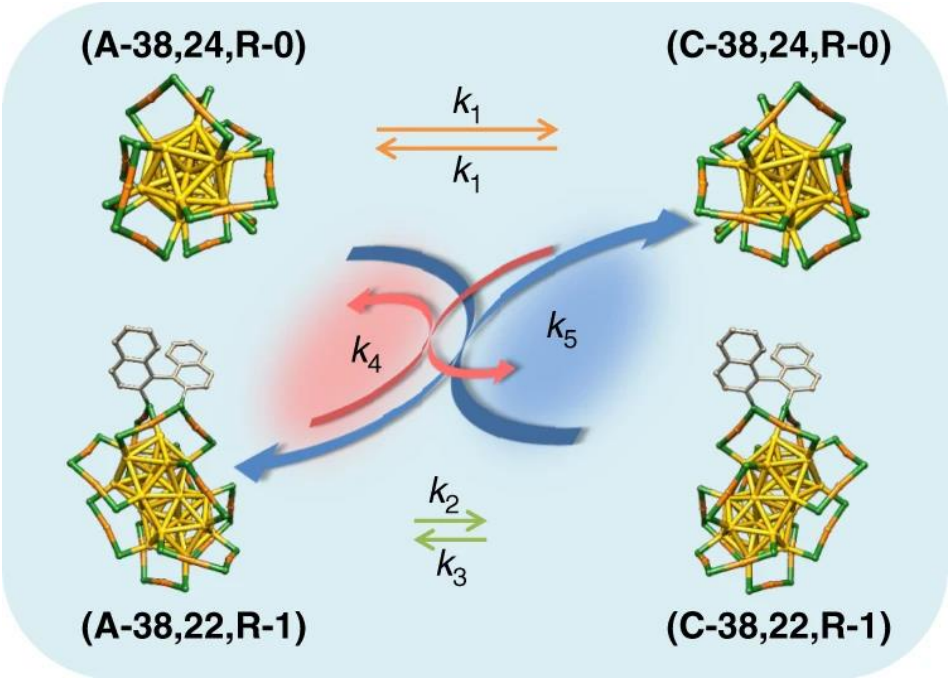

*The results described in this chapter were extracted from my own paper published in "Amplification of enantiomeric excess by dynamic inversion of enantiomers in deracemization of Au_{38} clusters" Y. Wang, B. Nieto-Ortega and T. Bürgi, Nat. Commun., 2020, 11, 4562.

5.1 Introduction

Chirality, which describes the symmetry properties of matter, is ubiquitous in nature[1,2] at very different length scales ranging from the very big down to the size of molecules. Many molecules of life, such as glucose, amino acid and DNA possess handedness, with tremendous consequences for example for the pharmaceutical industry, because enantiomers of a chiral molecule behave differently in a chiral environment. The development of chiral drugs[3] and catalysts[4], which afford high enantioselectivity therefore remains a central aspect of current chemical sciences. In addition, in the field of nanoscale materials, chirality significantly extends their application potential in optics (metamaterials) and materials science[5-8]. Chiral nanomaterials have therefore shifted in the centre of interest of many research groups[9-11].

Thiolate-protected gold nanoclusters $Au_m(SR)_n$, a special class of ultrasmall, atomically precise nanomaterials, have molecule-like and size-dependent properties which make them highly attractive for applications in fields like biology or catalysis, where chirality plays a central role. The preparation of chiral nanoclusters thus became an unremitting ambition in this field. Chirality in these systems can be imparted at different levels, as mentioned before in subchapter 1.5. Considering the general formula $Au_m(SR)_n$ chirality can be due to the ligands SR. Such chiral clusters can be prepared by direct synthesis using a chiral thiol[12]. Alternatively ligand exchange is a good method to incorporate chirality to achiral clusters. For example, ligand exchange on achiral $Au_{25}(SR)_{18}$ with chiral thiols (SR*), resulted in a series of chiral $Au_{25}(SR)_m(SR^*)_n$ clusters with chiroptical activity[13-16]. Alternatively, $Au_m(SR)_n$ can be intrinsically chiral due to a chiral metal core or due to the chiral arrangement of thiolates on the cluster surface. Of course, combinations of the different possibilities mentioned above are also possible, e.g. chiral ligand and chiral arrangement of the ligand. The $Au_{38}(GS)_{24}$ is an example of such a cluster (GS = glutathionate)[17]. In Au_{38} the ligands are chirally arranged on the surface of a symmetric gold core. $Au_{38}(SR)_{24}$ has six dimeric (-SR-Au-SR-Au-SR-) and three

monomeric staples (-SR-Au-SR-). The six dimeric staples are arranged in two propeller-like structures at the poles of the cluster. The two enantiomers of the cluster are described as A-$Au_{38}(SR)_{24}$ (anti-clockwise, left-handed) and C-$Au_{38}(SR)_{24}$ (clockwise, right-handed).

The chirality of the different structural elements (core, ligand arrangement, ligand) may not be independent of each other. In fact, it has been shown that the chirality of the Au_{38} cluster can be transferred to its ligands[18]. Specifically, the enantiomers of Au_{38}(2-PET)$_{24}$ (2-PET = 2-phenylethylthiolate) showed strong vibrational circular dichroism (VCD) signals in the 2-PET vibrations. 2-Phenylethylthiol is an achiral molecule without VCD activity. However, due to the interaction with the cluster, 2-PET adopts a chiral gauche conformation with preferential handedness. Put in other words: the cluster imposes its chirality onto the ligand. We reasoned whether the inverse could be possible as well namely that a chiral ligand imposes its chirality onto the cluster therefore leading to a deracemization of the cluster framework.

Deracemization[19,20] is the transformation of a racemic mixture into a nonracemic mixture by increasing the quantity of one enantiomer at the expense of the other. Due to the importance of enantiopure compounds in pharmaceutical industry and catalysis, in the past decades various deracemizational strategies were developed[19] and major works concentrated on using chemical reagents to separate or transform enantiomers[19,21-23]. In addition, recently many emerging technologies have also been developed to achieve this goal. Crystallisation of a racemic mixture is an effective approach to enrich one enantiomer by the formation of conglomerate crystals[24,25] or through spontaneous deracemization during crystallisation[26,27]. Futhermore, coherent laser light[28] and highly enantioselective enzymes[29] have been used for efficient deracemization. The development of deracemization strategies has brought tremendous impetus to the pharmaceutical and catalysis fields[3,19,30]. In contrast, the deracemization of gold nanoclusters, especially intrinsic chiral nanoclusters, has not been reported up to now.

The Au_{38} cluster seems an ideal candidate for such a study. The cluster enantiomers can be easily separated using chromatography[31] and the cluster racemizes at reasonably low temperature[32], which is also the basis for a deracemization imposed by the presence of a chiral ligand.

The activation barrier for the racemization of Au_{38}, 28.14±0.53 kcal mol^-1, is lower than the energy of a gold-sulfur bond[32]. This means that racemization takes place without complete Au-S bond breaking[32]. Very recently Häkkinen and coworkers proposed a mechanism for this inversion of the Au-S framework of $Au_{38}(2\text{-PET})_{24}$[33]. In this model no Au-S bonds are broken and the racemization proceeds via a rotational reconstruction of the metal core. Interestingly, after introducing of a rigid dithiolate, 1,1'-binaphthyl-2,2'-dithiol (BINAS), into the ligand shell of the cluster the racemization drastically slows down[34]. For example at 70 °C the racemization of $Au_{38}(2\text{-PET})_{22}(BINAS)_1$ is about 27 times slower compared to the parent cluster. Schematic potential energy diagrams are illustrated in Figure 5.1, where A and C (anti-clockwise, clockwise) describe the absolute configuration of the cluster Au-S framework.

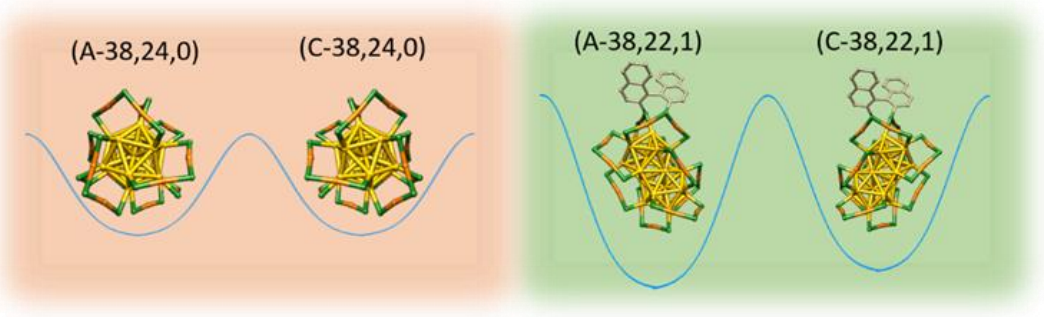

Figure 5.1 Potential energy curves of $Au_{38}(2\text{-PET})_{24}$ enantiomers and R-BINAS-substituted diastereomers. Color code: yellow, Au_{core}; orange, Au_{adatom}; green, S. The 2-PET ligand is omitted for clarity. The nomenclature described as follow: The anti-clockwise cluster with one R-BINAS and 22 2-PET ligands in its ligand shell will be called (A-38, 22, 1).

The inversion of the cluster is however not the only dynamic process of the system to be considered. In fact, thiolate-protected clusters can exchange ligands among each other upon collision[35], which has been shown for monothiol ligands. Here we further demonstrate such ligand exchange among clusters for a dithiol ligand. In the

following we show that indeed the chirality of a thiolate-protected gold cluster can be amplified by the presence of a chiral thiol in its ligand shell. The phenomenon relies on the dynamic nature of the clusters and we show that diastereospecific ligand exchange between clusters (in absence of free ligand) plays a crucial role.

5.2 Experimental

Chemicals and methods. All chemicals were purchased from commercial suppliers and used as received without any further treatment. R-BINAS was synthesized from BINOL as reported before[37,44]. Synthesis and size-selection of rac-$Au_{38}(2\text{-PET})_{24}$ clusters has been explained in subchapter 2.1 Protocol for synthesis of monodisperse gold nanoclusters. The measurements for UV-vis, CD, MALDI-TOF, HPLC characterization also been clarified in subchapter 2.3 Characterization of gold nanoclusters.

Ligand exchange reactions. Purified rac-$Au_{38}(2\text{-PET})_{24}$ and enantiopure R-BINAS were dissolved in toluene (1mg/mL) at a molar ratio of clusters to BINAS of 1:100. Ligand exchange was performed at room temperature. After reaction, the solution was concentrated and immediately passed over a size-exclusion column to remove the free ligands. The collected product was then ready for use in the HPLC experiments.

Simulation of kinetics. The kinetics of the system were simulated using MATLAB. The corresponding codes are shown in the Additional information. The rate constants for the racemization processes were taken from previous work[32,34].

5.3 Result and discussion

5.3.1 Characterization and Racemization of Au_{38} clusters

Rac-$Au_{38}(2\text{-PET})_{24}$ (racemic) clusters were synthesized and purified as reported[31]. The purification of *rac*-$Au_{38}(2\text{-PET})_{24}$ are proved by the related MALDI and UV-vis data. In chiral HPLC the sample showed two well-separated peaks with retention

times of 38 min and 81 min corresponding to the two enantiomers of the Au_{38} cluster (Fig. 5.2). The absolute configuration of the two enantiomers was successfully attributed using CD spectroscopy by comparison with calculated spectra[31]. The first (second) peak corresponds to the anti-clockwise A-$Au_{38}(SR)_{24}$ (clockwise C-$Au_{38}(SR)_{24}$) form of $Au_{38}(2\text{-PET})_{24}$.

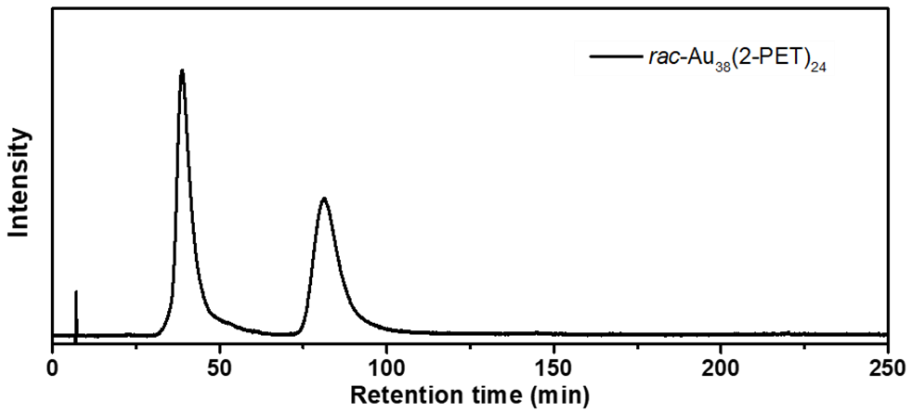

Figure 5.2 HPLC spectrum of rac-$Au_{38}(2\text{-PET})_{24}$ clusters.

R-BINAS was introduced via ligand exchange by mixing *rac*-$Au_{38}(2\text{-PET})_{24}$ and R-BINAS at molar ratio 1:100. The extent of ligand exchange depends on the reaction time. After some time the reaction mixture was passed over a size exclusion column to remove the free ligand. An example of the MALDI and HPLC data of the reaction mixture is shown in Figure 5.3. In addition to the first two peaks, which belong to the enantiomers of the $Au_{38}(2\text{-PET})_{24}$ cluster, several other peaks were observed in HPLC. Based on previous MALDI[34,36] (composition) and CD analysis (absolute configuraiton of the metal cluster)[31], those peaks in the chromatogram were assigned to different species containing R-BINAS in their ligand shell. We will use the following nomenclature to describe these species: The anti-clockwise cluster with one R-BINAS and 22 2-PET ligands in its ligand shell will be called (A-38, 22, R-1). Peaks at Fig. 5.3 B with retention time 107 min, 152 min and 270 min, are assigned to (A-38, 22, R-1), (C-38, 22, R-1) and (A-38, 20, R-2), respectively. We should mention that here R-BINAS was chosen as the chiral ligand because with S-BINAS the separation of the resulting cluster species in the chromatograms are not as good, which complicates quantitative analysis.

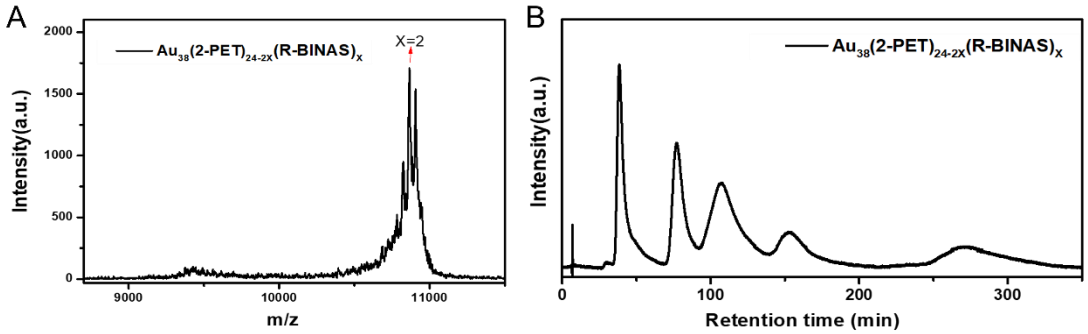

Figure 5.3 Characterization of Au_{38} clusters after ligand exchange reaction with R-BINAS. (A): MALDI-TOF signal. (B): HPL chromatogram.

We note that the ligand exchange was found to be diastereoselective[37]. Specifically, R-BINAS reacted with anti-clockwise cluster (A-38, 24, R-0) four times faster than with clockwise cluster (C-38, 24, R-0), as has been shown by analyzing the kinetics of the reaction. Therefore (A-38, 22, R-1) is more abundant than (C-38, 22, R-1) and (C-38, 24, R-0) is more abundant than (A-38, 24, R-0) after ligand exchange reaction[37], which directly evident from the HPLC data from Fig. 5.3 B of a sample after ligand exchange. The areas under the peaks reflects the relative abundances of the corresponding specises. For example, the ratio of (A-38, 22, R-1) to (C-38, 22, R-1) is around 3.1 derived from the integration of the two peaks at 107 and 152 min. However, ligand exchange does not affect the relative abundance of clockwise and anti-clockwise clusters in the system. The latter quantity can only be affected by an inversion of the Au-S framework.

Racemization is not the only process to be considered, as mentioned above. It has been shown that ligands can exchange between clusters even if no free ligands are present[35]. We therefore verified if R-BINAS can exchange between clusters. Experiments with $Au_{25}(2\text{-PET})_{18}$ and $Au_{38}(2\text{-PET})_{24-2x}(R\text{-BINAS})_x$ (average number of x = 2) were performed. The mixture of Au_{25} and Au_{38} was heated to 70°C for 24h followed by analysis by MALDI-TOF. Ligand exchange between the clusters was clearly evidenced by the observation of $Au_{25}(2\text{-PET})_{16}(R\text{-BINAS})_1$. Therefore ligand exchange between clusters has to be considered in the following discussion.

5.3.2 Deracemization of Au_{38} clusters.

For the deracemization studies, the sample after ligand exchange reaction and after removing any free ligand was heated to 70°C in toluene, and HPL chromatograms were recorded at different reaction times (up to 4 days) as illustrated in Fig. 5.4 in order to follow the evolution of the different species. 70°C was chosen because at this temperature racemization of the $Au_{38}(2\text{-PET})_{24}$ cluster is fast whereas inversion of the Au-S framework of $Au_{38}(2\text{-PET})_{22}(R\text{-BINAS})_1$ is slow. We note that the anti-clockwise (A) and clockwise (C) versions of the latter clusters are not true enantiomers but diastereomers, however, their Au-S framework have opposite absolute configuration. From Fig. 5.4 it is evident that the relative peak areas evolve with time. This is maybe most evident from the comparison of peaks 2 and 3, which change relative intensity. Most importantly, the relative intensity of peaks 3 and 4, belonging to (A/C-38, 22, R-1) species showed sign of a deracemization of the Au-S cluster framework.

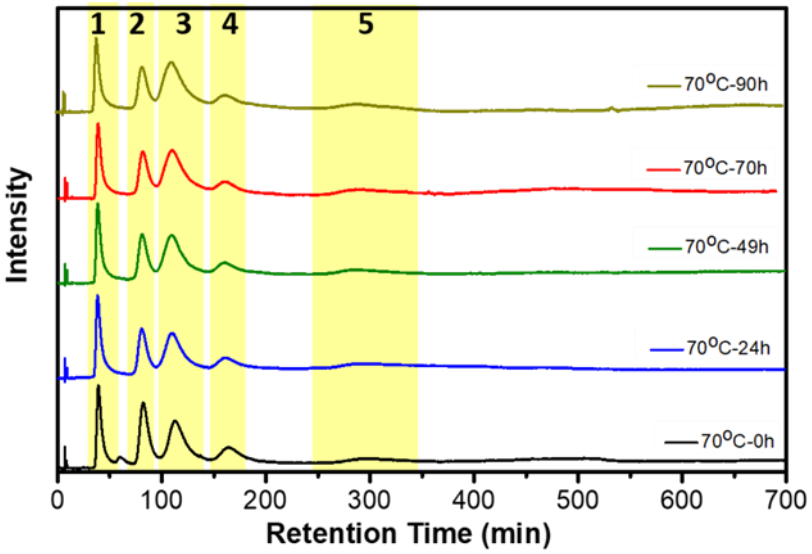

Figure 5.4 Exemplary HPL chromatograms. The sample was prepared by ligand exchange of rac-$Au_{38}(2\text{-PET})_{24}$ with R-BINAS, followed by removal of free ligands. On average the number of incorporated R-BINAS in this sample was $\bar{x}_{R-BINAS}$=0.514, as determined from the HPL chromatograms. The sample was then heated to 70 °C and chromatograms were measured as a function of time. The peaks are assigned as follows: Peak 1, (A-38, 24, R-0); Peak 2, (C-38, 24, R-0); Peak 3, (A-38, 22, R-1); Peak 4, (C-38, 22, R-1); Peak 5, (A-38, 20, R-2).

At the beginning of the experiment the anti-clockwise cluster (A-38, 22, R-1) was more abundant due to the diastereoselective ligand exchange during sample preparation. However, in the course of the experiment, in absence of free ligand, the abundance of this cluster with respect to its antipode (C-38, 22, R-1) further increased. The behaviour of the unexchanged A/C-$Au_{38}(2\text{-PET})_{24}$ cluster is different. Due to the diastereoselective ligand exchange[37], the clockwise version is more abundant at the beginning of the experiment. As expected, result from the fast racemization at 70°C, the relative abundance of the enantiomers approached a racemic mixture. Most importantly, the total abundance of anti-clockwise clusters in the system ((A-38, 24, R-0) + (A-38, 22, R-1)) increased with respect to the clockwise clusters ((C-38, 24, R-0) + (C-38, 22, R-1)). This ratio will be called A/C ratio in the following.

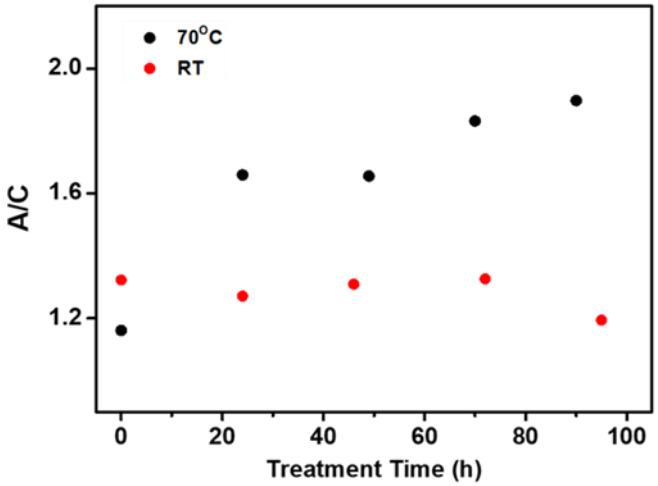

Figure 5.5 Ratio of anti-clockwise (A) to clockwise (C) clusters as a function of time at room temperature (red points, $\bar{x}_{R-BINAS}$=0.526) and at 70°C (black points, $\bar{x}_{R-BINAS}$=0.514). Concentrations of cluster species were derived from peak areas in HPL chromatograms. Anti-clockwise clusters (A): (A-38, 24, R-0) + (A-38, 22, R-1), clockwise clusters (C): (C-38, 24, R-0) + (C-38, 22, R-1).

The increase of the anti-clockwise (A) to clockwise (C) ratio of the clusters as a function of time is shown in Fig. 5.5. The black points correspond to the experiments performed at 70°C (data extracted from chromatograms shown in Fig. 5.4). The ratio increased from initially 1.16 to 1.90. For comparison the corresponding data is also shown for an experiment performed at room temperature (red points). As reflected in Fig. 5.5, The A/C ratio exhibited no obvious changes at room temperature. This

shows that the process can be initiated by adjusting the temperature. Further, the measurements also been carried out for Au_{38} clusters with lower average number of incorporated R-BINAS, the inversion also can be detected following heating.

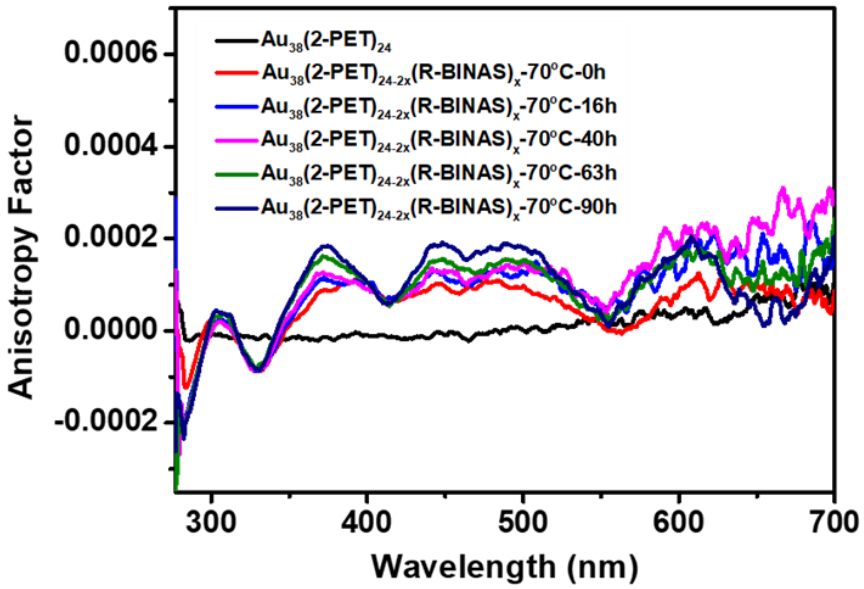

Figure 5.6 Anisotropy factors of $Au_{38}(SR)_{24}$ mixture during thermal treatment at different times. The clusters used have an average number of BINAS of $\bar{x}_{R-BINAS}$= 0.225.

Here, the UV-vis spectra of $Au_{38}(2\text{-}PET)_{24\text{-}2x}(R\text{-}BINAS)_x$ cluster mixture were measured after different heating times, and the related spectra exhibit the typical features of $Au_{38}(2\text{-}PET)_{24}$. This means the cluster is stable under these conditions and no significant decomposition was observed, in agreement with HPLC data, which do not give evidence for additional species formed. From recorded UV-vis and CD spectra, the concentration-independent anisotropy factors g=θ[mdeg] (32980xA)^-1 were calculated (Fig. 5.6). With longer heating time, the anisotropy factor of the sample increased. As the amount of R-BINAS was constant throughout the experiment, the increased chiroptical signals are derived from the combination of (1) the inversing of the Au-S cluster framework and (2) the changing distribution of R-BINAS on the two enantiomers in combination with the changes in the CD spectra induced by the presence of R-BINAS on the two enantiomers of the cluster. Since the chiroptical signal originating from the Au-S framework is expected to be more intense compared with the changes induced by the chiral ligand, the latter contribution to the optical activity may be minor but hinders quantitative analysis of the CD data[45].

5.3.3 BINAS content dependence of deracemization of Au_{38} clusters

A key parameter affecting the deracemization is the average number of R-BINAS ligands $\bar{x}_{R-BINAS}$ in the clusters, which was controlled by the ligand exchange time during the preparation of the sample. This number was determined from integrated areas of the first four peaks in the HPL chromatograms (species with x=0 and x=1). Au_{38} cluster samples with different average number of R-BINAS in their ligand shell then used as the starting material for deracemization experiments at 70°C. When the cluster with very low R-BINAS content of $\bar{x}_{R-BINAS} = 0.225$ after heating at 70°C up to 90h, the changes in the relative peak areas were very small. At higher R-BINAS content, for instance $\bar{x}_{R-BINAS} = 0.666$, obvious changes of the abundance of different cluster species during thermal treatment could be observed.

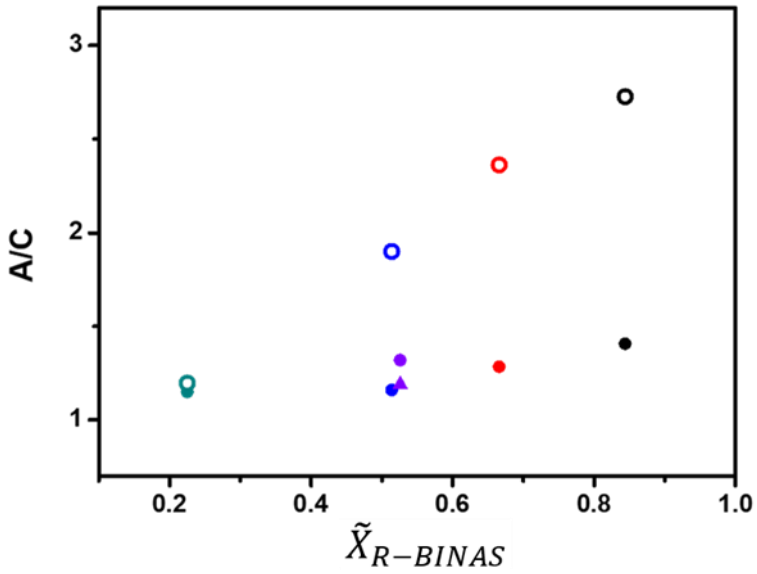

Figure 5.7 Dependence of A/C ratio on the average number of incorporated BINAS ligands $\bar{x}_{R-BINAS}$. Solid spots, before thermal treatment; hollow spots, after thermal treatment at 70oC for more than 70h. Color code: green, $\bar{x}_{R-BINAS}$=0.225; blue, $\bar{x}_{R-BINAS}$=0.514; red, $\bar{x}_{R-BINAS}$=0.666; black, $\bar{x}_{R-BINAS}$=0.844; violet, $\bar{x}_{R-BINAS}$=0.526 (triangle spot: sample kept at room temperature for 95h).

These experiments by showing the different A/C ratio at the beginning of the experiment and after thermal treatment as a function of R-BINAS content $\bar{x}_{R-BINAS}$ were summarizes in Fig. 5.7. From this plot it is clear that, irrespective of the R-BINAS content, the amount of anti-clockwise clusters increased during thermal

treatment. Furthermore, the clusters with higher $\bar{x}_{R-BINAS}$ expressed larger increases of the A/C ratio, which means a higher tendency of the Au-S framework to invert to the anti-clockwise form. Specially, for the experiment with the highest R-BINAS content ($\bar{x}_{R-BINAS} = 0.844$,) the final A/C ratio was 2.7 corresponding to an enantiomeric excess of 46%. This result illustrates that the driving force for the deracemization is related to the abundance of R-BINAS in the ligand shell of the Au_{38} cluster.

The experiments reveal an increase of (A-38, 22, R-1) even when this cluster is already in excess at the beginning of the experiment. These observations may partly be due to the inversion of (A/C-38, 22, R-1). However, ligand exchange reactions between clusters couples the two cluster populations (A/C-38, 24, R-0) and (A/C-38, 22, R-1), thus they are not independent from each other. A strong indication for this is the observation that the cluster without R-BINAS (A/C-38, 24, R-0) does not reach the racemic state even after long heating at 70°C. This is most evident from the experiments with high R-BINAS content.

5.3.4 Kinetic model of the dynamic system

In order to better understand the bahaviour of this dynamic system we simulated its kinetics using a model (see MATLAB code in the additional information). As elementary reactions we considered (1) the racemization of the $Au_{38}(2\text{-}PET)_{24}$ cluster, (2) the racemization of the Au-S framework of the $Au_{38}(2\text{-}PET)_{22}(R\text{-}BINAS)_1$ cluster and (3) the ligand exchange between clusters. Explicit chemical equations for the three reactions are given below and are schematically illustrated in Fig. 5.8:

$$A - Au_{38}(2-PET)_{24} \underset{k_1}{\overset{k_1}{\rightleftarrows}} C - Au_{38}(2-PET)_{24} \qquad (1)$$

$$A - Au_{38}(2-PET)_{22}(R-BINAS)_1 \underset{k_3}{\overset{k_2}{\rightleftarrows}} C - Au_{38}(2-PET)_{22}(R-BINAS)_1 \qquad (2)$$

$$A - Au_{38}(2-PET)_{22}(R-BINAS)_1 + C - Au_{38}(2-PET)_{24} \underset{k_5}{\overset{k_4}{\rightleftarrows}} C - Au_{38}(2-PET)_{22}(R-BINAS)_1 + A - Au_{38}(2-PET)_{24} \qquad (3)$$

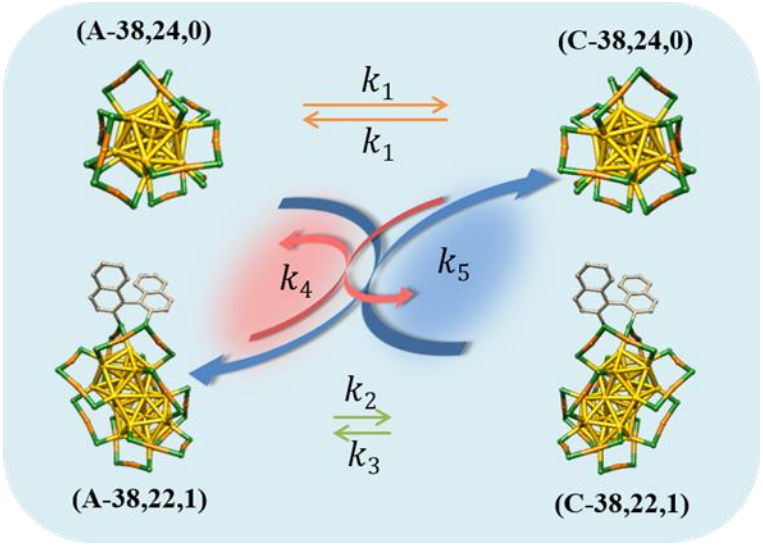

Figure 5.8 Schematics of the reactions, which are considedred in the dynamic system. The symbols k1 to k5 corresponded to the rate constant in the reactions.

From independent experiments[32,34] we know that k_1 is 27 times faster than k_2. We furthermore note that processes in Equation (3), ligand exchange between clusters, can be obtained by combining processes in Equation (1) and Equation (2), which means the five rate constants are not independent. Concretely, the ratio k_2 / k_3 is equal to k_4 / k_5. Importantly, the intercluster ligand exchange reactions (Equation (3)) do not change the global A/C ratio.

We used the data of the experiment with $\bar{x}_{R-BINAS} = 0.666$ as a reference for the modeling (Fig. 5.9 A). The time-dependent concentrations of the species in the experiment can be calculated. Note that the concentrations were referenced to the concentration of (A-38, 24, R-0), which was set to 1 at the beginning. Modeling was then done by taking into account the relative concentrations of the four clusters (A-38, 24, R-0), (C-38, 24, R-0), (A-38, 22, R-1) and (C-38, 22, R-1) at the beginning of the experiment as determined from the peak areas in the corresponding chromatograms as [1.0, 1.60, 3.37, 1.80]. The rate constants k_4 and k_5 were adjusted in order to reproduce the experimental data, whereas fixing k_1 and k_2 at the ratios given above. When setting $k_2 = k_3$ and $k_4 = k_5$, modeling was not able to reproduce the increase of the concentration of (A-38, 22, R-1) but readily produced racemic mixture. When setting $k_2 > k_3$ and $k_4 > k_5$, modeling produce the increase of the concentration of (C-38,

22, R-1) which is opposite with our observation. Only by setting $k_2 < k_3$ and $k_4 < k_5$, the increase of (A-38, 22, R-1) at the expense of (C-38, 22, R-1) could be modeled (Fig. 5.9 B). This means that the ligand exchange between clusters is diastereoselective, which is a critical point in this system. As mentioned above the ligand exchange does not alter the anti-clockwise/clockwise (A/C) ratio of the clusters in the system. However, we note that the reaction associated with rate constant k_5 produces (C-38, 24, R-0), which easily inverts to (A-38, 24, R-0) at 70°C and hence the combination of the diastereoselective ligand exchange and the fast inversion (racemization) of the (C-38, 24, R-0) cluster leads to the overall increase of the A/C ratio.

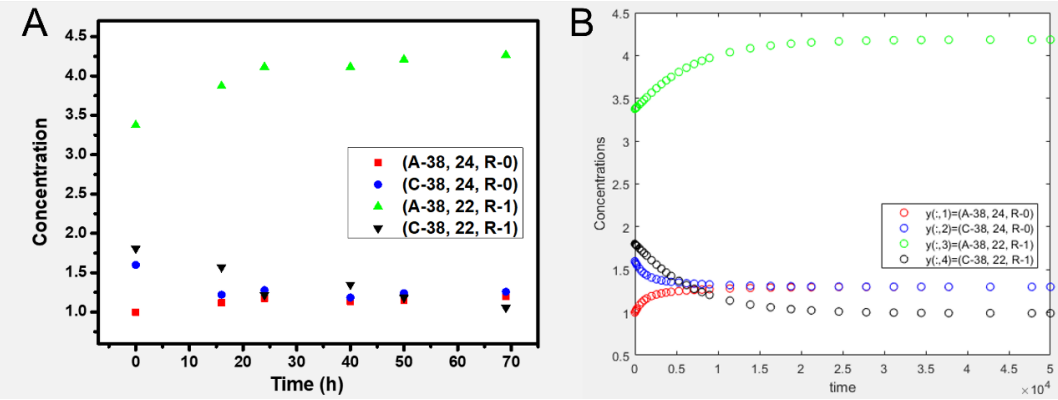

Figure 5.9 (A) Time-dependent concentrations of cluster species. The concentrations are relative to the initial concentration of (A-38, 24, R-0) which set as 1.0. The sample was heated to 70°C. The data extract from the reaction with cluster ($\bar{x}_{R-BINAS}$= 0.666). (B) Simulated time-dependent concentrations of cluster species using the kinetic model (k2<k3 and k4<k5). Initial concentrations are the same as the ones shown at A.

The reaction scheme considered here bears similarities to some known processes. For instance it is similar to a dynamic kinetic resolution[38-40], in which two enantiomers, which interconvert fast, react at different rates to form the corresponding products. In contrast to a conventional dynamic kinetic resolution, in our case the reactants (A/C-38, 24, R-0) react with the products of the other enantiomer (C/A-38, 22, R-1) in the diastereoselective process. Furthermore, this dynamic process is also similar to Viedma ripening, which is a solid-state method for the deracemization of racemic mixtures of crystalline compounds into single chirality, simply by continuously

grinding a suspension[41-43]. Viedma ripening has been used in deracemization of a varity of chiral compounds but not in the cluster field.

In order to gain further confidence in our modeling we then fixed the rate constants found to reproduce the time evolution of the cluster species in the experiment shown in Fig. 5.9 B and changed the initial concentrations in order to verify if the model correctly reproduces the experimentally observed increase (Fig. 5.7) of the overall A/C ratio with increasing R-BINAS content. The comparison of the final A/C ratios of the experiment and the simulations agree well (Fig. 5.10 A) and the simulations are able to reproduce the increase of the A/C ratio with increasing R-BINAS content. Our simulations indicate a ratio k_4 / k_5 (= k_2 / k_3) of 0.24.

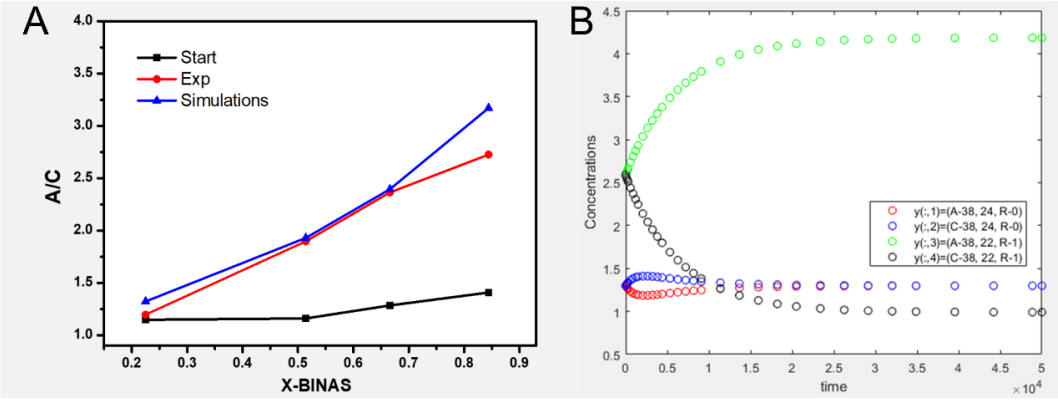

Figure 5.10 (A) Plot of final A/C ratio as a function of $\bar{x}_{R-BINAS}$. Black: experiment, before heating; red: experiment after heating to 70°C; blue: simulations. (B) Simulated time-depended concentrations of four cluster species. The R-BINAS content of the sample was the same as for the experiment and simulations shown in Fig. 5.9, however now starting from a mixture containing equal amounts of clockwise and anti-clockwise clusters.

It is worth to mention here that at elevated R-BINAS content there is evidence of doubly exchanged species (A-38, 20, R-2), peak 5 in the chromatograms. We did not try to include these species in the modeling as the number of reactions to consider would drastically increase. Instead we tried to keep the concentration of these species low by choosing low average R-BINAS content ($\bar{x}_{R-BINAS}$). Some of the discrepancies between experiment and simulations (Fig. 5.10 A) could therefore arise from neglecting higher exchanged species in the modeling. We also note that the initial overall A/C ratio is not exactly 1 at the beginnig of the experiments and slightly

increases with $\bar{x}_{R-BINAS}$. The exact reason for that is unknown, probably the processes described above take place slowly already during the preparation of the starting sample by ligand exchange.

We furthermore simulated a system that initially contained equal amounts of clockwise and anti-clockwise clusters. We used the same R-BINAS content as in the experiment shown in Fig. 5.9 A (simulation shown in Fig. 5.9 B). As shown in Fig. 5.10 B, the system deracemizes to basically the same final ratio A/C (A/C=2.395 in Fig. 5.9 B, and A/C=2.394 in Fig. 5.10 B). This shows that the important factor is the R-BINAS content in the system but not the initial A/C ratio.

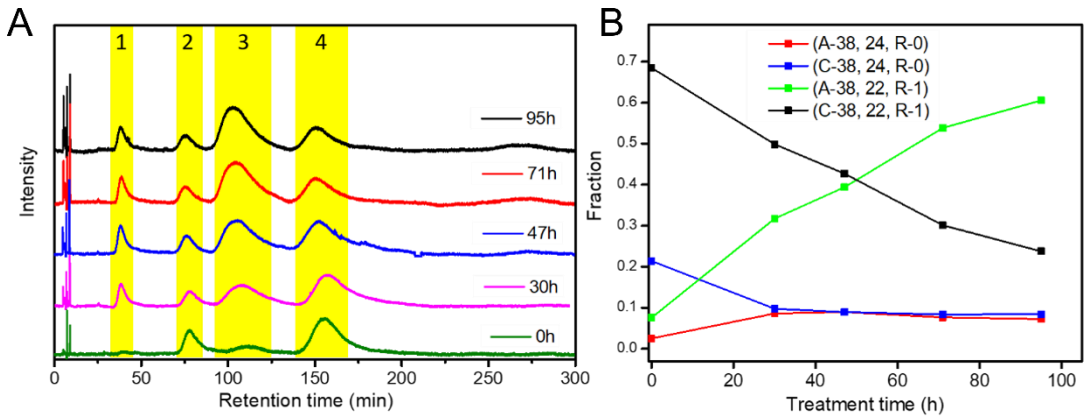

Figure 5.11 Experiment showing the conversion of clockwise to anti-clockwise clusters. HPL chromatograms (A) and evolution of different clusters species as a function of time (B). The sample was prepared by ligand exchange reaction of (C-38, 24, R-0) and R-BINAS. Some enantiopure cluster (C-38, 24, R-0), was added to adjust the average number of incorporated R-BINAS in the sample, which was $\bar{x}_{R-BINAS}$=0.76. The sample was then heated to 70 °C and chromatograms were measured as a function of time. The peaks are assigned as follows: Peak 1, (A-38, 24, R-0); Peak 2, (C-38, 24, R-0); Peak 3, (A-38, 22, R-1); Peak 4, (C-38, 22, R-1).

To further confirm the transformation of clockwise to anti-clockwise clusters, a sample was prepared that contained initially a high fraction of clockwise clusters (with $\bar{x}_{R-BINAS} = 0.76$). This sample was prepared by isolating (C-38, 22, R-1) and (C-38, 24, R-0) clusters by semipreparative HPLC. As the separation was not perfect some anti-clockwise clusters were also present and the initial A/C ratio was 0.11. The sample was then heated to 70 °C and HPL chromatograms were measured as a function of time (Fig. 5.11 A). The (A/C-38, 24, R-0) clusters reached a nearly

racemic state quite rapidly, as expected. In contrast the (A/C-38, 22, R-1) clusters changed from predominantly clockwise to predominantly anti-clockwise. After 95h heating, the A/C ratio increased to 2.11 (from 0.11) and continued increasing. The experiment clearly shows the predominance of anti-clockwise clusters in this dynamic system (Fig. 5.11 B).

In the dynamic situation described here, the interplay between diastereoselective intercluster ligand exchange and fast racemization of (A/C-38, 24, R-0) leads to amplification of the enantiomeric excess of the cluster (Au-S framework). This shows that the dynamic nature of these thiolate-protected gold clusters enables them to respond to changes in their environment (in the current example a chiral ligand) by shifting equilibria. This property may be of use for future applications for example, as shown here, to amplify enantiomeric excess.

5.4 Conclusion

In summary, we present the first successful deracemization of a thiolate-protected nanocluster. Mixtures of $Au_{38}(2\text{-PET})_{24}$ and $Au_{38}(2\text{-PET})_{22}(R\text{-BINAS})_1$ were prepared by ligand exchange reactions. The concentration of the four species in the system evolved with time at 70°C, leading to an accumulation of the anti-clockwise version of the $Au_{38}(2\text{-PET})_{22}(R\text{-BINAS})_1$ cluster, at the expense of the clockwise antipode. The overall excess of the anti-clockwise clusters in the system increased with increasing R-BINAS content in the system. Simulations of this dynamic process revealed that ligand exchange between clusters is diastereospecific and the resulting amplification of enantiomeric excess relies on the interplay between the ligand exchange and the racemization of the cluster. This means that the selectivity step (ligand exchange) and the step, which leads to the accumulation of anti-clockwise clusters (racemization), are separated. In general, our findings show that the interplay between different dynamic processes (racemization and ligand exchange), can lead to amplified phenomena at the nanoscale.

5.5 Additional information

5.5.1 HPL chromatograms of sample containing $Au_{38}(2\text{-PET})_{24}$ and R-BINAS substituted Au_{38}-derivatives with different BINAS contents.

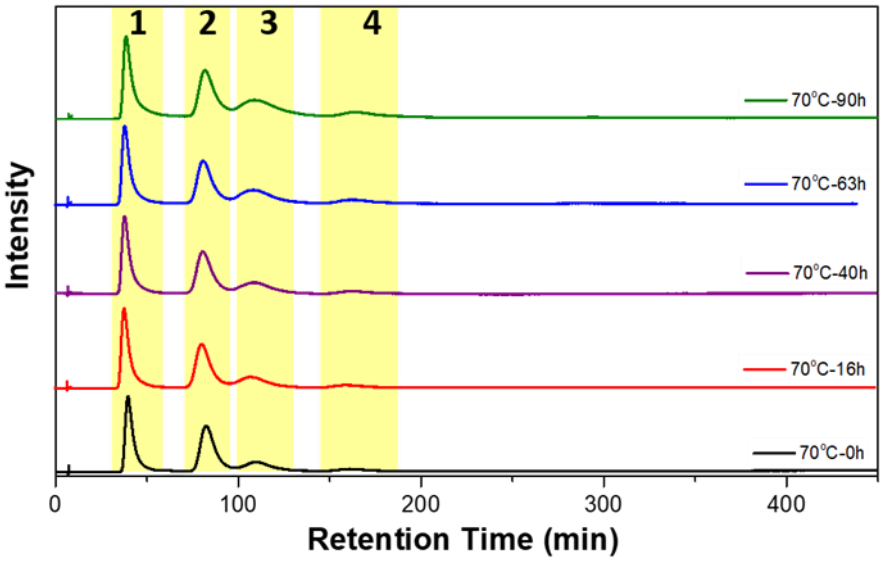

Figure 5.12 HPL chromatograms (0-450min) of a sample containing $Au_{38}(2\text{-PET})_{24}$ and R-BINAS-substituted Au_{38}-derivatives. The sample was heated to 70°C. The average number of BINAS per cluster was $\bar{x}_{R-BINAS}$= 0.225.

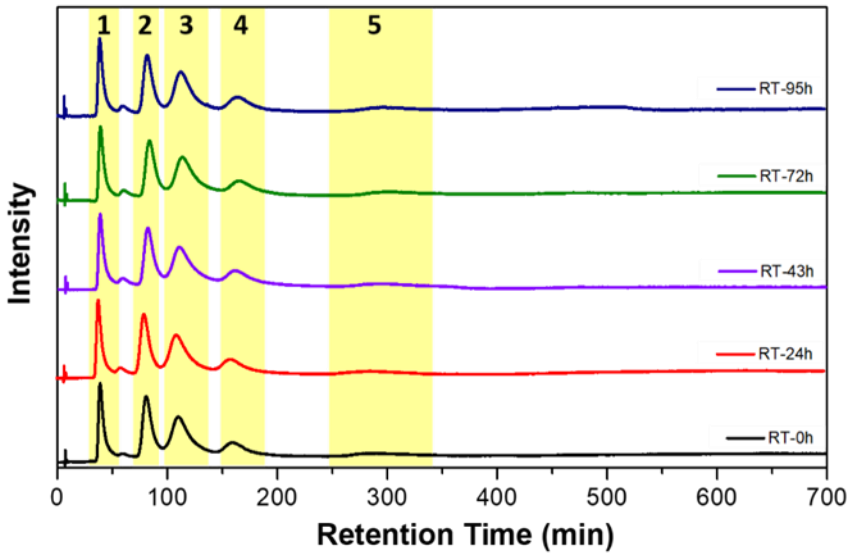

Figure 5.13 HPL chromatograms (0-700min) of a sample containing $Au_{38}(2\text{-PET})_{24}$ and R-BINAS-substituted Au_{38}-derivatives. The sample was kept at room temperature. The average number of BINAS per cluster was $\bar{x}_{R-BINAS}$= 0.526.

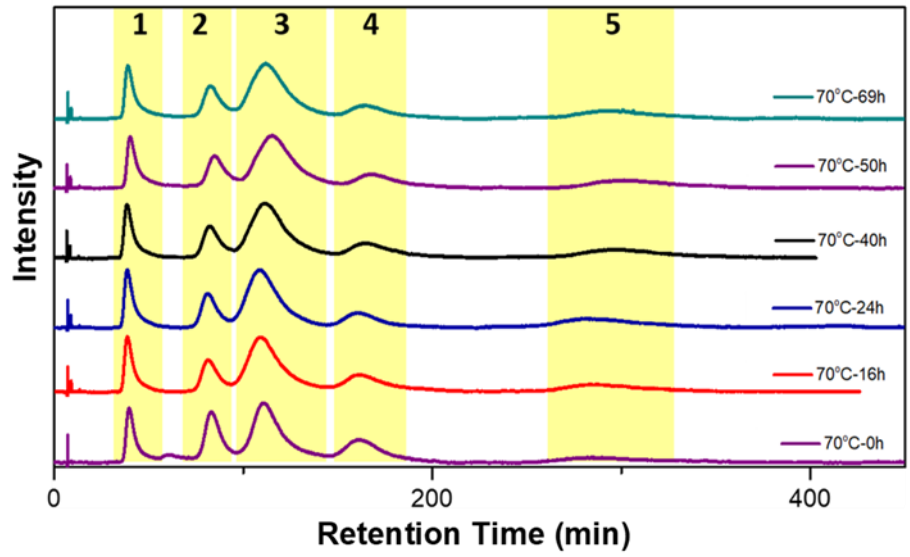

Figure 5.14 HPL chromatograms (0-450min) of a sample containing $Au_{38}(2\text{-PET})_{24}$ and R-BINAS-substituted Au_{38}-derivatives. The sample was heated to 70°C. The average number of BINAS per cluster was $\bar{x}_{R-BINAS}$= 0.666.

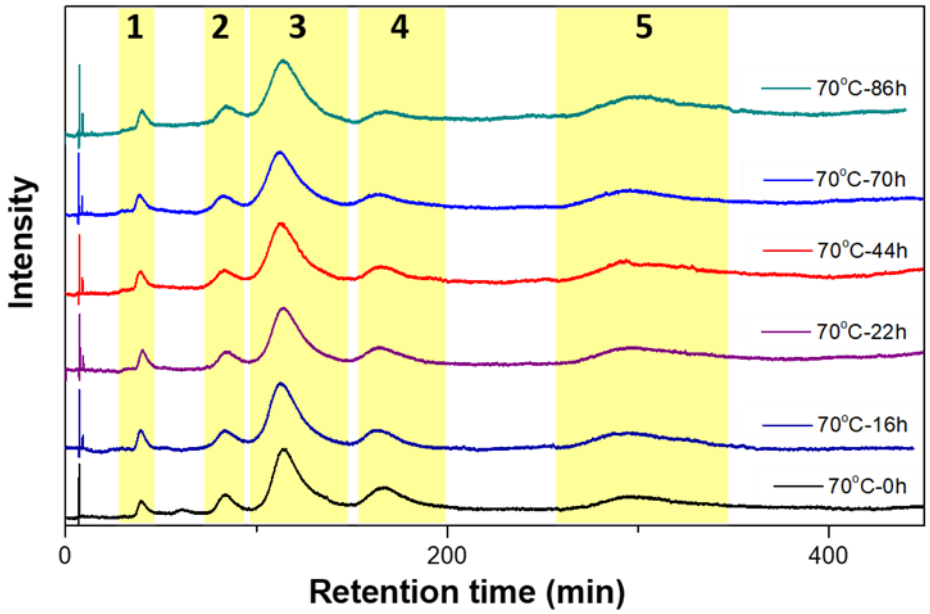

Figure 5.15 HPL chromatograms (0-450min) of a sample containing $Au_{38}(2\text{-PET})_{24}$ and R-BINAS-substituted Au_{38}-derivatives. The sample was heated to 70°C. The average number of BINAS per cluster was $\bar{x}_{R-BINAS}$= 0.844.

5.5.2 Kinetic model and MATLAB routine

$$A - Au_{38}(2-PET)_{24} \underset{k_1}{\overset{k_1}{\rightleftarrows}} C - Au_{38}(2-PET)_{24} \quad (1)$$

$$A - Au_{38}(2-PET)_{22}(R-BINAS)_1 \underset{k_3}{\overset{k_2}{\rightleftarrows}} C - Au_{38}(2-PET)_{22}(R-BINAS)_1 \quad (2)$$

$$A - Au_{38}(2-PET)_{22}(R-BINAS)_1 + C - Au_{38}(2-PET)_{24} \underset{k_5}{\overset{k_4}{\rightleftarrows}} C - Au_{38}(2-PET)_{22}(R-BINAS)_1 + A - Au_{38}(2-PET)_{24} \quad (3)$$

File 1: 'derac_mechanism.m'

```
function dC = derac_mechanism(t,C)

% User friendly variable names.
AR0 = C(1);
CR0 = C(2);
AR1 = C(3);
CR1 = C(4);

% Rate constants.
k1 = 0.000385;
k2 = 0.0000142;
k3 = 0.0000600;
k4 = 0.0000142;
k5 = 0.0000600;

% Rate laws.
r1 = k1*AR0;
r2 = k1*CR0;
r3 = k2*AR1;
r4 = k3*CR1;
r5 = k4*AR1*CR0;
r6 = k5*CR1*AR0;

% Mass balances.
dAR0 = -r1 + r2 + r5 – r6;
dCR0 = r1 - r2 – r5 + r6;
dAR1 = -r3 + r4 - r5 + r6;
dCR1 = r3 - r4 + r5 - r6;

% Assign output variables
dC(1,:) = dAR0;
dC(2,:) = dCR0;
dC(3,:) = dAR1;
```

```
dC(4,:) = dCR1;
```

File 2: ‘derac_runfile.m’

```
clear all

% Define initial concentrations.
C0 = [1.0, 1.598, 3.376, 1.8];

% Define time span.
tspan = [0, 50000];


% Run ODE solver.
[t, y] = ode15s(@derac_mechanism, tspan, C0);

%Plot.
plot(t, y(:,1),'ro',t ,y(:,2),'bo',t ,y(:,3),'go',t , y(:,4),'ko');
xlabel('time');
ylabel('Concentrations');
legend ({'y(:,1)=AR0','y(:,2)=CR0','y(:,3)=AR1','y(:,4)=CR1'},'Location','southeast');

% prepare for output writing

reswrite = [t,y];

% write to excel file
xlswrite('results.xls', reswrite, 1, 'A1');
```

5.6 References

(1) Blackmond, D. G. *Cold Spring Harb.* **2010**, *2*, a002147.

(2) Wagnière, G. H. *On Chirality and the Universal Asymmetry: Reflections on Image and Mirror Image*. **2007**, 256 (WILEY-VCH).

(3) Glunz, P. W. *Bioorg. Med. Chem. Lett.* **2018**, *28*, 53.

(4) Tang, X., He, H., Fang, X., Chang, Z. & Antilla, J. C. *Chirality* **2019**, *31*, 592.

(5) Collins, J. T. *et al. Adv. Opt. Mater.* **2017**, *5*, 1700182.

(6) Đorđević, L. *et al. Nat. Commun.* **2018**, *9*, 3442.

(7) Gautier, C. & Bürgi, T. *ChemPhysChem* **2009**, *10*, 483.

(8) Kumar, J. & Liz-Marzán, L. M. *Bull. Chem. Soc. Jpn.* **2019**, *92*, 30.

(9) Hao, C. *et al. J. Am. Chem. Soc.* **2019**, *141*, 1091.

(10) Sun, M. *et al. Nat. Commun.* **2018**, *9*, 4494.

(11) Chen, S., Tang, Z. & Xie, J. *Part. Part. Syst. Charact.* **2019**, *36*, 1900129.

(12) Zhu, M. *et al. Nano Lett.* **2011**, *11*, 3963.

(13) Si, S. *et al. J. Phys. Chem. C* **2009**, *113*, 12966.

(14) Knoppe, S., Kothalawala, N., Jupally, V. R., Dass, A. & Bürgi, T. *ChemComm.* **2012**, *48*, 4630.

(15) Kumar, S. & Jin, R. *Nanoscale* **2012**, *4*, 4222.

(16) Wang, Y., Nieto-Ortega, B. & Bürgi, T. *ChemComm.* **2019**, *55*, 14914.

(17) Schaaff, T. G. & Whetten, R. L. *J. Phys. Chem. B* **2000**, *104*, 2630.

(18) Dolamic, I., Varnholt, B. & Bürgi, T. *Nat. Commun.* **2015**, *6*, 7117.

(19) Palmans, A. R. A. *Mol. Syst. Des. Eng.* **2017**, *2*, 34.

(20) Pirkle, W. H. & Reno, D. S. *J. Am. Chem. Soc.* **1987**, *109*, 7189.

(21) Noyori, R. *Angew. Chem. Int. Ed.* **2002**, *41*, 2008.

(22) McKendry, R., Theoclitou, M.-E., Rayment, T. & Abell, C. *Nature* **1998**, *391*, 566.

(23) Lorenz, H. & Seidel-Morgenstern, A. *Angew. Chem. Int. Ed.* **2014**, *53*, 1218.

(24) Majumder, A. *Processes* **2018**, *6*, 247.

(25) Xiouras, C. *et al. Cryst. Growth Des.* **2018**, *18*, 3051.

(26) Yoshioka, R. *ChemInform* **2008**, *39*.

(27) Brands, K. M. J. & Davies, A. J. *Chem. Rev.* **2006**, *106*, 2711.

(28) Thomas, E. F. & Henriksen, N. E. *J. Chem. Phys.* **2019**, *150*, 024301.

(29) Prier, C. K., Zhang, R. K., Buller, A. R., Brinkmann-Chen, S. & Arnold, F. H. *Nat. Chem.* **2017**, *9*, 629.

(30) Amabilino, D. B. & Kellogg, R. M. *Isr. J. Chem.* **2011**, *51*, 1034.

(31) Dolamic, I., Knoppe, S., Dass, A. & Bürgi, T. *Nat. Commun.* **2012**, *3*, 798.

(32) Knoppe, S., Dolamic, I. & Bürgi, T. *J. Am. Chem. Soc.* **2012**, *134*, 13114.

(33) Malola, S. & Häkkinen, H. *J. Am. Chem. Soc.* **2019**, *141*, 6006.

(34) Knoppe, S., Michalet, S. & Bürgi, T. *J. Phys. Chem. C* **2013**, *117*, 15354.

(35) Salassa, G., Sels, A., Mancin, F. & Bürgi, T. *ACS Nano* **2017**, *11*, 12609.

(36) Dass, A., Stevenson, A., Dubay, G. R., Tracy, J. B. & Murray, R. W. *J. Am. Chem. Soc.* **2008**, *130*, 5940.

(37) Knoppe, S., Azoulay, R., Dass, A. & Bürgi, T. *J. Am. Chem. Soc.* **2012**, *134*, 20302.

(38) Wang, Y. *et al. J. Am. Chem. Soc.* **2016**, *138*, 3278.

(39) Qian, H., Zhu, Y. & Jin, R. *ACS Nano* **2009**, *3*, 3795.
(40) Jin, R. *Nanoscale* **2015**, *7*, 1549.
(41) Iggland, M. & Mazzotti, M. *Cryst. Growth Des.* **2011**, *11*, 4611.
(42) Viedma, C. *Phys. Rev. Lett.* **2005**, *94*, 065504.
(43) Sögütoglu, L.-C., Steendam, R. R. E., Meekes, H., Vlieg, E. & Rutjes, F. P. J. T. *Chem. Soc. Rev.* **2015**, *44*, 6723.
(44) Fabbri, D., Delogu, G. & De Lucchi, O. *J. Org. Chem.* **1993**, *58*, 1748.
(45) Knoppe, S., Dass, A. & Bürgi, T. *Nanoscale* **2012**, *4*, 4211.

Chapter 6

Absolute configuration retention of a configurationally labile ligand during dynamic processes of thiolate protected gold cluster

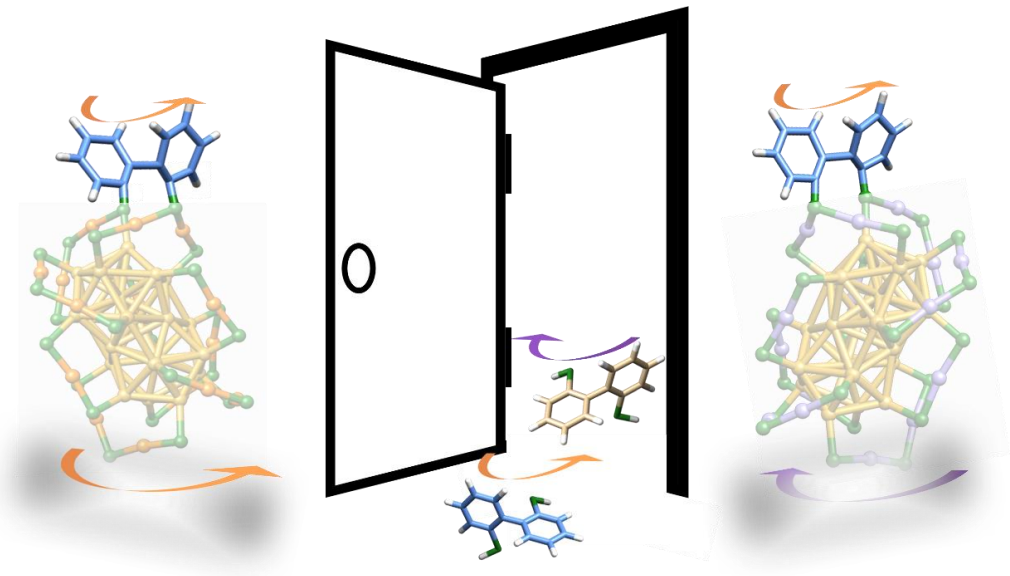

*The results described in this chapter were extracted from my own paper published in "Absolute configuration retention of a configurationally labile ligand during dynamic processes of thiolate protected gold clusters"- Y. Wang, E. Makkonen, X. Chen, T. Bürgi, Chem. Sci., 2021,12, 9413-9419.

6.1 Introduction

Precise gold nanoclusters, as kind of materials with well-defined composition and structure, have attracted wide interest during the past decades[1-3]. Up to now, examples such as $Au_{25}(SR)_{18}$, $Au_{38}(SR)_{24}$, $Au_{40}(SR)_{24}$, $Au_{102}(SR)_{44}$ and $Au_{140}(SR)_{60}$ (SR stands for thiolate) have already become excellent candidates as catalyst[4,5], as optical active materials[6,7], for chemical sensing[8,9], and biological applications[10,11]. Preparation of $Au_n(SR)_m$ nanoclusters is normally done through direct synthesis using neutral and anionic thiolate ligands[12]. However, due to the low solubility and steric and electrostatic effects, some ligands cannot be used in direct synthesis, which severely limits the diversity of surface properties of the accessible clusters[13,14].

Ligand exchange reactions (LERs), which introduce new ligands to the parent nanoclusters[15-20], are widely applied for adding functionalities or chemical properties to clusters as a versatile post-modification method[14,21]. This methodology drastically extends the possibilities to attain the required surface properties without changing the metal core structure[14]. Up to now, these dynamic exchange processes were mostly investigated with $Au_{25}(SR)_{18}$ and $Au_{38}(SR)_{24}$ clusters[22,23], which benefit from simple synthesis and stability. $Au_{25}(SR)_{18}$ cluster has an icosahedral Au_{13} core surrounded by six dimeric SR-Au-SR-Au-SR staple units[18,20,24-27]. $Au_{38}(SR)_{24}$ has an elongated structure with three monomeric SR-Au-SR staples at the equator of the cluster and three dimeric staples at each pole[28]. The SR groups in one dimeric staple can be classified into terminal SR groups, which are linked to the gold core, and central SR group[29]. Owing to the geometry of these clusters, the SR groups in staples possess different chemical environment, thus there exist preferential exchange sites during LERs[17,20, 22,30].

Experimental and computational studies for $Au_{25}(SR)_{18}$ and $Au_{38}(SR)_{24}$ clusters indicate that LERs start preferentially at the terminal SR groups[20,29,30], which

are directly bound to the metal core, via an associative S_N2-like mechanism[17]. Negishi and co-workers also found that Pd doping of $Au_{25}(SR)_{18}$ drastically increases the rate of ligand exchange reaction[25]. Dass and co-workers systematically studied LERs with aliphatic dithiol ligands HS-$(CH_2)_n$-SH with various chain length n[31]. They documented that C3 and C4 prefer interstaple coupling, and C5 and C6 are good candidates for intrastaple binding, whereas C2 is too short for the bidentate binding. In addition to aliphatic ligands, aromatic dithiols also have been used for LERs, such as 1,1'-binaphthalene-2,2'-dithiol (BINAS), which is a chiral rigid ligand, which we already mentioned before[18,32]. Experimental and theoretical studies of Au_{25} and Au_{38} clusters[18,32-35] show that the bidentate ligand connects preferentially to two neighboring staples thus forming a bridge between the latter[32]. Furthermore, the LER Between the R-BINAS and intrinsically chiral Au_{38} is diastereoselective which has been revealed by in-situ HPL chromatography[28].

Apart from the ligand exchange reaction via free thiols, it has been shown that ligands can exchange between clusters in the absence of free thiols. In 2013 the intercluster LERs between $Au_{25}(SC_{10}H_{21})_{18}$ and $Au_{25}(SC_{12}H_{25})_{18}$ was observed and the authors assumed that this exchange resulted from the detachment of ligand or gold-ligand species from the cluster[25]. Later, Salassa and co-workers carried out ligand exchange between $Au_{25}(SBut)_{18}$ and $Au_{25}(2\text{-PET})_{18}$ (2-PET: 2-phenylethylthiolate, a monothiol) at room temperature. Their results indicated that the exchange proceeds in a cluster collision mechanism without release of free thiol or thiol-gold complex from the cluster[13].

As we confirmed from last chapter, the bidentate ligands exchange between clusters by observing the mass peak belonging to $Au_{25}(2\text{-PET})_{16}(R\text{-BINAS})_1$ after mixing $Au_{38}(2\text{-PET})_{24-2x}(R\text{-BINAS})_x$ and $Au_{25}(2\text{-PET})_{18}$ clusters at 70^{o}C for 24 hours[36]. This study also showed that higher temperatures are needed for the intercluster ligand exchange with dithiols compared to monothiols. In addition, it has been shown that the intercluster BINAS exchange between

chiral $Au_{38}(SR)_{24}$ clusters is diastereoselective. This, together with fast racemization of $Au_{38}(2\text{-PET})_{24}$, led to an amplification of the enantiomeric excess of the cluster[36]. Au_{38} clusters can racemize in solution[37]. Experimental activation energies show that this process proceeds without complete Au-S bond breaking[37]. Recent calculations indicate that this racemization involves a concerted rotation of three gold atoms of the core, which drag along the staples[38]. After addition of BINAS dithiol to the ligand shell the racemization is still observed experimentally, however at considerably higher temperatures[34].

There are still many open questions concerning intercluster ligand exchange reaction and racemization, especially when dithiol ligands are involved. Here we use a new bidentate ligand biphenyl-2,2'-dithiol (in the following R/S-BiDi for short) as a molecular probe in order to shed some more light on these processes. Compared with BINAS, which has a rigid structure, R/S-BiDi is more flexible owing to the small steric hindrance of the two benzene rings and therefore R/S-BiDi racemizes rapidly in solution. It can therefore be used as a probe to test whether, during the dynamic cluster processes (exchange and racemization) the ligands are confined or not. In the latter case, we may expect a racemization of the R/S-BiDi ligand during these processes.

6.2 Experimental

Chemicals and methods. All chemicals were purchased from commercial suppliers and used as received without any further treatment. Biphenyl-2,2'-dithiol (BiDi) was synthesized from the biphenyl-2,2`-diol following the protocol for synthesis of BINAS reported before[39]. Synthesis, size-selection and separation of the two enantiomers of rac-$Au_{38}(2\text{-PET})_{24}$ clusters has been explained in subchapter 2.1 Protocol for synthesis of monodisperse gold nanoclusters. The measurements for UV-vis, CD, MALDI-TOF, HPLC characterization also been clarified in subchapter 2.3 Characterization of gold nanoclusters.

Ligand exchange reactions with free BiDi. Purified rac-Au_{38}(2-PET)$_{24}$, A-Au_{38}(2-PET)$_{24}$ and C-Au_{38}(2-PET)$_{24}$, respectively were mixed with BiDi in toluene (cluster concentration 1mg/mL) at a molar ratio of cluster to free ligand of 1:50[28,40]. Ligand exchange was performed at room temperature. After reaction, the solution was concentrated and immediately passed over a size-exclusion column to remove the free ligands. The collected product was then ready for use in the HPLC experiments.

Thermal treatment of Au_{38}. The collected Au_{38} clusters with one BiDi in its ligand shell was concentrated to 10 mg/mL, heated in an oil bath to 70ºC, and injected to HPLC after various times.

Density Functional Theory (DFT) Calculations. In this work, we applied the GPAW software package[41] to do all the calculations. PBE functional[42,43] was used for the exchange-correlation energy, and the van der Waals interactions were described by the Tkatchenko-Scheffler model[44]. The clusters and ligand molecules were placed into a rectangle unit cell with an 8 Å vacuum extension in each dimension from the edge of the molecule or the cluster. Per atom, the electronic configuration of valence electrons is H($1s_1$), C($2s_2$ $2p_2$), S($3s_2$ $3p_4$) and Ag($4d_{10}$ $5s_1$). The remaining electrons were treated as a frozen core. The default PAW dataset package 0.9.20000 was used for all the atoms. The 2-PET ligands were replaced by $HSCH_3$ in all the calculations.

The structure optimizations were done using the GPAW grid mode. The real-spacing was chosen as h=0.2 Å. For geometry optimizations, the geometry was converged when the maximum residual force was below 0.05 eV/Å. The racemization energy barrier of BiDi molecule was calculated by the nudged elastic band (NEB) method[45]. The barrier was computed by PBE+TS[46,47].

The CD spectra were simulated by the real-time-propagation time-dependent density functional theory (RT-TDDFT) method implemented in GPAW with localized basis sets (LCAO) [48]. In the LCAO mode, the default GPAW double-zeta polarized (dzp) basis sets were used for C, H, S, while the optimized double-zeta basis set (so-called

"p-valence" basis set) was used for Ag atoms. The real-spacing h=0.3 and vacuum size 8 Å were chosen for the RT-TDDFT calculations. The XYZ coordinates of all the structures mentioned in this study are included in the Additional information.

6.3 Results and discussion

As one prominent example of an intrinsically chiral cluster, Au_{38}(2-PET)$_{24}$ has been used for many studies. The cluster is easily prepared and stable. Following a previous report[1], rac-Au_{38}(2-PET)$_{24}$ was synthesized and purified. The purity of the cluster was demonstrated by UV-Vis spectra and MALDI-TOF mass spectra as mentioned before. R/S-BiDi was prepared analogously to BINAS starting from the biphenyl-2,2`-diol[39]. Compared with BINAS, biphenyl-2,2'-dithiol (R/S-BiDi) is more flexible due to the lower steric hindrance as shown in Fig. 6.1 A. We optimized R/S-BiDi structures with different dihedral angles of the carbon rings by Density Functional Theory (DFT) with PBE+TS functional and found that R/S-BiDi has two global minimum structures with the dihedral angles 91.45° and 268.36°, corresponding to the two enantiomers (Fig. 6.1 B). We also mentioned the dihedral angles may change after link on the surface of clusters. In order to estimate the barrier for interconversion between the two enantiomers (racemization), nudged elastic band (NEB) calculations were performed (Fig. 6.1 B) [45]. The racemization barrier for R/S-BiDi is about 0.69 eV (16 kcal/mol), which is less than the barrier (23 kcal/mol) to undergo torsional isomerization of other biphenyl derivatives[49,50]. The corresponding rate constant k can be estimated from the Arrhenius formula $k = A\ \exp(-E_a/k_BT)$. If we use typical molecular vibrational frequency 10^{13} to 10^{14} s^{-1} as A, the constant k of R/S-BiDi is around 26 s^{-1} to 256 s^{-1} at T=300 K. In conclusion, R/S-BiDi racemizes fast at room temperature and the enantiomers are therefore not separable. As expected free R/S-BiDi ligand does not show CD signals and the absorption spectrum of

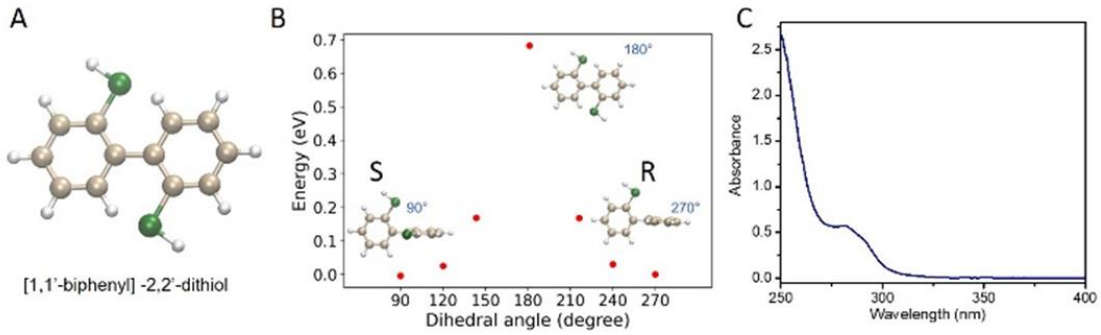

Figure 6.1 Characterization of [1,1`-biphenyl]-2,2`-dithiol. (A) Structure of [1,1`-biphenyl]-2,2`-dithiol. Color code: tan: C atoms, white: H atoms and green: S atoms. (B) Calculated energies for BiDi configuration at different dihedral angles. (C) UV-Vis spectrum of BiDi ligand in dichloromethane.

R/S-BiDi is characterized by a peak at 280 nm with a shoulder at 295 nm (Fig. 6.1 C). R/S-BiDi was introduced to the $Au_{38}(2\text{-PET})_{24}$ clusters by ligand exchange reactions, and the evolution of the process was followed by HPL chromatography. As we illustrated on last chapter, rac-$Au_{38}(2\text{-PET})_{24}$ showed two well-defined peaks with retention times of 38 min (anti-clockwise, A) and 78 min (clockwise, C) in chiral HPLC. Under the same conditions the free ligand R/S-BiDi eluted at retention time of 10 min.

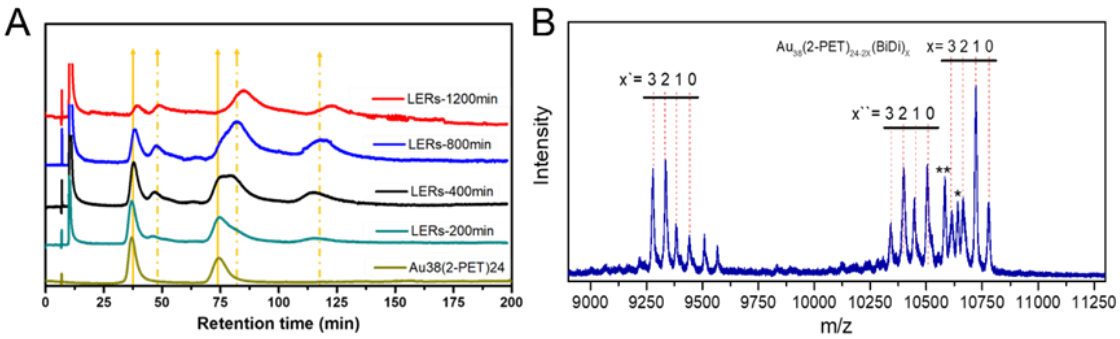

Figure 6.2 Characterization of the rac-$Au_{38}(2\text{-PET})_{24}$ during ligand exchange reaction with BiDi. (A) HPL Chromatograms. The sample was put at room temperature and solid arrows indicate the two enantiomers of $Au_{38}(2\text{-PET})_{24}$ and dashed arrows indicate the new peaks. (B) MALDI-TOF spectrum of ligand exchange reaction between rac-$Au_{38}(2\text{-PET})_{24}$ and BiDi, at room temperature for 18 hours. The $Au_{38}(2\text{-PET})_{24\text{-}2x}(BiDi)_x$ species are marked with different values of x, and the related fragments $Au_{34}(2\text{-PET})_{20\text{-}2x`}(BiDi)_{x`}$ after release of $Au_4(2\text{-PET})_4$ are also visible, as the signal at 9442.1 (x`=0) corresponds to $Au_{34}(2\text{-PET})_{20}$ (calculated mass 9441.5). In addition, the fragement $Au_{38}(2\text{-PET})_{22\text{-}2x``}(BiDi)_{x``}$ after release two 2-PET ligand also marked, as the signal at 10506.6 (x``=0) corresponds to $Au_{38}(2\text{-PET})_{22}$ (calculated mass 10503.9). The signal at 10641.28 (*) corresponds to $Au_{38}(2\text{-PET})_{23}$ (calculated

mass 10641.15), the signal at 10583.26 (**) corresponds to $Au_{37}(2\text{-PET})_{24}$ (calculated mass 10581.41).

For the ligand exchange reactions, rac-$Au_{38}(2\text{-PET})_{24}$ was mixed with free R/S-BiDi at molar ratio 1:50. The sample was kept at room temperature and analysed by HPLC every 200 minutes. The time-resolved chromatograms (Fig. 6.2 A) show that after 200 min new peaks arise at 48 min, 83 min and 120 min, whereas the two peaks from parent cluster decreased with increasing reaction time. We anticipated that the new peaks originate from clusters with one ligand exchange, $Au_{38}(2\text{-PET})_{22}(R/S\text{-BiDi})_1$, which is confirmed by the MALDI-TOF mass spectrum of a sample taken at 18h (Fig. 6.2 B).

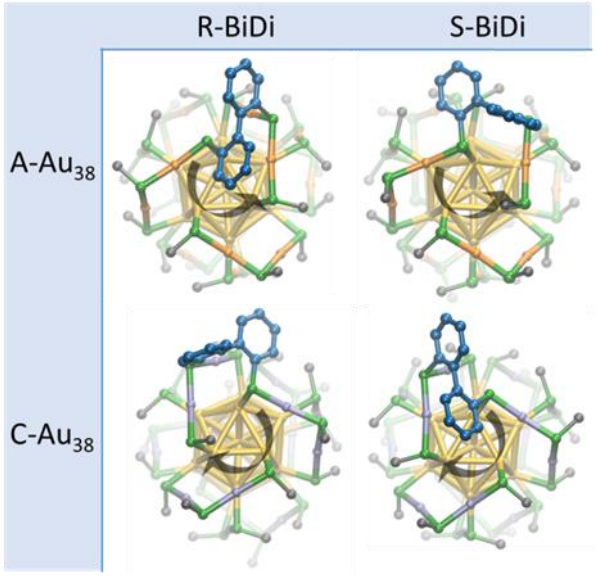

Figure 6.3 Structures of $Au_{38}(SR)_{24}$ with one BiDi adsorbed. Different atoms are depicted in gray (C atom), golden (Au atom), and green (S atom) colors. The color of the gold atoms in staples of clockwise (anti-clockwise) clusters, which named as C-Au_{38} (A-Au_{38}) is violet (orange) and the color of C atom in R/S-BiDi is cornflower blue. H-atoms been emitted. The four structures above are named as A-Au_{38}-R-BiDi (left-top), A-Au_{38}-S-BiDi (right-top), C-Au_{38}-R-BiDi (left-bottom), and C-Au_{38}-S-BiDi (right bottom).

In view of this composition after ligand exchange, each enantiomer of $Au_{38}(2\text{-PET})_{24}$ may be substituted with one of the two enantiomers of R/S-BiDi, resulting in four stereoisomers as shown in Fig. 6.3. Here we assume that R/S-BiDi prefers the same adsorption site as BINAS (bridging two dimeric staples, see Fig. 6.3), which seems reasonable given the structural similarity of

the two molecules. Note that once adsorbed, the R/S-BiDi molecule cannot easily racemize anymore. Due to peak overlap only three out of the four possible $Au_{38}(2\text{-PET})_{22}(R/S\text{-BiDi})_1$ stereoisomers are clearly observed in the chromatogram (Fig. 6.2 A), which hinder further analysis.

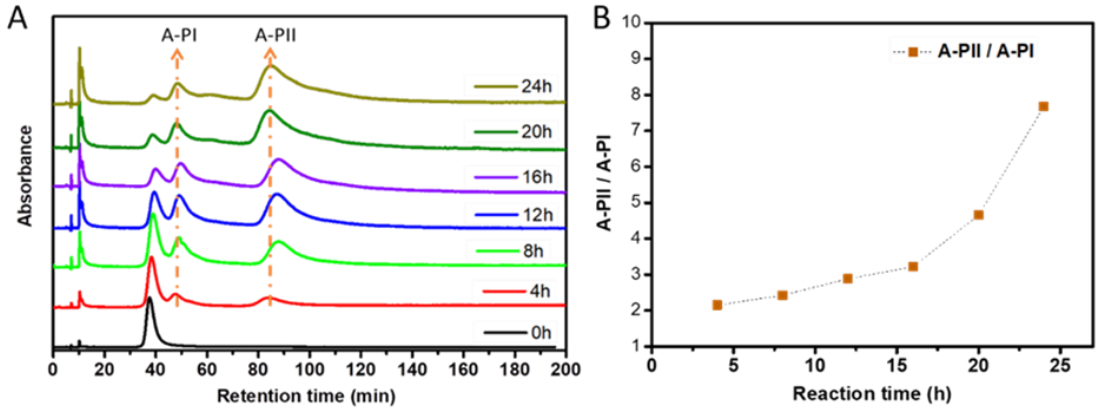

Figure 6.4 Characterization of A-$Au_{38}(2\text{-PET})_{24}$ ligand exchange with BiDi. (A) Evolution of chiral HPL chromatogram during ligand exchange reaction between A-$Au_{38}(2\text{-PET})_{24}$ and R/S-BiDi. The sample was at room temperature and the chromatogram has been recorded every 4 hours. Two main peaks are marked as A-PI (48min) and A-PII (83min). (B) Plot of the ratio of peak areas A-PII/A-PI as a function of time.

In order to partially avoid peak overlap and to help the assignment of the peaks, ligand exchange reactions were carried out with enantiopure Au_{38} clusters. The two enantiomers of $Au_{38}(2\text{-PET})_{24}$ were separated following the reported procedure[40], and the purity of the enantiomers was confirmed by chiral HPLC. A-$Au_{38}(2\text{-PET})_{24}$ (Fig. 6.4) clusters were mixed with free R/S-BiDi at molar ratio 1:50 at room temperature and HPL chromatograms were recorded every 4 hours. Fig. 6.4 A shows that two new peaks arise simultaneously at retention times of 48min (A-PI) and 83min (A-PII) already after 4 hours. The two peaks arise simultaneously, as expected for parallel reactions, indicating that they belong to the two diastereomers of A-$Au_{38}(2\text{-PET})_{22}(R/S\text{-BiDi})_1$. With increasing reaction time, the intensity of A-$Au_{38}(2\text{-PET})_{24}$ decreases and A-PI and A-PII increase progressively. Interestingly, the intensity of the A-PI and A-PII peaks is not equal, A-PII being predominant. The peaks were integrated and a plot of the ratio of peak areas A-PII/A-PI as a function of time is shown

in Fig. 6.4 B. At short reaction times (before 20h) the ratio between A-PII and A-PI was nearly stable and increased afterwards, which may be due to subsequent further exchange reactions (second exchange etc). The above experiment shows that the ligand exchange is diastereoselective in a similar fashion as was reported for the rigid chiral dithiol BINAS. In that case R-BINAS preferably reacted with A-$Au_{38}(2\text{-PET})_{24}$[28]. Here the initial A-PII/A-PI peak ratio is 2.15 (Fig. 6.4 B), which corresponds to the ratio of the rate constants at 4h (parallel reaction). This translates into a diastereomeric excess of 36%. For the BINAS case the diastereomeric excess was 60%[28]. The higher value for BINAS seems reasonable given the larger size of BINAS compared to R/S-BiDi, which enhances the influence of steric factors.

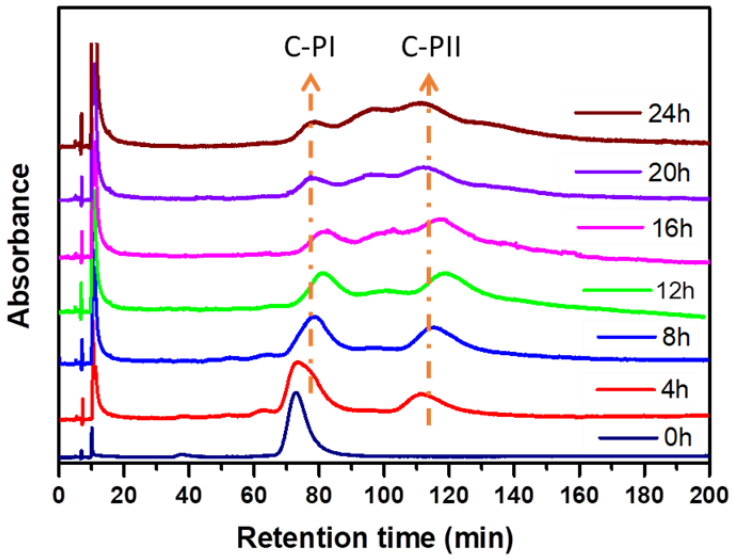

Figure 6.5 HPL Chromatograms of ligand exchange reaction between C-$Au_{38}(2\text{-PET})_{24}$ and Bi-Di. The sample was put at room temperature and the chromatograms were recorded every 4 hours. Two main peaks are marked as C-PI (80min) and C-PII (112min).

The reaction between C-$Au_{38}(2\text{-PET})_{24}$ and R/S-BiDi shows similar behavior as shown in Fig. 6.5. A new peak at retention time of 115 min (C-PII) is evident. Another peak (C-PI) appears as a shoulder peak around 80 min partly overlapping with parent cluster. From the evolution of the peaks with time it becomes clear that C-PII is the predominant peak. Further peaks appear as these reactions progress at 60 min and 110 min (Fig. 6.4 A) from A-$Au_{38}(2\text{-PET})_{24}$,

and at 95 min and 125 min (Fig. 6.5) from C-Au_{38}(2-PET)$_{24}$. The peaks are proposed to belong to exchange species with two BiDi molecules in their ligands shell.

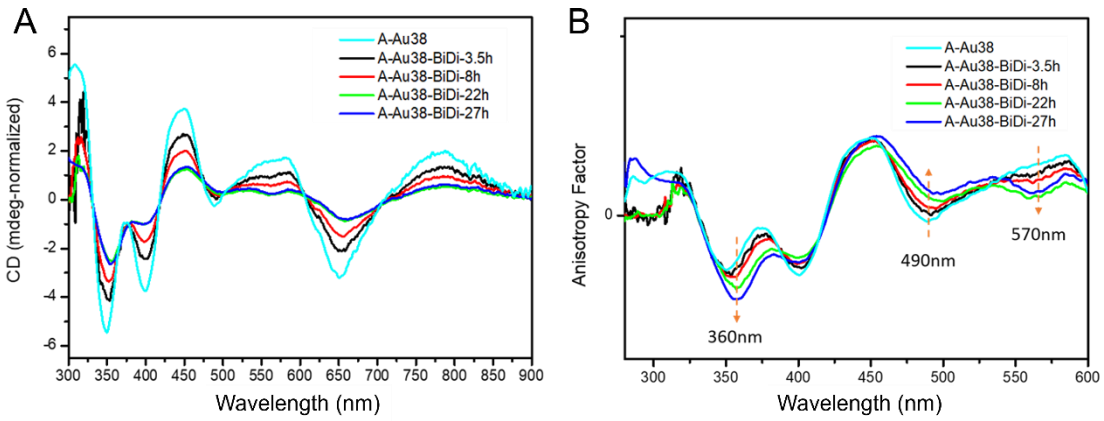

Figure 6.6 (A) CD spectra and (B) Anisotropy factors of A-Au_{38}(2-PET)$_{24}$ during ligand exchange reaction with BiDi. The sample was at room temperature and the spectrum was recorded over time. CD spectra have been normalized to -1 at 375nm.

The diastereoselective ligand exchange process can also be evidenced by circular dichroism (CD), as showed in Fig. 6.6 A. CD spectra of A-Au_{38}(2-PET)$_{24}$ during ligand exchange with R/S-BiDi have been recorded over time. The normalized spectra (at 375 nm, -1) clearly showed changes with reaction time. To investigate the evolution of optical activity, the concentration-independent anisotropy factors g=θ[mdeg]/(32980xA) were calculated (Fig. 6.6 B). With longer reaction time, the anisotropy factor of the sample increased at 360 nm and 490 nm, in addition, a new peak appeared around 570 nm. As we stated before, the free R/S-BiDi molecule is not optically active, so the changes observed in the CD spectra result from the ligand exchange of R/S-BiDi on the cluster. The change in the optical activity is because the two formed diastereomers A-Au_{38}(2-PET)$_{22}$(R-BiDi)$_1$ and A-Au_{38}(2-PET)$_{22}$(S-BiDi)$_1$ have different CD spectra and in addition they are not equally abundant. Furthermore, instead of A-Au_{38}(2-PET)$_{24}$, achiral Au_{25}(2-PET)$_{18}$ clusters were used for the ligand exchange reaction with R/S-BiDi (Additional information). After ligand exchange reaction the clusters

were passed through a SEC column and the composition of different fractions were revealed with MALDI-TOF, which indicated that fraction 1 and fraction 2 mainly contain Au_{25} clusters with one R/S-BiDi ligand in their ligand shell. As expected the corresponding CD spectra show no signal (Additional information).

To assign the predominant diastereomer, A-Au_{38}(2-PET)$_{22}$(S-BiDi)$_1$ or A-Au_{38}(2-PET)$_{22}$(R-BiDi)$_1$, (C-Au_{38}(2-PET)$_{22}$(R-BiDi)$_1$ or C-Au_{38}(2-PET)$_{22}$(S-BiDi)$_1$), Density Functional Theory (DFT) was used to calculate the corresponding energy of the four clusters as illustrated in Fig. 6.3. Here, –SCH_3 was used as the ligand to reduce computational cost. Table 6.1 gives the energies of the different stereoisomers, relative to the most stable one, C-Au_{38}(SCH_3)$_{22}$(S-BiDi)$_1$. From the relative energy of those four stereoisomers, it can be inferred that A-Au_{38}(2-PET)$_{22}$(R-BiDi)$_1$ is more stable than A-Au_{38}(2-PET)$_{22}$(S-BiDi)$_1$ and C-Au_{38}(2-PET)$_{22}$(S-BiDi)$_1$ is more stable than C-Au_{38}(2-PET)$_{22}$(R-BiDi)$_1$. We note that the calculated energy of the enantiomeric structures is not identical, which is due to the slightly different orientation of the –CH_3 groups in the corresponding structures after DFT optimization. It is important to note that the experiment shows that the rate constants for the formation of the two possible cluster diastereomers are different whereas the DFT calculations refer to the relative stability of the diastereomers.

Table 6.1 Relative energy of Au_{38} clusters with one BiDi ligand in the ligand shell, calculated by DFT.

Enantiomer	Cluster	Potential energy
A-Au38	A-Au38-R-BiDi	0.032 eV
	A-Au38-S-BiDi	0.128 eV
C-Au38	C-Au38-R-BiDi	0.100 eV
	C-Au38-S-BiDi	0.0 eV

To support this assignment CD spectroscopy was used. We collected the predominant cluster species in HPLC experiments (clusters from A-PII (Fig.

6.4 A) and C-PII (Fig. 6.5)) and recorded the corresponding CD spectra separately (Fig. 6.7 A). CD spectra were then calculated using a model $Au_{38}(SCH_3)_{24}$ cluster instead of $Au_{38}(2\text{-PET})_{24}$ used in the experiments. This approximation was justified by the good agreement between the experimental CD spectra of enantiopure $Au_{38}(2\text{-PET})_{24}$ and the calculated CD spectra of $Au_{38}(SCH_3)_{24}$ clusters (Additional information). As shown in Fig. 6.7 A, upon exchange with R/S-BiDi the band at 350 nm (band f in the figures) became more dominant with respect to the 400 nm band, such that the latter became a shoulder peak.

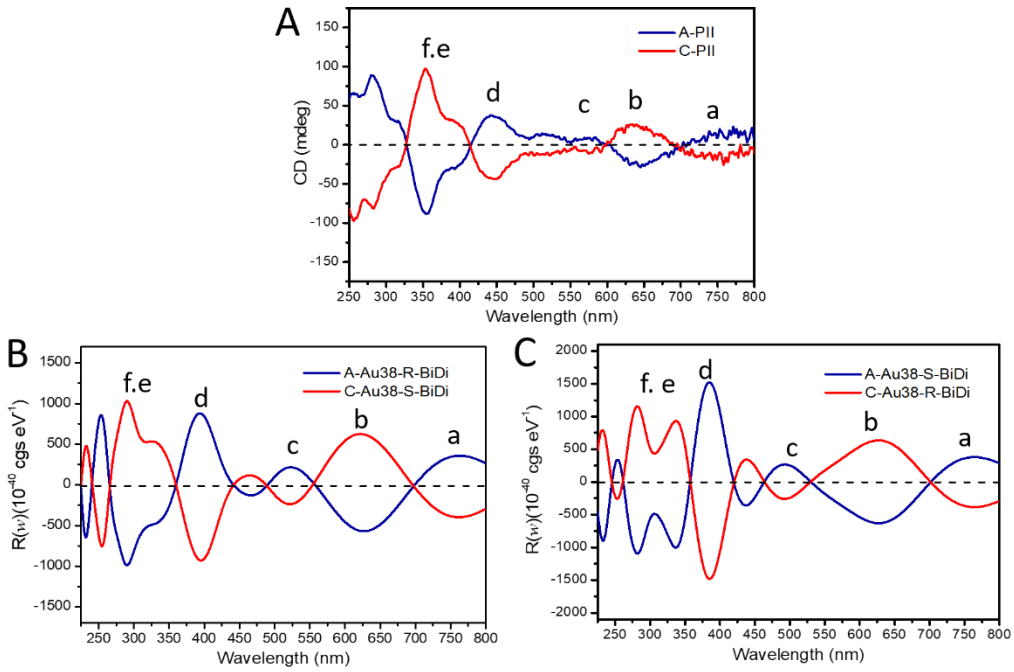

Figure 6.7 Experimental and calculated CD spectra of Au_{38} species. (A) Experimental samples were collected from A-PII and C-PII, (B) Calculated CD spectra of A-$Au_{38}(SCH_3)_{22}$(R-BiDi)$_1$ and C-$Au_{38}(SCH_3)_{22}$(S-BiDi)$_1$, (C) Calculated CD spectra of A-$Au_{38}(SCH_3)_{22}$(S-BiDi)$_1$ and C-$Au_{38}(SCH_3)_{22}$(R-BiDi)$_1$. Calculations were done by real-time propagation time-dependent DFT method using GPAW code[48]. For the calculations 2-PET ligands were substituted by $–SCH_3$.

The salient chiroptical signal at 280 nm corresponds to absorption of free R/S-BiDi (Fig. 6.1 C). CD spectra calculated for the more stable species A-$Au_{38}(SCH_3)_{22}$(R-BiDi)$_1$ and C-$Au_{38}(SCH_3)_{22}$(S-BiDi)$_1$ are shown in Fig. 6.7 B. These spectra match very well with the experimental CD spectra of the

dominant $Au_{38}(2\text{-}PET)_{22}(R/S\text{-}BiDi)_1$ species in the ligand exchange experiment apart from a shift of maximum 50 nm. The calculated CD spectra of the minor species (according to the calculated energies) A-$Au_{38}(SCH_3)_{22}$(S-BiDi)$_1$ and C-$Au_{38}(SCH_3)_{22}$(R-BiDi)$_1$ are shown in Fig. 6.7 C. The match with the experimental CD spectra in Fig. 6.7 A is less good compared to the CD spectra of the more stable species, particularly in the region between 300 nm and 400 nm (bands d-f). Note that we were not able to record the CD spectra of the minor species (peaks A-PI and C-PI) due to the very low amount of sample and the peak overlaps in the HPLC separation.

In order to highlight the influence of the chiral ligand on the chiroptical properties, we subtracted the CD spectra of the pure Au_{38} cluster from the corresponding $Au_{38}(SR)_{22}(R/S\text{-}BiDi)_1$ species both for the experimental and for the calculated spectra. These difference spectra show still good agreement between experiments and calculation (Additional information). Based on the analysis above we assign the major peaks in the HPLC experiments, A-PII and C-PII, respectively, to A-$Au_{38}(2\text{-}PET)_{22}$(R-BiDi)$_1$ and C-$Au_{38}(2\text{-}PET)_{22}$(S-BiDi)$_1$, respectively. Therefore, the minor peaks in the HPLC experiments A-PI and C-PI, respectively, correspond to A-$Au_{38}(2\text{-}PET)_{22}$(S-BiDi)$_1$ and C-$Au_{38}(2\text{-}PET)_{22}$(R-BiDi)$_1$, respectively. Thus, R-BiDi preferentially exchanges with anti-clockwise A-Au_{38} and S-BiDi prefers the clockwise C-Au_{38} cluster. This is consistent with the diastereoselective ligand exchange between Au_{38} and BINAS, where the same preferences (R-BINAS prefers A-Au_{38}) were found[28].

With these assignments at hand, we can now focus on dynamic processes of the ligand exchanged species $Au_{38}(2\text{-}PET)_{22}(R/S\text{-}BiDi)_1$, namely racemization of the cluster framework and intercluster ligand exchange, with a focus on the configuration of R/S-BiDi during these processes. Intercluster ligand exchange of the dithiol BINAS takes place at 70^{o}C but not at room temperature as has been shown recently[36]. Note that this is in contrast to monothiols like

1-butanethiol and 2-PET which easily exchange at room temperature[13]. Here we studied the behavior of R/S-BiDi in intercluster ligand exchange at room temperature and at 70°C. For this purpose, $Au_{25}(2\text{-PET})_{18}$ and $Au_{38}(2\text{-PET})_{24-2x}(R/S\text{-BiDi})_x$ were mixed (average x = 1.95), then the sample was put at 70°C for 24h followed by recording MALDI-TOF. A reference sample was kept at room temperature. The conclusion that intercluster R/S-BiDi ligand exchange needs elevated temperatures was clearly evidenced by the observation of $Au_{25}(2\text{-PET})_{16}(R/S\text{-BiDi})_1$ at 70°C and its absence at room temperature. However, we should mention that even at 70°C the ligand exchange is not very fast considering that on average 0.42 R/S-BiDi ligands were observed on the Au_{25} clusters after 24h whereas the initial Au_{38} sample contained on average 1.95 R/S-BiDi ligands.

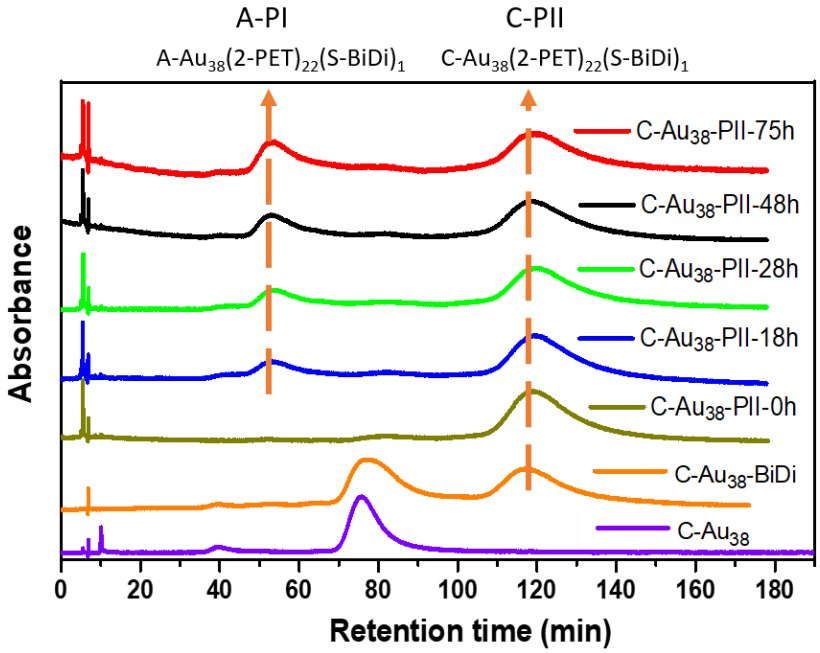

Figure 6.8 Evolution of HPL chromatograms with time when heating $C\text{-}Au_{38}(2\text{-PET})_{22}(S\text{-BiDi})_1$ (C-PII) to 70°C. As reference the chromatograms of $C\text{-}Au_{38}(2\text{-PET})_{24}$ (bottom) and after ligand exchange with BiDi (second from bottom) are shown. The latter sample was used for the collection of $C\text{-}Au_{38}(2\text{-PET})_{22}(S\text{-BiDi})_1$.

In order to study the dynamic processes of $Au_{38}(2\text{-PET})_{22}(R/S\text{-BiDi})_1$ (ligand exchange, racemization), we collected $C\text{-}Au_{38}(2\text{-PET})_{22}(S\text{-BiDi})_1$ in several HPLC runs (peak C-PII, Fig. 6.5). As illustrated in Fig. 6.8 this species can be

isolated and is stable at room temperature as re-injection into the HPLC system shows only one major peak besides a trace amount of C-Au_{38}(2-PET)$_{24}$ (small peak at 80 min likely due to incomplete initial separation). The sample was then heated to 70^{o}C and HPL chromatograms were measured over time. After 18 hours, a new peak with retention time around 50 min was observed corresponding to peak A-PI (A-Au_{38}(2-PET)$_{22}$(S-BiDi)$_1$), and the intensity of the new peak increased with heating time. However, there was no visible peak at 83 min (A-PII) which would indicate A-Au_{38}(2-PET)$_{22}$(R-BiDi)$_1$. These experiments clearly show that the system evolves as part of the clusters invert the handedness of the Au-S framework. However, during these processes the configuration of R/S-BiDi ligand is retained, despite the fact that free R/S-BiDi easily racemizes. We conclude that R/S-BiDi does not desorb from the cluster, which would cause the appearance of the other enantiomer of R/S-BiDi. In contrast, the conservation of the configuration of R/S-BiDi indicates that during the dynamic cluster processes the R/S-BiDi ligand is sufficiently confined to prevent inversion. An analogous experiment was performed with A-Au_{38}(2-PET)$_{22}$(R-BiDi)$_1$ (Additional information). After ligand exchange with A-Au_{38}(2-PET)$_{24}$ and R/S-BiDi, A-PII was collected, the sample was heated to 70^{o}C, and the reaction was followed by HPL chromatography. Although in this case C-PI and A-PII peaks overlap, it is clear that with time peak C-PI appears, belonging to C-Au_{38}(2-PET)$_{22}$(R-BiDi)$_1$ and no C-PII is visible at 120 min, which would indicate C-Au_{38}(2-PET)$_{22}$(S-BiDi)$_1$. Hence, also in this experiment the absolute configuration of R/S-BiDi is retained.

The evolution of species as observed by HPLC (Fig. 6.8) may involve several processes, notably the inversion of the Au-S framework of Au_{38}(2-PET)$_{22}$(R/S-BiDi)$_1$ and the exchange of R/S-BiDi between clusters. The contribution of each process to the overall observation is difficult to judge. To explain the observations, we can propose two mechanisms as shown in Scheme 6.1 and both could actually contribute. Mechanism I is simply the inversion of

the Au-S framework of the $Au_{38}(2\text{-PET})_{22}(R/S\text{-BiDi})_1$ clusters (epimerization), for example C-$Au_{38}(2\text{-PET})_{22}(S\text{-BiDi})_1$ is directly transformed to A-$Au_{38}(2\text{-PET})_{22}(S\text{-BiDi})_1$. In mechanism II, the overall result is the same, but it is a two steps mechanism involving ligand exchange. We note that in the experiments we see traces of A-$Au_{38}(2\text{-PET})_{24}$ and C-$Au_{38}(2\text{-PET})_{24}$ clusters, probably stemming from the HPLC separation/collection process. These clusters racemize very fast at 70°C[37]. This could be the main mechanism for the inversion of the Au-S framework. In addition, ligand exchange between clusters could take place: C-$Au_{38}(2\text{-PET})_{22}(S\text{-BiDi})_1$ reacts with A-$Au_{38}(2\text{-PET})_{24}$ to form A-$Au_{38}(2\text{-PET})_{22}(S\text{-BiDi})_1$ and C-$Au_{38}(2\text{-PET})_{24}$ (the latter can racemize easily).

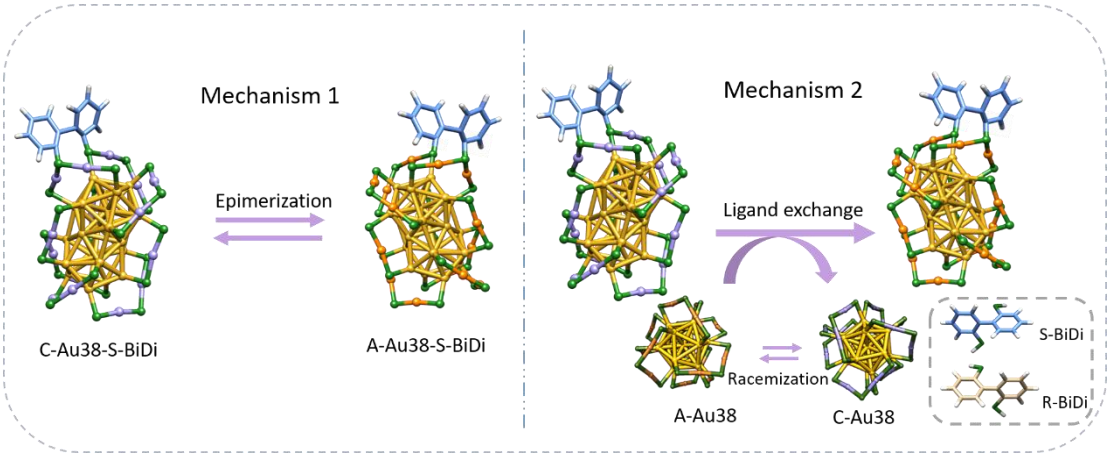

Scheme 6.1 The evolution of Au-S framework via simple inversion (M1) and two steps mechanism (M2). For clockwise (counter-clockwise) clusters the color of the gold atom in staples is violet (orange).

From the experimental data shown above it is clear is that during the step involving the epimerization of $Au_{38}(2\text{-PET})_{22}(S\text{-BiDi})_1$ and/or intercluster ligand exchange of R/S-BiDi, the absolute configuration of the ligand is retained. This excludes mechanisms where R/S-BiDi desorbs from the cluster (which would lead to its racemization, in contrast to observation), and furthermore indicates that during these processes the ligand is confined, which prevents its racemization. We note that this finding is in support of a mechanism where ligand exchange takes place during a collision between

clusters within a dimeric species as suggested before[13,51]. This ligand offers a powerful strategy to study molecular level details of dynamic processes involving thiolate-protected metal clusters.

6.4 Conclusion

In summary, ligand exchange with chiral dithiol (R/S-BiDi) has been shown to be diastereoselective. Calculations show that R-BiDi (thermodynamically) prefers A-Au_{38} clusters and S-BiDi is more stable on C-Au_{38} clusters. The same preference was found experimentally for the kinetics of the ligand exchange (R-BiDi reacts faster with A-Au_{38} clusters). More importantly, it was observed that the configurationally labile BiDi ligand retains its configuration during dynamic cluster processes i. e. cluster epimerization and/or intercluster ligand exchange. Racemization of the configurationally labile BiDi molecule is hindered after adsorption on the cluster surface. The absence of racemization of the ligand during epimerization of the cluster and/or ligand exchange shows that the ligand is confined during these processes and does not desorb into solution.

6.5 Additional information

6.5.1 external characterization of CD, MALDI and HPLC spectra

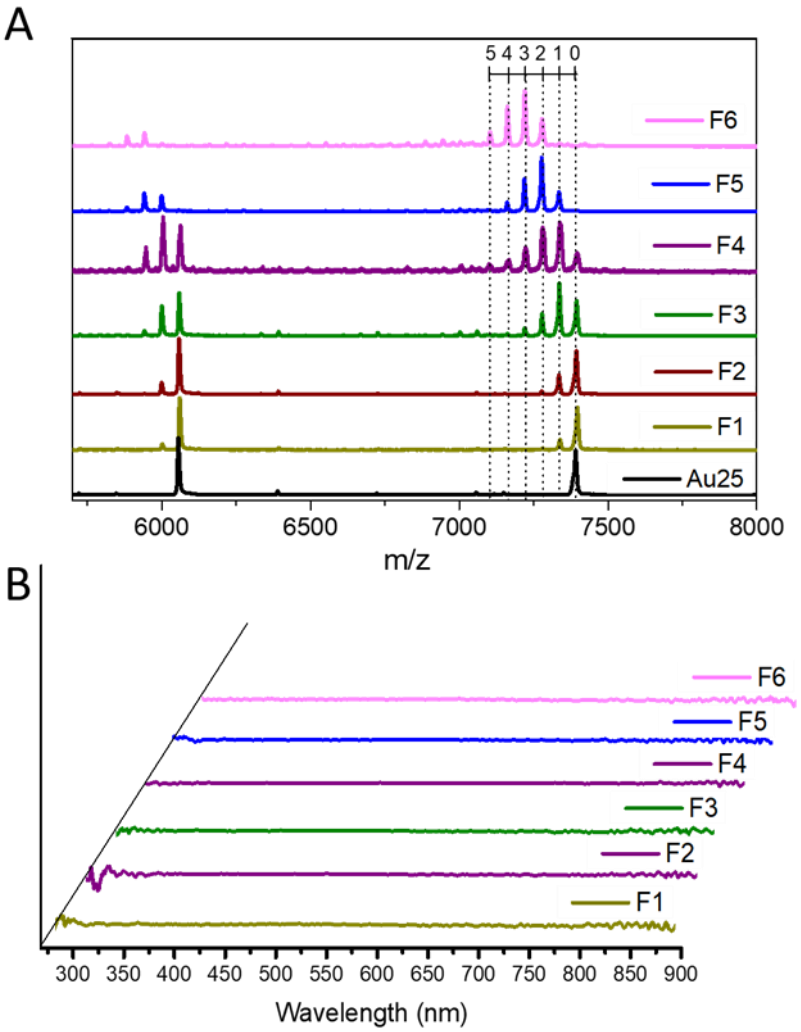

Figure 6.9 MALDI-TOF (A) and CD spectra (B) of a sample prepared by ligand exchange of $Au_{25}(2\text{-PET})_{18}$ cluster with BiDi. After ligand exchange the sample was passed over a size exclusion column and six fractions were collected. The labels in panel A corresponds to the number of BiDi ligands of the cluster.

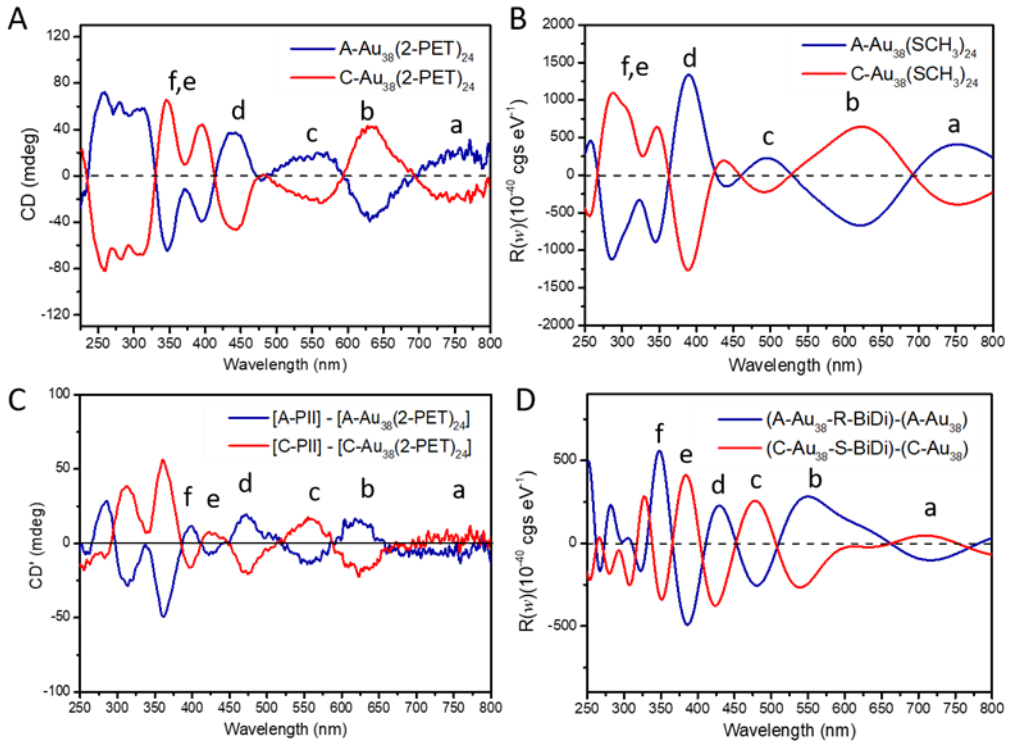

Figure 6.10 Experimental and calculated CD spectra of $Au_{38}(SR)_{24}$ clusters. (A) Experimental CD spectra of enantiopure A/C-$Au_{38}(2\text{-PET})_{24}$; (B) Calculated CD spectra of enantiopure A/C-$Au_{38}(SCH_3)_{24}$; (C) and (D) Experimental and calculated signal after subtracting the CD spectra of enantiopure $Au_{38}(SR)_{24}$ from the corresponding cluster with one BiDi in its ligand shell. Calculations were performed with real-time Density Functional Theory Method in GPAW code. For the experimental spectra the clusters were dissolved in dichloromethane and the spectra were recorded at the same concentration for the two enantiomers.

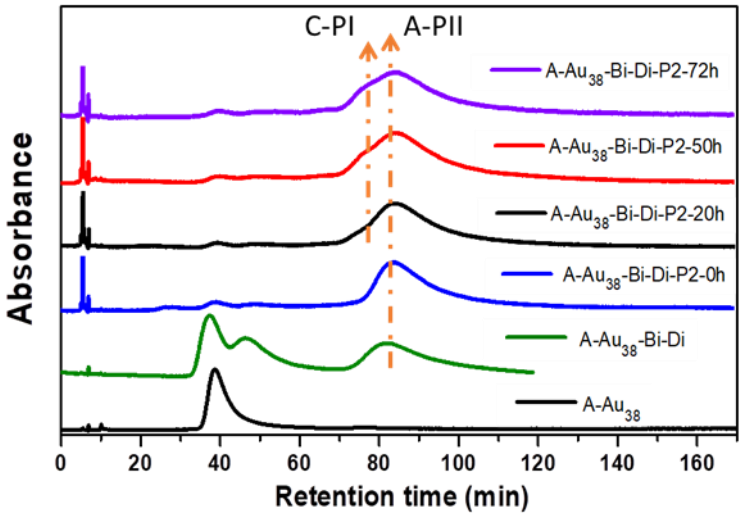

Figure 6.11 HPL Chromatograms of A-$Au_{38}(2\text{-PET})_{22}(R\text{-BiDi})_1$ sample at 70°C as a function of time. A-PII corresponds to A-$Au_{38}(2\text{-PET})_{22}(R\text{-BiDi})_1$, and C-PI corresponds to C-$Au_{38}(2\text{-PET})_{22}(R\text{-BiDi})_1$.

6.5.2 XYZ coordinates of the clusters mentioned in this study

XYZ structure coordinates of [A-Au_{38}-R-BiDi], [A-Au_{38}-S-BiDi], [C-Au_{38}-R-BiDi], [C-Au_{38}-S-BiDi], [A-Au_{38}] and [C-Au_{38}] available, see DOI :10.1039/d1sc01702k

6.6 References

(1) Qian, H.; Zhu, M.; Wu, Z.; Jin, R. *Acc. Chem. Res.* **2012**, *45*, 1470.

(2) Tsukuda, T. *Bull. Chem. Soc. Jpn.* **2012**, *85*, 151.

(3) Aikens, C. M. *Acc. Chem. Res.* **2018**, *51*, 3065.

(4) Li, G.; Jin, R. *Acc. Chem. Res.* **2013**, *46*, 1749.

(5) Kawawaki, T.; Negishi, Y. *Nanomaterials* **2020**, *10*, 238.

(6) Zhou, M.; Higaki, T.; Li, Y.; Zeng, C.; Li, Q.; Sfeir, M. Y.; Jin, R. *J. Am. Chem. Soc.* **2019**, *141*, 19754.

(7) Sels, A.; Azoulay, R.; Buma, W. J.; Koenis, M. A. J.; Nicu, V. P.; Bürgi, T. *The Journal of Physical Chemistry C* **2019**, *123*, 22586.

(8) Wu, Z.; Wang, M.; Yang, J.; Zheng, X.; Cai, W.; Meng, G.; Qian, H.; Wang, H.; Jin, R. *Small* **2012**, *8*, 2028.

(9) Shu, T.; Wang, J.; Su, L.; Zhang, X. *Anal. Chem.* **2016**, *88*, 11193.

(10) Katla, S. K.; Zhang, J.; Castro, E.; Bernal, R. A.; Li, X. *ACS Appl. Mater. Interfaces* **2018**, *10*, 75.

(11) Yang, D.; Yang, G.; Gai, S.; He, F.; An, G.; Dai, Y.; Lv, R.; Yang, P. *Nanoscale* **2015**, *7*, 19568.

(12) Huang, Z.; Ishida, Y.; Narita, K.; Yonezawa, T. *J. Phys. Chem. C* **2018**, *122*, 18142.

(13) Salassa, G.; Sels, A.; Mancin, F.; Bürgi, T. *ACS Nano* **2017**, *11*, 12609.

(14) Shibu, E. S.; Muhammed, M. A. H.; Tsukuda, T.; Pradeep, T. *J. Phys. Chem. C* **2008**, *112*, 12168.

(15) Wang, Y.; Nieto-Ortega, B.; Bürgi, T. *Chemical Communications* **2019**, *55*, 14914.

(16) Kluenker, M.; Mondeshki, M.; Tahir, M. N.; Tremel, W. *Langmuir* **2018**, *34*, 1700.

(17) Heinecke, C. L.; Ni, T. W.; Malola, S.; Mäkinen, V.; Wong, O. A.; Häkkinen, H.; Ackerson, C. J. *J. Am. Chem. Soc.* **2012**, *134*, 13316.

(18) Knoppe, S.; Bürgi, T. *PCCP* **2013**, *15*, 15816.

(19) Ni, T. W.; Tofanelli, M. A.; Phillips, B. D.; Ackerson, C. J. *Inorg. Chem.* **2014**, *53*, 6500.

(20) Niihori, Y.; Kikuchi, Y.; Kato, A.; Matsuzaki, M.; Negishi, Y. *ACS Nano* **2015**, *9*, 9347.

(21) Rojas-Cervellera, V.; Raich, L.; Akola, J.; Rovira, C. *Nanoscale* **2017**, *9*, 3121.

(22) Beqa, L.; Deschamps, D.; Perrio, S.; Gaumont, A.-C.; Knoppe, S.; Bürgi, T. *J. Phys. Chem. C* **2013**, *117*, 21619.

(23) Kang, X.; Chong, H.; Zhu, M. *Nanoscale* **2018**, *10*, 10758.

(24) Fields-Zinna, C. A.; Parker, J. F.; Murray, R. W. *J. Am. Chem. Soc.* **2010**, *132*, 17193.

(25) Niihori, Y.; Kurashige, W.; Matsuzaki, M.; Negishi, Y. *Nanoscale* **2013**, *5*, 508.

(26) Pengo, P.; Bazzo, C.; Boccalon, M.; Pasquato, L. *Chem. Commun.* **2015**, *51*, 3204.

(27) Hossain, S.; Kurashige, W.; Wakayama, S.; Kumar, B.; Nair, L. V.; Niihori, Y.; Negishi, Y. *J. Phys. Chem. C* **2016**, *120*, 25861.

(28) Knoppe, S.; Azoulay, R.; Dass, A.; Bürgi, T. *J. Am. Chem. Soc.* **2012**, *134*, 20302.

(29) Fernando, A.; Aikens, C. M. *J. Phys. Chem. C* **2015**, *119*, 20179.

(30) Fernando, A.; Aikens, C. M. *J. Phys. Chem. C* **2016**, *120*, 14948.

(31) Jupally, V. R.; Kota, R.; Dornshuld, E. V.; Mattern, D. L.; Tschumper, G. S.; Jiang, D.-e.; Dass, A. *J. Am. Chem. Soc.* **2011**, *133*, 20258.

(32) Molina, B.; Sánchez-Castillo, A.; Knoppe, S.; Garzón, I. L.; Bürgi, T.; Tlahuice-Flores, A. *Nanoscale* **2013**, *5*, 10956.

(33) Knoppe, S.; Dharmaratne, A. C.; Schreiner, E.; Dass, A.; Bürgi, T. *J. Am. Chem. Soc.* **2010**, *132*, 16783.

(34) Knoppe, S.; Michalet, S.; Bürgi, T. *J. Phys. Chem. C* **2013**, *117*, 15354.

(35) Si, S.; Gautier, C.; Boudon, J.; Taras, R.; Gladiali, S.; Bürgi, T. *J. Phys. Chem. C* **2009**, *113*, 12966.

(36) Wang, Y.; Nieto-Ortega, B.; Bürgi, T. *Nature Communications* **2020**, *11*, 4562.

(37) Knoppe, S.; Dolamic, I.; Bürgi, T. *J. Am. Chem. Soc.* **2012**, *134*, 13114.

(38) Malola, S.; Hakkinen, H. *J. Am. Chem. Soc.* **2019**, *141*, 6006.

(39) Fabbri, D.; Delogu, G.; De Lucchi, O. *J. Org. Chem.* **1993**, *58*, 1748.

(40) Dolamic, I.; Knoppe, S.; Dass, A.; Bürgi, T. *Nat. Commun.* **2012**, *3*, 798.

(41) Enkovaara, J.; Rostgaard, C.; Mortensen, J. J.; Chen, J.; Dułak, M.; Ferrighi, L.; Gavnholt, J.; Glinsvad, C.; Haikola, V.; Hansen, H. A.; Kristoffersen, H. H.; Kuisma, M.; Larsen, A. H.; Lehtovaara, L.; Ljungberg, M.; Lopez-Acevedo, O.; Moses, P. G.; Ojanen, J.; Olsen, T.; Petzold, V.; Romero, N. A.; Stausholm-Møller, J.; Strange, M.; Tritsaris, G. A.; Vanin, M.; Walter, M.; Hammer, B.; Häkkinen, H.; Madsen, G. K. H.; Nieminen, R. M.; Nørskov, J. K.; Puska, M.; Rantala, T. T.; Schiøtz, J.; Thygesen, K. S.; Jacobsen, K. W. *J. Phys.: Condens. Matter* **2010**, *22*, 253202.

(42) Perdew, J. P.; Burke, K.; Ernzerhof, M. *Phys. Rev. Lett.* **1996**, *77*, 3865.

(43) Perdew, J. P.; Burke, K.; Ernzerhof, M. *Phys. Rev. Lett.* **1997**, *78*, 1396.

(44) Tkatchenko, A.; Scheffler, M. *Phys. Rev. Lett.* **2009**, *102*, 073005.

(45) Henkelman, G.; Jónsson, H. *J. Chem. Phys* **2000**, *113*, 9978.

(46) Becke, A. D. *Physical Review A* **1988**, *38*, 3098.

(47) Lee, C.; Yang, W.; Parr, R. G. *Physical Review B* **1988**, *37*, 785.

(48) Makkonen, E.; Rossi, T. P.; Larsen, A. H.; Lopez-Acevedo, O.; Rinke, P.; Kuisma, M.; Chen, X. *arXiv: Chemical Physics* **2020**.

(49) Kessler, H. *Angew. Chem. Int.* **1970**, *9*, 219.

(50) Masson, E. *Org. Biomol. Chem* **2013**, *11*, 2859.

(51) Krishnadas, K. R.; Baksi, A.; Ghosh, A.; Natarajan, G.; Som, A.; Pradeep, T. *Acc. Chem. Res.* **2017**, *50*, 1988.

General conclusion and outlook

Ligand exchange reaction on thiolate-protected clusters, after more than 20 years since the first report by Murry and co-workers, has become an important propulsion for the development and application of clusters. Many studies on the reaction mechanism and processes such as addition of various functions to clusters, and surface modification have been launched and flourished. In this thesis, we have explored several different topics in this field to further deepen the understanding of the ligand exchange reactions.

During the ligand exchange reaction between $Au_{25}(SR)_{18}$ clusters and chiral ligand (R- or S-2-phenyl-propane-1-thiol), a size transformation from $Au_{25}(SR)_{18}$ to $Au_{28}(SR)_{21}$ has been discovered. Unexpectedly, the process occurred under mild condition (room temperature, low ligand excess), which is in contrast with the reported cases. The Van der Waals interactions within the ligand shell and the 'bulkiness' of the methyl are the inferred driving force for the reaction here. The new $Au_{28}(SR)_{21}$ cluster is a side-product of the LERs and has been isolated from the reaction mixture for the first. The observations indicates that the steric hindrance and geometry of the ligand play an important role for the transformation.

By using a chiral fluoro-substituted R-BINAS ligand and the related enantiopure R/S-BINAS molecule, the stereoelectronic and stereospecific effects of ligand during LER on achiral Au_{25} cluster has been investigated. Here the fluoro-substituted BINAS slows down the LER reaction on the molecular and related clusters level even when only one ligand has been exchanged. This indicated that the stereoelectronic effect is global and can be transmitted at the entire cluster surface. However, no significant stereospecific effect could be observed as the different enantiomers did not display visible difference during LERs with the achiral clusters, at least for the initial stage of the ligand exchange, which means that this function is more local and limited. Electronic effects could emerge as a potential strategy to better control the

modification of the ligand shell of clusters by LERs.

As proved before, the LERs with intrinsically chiral Au_{38} clusters and chiral dithiol BINAS ligand is diastereoselective. During our project we further confirmed that with small amount of chiral molecular adsorbed on the surface of $Au_{38}(2\text{-PET})_{24}$. Surprisingly the system can amplify the enantiomeric excess at 70ºC without free ligand. Here the balance between left- and right-handed intrinsically chiral metal clusters has been broken, and the species evolve towards anticlockwise clusters. It is shown that the interplay between the diastereoselective ligand exchange, which introduces selectivity but does not change the A/C ratio, and the fast racemization of the $Au_{38}(2\text{-PET})_{24}$ is at the origin of this deracemization. By defining the chirality of the external ligand, we can determine the specific amplification of enantiomeric excess at nanoscale.

LERs with dithiols will drastically reduce the exchange numbers and number of possible diastereomers, and therefore it is easier to isolate isomers of clusters with mixed ligand shell. The dithiol ligand exchange between clusters also been demonstrated in this thesis. In addition, using a configurationally labile BiDi ligand, molecular level details of the dynamic processes of thiolate-protected clusters have been investigated. The absolute configuration retention of BiDi ligand during cluster racemization and/or ligand exchange between clusters, reveal that the ligand was confined on the cluster surface, and does not desorb into solution.

This thesis provides new insight into the LERs on gold nanoclusters and indicates new possibilities to make use of the dynamic nature of the clusters. As shown, this reaction really imparts various functions and offers great potential to modify the properties of the cluster. Future effort can focus on the LERs induced phase transfer, which will bridge the organic and inorganic phase systems and provide versatile nanomaterials. Also, concerning the flexible functionalization and preparation of multipurpose clusters, ligands which contain functional groups that are able to further react will be good candidates. In this flurishing field, there are still many bare avenues

that call for more exploration in the future.

List of Publications

1. **Wang, Y.**; Esko, M., Xi, C., Bürgi, T. Absolute configuration retention of a configurationally labile ligand during dynamic processes of thiolate protected gold cluster. *Chemical Science* **2021**, DOI: 10.1039/d1sc01702k.
2. **Wang, Y.**; Bürgi, T., Ligand exchange reactions on thiolate-protected gold nanoclusters. *Nanoscale Advances* **2021**, 3 (10), 2710
3. **Wang, Y.**; Nieto-Ortega, B.; Bürgi, T., Amplification of enantiomeric excess by dynamic inversion of enantiomers in deracemization of Au_{38} clusters. *Nature Communications* **2020**, 11 (1), 4562.
4. **Wang, Y.**, Nieto-Ortega, B., and Bürgi, T. Transformation from $[Au_{25}(SCH_2CH_2CH_2CH_3)_{18}]^0$ to $Au_{28}(SCH_2CH(CH_3)Ph)_{21}$ gold nanoclusters: gentle conditions is enough, *Chemical Communications* **2019,** *55*, 14914-14917.
5. **Wang, Y.**, Wang, X., Ma, X., Chen, Q., He, H., Nau, W. M., and Huang, F. Coassembly of Gold Nanoclusters with Nucleic Acids: Sensing, Bioimaging, and Gene Transfection, *Particle & Particle Systems Characterization* **2019,** *36*, 1900281.
6. Wang, X., **Wang, Y.**, He, H., Ma, X., Chen, Q., Zhang, S., Ge, B., Wang, S., Nau, W. M., and Huang, F. Deep-Red Fluorescent Gold Nanoclusters for Nucleoli Staining: Real-Time Monitoring of the Nucleolar Dynamics in Reverse Transformation of Malignant Cells, *ACS Applied Materials & Interfaces* **2017,** *9*, 17799-17806.
7. Wang, X., **Wang, Y**., He, H., Chen, X., Sun, X., Sun, Y., Zhou, G., Xu, H., and Huang, F. Steering graphene quantum dots in living cells: lighting up the nucleolus, *Journal of Materials Chemistry B* **2016,** *4*, 779-784.
8. Wang, X., He, H., **Wang, Y.,** Wang, J., Sun, X., Xu, H., Nau, W. M., Zhang, X., and Huang, F. Active tumor-targeting luminescent gold clusters with efficient urinary excretion, *Chemical Communications* **2016,** *52*, 9232-9235.

Curriculum vitae – Yanan Wang

Name, Surname**:**	**Yanan Wang**
Date of birth:	07.10.1991 in Shandong, P.R.China
Working address:	Department of physical chemistry University of Geneva Quai Ernest-Ansermet 30 CH-1211 Geneva 4, Switzerland
Tel:	+41(0)22 379 64 04
E-Mail:	Yanan.Wang@unige.ch

Education

Since 12/2017 **PhD student**,
Department of physical chemistry, University of Geneva, Switzerland
Supervisor: Prof. Dr. Thomas Bürgi

09/2010 - 07/2017 **Undergraduate & Graduate study**,
Department of Chemical Engineering, China University of Petroleum (East China), Qingdao, China
M.Sc. in Bioengineering GPA: 3.7/4
B.Sc. in Applied Chemistry GPA: 3.4/4

Awards and Prizes

2020 Chemistry travel award 2020, Switzerland

2017 Chinese Government Scholarship (2017-2021) CSC No.201706450070

2016 National Scholarship for graduate student (May)
The Excellent Graduate Student Oral Presentation Award of The 4th National Biophysical Chemistry Conference (June)

2015 The first class scholarship for Excellent Graduate Student Cadre

2013 National Encouragement Scholarship

Research Experience

05/2021 – date Ligand exchange reaction induced phase transfer of nanoclusters and probe functionalization.

11/2019 - 04/2021 Intercluster bidentate ligand exchange reactions: construction maintain and individual communication.

11/2018 - 10/2019 Amplification of enantiomeric excess of the $Au_{38}(2\text{-PET})_{24}$ cluster.

09/2017 - 10/2018 Size transformation of clusters induced by chiral LERs.

08/2016 - 07/2017 Characterization and application of Nucleic acid compounds with fluorescent gold nanoclusters.

08/2015 - 07/2016 Deep -Red Fluorescence Gold Nanoclusters for Nucleoli

Staining.

02/2015 - 08/2015 Steering graphene quantum dots in living cells: lighting up nucleolus.

08/2014 - 02/2015 Active tumor-targeting luminescent gold clusters with efficient urinary excretion.

10/2013 - 07/2014 Expression、purification and characterization of Bacteriorhodop in small fragment BR-CDEF protein.

Conferences

2021 5th SEED4CD Virtual Seminar (via Zoom), Chirality and its amplification in precise gold nanoclusters (invited talk).

2019 Chirality @ The Nanoscale conference (poster), Ascona, Switzerland.
The 6th International Symposium on Monolayer Protected Clusters (talk), Xiamen, China.

2016 Asian Federation of Biotechnology (AFOB) Summer Forum 2016, Qingdao, China.
The 7th International Symposium on Bioanalysis, Biomedical Engineering and Nanotechnology (poster), Changsha, China.
The 4rd National Conference on Biophysical Chemistry (talk), Hefei, China.

2014 The 3th National Conference on Biophysical Chemistry, Qingdao, China.

Research Interests

- Synthesis, decoration and functionalization of precise gold nanoclusters.
- Enantioseparation and application of chiral nanoclusters.
- Clinical Nanomedicine for diagnosis and therapy to cancer or other disease.

Technical Skills

- Knowledge of the synthesis of precise gold nanoclusters, fluorescent gold nanoclusters and cell cultivation techniques.
- Experience on purification of nanoclusters and chiral HPLC enantioseparation;
- Cell imaging with light microscopy, inversion fluorescence microscope, systematic training and skilful operation of Confocal Laser Scanning Microscopy (CLSM);
- Knowledge of the instruments utilized in academic research, such as UV-vis, FL, CD, HPLC, DLS, TEM, SEM and AFM.